

Technical Report

TR-24-01

December 2024



KINA (Kiruna Natural Analogue) project

Final report

W Russell Alexander (ed)

Ulf B Andersson (ed)

Rizlan Bernier-Latmani

Evelyne M Delbos

W Crawford Elliott

Tatsuya Fujimura

H Albert Gilg

Takahiro Goto

Natalia Jakus

Ryosuke Kikuchi

Leena Kiviranta

Sirpa Kumpulainen

Olivier X Leupin

Shuhei Nemoto

Tsubasa Otake

Cyprian Ozigbo

Helen A Pendlowski

Tsutomu Sato

Raphael Schneeberger

Patrik Sellin

Holly Stein

Satoru Suzuki

Daniel Svensson

Igor M Villa

J Marion Wampler

Aaron Zimmerman

SVENSK KÄRNBRÄNSLEHANTERING AB

SWEDISH NUCLEAR FUEL
AND WASTE MANAGEMENT CO

Box 3091, SE-169 03 Solna
Phone +46 8 459 84 00
skb.se

SVENSK KÄRNBRÄNSLEHANTERING

KINA (Kiruna Natural Analogue) project

Final report

W Russell Alexander¹ (editor), Ulf B Andersson² (editor), Rizlan Bernier-Latmani³, Evelyne M Delbos⁴, W Crawford Elliott⁵, Tatsuya Fujimura⁶, H Albert Gilg⁷, Takahiro Goto⁸, Natalia Jakus³, Ryosuke Kikuchi⁶, Leena Kiviranta⁹, Sirpa Kumpulainen⁹, Olivier X Leupin¹⁰, Shuhei Nemoto⁸, Tsubasa Otake⁶, Cyprian Ozigbo⁵, Helen A Pendlowski⁴, Tsutomu Sato⁶, Raphael Schneeberger¹⁰, Patrik Sellin¹¹, Holly Stein¹², Satoru Suzuki⁸, Daniel Svensson¹¹, Igor M Villa¹³, J Marion Wampler⁵, Aaron Zimmerman¹²

1 Bedrock Geosciences

2 Luossavaara-Kiirunavaara Aktiebolag (LKAB)

3 École Polytechnique Fédérale de Lausanne (EPFL)

4 James Hutton Institute

5 Georgia State University

6 Hokkaido University

7 Technische Universität München (TUM)

8 The Nuclear Waste Management Organization of Japan (NUMO)

9 Mitta

10 Nationale Genossenschaft für die Lagerung radioaktiver Abfälle (Nagra)

11 Svensk Kärnbränslehantering AB (SKB)

12 Applied Isotope Research for Industry and the Environment (AIRIE)

13 University of Bern and University of Milano Bicocca

Preface

The Kiruna Natural Analogue (KINA) is a collaborate project within the framework of the Implementing Geological Disposal of Radioactive Waste Technology Platform (IGT-TP).

The KINA project aims at investigating a smectite clay that has been in contact to a magnetite ore body for hundreds of millions of years under repository like conditions.

As significant clay alteration zones have been encountered in the Kiruna-type magnetite(-hematite)-apatite deposits, which are hosted in weakly to strongly altered/metamorphosed intermediate to acid volcanic and subvolcanic rocks. These up to 50 m thick soft alteration zones occur within ores and within the country rocks along the ore contact of the southern Kiirunavaara ore body, at various levels to depths of at least 1 200 m below surface, but also in zones further into the hanging wall and footwall lithologies of the deposit. The predominant clay mineral in the alteration zones of all deposits is a dioctahedral Fe-poor montmorillonite, but locally interstratified illite-smectite minerals are observed at Kiirunavaara and Malmberget. The expandable clay minerals have variable exchangeable cation compositions including significant Ca and in part Na and K.

The clays are locally associated with a distinct stilbite/stellerite mineralization that is characteristic for formation temperatures between about 50 and 120 °C. K-Ar data of various Na-exchanged size fractions from two soft altered gneiss samples from the Johannes ore body, Malmberget, which are dominated by R3-ordered illite-smectite, yielded age values ranging from 837 ± 14 Ma to 941 ± 15 Ma.

Preliminary data indicates that the clay contain a high amount of montmorillonite and that the swelling pressure and hydraulic conductivity is similar to that of commercial bentonites intended for repository use.

The driver for conducting the project was the unique opportunity to investigate bentonite that was buried under repository-like conditions and in contact to magnetite-hematite interfaces for hundreds of millions of years

The project scope was to show based on a natural analogue study:

- i. The durability of safety relevant properties of bentonite under repository like conditions for timescales the exceeds the repository time frame with orders of magnitude.
- ii. The chemical investigation of an Iron corrosion product-Bentonite interface.
- iii. Information on the erosion properties of bentonite.
- iv. The physical state of bentonite for retrievability.

The project methodology and task breakdown were:

- i. Sampling and in-situ characterization of the alteration zones.
- ii. Physico-chemical and mineralogical analyses of the smectite.
- iii. Age determination of the smectite and related phases.
- iv. Swelling pressure and hydraulic conductivity tests of smectite.

The KINA project is financed by Andra (F), Nagra (CH), NUMO (J), NWMO (CA), NWS (UK), Posiva (FI) and SKB (S) with in-kind contributions from LKAB (S).

Summary

The KINA project investigates the long-term behavior of bentonite as a barrier material in deep geological repositories for radioactive waste. By studying the natural clay transformation zones at the Kiirunavaara iron ore deposit in Kiruna, Sweden, the project provides critical insights into processes relevant to repository safety.

The project aims to investigate smectite-rich clay (effectively bentonite) that has been in contact with a magnetite ore for an extended period (probably in the order of hundreds of millions of years) under repository-relevant conditions in the Kiirunavaara ore body, northern Sweden. In many respects, the clay bodies in the Kiirunavaara deposit resemble a bentonite barrier in a repository. The project was initiated to further study the Kiirunavaara clay with focus on:

- understanding the very long-term behaviour of bentonite under conditions of direct relevance to deep geological disposal of radioactive waste,
- examination of potential long-term iron oxide minerals – bentonite interaction (as may occur in a repository),
- the potential for erosion of the bentonite barrier by groundwater in a deep geological repository,
- the potential impact of microbial populations in bentonite under repository conditions.

The key findings were:

1. **Geological Context:** The Kiirunavaara site hosts significant clay transformation zones associated with magnetite ore. These zones exhibit mineralogical changes over hundreds of millions of years, offering a natural laboratory for studying bentonite analogues.
2. **Mineral stability:** the clay zones in the Kiirunavaara site are rich in smectite and are placed in an environment that is similar to that of a nuclear waste repository. Both mineralogical and hydromechanical properties in Kiirunavaara clays are similar to those of industrial bentonites. This shows that bentonite can be stable over very long time scales in a repository environment.
3. **Bentonite-Iron Interaction:** novel data presented here indicate that Fe uptake by the natural, smectite-rich clays under repository-relevant conditions is minimal, even when the clays are in close proximity to the magnetite for extended periods of time.
4. **Microbial and Chemical Processes:** Ultra-pure DNA extraction has provided the first evidence for the presence of biomolecules in clays from the Kiirunavaara area. In addition, the study supports the existence of active microbial life related to Fe(III), NO_3^- and SO_4^{2-} metabolism with low molecular weight organic acids.
5. **Bentonite Erosion:** no chemical erosion through colloid formation, or sedimentation, will take place in the particular Kiruna smectite samples analysed here. It was noted that this is possibly because it is unlikely this sample has ever been exposed to Na-rich dilute groundwaters and that the amount of calcite present in the material has been sufficient to buffer the composition of the exchanger to a 100 % calcium form.

The question of clay age(s) has been addressed here with the novel data produced in the project indicating that the system is, not surprisingly, complex. Nevertheless, it is clear that all historical and novel data on the smectite-rich natural clays presented here indicate that they are significantly older than any timescales of relevance to a repository safety case.

The study underscores bentonite's stability as a barrier material but highlights some areas requiring attention, including:

- The potential impact of iron-clay interactions on bentonite performance.
- The importance of controlling groundwater chemistry to mitigate erosion.
- Long-term microbial activity and its effects on repository safety.

The findings contribute to global safety cases for deep geological repositories and emphasize the importance of natural analogues in understanding long-term barrier performance.

Sammanfattning

KINA-projektet undersöker bentonits långsiktiga beteende som barriärmaterial i djupa geologiska slutförvar för radioaktivt avfall. Genom att studera de naturliga lertransformationzonerna vid Kiirunavaaras järnmalmfyndighet i Kiruna, Sverige, ger projektet viktiga insikter i processer som är relevanta för slutförvarsäkerhet.

Projektets syfte är att undersöka smektitrik lera (i praktiken bentonit) som har varit i kontakt med magnetitmalm under en mycket lång tid (troligen i storleksordningen hundratals miljoner år) under förhållanden som är relevanta för slutförvar i Kiirunavaaras malmkropp i norra Sverige. I många avseenden liknar lerkropparna i Kiirunavaarafyndigheten en bentonitbarriär i ett slutförvar. Projektet initierades för att ytterligare studera Kiirunavaaralera med fokus på:

- att förstå bentonits mycket långsiktiga beteende under förhållanden som är direkt relevanta för djupa geologiska slutförvar för radioaktivt avfall,
- att undersöka potentiella långsiktiga interaktioner mellan järnoxidmineraler och bentonit (som kan uppstå i ett slutförvar),
- att utvärdera risken för erosion av bentonitbarriären genom grundvatten i ett djupt geologiskt slutförvar,
- att bedöma den potentiella påverkan av mikrobiella populationer i bentonit under slutförvarsförhållanden.

Nyckelresultaten var följande:

1. **Geologisk kontext:** Kiirunavaaraområdet har betydande lertransformationzoner kopplade till magnetitmalmen. Dessa zoner visar mineralogiska förändringar över hundratals miljoner år och fungerar som ett naturligt laboratorium för att studera bentonitanaloger.
2. **Mineralstabilitet:** Lerzonerna i Kiirunavaara är rika på smektit och finns i en miljö som liknar den i ett slutförvar för kärnavfall. Både de mineralogiska och hydromekaniska egenskaperna hos lerorna i Kiirunavaara liknar dem hos industriell bentonit. Detta visar att bentonit kan vara stabil över mycket långa tidsperioder i en slutförvarsmiljö.
3. **Bentonit-järninteraktioner:** Ny data visar att järnupptaget i de naturliga, smektitrika lerorna under förvarrelevanta förhållanden är minimalt, även när lerorna är i nära kontakt med magnetit under långa tidsperioder.
4. **Mikrobiella och kemiska processer:** Ultraren DNA-extraktion har för första gången påvisat närvaro av biomolekyler i lera från Kiirunavaaraområdet. Studien stöder också förekomsten av aktiv mikrobiell aktivitet kopplad till Fe(III)-, NO³⁻ och SO₄²⁻-metabolism med lågmolekylära organiska syror.
5. **Bentoniterosion:** Ingen kemisk erosion genom kolloidbildning eller sedimentation kommer att ske i de analyserade Kiirunasmektitproverna. Det noterades att detta sannolikt beror på att provet aldrig har utsatts för Na-rikt utspätt grundvatten och att mängden kalcit i materialet varit tillräcklig för att buffra sammansättningen av utbyteskationer till en 100 % kalciumform.

Frågan om lerans ålder har behandlats här, och den nya data som tagits fram inom projektet visar att systemet, föga förvånande, är komplext. Trots detta är det tydligt att alla historiska och nya data om de smektitrika naturliga lerorna som presenteras här indikerar att de är betydligt äldre än några tidsramar som är relevanta för en säkerhetsanalys av ett slutförvar.

Studien understryker bentonitens stabilitet som barriärmaterial men pekar på vissa områden som kräver vidare uppmärksamhet, inklusive:

- Den potentiella påverkan av järn-lera-interaktioner på bentonitens prestanda.
- Betydelsen av att kontrollera grundvattenkemin för att minska erosion.
- Långsiktig mikrobiell aktivitet och dess påverkan på slutförvarssäkerheten.

Resultaten bidrar till globala säkerhetsanalyser för djupa geologiska slutförvar och betonar vikten av naturliga analoger för att förstå långsiktig barriärprestanda.

Contents

| | | |
|----------|---|----|
| 1 | Introduction | 11 |
| 1.1 | Background to the Kiruna Natural Analogue study (KINA) | 11 |
| 1.1.1 | Introduction to the project | 11 |
| 1.1.2 | Project objectives and aims | 12 |
| 1.2 | Safety relevant properties of bentonite | 12 |
| 1.3 | The role of natural analogues in the safety case | 14 |
| 1.4 | Overview of existing natural analogue information | 16 |
| 1.4.1 | Bentonite-iron reaction | 16 |
| 1.4.2 | Microbial populations in bentonite | 18 |
| 1.4.3 | Bentonite erosion | 18 |
| 1.4.4 | Bentonite longevity | 17 |
| 1.5 | Report structure | 19 |
| 2 | Geological setting of the deep clay transformation zones in the Kiirunavaara iron ore deposit, northern Norrbotten, Sweden | 21 |
| 2.1 | Introduction | 21 |
| 2.2 | Regional geological setting | 21 |
| 2.3 | Local geological setting of the Kiirunavaara Fe deposit | 25 |
| 2.4 | Clay alteration zones | 27 |
| 3 | Physico-chemical properties of the Kiirunavaara clay | 29 |
| 3.1 | Introduction | 29 |
| 3.2 | X-Ray Powder Diffraction Analysis of Deep Clay Transformation at the Kiirunavaara and related deposits | 29 |
| 3.2.1 | Introduction | 29 |
| 3.2.2 | Materials | 29 |
| 3.2.3 | Methods | 30 |
| 3.2.4 | Results | 31 |
| 3.2.5 | Conclusions | 33 |
| 3.3 | Analytical results for a sample from the Kiirunavaara mine, Sweden | 34 |
| 3.3.1 | Introduction | 34 |
| 3.3.2 | Sample description | 34 |
| 3.3.3 | Methods | 34 |
| 3.3.4 | Results | 36 |
| 3.4 | Mineralogy of Thirteen Samples from the Kiirunavaara mine, Sweden | 41 |
| 3.4.1 | Introduction | 41 |
| 3.4.2 | Sample description | 41 |
| 3.4.3 | Methods | 41 |
| 3.4.4 | Results | 42 |
| 3.4.5 | Discussion | 45 |
| 3.5 | Potassium-Argon Geochronology of Clays from Northern Sweden | 45 |
| 3.5.1 | Introduction | 45 |
| 3.5.2 | Sample description | 45 |
| 3.5.3 | Methods | 46 |
| 3.5.4 | Results | 51 |
| 3.5.5 | Discussion | 53 |
| 3.6 | Rb-Sr dating attempts on Kiruna clays | 55 |
| 3.6.1 | Introduction | 55 |
| 3.6.2 | Sample description | 55 |
| 3.6.3 | Methods | 55 |
| 3.6.4 | Results | 55 |
| 3.6.5 | Discussion | 56 |

| | | |
|----------|--|-----------|
| 3.7 | Kiruna clay: Relevant properties and processes | 61 |
| 3.7.1 | Introduction | 61 |
| 3.7.2 | Mineral composition | 61 |
| 3.7.3 | Hydraulic conductivity and swelling pressure | 63 |
| 3.7.4 | Mineral stability | 65 |
| 3.7.5 | Interaction with other repository components | 65 |
| 3.7.6 | Sulphate reduction | 66 |
| 4 | Description of the iron-clay interface in the Kiirunavaara mine (and assessment of potential iron-clay interaction) | 67 |
| 4.1 | Introduction | 67 |
| 4.2 | Sample details | 68 |
| 4.3 | Analytical methods | 69 |
| 4.3.1 | Microscopy | 69 |
| 4.3.2 | X-ray diffraction (XRD) | 69 |
| 4.3.3 | SEM-EDS | 70 |
| 4.3.4 | FE-EPMA | 70 |
| 4.3.5 | LA-ICP-MS | 70 |
| 4.3.6 | K-Ar dating | 70 |
| 4.4 | Results | 70 |
| 4.4.1 | Morphological observation of samples and chemical analysis of major constituent minerals | 70 |
| 4.4.2 | XRD Analysis | 71 |
| 4.4.3 | SEM-EDS observation and analysis | 72 |
| 4.4.4 | FE-EPMA observation and analysis | 74 |
| 4.4.5 | Trace Element Analysis of Magnetite | 75 |
| 4.4.6 | Dating of major minerals | 75 |
| 4.5 | Discussion on magnetite-smectite interaction | 76 |
| 4.5.1 | Estimation of formation age of magnetite and clay | 76 |
| 4.5.2 | Estimation of magnetite formation environment | 76 |
| 4.5.3 | Formation environment and time transition of magnetite-smectite and discussion on formation process of magnetite-smectite | 76 |
| 4.6 | Discussion on the formation process of the magnetite-smectite interface | 77 |
| 4.7 | Conclusion | 77 |
| 4.7.1 | Overview | 77 |
| 4.7.2 | How to proceed with future studies | 78 |
| 5 | Microbial metabolic potential in a natural clay analogue for deep geological radioactive waste repositories | 79 |
| 5.1 | Introduction | 79 |
| 5.2 | Methods | 79 |
| 5.2.1 | Drilling | 79 |
| 5.2.2 | Sample handling | 81 |
| 5.2.3 | Microbial cultivation | 81 |
| 5.2.4 | Ancient DNA extraction | 82 |
| 5.2.5 | Mineralogical and microscopic characterisation | 82 |
| 5.2.6 | Organic matter content | 82 |
| 5.2.7 | Iron content | 83 |
| 5.3 | Results and discussion | 83 |
| 5.3.1 | Solid phase characterisation | 83 |
| 5.3.2 | Microbial characterisation | 84 |
| 5.4 | Conclusions and future work | 86 |

| | | |
|--------------------|---|-----|
| 6 | Erosion properties of the clay from the Kiirunavaara mine | 87 |
| 7 | Conclusions | 91 |
| 7.1 | Introduction | 91 |
| 7.2 | Examination of potential long-term iron oxide minerals – bentonite interaction | 91 |
| 7.3 | Understanding the very long-term behaviour of bentonite under conditions of direct relevance to deep geological disposal of radioactive waste | 92 |
| 7.3.1 | Introduction | 92 |
| 7.3.2 | Mineralogy | 92 |
| 7.3.3 | Age of the natural Kiirunavaara clay | 94 |
| 7.3.4 | Further considerations | 94 |
| 7.4 | Potential impact of microbial populations in bentonite under repository conditions | 95 |
| 7.5 | Potential for erosion of the bentonite barrier by groundwater in a deep geological repository | 96 |
| 7.6 | Final comments | 96 |
| 8 | Acknowledgements | 99 |
| | References | 101 |
| | Appendices | 115 |
| Appendix A | TUM samples (Chapter 3.2) | 117 |
| Appendix B | Sample locations of samples from the Kiirunavaara mine described in the various chapters (all maps courtesy of LKAB) | 125 |
| Appendix C | Procedures of separation of clay minerals (M. Szczerba, Polish Academy of Sciences) | 131 |
| Appendix D | TUM X-ray diffractograms for bulk samples | 133 |
| Appendix E | TUM X-ray diffractograms for separated ultrafine fractions | 137 |
| Appendix F | James Hutton XRPD scan plots | 159 |
| Appendix G | GSU XRD plots for samples K1-01 to -05 and MA-01 | 161 |
| Appendix H1 | Re-Os dating of clay-associated pyrite | 203 |
| Appendix H2 | Re-Os data tables and plots | 213 |
| Appendix I | Example of the ongoing work on the iron-clay interface (University of Hokkaido) | 227 |
| Appendix J | SKB raw data for samples Kiruna 2018 and 2019 | 231 |

1 Introduction

1.1 Background to the Kiruna Natural Analogue study (KINA)

1.1.1 Introduction to the project

W. Russell Alexander and Raphael Schneeberger

Disposal of high-level radioactive waste typically involves a system of multiple engineered barriers (EBS; Figure 1-1), where the selected barriers are intended to retain their properties for hundreds of thousands of years. To demonstrate such long-term stability, short-term laboratory and medium-term underground rock laboratory experiments can be complemented with studies of long-term processes observed in natural systems (also called natural analogues, NA, see Chapman et al. 1984; Miller et al. 2000; Reijonen et al. 2023a for details).

Bentonite is a common barrier material in many repository concepts. Natural bentonite deposits are generally millions to billions of years old and the material can therefore be considered to be a natural analogue of itself (cf. Reijonen and Alexander, 2015). The environment in a bentonite deposit is, however, generally rather different from a repository environment and observations may not always be directly applicable to a repository safety case (see further discussions in sections 1.1.2 and 1.1.3).

Significant clay transformation/neoformation zones¹ have been encountered in the Kiirunaavara (Kiruna, Norrbotten, Sweden) magnetite(-haematite)-apatite deposits, which are hosted in low- to high-grade metamorphosed intermediate to acid volcanic and subvolcanic country (ore host) rocks. These up to 50 m thick, soft clay transformation zones occur within the ores and within the country rocks along the ore contact of the southern parts of the Kiirunaavara ore body (Berglund and Andersson, 2013). They are found at various levels to depths of at least 1200 m below the surface, in zones further into the hanging wall and footwall lithologies of the deposit. The predominant clay mineral in the transformation zones of all deposits is a dioctahedral Fe-poor montmorillonite (Section 3.2 and Rieger, 2016). K-Ar data of various Na-exchanged size fractions from two clay-altered gneiss samples from the nearby Johannes ore body, Malmberget, which are dominated by R3-ordered illite-smectite, yield age values ranging from 837 ± 14 Ma to 941 ± 15 Ma. Additional dating efforts are supplied in this report.

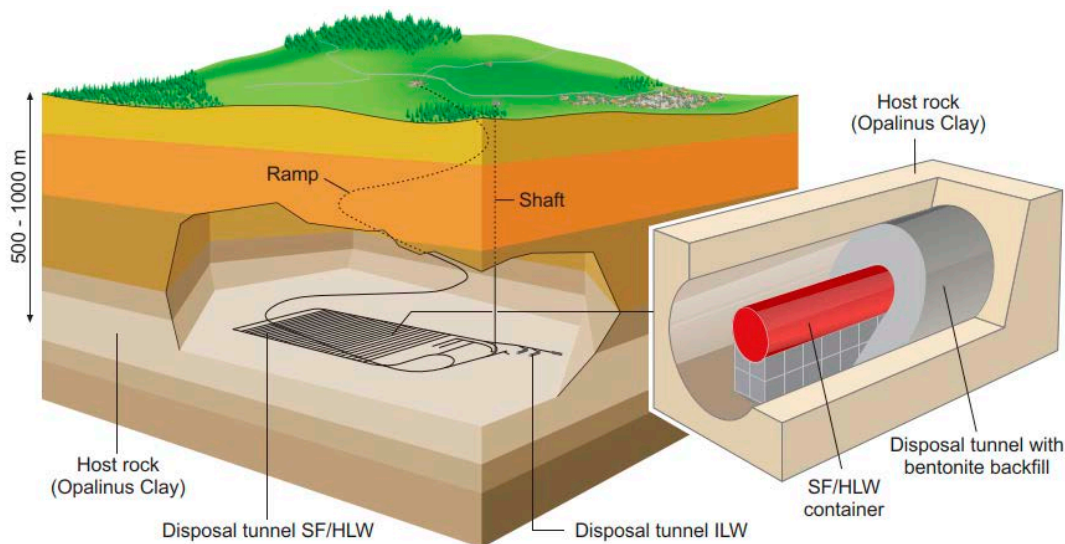


Figure 1-1. Example of the multiple engineered barrier concept for radioactive waste disposal in steel canisters, with a bentonite backfill (Nagra 2002).

¹ In most cases in Kiruna, it would appear to be clay transformation (cf. Eberl, 1983), but some suggestions of clay neoformation are also present (see Chapter 5).

1.1.2 Project objectives and aims

W.R.Alexander

The project aims to investigate smectite-rich clay (effectively bentonite²) that has been in contact with a magnetite ore for an extended period (probably in the order of hundreds of millions of years) under repository-relevant conditions in the Kiirunavaara ore body, northern Sweden. In many respects, the clay bodies in the Kiirunavaara deposit resemble a bentonite barrier in a repository: the magnetite ore could serve as an analogue for corrosion products in a steel waste canister produced under anoxic conditions, the metres thick clay layers represent the bentonite barrier and the surrounding country rock represents the repository host rock³. As such, the project has been initiated to further study the Kiirunavaara clay with focus on:

- understanding the very long-term behaviour of bentonite under conditions of direct relevance to deep geological disposal of radioactive waste (cf. Sellin and Leupin, 2013),
- examination of potential long-term iron oxide minerals – bentonite interaction (as may occur in a repository, cf. Wersin et al. 2023),
- the potential for erosion of the bentonite barrier by groundwater in a deep geological repository (cf. Missana et al. 2018),
- the potential impact of microbial populations in bentonite under repository conditions (cf. Beaver et al. 2022).

1.2 Safety relevant properties of bentonite

Patrik Sellin and Olivier X. Leupin

An important safety function of the bentonite buffer surrounding the canister is to limit the transport of dissolved species that could cause canister corrosion and potential radionuclide release from a damaged canister. The buffer material is selected so as to inhibit advective transport in the repository near-field. A thereof deduced safety guideline is that the hydraulic conductivity of the saturated buffer should be sufficiently low as to ensure that diffusion is the dominant transport mechanism.

The buffer homogeneity is ensured partially by the fact that the buffer consists of bentonite, a clay material that swells when reacted with water. The swelling enables the dry-installed clay to fill gaps and voids in the EBS as well as to balance the buffer mass between components installed with different initial densities (e.g. compacted bentonite blocks and bentonite pellets). A swelling pressure criterion has, therefore, also been formulated in repository designs (see, for example, Posiva, 2023a, for details).

Wersin et al. (2008) noted that a simple mass balance estimate indicates that substantial amounts of smectite (10–30 %) would be transformed if all the iron from Posiva’s super-container steel shell reacted with the bentonite buffer at the Olkiluoto site to produce a non-swelling Fe-dominated clay. This would induce a decrease in swelling pressure from 7 MPa to 2 MPa.

² Before looking any further at bentonite, it is important to clarify the terminology surrounding the material and the use of the term in this report. The term bentonite was first proposed in the 19th century by Knight (1898) and the name is from the Benton Shale in which the clay was thought at that time to occur. Once the origins of bentonite were understood, several updated definitions followed, but all have limitations. The strict geological definition of “bentonite” is a soft, plastic, porous light-coloured rock composed essentially of clay minerals from the smectite group plus colloidal silica and produced by chemical alteration of volcanic ash (cf. Hallsworth and Knox, 1999). The name implies a definite genetic origin from alteration of volcanic ash, either in situ or transported material, but see also the discussion in Alexander et al. (2012).

³ While the original reducing conditions have now been impacted by mining, the presence of many reducing minerals in the Kiirunavaara clays and host rock (see chapters 3 and 4) suggest that the original redox buffer capacity has survived to date, increasing the value of the analogy.

When interpreting data from the NF-PRO URL experiments, Milodowski et al. (2009) noted that bentonite immediately adjacent to corroding steel was found to have interacted with Fe released from the corroding metal. Narrow haloes of altered bentonite, in which the clay matrix was significantly enriched in Fe, were formed around the corroding steel wires. No evidence was found for the formation of discrete iron oxide or iron oxyhydroxide phases within the clay matrix, but the clay particles themselves had become enriched in Fe. XRD indicated a slight increase in the d002/d003 peak ratio, possibly due to some substitution of Fe into the octahedral layers of the montmorillonite. If so, this alteration might represent the early stages of conversion of the dioctahedral montmorillonite to an iron-rich dioctahedral smectite such as nontronite. Alternatively, displacement of exchangeable interlayer cations by Fe and subsequent conversion to form additional Fe-rich octahedral layers could produce the same effect. Either way, the petrographical observations are consistent with the XRD results, possibly indicating the early stages of conversion of montmorillonite into an iron-rich clay mineral as a result of interaction with Fe released by the corrosion of an iron (or steel) waste canister.

The bentonite in the haloes was also seen to be subtly affected by interaction with Fe, displaying a slightly reduced cation-exchange capacity (CEC), and depletion in exchangeable Ca and Na and an increase in exchangeable Fe. This is consistent with some displacement of the interlayer cations in montmorillonite by Fe. The loss in CEC might also correlate with a partial conversion of the montmorillonite to chlorite/serpentine, which is tentatively suggested from the XRD analyses (Milodowski et al. 2009). Fe displaced Ca^{2+} from the interlayer cation sites in the montmorillonite and was manifested by the marked concentration of Ca at the interface with the corroding metal and along the leading edges of ‘fronts’ of Fe diffusing into the bentonite matrix. The displaced Ca re-precipitated locally as aragonite.

The petrographical observations also showed that the bentonite within the haloes shows significantly reduced shrinkage on drying in comparison to the background, unaltered, bentonite (consistent with the results of a similar laboratory study by Carlson et al. 2008). This could be consistent with partial conversion of the montmorillonite to an iron-rich dioctahedral smectite such as nontronite, or to chlorite.

A recent review (Wersin et al. 2023) of the results of four Underground Research Laboratory (URL) experiments on the interaction of steel canister corrosion products and bentonite noted that “Systematic patterns can be deduced from the results, irrespective of carbon steel grade, type of bentonite and its degree of compaction, geochemical environment or experimental setup.” However, it was also noted that the availability of H_2O and O_2 from the bentonite in the experiments was crucial in initiating corrosion. So, while URL experiments might be assumed to be representative of the early post-closure processes in a repository EBS, they are not necessarily representative of the longer-term evolution of the EBS when any O_2 initially present directly after EBS emplacement has been consumed.

Sulphide production by sulphate-reducing bacteria initially present in the buffer and in the host rock (or introduced during the construction of the near-field barriers) is, in the long term, normally restricted to insignificant levels by the reliance of the bacteria on nutrients present in the groundwater. In certain transient situations, access to nutrients could be significant, e.g. due to degradation of construction materials and the presence of stray materials in the repository during construction (see, for example, the discussion in Vieno et al. 2003; Alexander and Neall, 2007). The microbial activity can be limited by increasing the buffer swelling pressure, which can be achieved by increasing the material density and, thus, reducing the buffer pore size and diffusivity of nutrients.

The buffer must also resist transformation in order to maintain its long-term safety functions. At elevated temperatures, chemical alteration of the swelling clays acting to decrease the development of swelling pressure would occur (Leupin et al. 2016).

To maintain the safety functions, a certain minimum buffer density is required as mass loss would lead to a decrease in density and thereby potentially jeopardise these safety functions. The most critical process leading to mass loss over time is chemical erosion of the buffer, but this will not occur if the groundwater has sufficient ionic strength. Laboratory chemical erosion tests in horizontal and inclined artificial fractures have shown that, if the charged cation concentration is <4 mM, pure Na- and Na/Ca-bentonites are prone to erosion (see Smith et al. 2017 for details).

1.3 The role of natural analogues in the safety case

W. Russell Alexander

In the initial selection of materials for the repository designs, natural materials were considered from the very beginning (cf. USNRC, 1957) as most EBS materials also occur in nature (e.g. native metals, metal alloys, clays, natural concretes; see Miller et al. 2000; Alexander et al. 2024, for details). NAs have provided useful input to repository safety cases for decades (Table 1-1) for conceptual model development, model testing and as direct input data. The processes covered reflect the wide range of scenarios considered in the long-term repository safety assessments, including potential material degradation based not just on the current conditions, but also covering foreseen (such as impacts of climate evolution) and unlikely scenarios that might happen in the future.

Table 1-1. Examples of the use of NAs in safety cases over the last four decades (after Reijonen et al. 2023a).

| Safety case (reference) | Conceptual model development | Model testing/development | Direct data input |
|---|---|--|--|
| KBS-3 (SKB 1983) | Radiolytic oxidation of SF | | Maximum rate for pitting of copper. Bentonite stability at T<100 °C |
| Projekt Gewähr (Nagra 1985) | Borosilicate glass stability Cement and concrete stability Bitumen stability Radionuclide migration | | Long-term corrosion rates of iron SF corrosion rates Estimates of rates of illitisation of bentonite |
| SKB-91 (SKB 1992) | Long-term stability of bentonite Matrix diffusion concept Defining relevance of colloids | Redox front propagation Radionuclide solubilities | Radiolytic oxidation rates |
| TVO-92 (Vieno et al. 1992) | Definition of glacial impact on the repository Copper corrosion processes Impact of colloids and microbes | SF dissolution | Matrix diffusion depths |
| Kristallin-1 (Nagra 1994) | Temperature dependence of illitisation of bentonite Radiolytic oxidation of the canister Glass corrosion rates Radiolytic oxidation of SF Microbial radionuclide retardation | Radionuclide solubilities Canister corrosion rates Redox front development | Thermal alteration of bentonite Long-term corrosion rates of iron Matrix diffusion depths Estimates of redox front development rates |
| AECL EIS (AECL 1994) | SF and copper canister corrosion rates Long-term behaviour of bentonite Radionuclide retardation | Radionuclide solubilities Colloid and organic complexation of radionuclides Copper corrosion rates | SF stability Radiolysis parameters Copper canister corrosion rates Bentonite illitisation rates Matrix diffusion depths |
| NRC IPA (1995) | Development of repository disruption scenarios Source-term model development Gas phase transport Relative importance of small- and large-scale fractures on radionuclide migration | Radionuclide transport in unsaturated media Radionuclide transport in fractured media | Definition and relevance of secondary phases following SF corrosion |
| SFR-1, Project Safe (Andersson et al. 1998) | Long-term stability of cementitious materials Development of a alkaline disturbed zone around a cementitious repository | Blind Predictive Model (BPM) testing of thermodynamic databases for alkaline conditions | Development of secondary CSH, CASH and zeolites within the hyperalkaline disturbed zone pH buffering by reaction with aluminosilicates in the host rock Realistic parameters for the release of KOH/NaOH/Ca(OH) ₂ leachates from the concrete |

| Safety case (reference) | Conceptual model development | Model testing/development | Direct data input |
|--|--|--|--|
| TILA-99 (Vieno and Nordman 1999) | Support for the assumed conservatism of the SF dissolution model | | Copper canister corrosion rates |
| SR-97 (SKB 1999) | Inclusion of permafrost data in the glacial scenarios Inclusion of post-glacial tectonics information in the glacial scenarios | Radiolytic oxidation of SF Radionuclide retardation via matrix diffusion Redox front propagation Mixing of different groundwaters | Bentonite illitisation rates Bentonite thermal stability Bentonite as a barrier to microbial activity Low colloid populations in deep groundwaters Gas transport in the host rock Maximum depth penetration of oxidising surface waters Long-term redox buffer capacity of the host rock |
| JNC (2000) | Temperature dependent mineralisation of the bentonite | | Conservative corrosion rates for steel canister Conservative dissolution rates for vitrified waste Matrix diffusion depths Bedrock stability from the Tono site |
| Opalinus Clay (Nagra 2002) | Interaction of the hyperalkaline leachates from the near-field with the far-field High temperature interaction of the host rock and bentonite Chemical alteration of bentonite Impact of radiolysis | | Radionuclide solubilities Corrosion rates of the steel canister Dissolution rates of SF |
| JAEA (2007) | Impact of secondary mineral crystallisation on radionuclide retardation on cementitious materials | | |
| TURVA-2012 e.g. Posiva (2012a,b) | Use of complementary data from NAs for uranium migration, copper corrosion, iron corrosion, and thermal, mechanical chemical alteration of bentonite buffers, and cement-rock interactions for input to the safety case for the disposal of SF at Olkiluoto (Posiva 2012a) Inclusion in FEP ⁴ report (Posiva 2012b). | | Copper canister corrosion rates Support for conservative dissolution rates of SF. |
| SR-Site (SKB 2011) | Complementary considerations approach + wide use in specific process discussion (FEP based approach, see example on the right) | | Support for conservative dissolution rates for SF (SKB 2010) NAs supporting the data on speciation of radionuclides and colloid formation (SKB 2010) |
| Forsmark 2014 (Sidborn et al. 2014) | Development of evolutionary models for a hyperalkaline plume from OPC grouts, and its interaction with bentonite backfill material, and the development of the geochemical environment within an alkaline disturbed zone in the host rock for a repository. Development of conceptual models to evaluate the impact of climate change. | Integration of information from NA studies with laboratory, URL and modelling studies | |

⁴ Features, events and processes

| Safety case (reference) | Conceptual model development | Model testing/development | Direct data input |
|--|--|---|--|
| NUMO (2021) | Safety case supporting evidence Specific system support | “Safety will be demonstrated in a logical manner by way of a “safety assessment”, together with “supporting evidence”, such as that provided by natural analogues, that will reinforce/support the assessment results.” Alkali cement leachate/host rock interaction | Direct use of NA information on siting |
| Posiva’s operating licence application 2023 (Posiva 2023a) | Case specific review on natural analogues supporting safety case as complementary considerations (Posiva 2023b) on SF, canister, buffer & backfill, closure, foreign materials, and geosphere. Biosphere analogues are included elsewhere (Posiva, 2023c). | Input via process understanding (e.g. Posiva 2022) plus input in biosphere modelling (details in Posiva, 2023c) | Support on conservative estimates on dissolution of SF. Support on low corrosion rates of copper. Support on stability of buffer and backfill materials including concrete. Support to low seismic risks via palaeoseismic studies. |

1.4 Overview of existing natural analogue information

W. Russell Alexander

1.4.1 Bentonite-iron reaction

Bentonite-iron interactions may be due to direct contact between Fe(0) and smectite, or between Fe-bearing phases (e.g. oxides) and smectite or Fe-rich solution and smectite (e.g. Guillaume et al. 2004). Although such environments do exist (see Miller et al. 2000, for details), they have never been successfully studied to date (see also comments in Wilson et al. 2016; Alexander, 2018). In a more recent review of natural and archaeological analogues of canister corrosion, King et al. (2023) note that there are few reported NA studies of direct relevance⁵. Nevertheless, several NA studies of iron reaction with bentonite have been reported. For example, Marcos (2004) assessed the Pecho de los Cristos (Spain) site where bentonite was affected by iron-rich solutions coming from faults (Figure1-2).



Figure 1-2. View of the bentonite sampling site at Cortijo del Aire, Almería, Spain (left). The red staining of the bentonite is clear during sampling (right). From Marcos (2004)

⁵ Frustratingly, those cases which are noted to support the safety case are not directly cited, so rather limiting the value of this review.

It was noted that the content of iron was almost two-fold greater in the redder samples than in the greyer ones. However, the origin of the haematite pigment was unclear, although migration of structural Fe from smectite was noted to be a possibility. However, no further work was conducted on the samples as the smectite content of the bentonite was deemed too low (maximum 15 %) for the material to be of relevance to most repository designs.

More recently, Fukushi et al. (2010) reported alteration of bentonite at the Kawasaki bentonite deposit in Zao, Japan. The bentonite consists of Na-Ca smectite with subordinate opal-CT, quartz and zeolite (Takagi et al. 2005) and includes greenish hydrothermal veins. They are composed of mixed-layer minerals consisting of smectite and glauconite, pyrite and opal. The mineral assemblages of the greenish veins and their surroundings indicate that the hydrothermal activity had most likely taken place at a temperature of less than 100 °C and that the pH and Eh conditions of the reacted solution were neutral to alkaline pH and reducing. The bulk (unaltered) bentonite is composed mainly of Al smectite and opal whereas the bentonite in contact with the greenish veins appears mineralogically and petrographically altered and consists of discrete opal grains and dioctahedral Al smectite containing Fe.

The authors contend that the conditions of alteration are similar “...to those in the geological disposal environment,” and therefore were worth study. However, the secondary clay and opal were formed by dissolution and subsequent precipitation from the interaction of the original bentonite with hydrothermal solutions and this is not what would be expected in a repository EBS.

Interestingly, in a NA study which was focussed on reaction of bentonite with high pH groundwaters, Fujita et al. (2010) and Fujii et al. (2015) noted the presence of secondary phases including Fe-smectite/saponite (nontronite), K-feldspar and Ca-zeolite within a Fe-enriched zone in the bentonite. However, the production of the secondary phases is complicated, with the Fe in the smectite/saponite probably released from volcanic glass rims on underlying pillow lavas and the presence of free Fe-oxides also suggesting microbial influences (cf. Hedrich et al. 2011).

A review (Laine & Karttunen, 2010) of NA information on the interaction between iron and clays under reducing conditions found little additional data, but more recent work by Alexander (2018) noted two examples of bentonite-magnetite mixtures which could be worth further study:

- Er-ramly & Ider (2014) reported a smectite-rich (49 wt%) bentonite in Morocco which includes 7 wt% magnetite.
- Cleveland (1960) noted admixtures of minor magnetite in the Otay bentonite in California, USA.

Alexander & Reijonen (2024) also noted an example of approximately 61-million-year-old native iron microspherules present in a meteoritic ejecta layer of volcanic ash altered to a potassium-rich clay not unlike bentonite. Finally, Milodowski & Alexander (2024) also note that work on the oldest steel (rather than iron) ever recovered opens the possibility of the examination of steel-clay reactions over the last 2.5 ka.

It is intended that the current KINA study of iron corrosion products-clay interaction (Chapter 5) shall add significantly to this relatively small body of extant data.

1.4.4 Bentonite longevity

Few bentonite NAs have been focussed on bentonite longevity *per se*, but several studies have examined various aspects of the long-term behaviour of bentonite in some form or another (see Table 1-2 for details). Previous unpublished studies of the Kiruna clay have suggested that it is several hundred million years old and it was intended that the age(s) of the clay will be established more precisely within this project (see discussions in Chapter 7), so adding to the more general studies noted below.

Table 1-2. Examples of NA studies which have examined some aspects of bentonite longevity.

| Project (references) | Aspect of bentonite longevity studied | Comments |
|---|--|---|
| IPHAP (International Philippines Hyperalkaline Analogue Project) (Alexander et al. 2008; Fujii et al. 2015) | High pH cement leachate reaction with bentonite | Interaction of high pH groundwater with bentonite for an unknown period indicated limited reaction of the bentonite. See also comments in Section 1.4.1 |
| Forsmark site assessment (Reijonen and Alexander, 2015; Kremer and Alexander, 2015; Reijonen et al. 2023b, 2024) | Suggested using natural host rock smectites to assess the likely longevity of industrial EBS bentonite | Used information available from candidate repository sites in Finland, Sweden and Canada |
| CNAP (Cyprus Natural Analogue Project) (Milodowski et al. 2016) | High pH cement leachate reaction with bentonite | Interaction of high pH groundwater with bentonite for 0.5 Ma indicated limited reaction of ca. 1 % of the total bentonite (limited to a very thin zone at the reaction front) |
| LPB (Long-term performance of bentonite) (Alexander et al. 2017) | Potential load displacement of the bentonite buffer around radioactive waste containers | While minor amounts of physical creep (over a 0.5 Ma period) were observed, no other physico-chemical degradation of the bentonite was observed |
| Borehole Sealing (Alexander, 2018) | Potential degradation of bentonite borehole seals by reaction with metal boreholes, concrete supports and host rocks | Wide ranging review of existing bentonite NA studies found little evidence of long-term bentonite degradation |
| IBL (International Bentonite Longevity) (Reijonen and Alexander, 2024) | Various aspects of bentonite longevity are currently being studied in the Tsukinuno mine in Japan | Results to date indicate limited chemical alteration of the bentonite following groundwater reaction. No mineral alteration or physical degradation has been observed |

1.4.2 Microbial populations in bentonite

Laboratory (e.g. Stroes-Gascoyne et al. 2008; Gilmour et al. 2022; Beaver et al. 2024) and URL studies (e.g. Stroes-Gascoyne, 2010) of microbial populations in bentonite are well established, but *in situ* studies in natural clays have only just begun (e.g. Beaver et al. 2022). It was decided to significantly expand this limited database by investigating microbial populations of the Kiirunavaara clays following a dedicated sampling campaign on 9–13th May 2022 and preliminary details are presented in Jakus et al. (2023) and Chapter 5.

1.4.3 Bentonite erosion

Although numerous laboratory (e.g. Jansson, 2009; Elo et al. 2019) and URL (e.g. Möri et al. 2003; Schaeffer et al. 2012) experiments on bentonite erosion have been reported, several reviews (e.g. Alexander et al. 2011; Reijonen and Alexander, 2015; Reijonen and Marcos, 2016) of available NA data show that little information is available from natural systems. This has prompted several new studies (e.g. Reijonen et al. 2023b, 2024) and focussed work on *in situ* bentonite erosion is planned in the IBL project (see Reijonen and Alexander, 2024 for details) and was considered here in the KINA project. Unfortunately, the COVID pandemic disrupted planned field work and related experiments and, as such, only an abbreviated laboratory programme could be carried out on clay samples from the mine and the results are reported in Chapter 6.

1.5 Report structure

W. Russell Alexander

Following this introduction, the report continues with (Chapter 2) an overview of Kiruna geology. Chapter 3 presents the results of the analyses of the physico-chemical properties of the Kiirunavaara clays with results from a number of analytical groups (and a brief overview of data from an additional group presented in the appendices).

As is to be expected considering the fact that the Kiruna mine has been operating for some 125 years (Mining-technology, 2010) much is already known about the ore itself but, as the clay has no monetary value, it has been largely ignored to date. Chapter 4 presents the first results on the details of the magnetite-clay interface providing novel information on the long-term behaviour of the clay following potential very long-term reaction with the iron corrosion products.

Chapter 5 presents the preliminary results of microbial analyses of the clays following a dedicated sampling campaign in mid-2022. Once again, significant delays induced by the COVID pandemic means that the timing of this work has been impacted significantly and full reporting of the results will follow at a later date. Nevertheless, the currently available information is very apt as it allows direct comparison with the results of microbial analyses of the bentonite in the Tsukinuno mine in Japan (see Beaver et al. 2022 for details). Chapter 6 briefly reports the results of the abbreviated bentonite erosion study, with focus on the laboratory results. Finally, Chapter 7 provides the conclusions of the report with comments on the relevance of the KINA study to repository safety cases.

2 Geological setting of the deep clay transformation zones in the Kiirunavaara iron ore deposit, northern Norrbotten, Sweden

H. Albert Gilg and Ulf B. Andersson

2.1 Introduction

Significant clay transformation zones were encountered in the southern deep part of the Kiirunavaara iron oxide-apatite mine at Kiruna in the Precambrian Shield of northern Norrbotten, Sweden (Rieger, 2016; Gilg and Andersson, 2020). They were also observed in other Kiruna-type Fe deposits, such as Malmberget near Gällivare, Gruvberget, Leveäniemi and Mertainen near Svappavaara (e.g. Geijer, 1930; Frietsch, 1960, 1966; Rieger, 2016), and at the Vahtanvaara skarn-rich Fe deposit near Vittangi (Bergman et al. 2001; Rieger, 2016). In the latter deposits, clays are sometimes associated with zeolites (Cronstedt, 1756; Bygdén, 1902; Romer, 1996; Romer and Rocholl, 2004; Colella and Gualtieri, 2007; Rieger, 2016). The present section summarises existing data of the geological setting, petrography and geochronological data of the host rocks to the clays in the Kiirunavaara deposit.

2.2 Regional geological setting

The Kiruna iron oxide-apatite deposit is located in the northern Norrbotten County of Sweden within the Fennoscandian Shield (Figure 2-1). The Precambrian rocks in northern Norrbotten have been subjected to the 2.0 to 1.8 Ga Svecokarelian orogeny and are overlain in the western part by the Caledonian nappes with some rare outcrops of Cambrian sediments at the nappe front (Bergman et al. 2001; Bergman, 2018; Bergman and Weihed, 2020).

The oldest rocks in the area, of Archean age, are exposed about 15 km north of Kiruna. They consist mostly of granodioritic to tonalitic orthogneisses and minor supracrustal rocks (the Råstojaure complex) with a formation age of about 2.8 to 2.7 Ga and a regional metamorphic overprint at 2.7 Ga (e.g., Welin et al. 1971; Martinsson et al. 1999; Bergman and Weihed, 2020). Within the Archean bedrocks, minor ultramafic-mafic intrusives with an estimated age of about 2.5 to 2.4 Ga are found (Bergman and Weihed, 2020). The Archean rocks are unconformably overlain by a series of Early Proterozoic Karelian (~2.5 to 2.0 Ga; Rhyacian) and Svecofennian (~2.0 to 1.8 Ga, Orosirian) supracrustal units.

The Karelian units comprise a basal clastic mostly metasedimentary (Tjärro quartzites) sequence, the Kovo Group, which is unconformably overlain by a 2- to 4-km thick pile of the Kiruna Greenstone Group, mostly dominated by mafic tholeiitic metavolcanics and minor metasediments that formed in an extensional geotectonic setting (Martinsson, 1997; Lynch et al. 2018). This unit is, in turn, unconformably overlain by the Svecofennian supracrustal units, starting with the basal Kurravaara metaconglomerates, including local intercalations of andesitic rocks (Porphyry Group) that mark the onset on convergent tectonics (Bergman et al. 2001; Martinsson, 2004). This was followed by the 2.5 km-thick Kiirunavaara Group (Figure 2-2), also known as the Porphyry Group, with intermediate to felsic metavolcanics, subdivided into the Hopukka, Luossavaara and Matojärvi Formations (Martinsson, 2004) and including the iron oxide-apatite ores all with ages in the range of ~1.89 to 1.87 Ga (Welin, 1987; Cliff et al. 1990; Romer et al. 1994; Westhues et al. 2016; Billström et al. 2019; Sarlus et al. 2020).

A slightly older chronology was suggested by Storey et al. (2007) and Smith et al. (2009), based on LA-ICP-MS U-Pb dating of titanite. The significance of these age dates is disputed due to a potential disturbance of the isotopic system and a problematic common Pb correction (Westhues et al. 2016; Billström et al. 2019). Iron ore formation was accompanied by an intense hydrothermal sodic, minor potassic, and chloride-rich alteration (e.g., Frietsch et al. 1997; Gleeson and Smith, 2009; Smith et al. 2013; Westhues et al. 2016, 2017a; Paolillo and Giapis 2021; Andersson et al. 2024). Its relationship to the regional scapolitisation of mafic to intermediate rocks in the area (Frietsch et al. 1997; Bernal et al. 2017) is not clear. Highly saline halite-bearing fluid inclusions are found in late-stage vein quartz in the iron oxide-apatite deposits (Gleeson and Smith, 2009; Smith et al. 2013; Martinsson et al. 2016)

and corroborated by a large release of salt during comminution and processing of the iron ore (Lundkvist, 1998; Westerstrand, 2009). The low Br/Cl ratio and $d^{37}\text{Cl}$ ratios of fluid inclusions are consistent with the derivation from a magmatic (mantle) source or by halite dissolution (Gleeson and Smith, 2009). The youngest supracrustal Svecofennian unit (Figure 2-2) is the < 1.88 Ga Hauki quartzite and metaconglomerate that unconformably overlies the rocks of the Luossavaara and Matojärvi Formations (Frietsch 1978; Martinsson 2004).

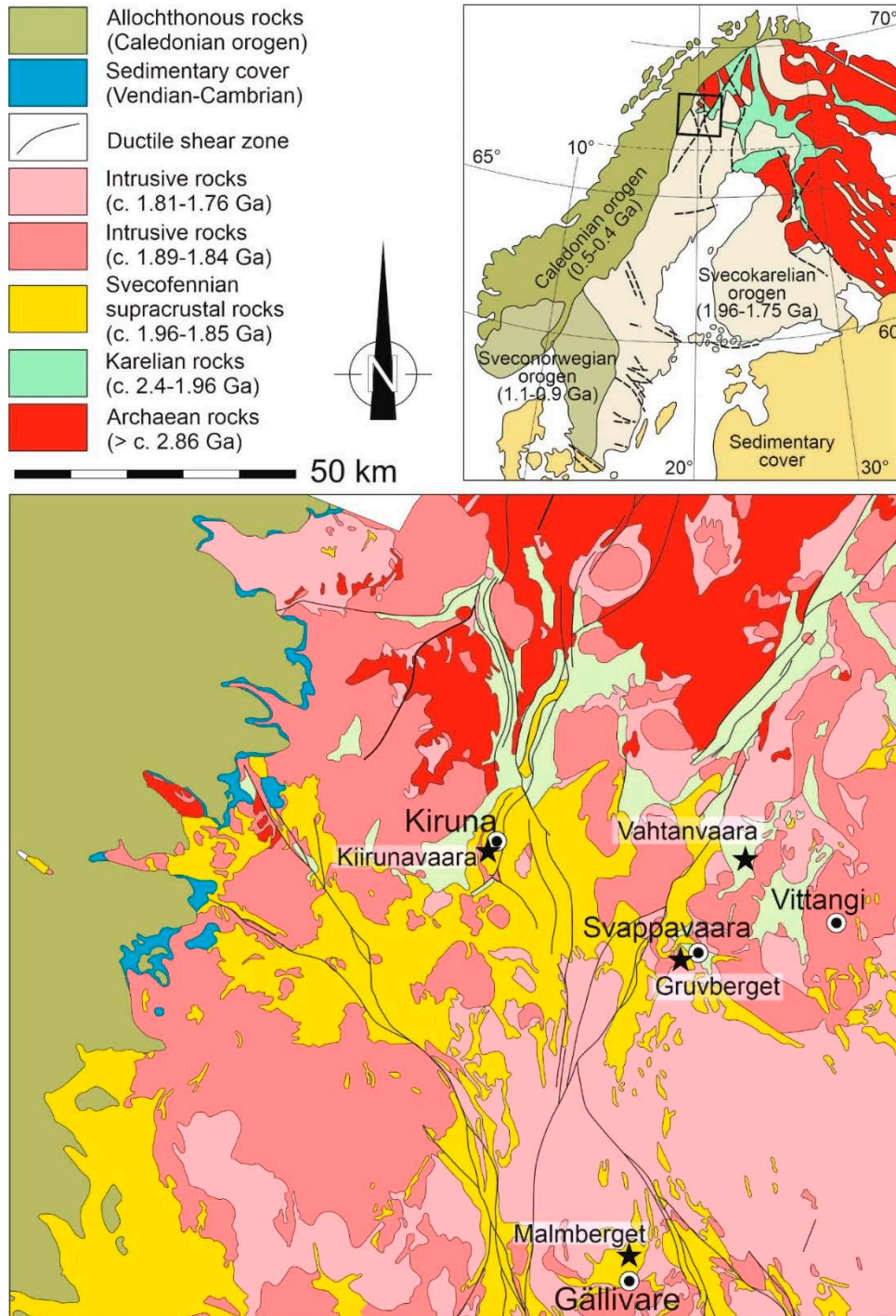


Figure 2-1. Simplified geological map of the Nordic countries (top) and northern Norrbotten (bottom, note black box in the top figure) with the location of the iron ore deposits with deep clay transformation indicated as black stars (modified from Bergman et al. 2001)

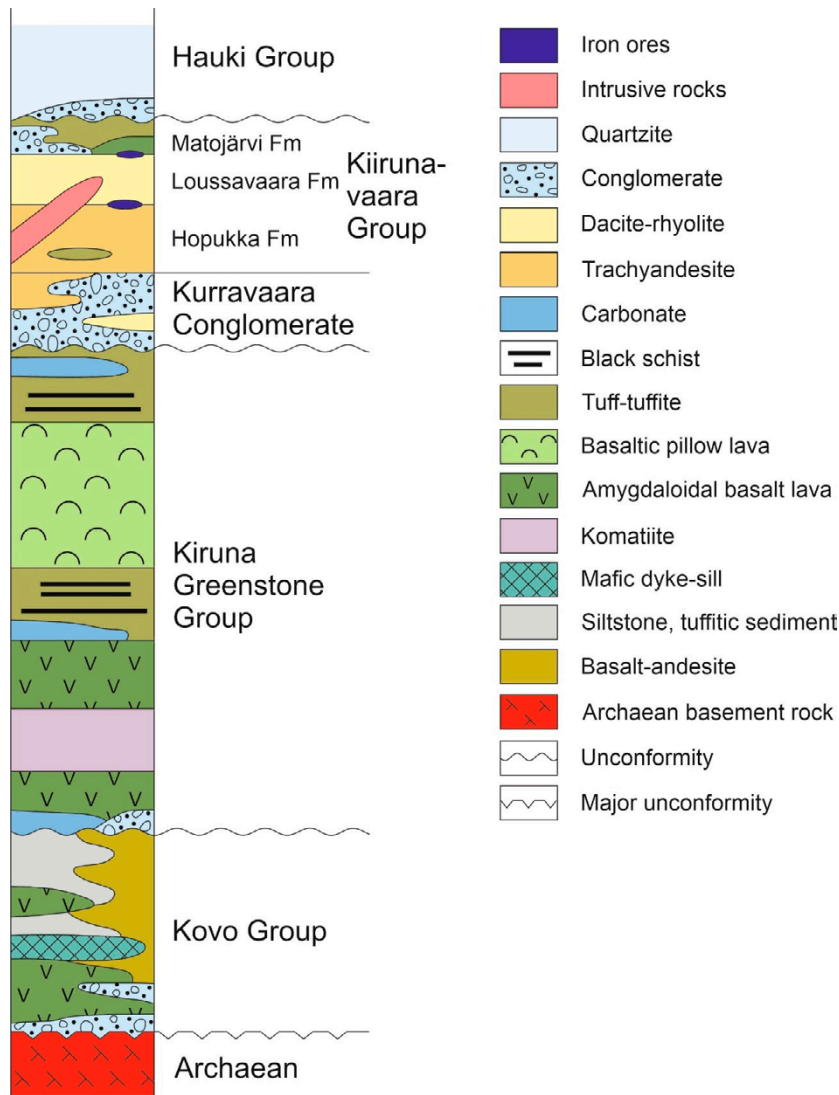


Figure 2-2. Simplified lithostratigraphic column of the Kiruna area (modified from Martinsson et al. 2016).

Several Svecofennian intrusive suites are noted in the region. The oldest intrusions (~1.89 to 1.86 Ga; Skiöld, 1986, 1987; Westhues et al. 2016; Sarlus et al. 2018; Bergman and Weihed, 2020) include the foliated Haparanda suite of gabbroic to granitic composition in the eastern part of Norrbotten and the, in part slightly younger, less foliated Perthite Monzonite suite, which is present in the near-Kiruna area (Figure 2-3). The partly porphyritic granitic-pegmatitic Lina suite (ca. 1.81 to 1.77 Ga Skiöld, 1988; Bergman et al. 2001; Sarlus et al. 2018, 2020) represents the youngest major magmatism in the area.

The Svecofennian supracrustals, and part of the intrusives, suffered a polyphase tectonic overprint between about 1.88 (D1 extension and basin development, or crustal shortening in some models) and 1.80 Ga (D2-D4 folding and thrusting) with a regional metamorphism of low-grade at Kiruna to high-grade at Malmberget (Vollmer et al. 1984; Forsell, 1987; Wright, 1988; Talbot and Koyi, 1995; Bergman et al. 2001; Bauer et al. 2018; Skelton et al. 2018; Andersson et al. 2020; 2021; 2022a; Sarlus et al. 2020). The pressures and temperatures of metamorphism and the timing have not yet been precisely determined at Kiruna. At Malmberget, the age of high-grade peak metamorphism has been variously attributed to the early deformation at 1.88 Ga (Bauer et al. 2018) or the later phase to 1.80 Ga (Sarlus et al. 2020; Yan et al. 2023a).

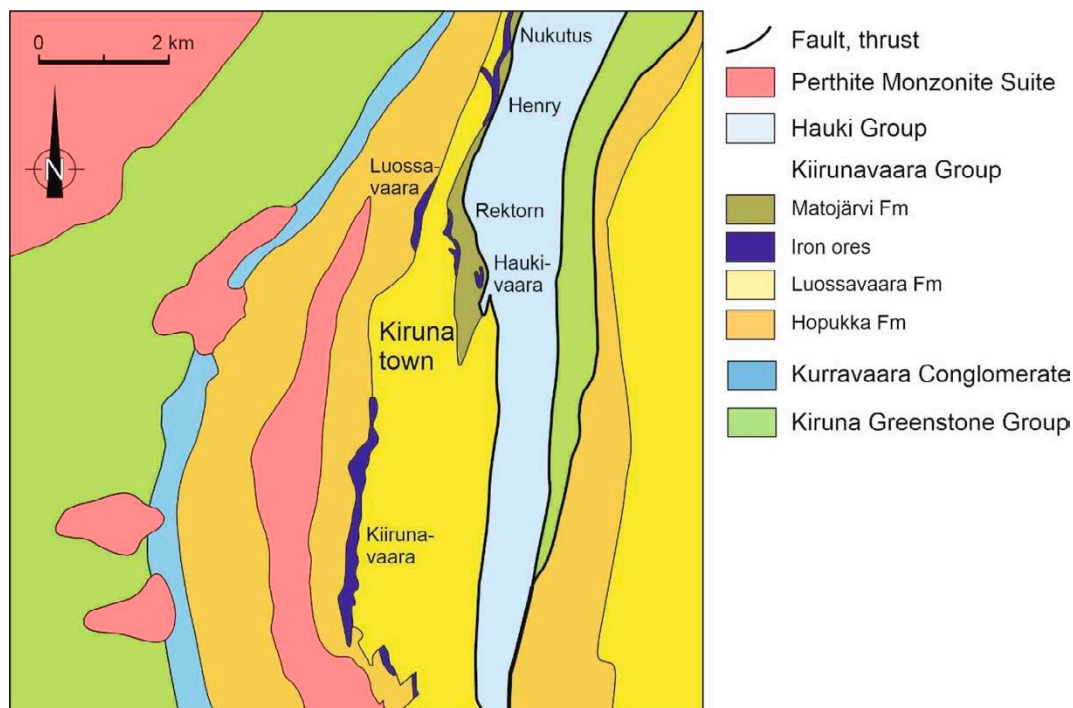


Figure 2-3. Simplified geological map of the Kiruna area (modified from Martinsson et al. 2016 and Grigull et al. 2018).

At Kiruna, an early alteration, close in time with ore emplacement, has been recorded in titanites (Romer et al. 1994; Martinsson et al. 2016; Westhues et al. 2016; Billström et al. 2019). A series of post-emplacement hydrothermal alteration events have been inferred at the iron oxide deposits of Kiruna, Gruvberget, Mertainen, and Malmberget between about 1.80 and 1.50 Ga with the formation of secondary phases (titanite, monazite, xenotime, uraninite, and stilbite) or overprints/resetting of isotopic systems (Cliff and Rickard, 1992; Romer et al. 1994; Romer, 1996; Romer and Rocholl, 2004; Storey et al. 2007; Aupers, 2014; Blomgren, 2015; Martinsson et al. 2016; Westhues et al. 2017a; Andersson et al. 2022b; Yan et al. 2023b). A similar age range of 1.74 to 1.53 Ga is recorded for Rb-Sr whole rock and mineral isochrons at Malmberget and Kiruna (Welin et al. 1971; Welin, 1980; Romer, 1996). In the Kiruna ore deposits in particular, three post-emplacement episodes of alteration have been recorded in secondary monazites, at c. 1.80, 1.73–1.72 and 1.64–1.62 Ga (Aupers, 2014; Blomgren, 2015; Andersson et al. 2022b; Yan et al. 2023b). Geochronological data for even younger events in the northern Svecofennian crystalline basement are rare (Romer and Wright, 1993). Rb-Sr ages of micas of nodules in the Kiirunavaara footwall porphyries have yielded ages around 1.4 Ga (Palm 2016). Determination of K-Ar ages of illite-bearing fault gouges in a tectonic window within the Caledonian nappes in NW Finnmark (Koehl et al. 2018) yielded Mesoproterozoic age data of about 1.05 Ga for the coarser fractions and Neoproterozoic age data of about 0.81 Ga for the finest fraction (<0.2 μm). A titanite fission-track age from Malmberget of 1.1 ± 0.3 Ga was reported by Ritter et al. (1984).

Early to Middle Cambrian autochthonous siliciclastic sediments of the Dividal Group with a thickness of about 100 m (e.g. Kulling, 1964; Jensen and Grant, 1998; Rehnström and Torsvik, 2003) are found unconformably overlying Svecofennian basement rocks at the base of the Caledonian front that is only about 30 km NW of Kiruna (Figure 2-1). The thrusting of the allochthonous Caledonian nappes occurred during the Silurian and Devonian (e.g., Gee and Stephens, 2020). The geometric reconstructions of the nappes (Hossack and Cooper, 1986) and metamorphism of the allochthonous sediments (Anderson, 1989) suggest that the nappes might have advanced up to 100 km further to the east and thus possibly reached the Kiruna area (Romer et al. 1994; Gee and Stephens, 2020). Geochronological evidence for a Caledonian event at Kiruna is, however, sparse and mostly observed as imprecise lower intercept ages of U-Pb discordia of zircons (e.g. Skiöld, 1988; Westhues et al. 2016).

Apatite fission track ages from Kiruna and Gällivare (Ritter et al. 1984; Hendriks and Andriessen, 2002; Hendriks, 2003) range between 320 and 240 Ma. Fission-track lengths indicate that the apatites resided for an extended period in the partial annealing zone between 60 to 100 °C (Hendriks, 2003).

2.3 Local geological setting of the Kiirunavaara Fe deposit

In the Kiruna area, several iron oxide-apatite ore bodies have been mined, many since the beginning of the last century: Kiirunavaara (still in operation), Luossavaara (–1985), Rektorn (–1961), Nukutus (–1967), Henry (–1987), Tuolluvaara (–1982) and other minor operations (e.g. Bergman et al. 2001). LKAB produced about 27.2 Mt of iron ore from the Kiirunavaara mine in 2019 and the total pre-mining ore reserves are estimated at about 2 Gt (Bergman et al. 2001). The Kiirunavaara and Luossavaara ores are magnetite-dominated, while the Rektorn, Nukutus and Henry ores, also known as “Per Geijer ores”, are magnetite-haematite ores (Geijer, 1910; Parák, 1975).

The iron ores

The Kiirunavaara ore consists of irregular lens-like bodies stretching 4 to 5 km long in a N-S direction, locally up to 200 m thick, on average 80 m and is magnetite-rich. It dips about 65° to the east and plunges about 45° to the north (e.g. Geijer, 1910; Bergman et al. 2001; Niiranen, 2006; Andersson and Rutanen 2016). At present, the main haulage level is at a depth of 1365 m below the pre-mining surface, but ores are known to extend to almost 2 km deep.

Ore veins occur in both footwall and hanging wall rocks (Geijer, 1910; Parák, 1975; Frietsch, 1978), but age relations in many places indicate contemporaneous formation with the wall rocks (Andersson, 2013; Pihl 2024). Five types of iron ore are distinguished during extraction: The Fe-rich (> 66 % Fe; B1) and Fe-poor (> 50 % Fe; B2, silicate-rich) low phosphorous (<0.05 % P) B ores and the phosphorous-rich D ores (> 50 % Fe) with D1 (0.1–0.8 % P), D3 (0.8–2.2 % P) and D5 (>2.2 % P) (Niiranen, 2006). The B1 ore is generally massive, fine-grained and magnetite-rich (90–98 vol.%); it is typically cut by calcite veinlets or open fractures with haematite formation and some porosity (Aupers, 2014). The high-silica, low-P B2 ore contains significantly more silicate minerals than the B1 ores, for example actinolite, F-rich phlogopite (rarely annite), talc, chlorite, titanite, epidote, allanite, zircon, thorite, but also other accessory phases such as hematite, ilmenite, monazite, xenotime, quartz, dolomite/ankerite, barite, anhydrite, gypsum, rutile, pyrite, and chalcocopyrite (Geijer, 1910; Nordstrand, 2012; Aupers, 2014, Augustsson, 2017). A calcite-chlorite-quartz-rich type can be distinguished from an actinolite-phlogopite-ilmenite-rich type (Aupers, 2014). The phosphorous-rich D ores are also fine-grained, have significantly higher apatite contents, but generally similar silicate, oxide, carbonate, sulphate and sulphide phases as the B ores (Nordstrand, 2012, Aupers, 2014).

Magnetite is, in general, Ti-poor and V-rich (e.g., Frietsch, 1970; Parák, 1975; Loberg and Horndahl, 1983; Nyström and Henríquez, 1994; Müller et al. 2003; Aupers, 2014; Augustsson, 2017; Broughm et al. 2017) has high $d^{18}\text{O}_{\text{VSMOW}}$ values (–1.0 to 4.1‰; Nyström et al. 2008; Troll et al. 2019) and high $d^{56}\text{Fe}$ values (+0.11 to +0.61‰; Troll et al. 2019). The zircons in the magnetite ores are texturally and chemically distinct (high Fe, P and H₂O; higher $d^{18}\text{O}$, and eHf values) from those in the host volcanic rocks indicating a larger mantle component (Westhues et al. 2017a, b). A few concordant zircon SIMS analyses yielded an age of $1\,874 \pm 7$ Ma (MSWD=1.7, n=4), while the discordia intercepted the concordia at an age of $1\,884 \pm 15$ Ma (MSWD=3.6, n=33; Westhues et al. 2016). Monazites occur mostly as alteration product of REE-rich apatite (Harlov et al. 2002). The hydrothermally altered apatite have yielded an U-Pb age of $1\,800 \pm 36$ Ma (Yan et al. 2023b). The monazites in the ores have been dated in-situ at $1\,638 \pm 39$ Ma (MSWD=0.40, n=111; Aupers, 2014), by LA-ICP-MS with two generations at $1\,718 \pm 12$ Ma and $1\,623 \pm 23$ Ma (both upper intercept ages of slightly discordant analyses; Blomgren, 2015) and by SIMS at $1\,628 \pm 12$ Ma (MSWD=1.3, n=45) and in another sample with more variable ages ranging from about 1 515 to 1 905 Ma (Westhues et al. 2016). Earlier geochronological data on bulk ore samples, in part including sulphides and host rock, yielded isochron age dates of $1\,540 \pm 70$ Ma by the Pb-Pb, $1\,490 \pm 130$ Ma by the Sm-Nd, and $1\,450 \pm 30$ Ma by the Rb-Sr method (Cliff and Rickard, 1992). The $^{87}\text{Rb}/^{86}\text{Sr}$ values may reach up to 52, while many samples have values of less than 1. The initial $^{87}\text{Sr}/^{86}\text{Sr}$ value of the Rb-Sr isochron is 0.7105 ± 2 , while a reported mean value of altered apatite is 0.7115 ± 6 (Yan et al. 2023b).

Footwall volcanics

The magnetite ores are underlain by mostly intermediate volcanic-subvolcanic rocks of the lower Porphyry Group (Hopukka Formation; Martinsson, 2004) with a total thickness of 300 to 1 400 m and a few intrusive bodies. In the mine, the footwall volcanic rocks are known traditionally as the “syenite porphyries” (Geijer, 1910) or more recently as “trachyandesite” (e.g. Martinsson and Perdahl, 1993; Bergman et al. 2001). The grey to reddish rocks consist of feldspar and, more rarely, amphibole phenocrysts of several mm length in an aphanitic matrix of albite, K-feldspar, mafic (amphiboles, rare clinopyroxene), opaque phases (mostly magnetite), as well as some carbonates, apatite, zircon, titanite and rare chalcopyrite (Geijer, 1910; Palm, 2015; Westhues et al. 2016; Sandberg, 2018). Conspicuous rounded nodular structures of a few mm to several cm in diameter are filled with actinolite, titanite, magnetite, apatite, phlogopite and locally with minor quartz, gypsum/anhydrite, albite, epidote, and calcite (Geijer, 1910; Palm, 2015; Gray, 2016). Veins of magnetite, titanite, actinolite and calcite are common. Major and trace element geochemical data (Westhues et al. 2016; Andersson et al. 2024)) indicate significant metasomatic alteration and are less conclusive with respect to precise protolith nomenclature. However, *sensu largo*, an intermediate, andesitic composition is probable (Westhues et al. 2016). Zircons are sparse in the footwall volcanic rocks and yielded $^{207}\text{Pb}/^{206}\text{Pb}$ weighted mean age for concordant and near-concordant data of $1\,884 \pm 4$ Ma (MSWD=0.69, n=4) and a concordia age of $1\,877 \pm 12$ Ma (Westhues et al. 2016). The zircons have $d^{18}\text{O}_{\text{VSMOW}}$ values of +5.1 to +7.1‰ (Westhues et al. 2017b). Titanite from the nodules were dated at $1\,876 \pm 9$ Ma (upper intercept; with an imprecise lower intercept at $562 + 197$ Ma) using the conventional zircon TIMS U-Pb method (Romer et al. 1994) as well as at $1\,876 \pm 17$ Ma concordia age by SIMS (Westhues et al. 2016) and at $1\,882 \pm 17$ Ma by LA-ICP-MS (Palm 2016). A titanite sample from a skarn in contact with the ore yielded a U-Pb age of $1\,878 \pm 4$ Ma (Martinsson et al. 2016).

Hanging wall volcanics

The felsic porphyritic volcanic rocks in the hanging wall belong to the Luossavaara Formation and reach a thickness of 800 m (Martinsson, 2004). The red to grey, massive or foliated, often jointed feldspar-phyric, often glomerophyric, rocks are interpreted as mostly pyroclastic flows (ignimbrites). K-feldspar phenocrysts (2–5 mm) are often replaced by albite and are embedded in an aphanitic groundmass of feldspar and quartz with minor magnetite, amphibole, clinopyroxene, apatite, biotite and titanite (Geijer, 1910; Westhues et al. 2016; Sandberg, 2018). They are traditionally termed “quartz-porphyry” (Geijer, 1910) or “quartz-bearing porphyry” (as they have no quartz phenocrysts) and more recently “rhyodacite” (Martinsson, 2004; Bergman et al. 2001). The acidic volcanic rocks are rich in zircons. Four samples have been dated by zircon SIMS at $1\,880 \pm 7$ Ma, $1\,881 \pm 5$ Ma, $1\,882 \pm 2$ Ma, and $1\,880 \pm 3$ Ma (Westhues et al. 2016) and by conventional multigrain zircon TIMS analysis at $1\,882 \pm 24$ Ma (Welin, 1987). Recently, dyke porphyries, transecting the footwall and ore but disappearing into the hanging wall porphyries have been U-Pb dated to $1\,880 \pm 4$ Ma, and considered feeder channels for hanging wall volcanism (Pihl 2024; Andersson et al. 2024). The stable oxygen isotope compositions of zircons from the hanging wall felsic volcanics are unusually low (+2.5 to +4.7‰) indicating assimilation of rocks with a strong meteoric water alteration in the magma chamber feeding the volcanic eruption (Westhues et al. 2017b).

Intrusive bodies

Within the footwall volcanic rocks, two intrusions occur approximately 1 km away from the ore body (e.g., Geijer, 1910; Westhues et al. 2016). Two samples of the syenite, which also outcrops at the surface, have been dated using U-Pb zircon SIMS at $1\,880 \pm 7$ Ma and $1\,896 \pm 19$ Ma, respectively, while a granitic intrusion, only known from underground workings at a similar position relative to the ore, yielded $1\,874 \pm 4$ Ma (Westhues et al. 2016). Conventional multigrain zircon TIMS analyses of the latter resulted in an age of $1\,880 \pm 3$ Ma (Cliff et al. 1990). The SIMS oxygen isotope data of zircons from the intrusive rocks (syenite, granite) show the same ^{18}O depletion as the hanging wall volcanics (Westhues et al. 2017b). Dykes of granophyre, diabase, as well as composite dykes, crosscut all volcanic lithologies in Kiirunavaara, and at least the former may have a direct magmatic relationship with the underlying granitic pluton (Andersson and Berglund 2024). A granophyric dike crosscutting the ore was dated with the U-Pb multigrain zircon TIMS method at $1\,880 \pm 35$ Ma (Cliff et al. 1990).

2.4 Clay alteration zones

Up to 50 m thick, soft clay alteration zones (Figure 2-4) occur in the southern Kiirunavaara mine along a horizontal stretch of about 1 km, at various levels and depths down to at least 1 200 m below surface (Berglund and Andersson 2013). They are often associated with so-called “crushed zones” of non-coherent rock masses showing brittle deformation and in part high porosity (Berglund and Andersson 2013). The clay alteration zones are found within the ore as well as the country rocks, particularly along the ore contacts, but also in zones further into the hanging wall and footwall lithologies of the deposit.

The clay alteration zones in some cases cut the ore and host rocks at high angle, i.e. with a strike about E-W (Berglund and Andersson 2013). They significantly affect the rock mechanical properties of the rock mass and influence the design of drifts and ore passes in the deep mine (Björnell et al. 2015; Andersson and Rutanen 2016). Additionally, they may negatively influence the recovery of the ore during processing as the clay minerals can stick to the ore minerals.

The clay alteration shows both sharp and more gradual transitions to unaltered rocks. Their colour in the wall rocks is generally whitish to grey (Figure 2-5a), but within the silica-rich B2 ore it may become greenish (Figure 2-6). Magnetite veinlets in the clay alteration zones appear unaltered (Figure 2-5b). The predominant clay mineral in the alteration zones is a dioctahedral Fe-poor Mg-bearing montmorillonite and, rarely, R0 illite-smectite (chapters 3 and 4; Rieger, 2016). Within the ore zone, other sheet silicates are detected within the <6 µm fraction, including phlogopite, talc and chlorite that probably are residual phases of alteration related to ore formation and/or later metamorphic/hydrothermal overprints. Calcite is frequently found in the fine fractions of the clay-altered rock and, rarely, traces of amphibole, feldspar and chlorite even in the <0.2 µm fractions (Rieger 2016). Detailed information in other chapters of this report.

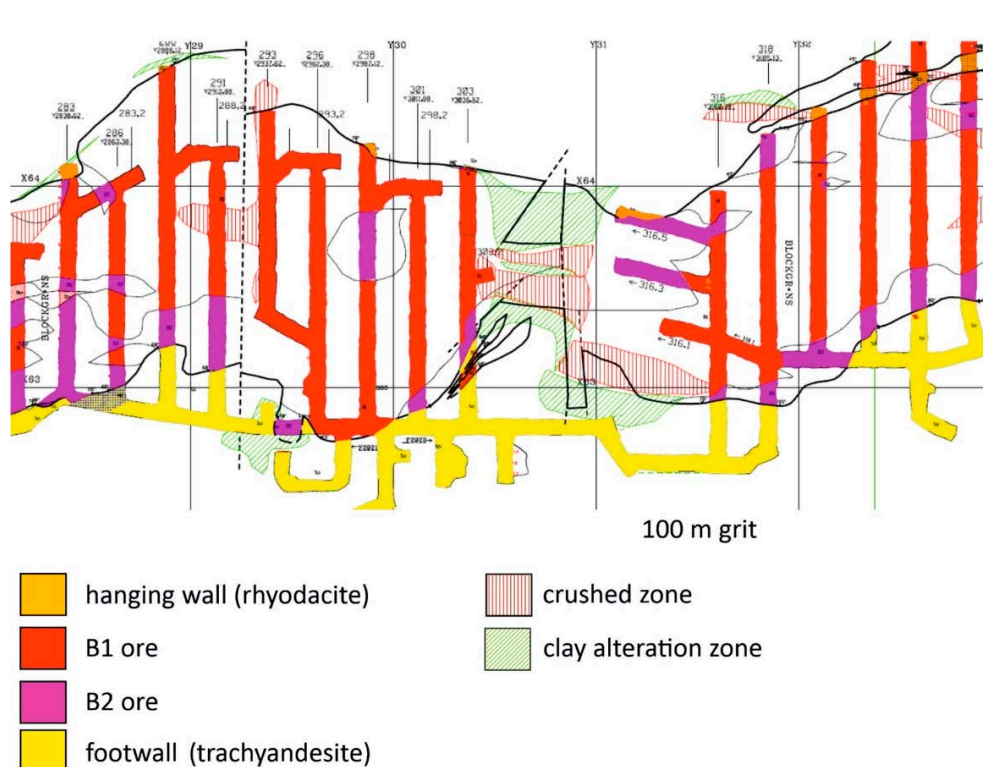


Figure 2-4. Geological map with outline of clay alteration within the iron ore body in an area of the southern part of the Kiirunavaara mine at level 1022 m. Block 30, level 1022.

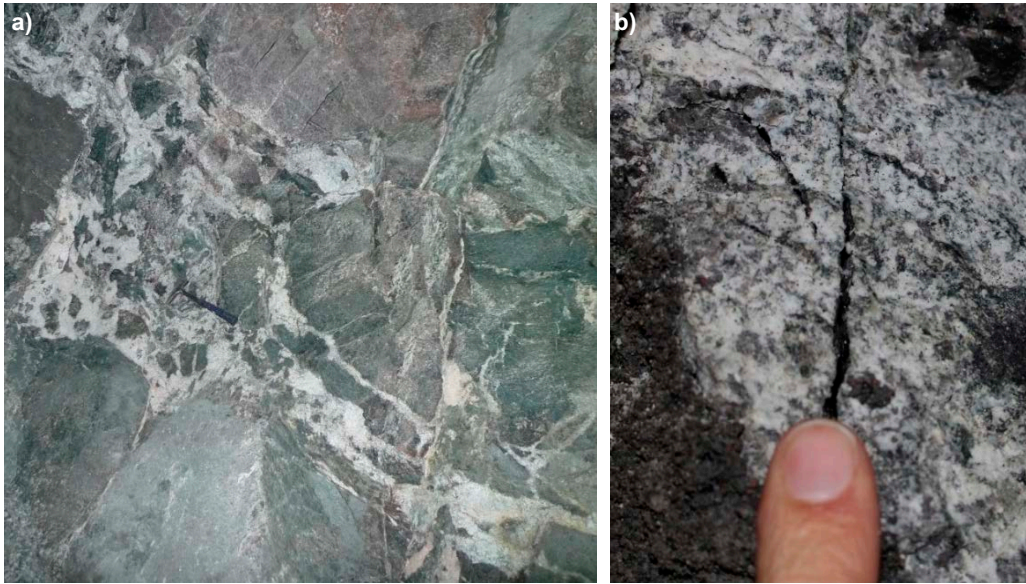


Figure 2-5. a) Incipient white clay alteration zone in rhyodacite of the hanging wall, level 1051 – crosscut 332, Kiirunavaara mine. Hammer in centre left of image for scale. b) Detail of clay alteration zone showing unaltered black magnetite veinlet. Images H.A. Gilg.



Figure 2-6. Greenish clay alteration zone within silicate-rich B2 ore, level 1079 – crosscut 316.3, Kiirunavaara mine, hammer as scale. Image H.A. Gilg.

3 Physico-chemical properties of the Kiirunavaara clay

3.1 Introduction

This chapter reports the results of the analyses of a range of Kiruna samples by six different laboratories utilising a wide range of analytical techniques.

3.2 X-Ray Powder Diffraction Analysis of Deep Clay Transformation at the Kiirunavaara and related deposits

H. Albert Gilg

3.2.1 Introduction

Bulk and various separated very fine size fractions from five clay-transformed metavolcanics rocks from the Kiirunavaara mine and two additional clay transformed samples, one each from the Malmberget mine, and the Vahtanvaara prospect, have been investigated by X-ray powder diffraction analyses for mineralogical characterisation. Separated $<0.2 \mu\text{m}$ fractions of most samples have been studied previously by Rieger (2016). The new analyses are intended to provide a mineralogical characterisation of the bulk clay-transformed samples, but also on the purity of various ultrafine separates ($<0.02 \mu\text{m}$, $0.02\text{--}0.05 \mu\text{m}$, $0.05\text{--}0.2 \mu\text{m}$) in preparation for further geochronological and stable and radiogenic isotope studies.

3.2.2 Materials

The investigated samples from the Kiirunavaara and Malmberget mines were collected from tunnel outcrops in 2015 and 2019 by the author and, in part, by Philip Rieger in 2016, both with the help of Ulf B. Andersson (LKAB). The sample from a drill core at the Vahtanvaara prospect was collected in 2013 at the SGU core shed by Dr. Adrian Hall, Stockholm University, Sweden.

Table 3-1 provides an overview of sample identification number, location, previous sample labelling in Rieger (2016) and a short description. Map locations of the sample sites as well as hand specimen images are provided in Appendix A. The five samples from the Kiirunavaara ore body include both transformed footwall (KI-02, KI-03, KI-05) and hanging wall metavolcanics (KI-01), as well as clay in very close contact to ores in the footwall (KI-04). The samples come from various levels ranging from 1 022 to 1 194 m below the pre-mining surface. Most samples have been identified by Rieger (2016) as containing a dioctahedral Mg-bearing smectite (montmorillonite) with one exception (KI-02), which was suggested to contain an interstratified illite-smectite mineral. The smectite in the selected samples display a restricted range of low boron contents suggesting low salinities of the transformation fluid (Rieger, 2016).

The clays in sample VA-01 from a clay-rich transformation of intermediate metavolcanics at the Vahtanvaara prospect are associated with zeolites of the stilbite – stellerite group (Rieger, 2016). The combined oxygen and stable isotope data of this location indicated a hydrothermal origin of the clays.

The sample MA-01 from the Johannes orebody, Malmberget, has been included as soft clay transformation at this location is dominated by an illite-rich R3 illite-smectite (Rieger 2016) and has been dated by the K-Ar method.

Table 3-1. Overview of sample identification numbers, previous labels, location and a short description from Kiirunavaara (KI) and Malmberget (MA) mines as well as the Vahtanvaara (VA) prospect.

| Sample ID | Old ID (Rieger 2016) | Location (level-block) | Description |
|-----------|----------------------|------------------------|---|
| KI-01 | K01 | 1051-332 | white clay in hangingwall rhyodacite |
| KI-02 | KP250202 | 1022-Y3110 (Block30) | greyish-reddish clay in trachyandesite footwall |
| KI-03 | KP01 | 1137-Y3090 | whitish fallout in trachyandesite footwall |
| KI-04 | - | 1194-301 | white clay transformation at contact to magnetite ore |
| KI-05 | KP03 | 1165-384 | clay-transformed trachyandesite footwall |
| MA-01 | MAB01 | JOH 635-2510 | greenish clay in muscovite gneiss with hematite mineralisation (Malmberget) |
| VA-01 | V133 | BH79001 – 33 m | white clay-zeolite transformed andesite (Vahtanvaara) |

3.2.3 Methods

Sample Preparation

Bulk oven dried (40 °C) samples have been gently disaggregated using an agate mortar to a size of <0.5 mm. Two grams of a sample aliquot were ground for 8 minutes with 10 mL of isopropyl alcohol in a McCrone micronising mill using ZrO₂ cylinder elements. The suspension was filtered, dried, and homogenized in an agate mortar by hand. The sample powders were side loaded into the cylindrical holders to minimize preferred orientation of minerals.

The size fractions have been separated from the dried clays (~80 to 190 g) in the laboratory of the Clay Minerals Research Group at the Institute of Geological Sciences, Polish Academy of Science, Krakow, Poland, under the supervision of Dr. Marek Szczerba. For sample KI-03, the separation of ultrafine subfractions (<0.02 μm, 0.02–0.05 μm, and 0.05–0.2 μm) was conducted on the clay in a natural state and in a Na-saturated state (NaCl) at high dilution to ensure “infinite” osmotic swelling using an ultra-centrifuge (JCF-Z rotor). As the amount of the smallest fraction (<0.02 μm) in both approaches was very small (<20 to 30 mg from 20 g), it was suspected that cements hindered the disaggregation of the swelling clay mineral. It was decided to use the Jackson (1979) treatment (for details see appendix B) to remove carbonates and exchangeable divalent cations with a Na acetate-acetic acid buffer, organic matter using Na hypochlorite, and iron oxides using Na dithionite with a bicarbonate-citrate buffer according to Jackson (1979). The received amounts after ultra-centrifugation were coagulated with NaCl, dialyzed, dried and split for geochronological analysis (Section 3.6) and X-ray diffraction analysis (below). The ultrafine subfractions were labelled with the sample ID as A (<0.02 μm), B (0.02–0.05 μm), C (0.05–0.2 μm) and D (0.2–2 μm). It is noted that the samples KI-02A, KI-02B, KI-03A, KI-03B, and, to a minor extent sample KI-04A, show a dark grey to blackish colour (Figure 3-1) related to minor contamination with eroded rubber seal material of the ultracentrifuge (*M. Szczerba, Polish Academy of Sciences, pers. comm. May, 2020*). All other samples are colourless and show no signs of such contamination.

The flakes of the nm-sized fractions were mounted on Si single crystal using acetone (Figure 3-1) and analysed in air-dried and ethylene-glycolated state (held in ethylene glycol vapor overnight at 60 °C). The XRD results showed a very strong preferred orientation of these mounts (see below). The phases that contaminated the finest fractions of samples KI-02 and KI-03 were not detectable by XRD.



Figure 3-1. Photograph of XRD specimen with mounted flakes of sample KI-03A ($<0.02\mu\text{m}$) on a Si single crystal (image H.A. Gilg).

X-Ray Diffraction Analysis

X-ray powder diffraction analysis of bulk samples was performed using Bruker D8 Advance Eco X-ray diffractometer ($\text{CuK}\alpha$, 40 kV, 25 mA, goniometer radius of 250 cm, 2° – 75° 2θ , 0.01° step size, counting time of 1 s/step, automatic divergent slit, 15 mm irradiated length, 2.5° primary and secondary sollers and a LynxEye XE-T detector). The phases in the whole rock powders were then quantified using the Rietveld program BGMN (Bergmann et al. 1998) and the Profex graphical user interface (Döbelin and Kleeberg, 2015) and presented as mass%.

As insufficient material of bulk sample VA-01 was available for a new bulk analysis using the setup described above, an existing measurement from 2015 using a Philips/Panalytical PW1800 X-ray diffractometer ($\text{CuK}\alpha$, 40 kV, 40 mA, 2° – 70° 2θ , 0.02° step size, counting time of 1 s/step, automatic divergent slit, 10 mm irradiated length, graphite monochromator) of the sample with 20 mass-% zincite added as internal standard was used for calculating phase composition.

As insufficient material of the various ultrafine fractions A, B, C, D was available for a standard non-oriented powder mount, only oriented mounts were analysed and interpreted in a qualitative manner. The oriented mounts were analysed in the same set-up as the bulk non-oriented powders except using a shorter counting time of only 0.1 s/step to avoid loss of ethylene-glycol during measurements.

3.2.4 Results

Bulk composition of clay-transformed metavolcanics

The patterns of XRPD analyses on non-oriented bulk powder samples are depicted in Appendix D and the results of quantitative phase analysis using a Rietveld approach shown in Table 3-2. The content of dioctahedral Al-rich smectite (montmorillonite) in clay-transformed samples from Kiirunavaara deposit (samples KI-01 to KI 05) ranges from about 44 to 79 %. All samples contain minor amounts of calcite (3 to 12 %). Zeolite minerals were not detected. In contrast, the sample from Vathanvaara (VA-01) shows the presence of the zeolite mineral stilbite (11 %), but no carbonate and a low smectite content of only 29 %. In the sample from Malmberget (MA-01), the main transformation phase is an illite-rich Reichweite 3 illite-smectite. Similarly, no carbonate minerals have been detected in this sample. The main residual phases in the Kiirunavaara and Vathanvaara samples include feldspars, mainly albite and occasionally microcline, quartz, biotite and minor amounts of chlorite, talc, actinolite, fluor-apatite, magnetite, rutile, and occasionally pyrite, while muscovite, quartz and haematite are detected in the Malmberget sample.

Table 3-2. Results of quantitative phase analysis of bulk samples in mass-%. Empty field indicates that the phase was not detected.

| XRD | KI-01 | KI-02 | KI-03 | KI-04 | KI-05 | MA-01 | VA-01 |
|---------------------------|-------|-------|-------|-------|-------|-------|-------|
| R3 I-S + Muscovite | | | | | | 84 | |
| Montmorillonite | 46 | 44 | 47 | 62 | 79 | | 29 |
| Calcite | 4 | 12 | 3 | 8 | 12 | | |
| Stilbite | | | | | | | 11 |
| Quartz | 6 | 8 | 16 | 6 | 3 | 4 | 2 |
| Albite | 36 | 19 | 29 | 14 | | | 55 |
| Microcline | | 3 | | | | | |
| Biotite | 5 | 8 | 2 | 4 | 3 | | |
| Talc | | | | 1 | | | |
| Actinolite | | <1 | <1 | | | | |
| Chlorite | <1 | 2 | | 1 | | <1 | 3 |
| Apatite | 1 | 1 | 1 | 1 | | | |
| Magnetite | 1 | 1 | <1 | 1 | | | |
| Haematite | | | | | | 11 | |
| Rutile | | <1 | 1 | 1 | 3 | | |
| Pyrite | | <1 | | <1 | | | |

Composition of size fractions of clay transformed metavolcanics

The XRPD analyses of oriented mounts of the various Na-exchanged ultrafine size fractions (<0.02 µm, 0.02–0.05 µm, 0.05–0.2 µm) in air-dried and ethylene-glycolated state and of non-oriented mount of the untreated <2 µm fractions are reported in appendix E. An overview of the detected phases in the separates with quantitative results for the <2 µm fractions.

A dioctahedral Al-rich smectite (Sm) dominates all ultrafine fractions in clay-transformed samples from the Kiirunavaara deposit. It amounts to 92 to 99 mass-% in the <2 µm fractions. Only the finest fractions A (<0.02 µm) contain exclusively smectite. In the coarser ultrafine fraction C (0.05–0.2 µm) of samples KI-01 and KI-02 and in the fraction D (0.2–2 µm) of sample KI-03, traces of feldspar (F, most probably albite) and in sample KI-02, additionally traces of chlorite (Ch) are detected. Ancillary mica (M, probably biotite) is found in sample KI-03B (0.02–0.05 µm).

The 001 peaks of the ethylene-glycolated specimens of the smectite display rational series with a coefficient of variation (CV) of $l \cdot d(001)$ varying between 0.43 and 0.78 and an average layer thickness of the ethylene-interlayered smectite yields 16.62 to 16.84 Å. The former indicates that the smectite does not contain any interstratified illite clearly detectable by XRD (Bailey, 1982), in agreement with the application of the various other methods described by Środoń (1980) and Moore and Reynolds (1997) on the measurements. The latter parameter could indicate a moderate to high layer charge (Brindley, 1966). The analysis of fraction D (0.2–2 µm) of sample KI-03 shows strong hkl reflections in addition to the 001 peaks indicating that this fraction is poorly oriented and thus dominated by smectite aggregates.

In sample VA-01, corrensite and feldspar are detected in both coarser fractions B and C, and only the finest fraction contains exclusively smectite. The CV of $l \cdot d(001)$ of the ethylene-glycolated smectite complex in this sample is slightly higher than the recommended value 0.75 for a rational series (Bailey, 1982), i.e. 0.82 for VA-01B and 0.88 for VA-01C, suggesting that minor amounts of randomly interstratified illite in smectite is possible for these fractions. The application of the three methods to identify and quantify interstratified illite in illite-poor R0 illite-smectite by Środoń (1980) were not, however, conclusive.

The sample MA-01 from Malmberget contains a dominant illite-rich R3 illite-smectite interstratified mineral and traces of chlorite in all three ultrafine size fractions. The positions of the illite 001/smectite 002 and illite 002/smectite 003 peaks indicates an illite content of about 92 % in the interstratified mineral.

Table 3-3. Mineral phases detected by XRD in the oriented specimen of the separated ultrafine fractions (Na-exchanged) after removal of organic matter, iron oxides and carbonates and quantitative mineral composition of untreated <2 µm fractions. Abbreviations: Ch = chlorite, Co = corrensite, F = feldspar, IS = illite-smectite, M = mica (biotite), Sm = dioctahedral smectite. Trace components are marked in brackets.

| | KI-01 | KI-02 | KI-03 | KI-04 | KI-05 | MA-01 | VA-01 |
|----------------------|--------|-------------|--------|-------|-------|----------|-------------|
| A (<0.02 µm) | Sm | Sm | Sm | Sm | Sm | IS, (Ch) | Sm |
| B (0.02–0.05 µm) | Sm | Sm | Sm,(M) | Sm | Sm | IS, (Ch) | Sm,(Co),(F) |
| C (0.05–0.2 µm) | Sm,(F) | Sm,(F),(Ch) | Sm | Sm | Sm | IS, (Ch) | Sm,(Co),(F) |
| D (0.2–2 µm) | | | Sm,(F) | | | | |
| E (<2µm) untreated | | | | | | | |
| Illite-Smectite (+M) | | | | | | 98.0 | |
| Smectite (Sm) | 92.3 | 97.9 | 98.5 | 97.0 | 99.5 | | |
| Chlorite (Ch) | 0.5 | 0.7 | | 0.1 | | 2.0 | |
| Calcite | 0.9 | 0.7 | | 1.5 | | | |
| Gypsum | | | 0.2 | | | | |
| Albite (F) | 5.5 | | 1.2 | 1.1 | | | |
| Quartz | 0.8 | 0.7 | 0.1 | 0.3 | 0.5 | | |

3.2.5 Conclusions

The mineralogical and chemical studies presented here show that deep clay transformation in the Kiirunavaara mine is related to the formation of significant amounts (44 to 81 wt.-%) of a high-charge montmorillonite with a generally Ca-rich exchangeable interlayer composition. Further chemical and mineralogical characterisation of the clay separates by energy-dispersive X-ray spectrometry in a scanning electron microscope, exchangeable cation determination, layer charge determination by the deuterium method (Kuligiewicz et al. 2015a, b), and thermal analysis confirm the high layer charge and a predominantly cis-vacant, Fe-poor montmorillonite composition with predominately exchangeable Ca in the interlayer. No interstratifications with illite were detected by XRD analysis. The <0.02 µm fractions of the material from the clay transformation zones consist of smectite while coarser fractions (0.02 to 0.2 µm) may contain ancillary feldspar, mica or chlorite.

The smectite compositions are similar in the transformation zone of the footwall and hanging wall volcanic rocks and within the ore. The iron contents of the dioctahedral smectites show minor variations with Fe₂O₃ ranging from 0.93 to 2.46 wt.-% that are not related to the presence or absence of residual magnetite in the transformed rocks or to proximity to magnetite ores.

Further electron microscopic and stable isotope studies of the calcites in the clays show that they are very fine grained (<2 µm), not relicts of ore-related carbonates, not in oxygen isotope equilibrium and thus not co-genetic with the clays but rather with present-day ground waters at low temperatures of 25 to 35 °C and therefore formed after clay formation (Gilg et al. 2022).

The stable hydrogen and oxygen isotope composition of the smectites corroborate the conclusions derived from low boron contents of the smectites (Rieger, 2016) indicating a meteoric source of the clay-forming fluids at Kiruna and Vahtanvaara. These data also suggest low temperatures of clay formation (<50 °C) at Kiruna consistent with the absence of stilbite and major illitic components in the smectites. The isotope compositions of the meteoric waters involved in smectite formation at Kiruna are similar to those forming the Mesozoic kaolins in Southern Sweden (Gilg et al. 2013).

3.3 Analytical results for a sample from the Kiirunavaara mine, Sweden

Sirpa Kumpulainen and Leena Kiviranta

3.3.1 Introduction

The aim of this work was to determine the composition and properties of a clay sample taken from the Kiruna mine, in order to assess the long-term stability of clays. The objectives of this work are to determine physico-chemical and mineralogical characteristics, swelling pressure and hydraulic conductivity of the clays in the sample provided.

3.3.2 Sample description

The studied sample (KINA ID c65f8c⁶) was delivered to Mitta on 23.6.2020 and is presented in Figure 3-2.

3.3.3 Methods

The list of analyses performed on clay sample c65f8c is presented in Table 3-4. Most of the analyses, namely cation exchange capacity (CEC), exchangeable cation extraction (ExC), aqueous soluble ion extraction (Aq.S.ions), chemical composition, mineralogical composition with X-ray diffraction (XRD) and subsequent Rietveld analysis and grain density determination were performed on the bulk sample, but CEC, citrate-bicarbonate-dithionite extraction (CBD), X-ray diffraction analysis of clay fraction (OXRd) and chemical composition were performed on the clay fraction to determine the clay composition. In addition, the coarse mineral fraction, was studied with optical microscopy to support the mineralogical interpretations from the bulk XRD. The analyses were performed as described in Kiviranta et al. (2018), with only the minor variations in the X-ray diffraction analyses described below in detail.

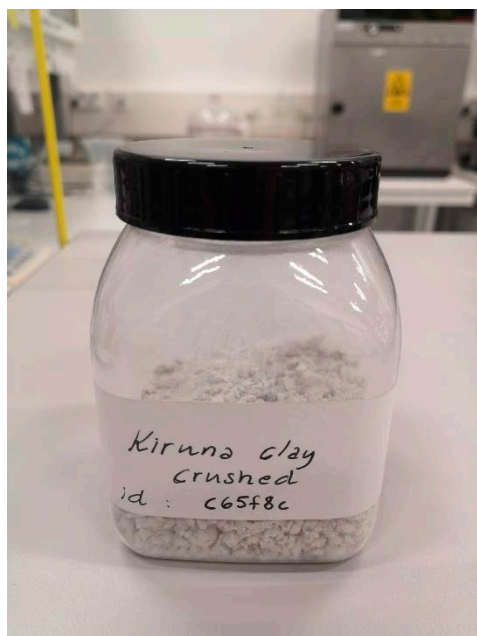


Figure 3-2. Clay sample c65f8c from the Kiirunavaara mine as delivered to the AINS (now Mitta) laboratory on 23.6.2020.

⁶ Also known as Kiruna 2019 solid c65ff9 (for location, see Appendix B).

XRD

Non-oriented XRD sample preparation was made at the Geological Survey of Finland (GTK) by grinding the sample in an agate mortar under acetone. The suspension was poured onto a glass slide, spread evenly and left to dry. After preparation, the sample mount was put into a desiccator that contained saturated $\text{Mg}(\text{NO}_3)_2$ solution in order to achieve standard relative humidity (54 % RH at 20 °C) and kept there for three days. The sample mount was then immediately transferred to a sample holder inside the instrument cabin. The relative humidity of the instrument cabin (48 %) was recorded at the beginning of the measurement and the room temperature was 24 °C.

The XRD instrument employed at GTK was a Bruker D8 Discover (A25) powder diffractometer, equipped with a LYNXEYE detector (semiconductor silicon strip in 1-D mode). X-ray tube (line focus) anode material was copper and the utilized wavelengths were $\text{Cu K}\alpha_1 = 1.5406 \text{ \AA}$, $\text{Cu K}\alpha_2 = 1.5444 \text{ \AA}$, ($\text{Cu K}\alpha$ average = 1.5418 \AA), and $\text{Cu K}\beta$ contamination = 1.3922 \AA .

The X-ray powder diffractogram was measured in the GTK laboratory from the 2θ -range $2.00\text{-}70.19^\circ 2\theta$ ($\text{CuK}\alpha$) in continuous measurement mode at $0.0205^\circ 2\theta/\text{s}$ angular velocity, which corresponds to $0.0102^\circ 2\theta$ -steps with the measurement time of 0.5 s/step. The primary optical path utilized a 0.6 mm opening (0.35°) fixed divergence slit and 2.5° soller slit. The secondary optical path contained a 2.5° soller slit and Ni-filter for $\text{Cu K}\beta$ suppression. Goniometer radius was 280 mm, beam knife reduces air scattering. The sample spinner was temporarily unserviceable due to a broken sample stage mechanism. Generator settings were 40 kV/40 mA.

Diffraction data were treated using 1) background fitting and 2) displacement correction using the samples' own quartz as an internal standard. Mineral phase identifications were conducted using Bruker EVA 5.2 software and ICDD (International Centre for Diffraction Data, Powder Diffraction File) PDF-4 Minerals 2020 database that contains only naturally occurring inorganic crystalline phases (minerals).

The mineralogical composition was determined at Mitta from non-oriented XRD patterns using a full-profile Rietveld refinement by the Siroquant v.4 software. First, the background was subtracted and refinement was done in several subsequent stages until no major improvement in pattern fit was achieved. Instrument zero, phase scales, half-widths, unit cell dimensions and preferred orientation were all refined.

Swelling pressure and hydraulic conductivity

Swelling pressure (SP) and hydraulic conductivity (HC) were performed on bulk sample as described in Kiviranta et al. (2018). The uncertainty analyses for swelling pressure, hydraulic conductivity and related water content and density values were performed according to Kiviranta and Kumpulainen (2011). The selected target dry density for clay sample c65f8c SP and HC measurements was 1.57 gcm^{-3} and the saturating and permeant solution 10 gL^{-1} PRS (Posiva Reference Solution with Na:Ca of 2:1, Kiviranta et al. 2018). The material was crushed gently before sample compaction to a disc of 35 mm diameter and approximately 12 mm thick.

Table 3-4. Analysis matrix for clay sample c65f8c.

| Chemical constituents and properties | | | | | | | | | | | Physical properties | | |
|--------------------------------------|-------------|------------|-------------|-----|------------|---------------|-----|------|-----------------|------------|---------------------|----|----|
| Sample | Bulk sample | | | | | Clay fraction | | | Coarse fraction | | Bulk sample | | |
| | CEC | Aq.S. ions | Chem. comp. | ExC | Min. comp. | CEC | CBD | OXRD | Chem. comp. | Microscopy | Grain density | SP | HC |
| c65f8c | x | x | x | x | x | x | x | x | x | x | x | x | x |

3.3.4 Results

Exchangeable cations and CEC

Results for exchangeable cation composition and CEC determined with Cu(II)-trien) determined from bulk sample are shown in Table 3-5.

Table 3-5. CEC (determined spectrophotometrically with the Cu(II)-trien method) and exchangeable cations of bulk materials (measured with the NH₄Cl-method) on clay sample c65f8c.

| Sample | Saturation of exchangeable sites | | | | Exchangeable cations in dry (105 °C) weight | | | | | CEC | CEC std |
|--------------|----------------------------------|-----|------|------|---|----------------------|-----------------------|-----------------------|------------------------|--------------------|--------------------|
| | Ca % | K % | Mg % | Na % | Ca eqkg ⁻¹ | K eqkg ⁻¹ | Mg eqkg ⁻¹ | Na eqkg ⁻¹ | Sum eqkg ⁻¹ | eqkg ⁻¹ | eqkg ⁻¹ |
| c65f8c, bulk | 79 | 1 | 14 | 6 | 0.67 | 0.01 | 0.12 | 0.05 | 0.85 | 0.80 | 0.01 |

Aqueous soluble ions

Results for water soluble ions determined from bulk sample are shown in Table 3-6.

Table 3-6. Water soluble anions (SO₄ and Cl), determined with IC and water-soluble cations (Al, Si, Cu, Ca, Mg, Na and K) determined with ICP-AES from 1:100 solid:solution extracts.

| Sample | IC | | ICP-AES | | | | | | |
|--------------|---------|----------------------|---------|---------|---------|--------|---------|---------|---------|
| | Cl mg/g | SO ₄ mg/g | Al mg/g | Ca mg/g | Cu mg/g | K mg/g | Mg mg/g | Na mg/g | Si mg/g |
| c65f8c, bulk | 0.06 | 0.05 | <0.01 | 0.20 | 0.01 | <0.06 | 0.03 | <0.11 | 0.06 |

Citrate-bicarbonate-dithionite extractable elements

Results for citrate-bicarbonate-dithionite (CBD) extractable elements presenting approximate content of poorly crystalline iron oxides determined from Na-exchanged clay (<0.5 mm) fraction are shown in Table 3-7. The results from CBD-extraction on iron was used for calculation of smectite composition (see below).

Table 3-7. Citrate-bicarbonate-dithionite extractable elements in purified Na-exchanged clay (<0.5 mm) fractions.

| Sample | Al ₂ O ₃ wt-% | Fe ₂ O ₃ wt-% | MgO wt-% | SiO ₂ wt-% |
|-----------------|-------------------------------------|-------------------------------------|----------|-----------------------|
| c65f8c, Na-clay | 0.34 | 0.33 | 0.16 | 0.83 |

Chemical composition

Results for chemical composition from the bulk sample and the Na-exchanged clay (<0.5 mm) fraction are shown in Tables 3-8 and 3-9.

Smectite composition

Smectite composition calculated from results of the chemical composition of Na-exchanged clay (<0.5 mm) fraction (Table 3-8), citrate-bicarbonate-dithionite extractable elements (Table 3-9) and mineralogical analyses from the clay fraction are shown in Table 3-10, together with CEC calculated from the smectite composition and determined from a purified clay fraction.

Table 3-8. Total chemical composition of bulk materials and Na-exchanged clay fractions: major elements as oxides (all in wt.%), LOI and speciation of Fe, C and S.

| Sample | SiO ₂ | Al ₂ O ₃ | Fe ₂ O ₃ | TiO ₂ | MgO | CaO | Na ₂ O | K ₂ O | P ₂ O ₅ | Cr ₂ O ₃ | MnO | LOI | Sum | Fe ³⁺ | Fe ²⁺ | C-tot | C-org | S-tot | S-S ₂ |
|-----------------|------------------|--------------------------------|--------------------------------|------------------|------|------|-------------------|------------------|-------------------------------|--------------------------------|------|------|-------|------------------|------------------|-------|-------|-------------------|------------------|
| c65f8c, bulk | 56.96 | 18.02 | 1.48 | 0.06 | 3.55 | 2.53 | 3.23 | 0.22 | 0.02 | 0.002 | 0.07 | 13.8 | 99.94 | 0.71 | 0.33 | 0.17 | 0.02 | 0.09 | 0.05 |
| c65f8c, Na-clay | 59.17 | 19.67 | 0.84 | <0.01 | 4.82 | 0.02 | 3.55 | 0.02 | 0.02 | <0.002 | 0.06 | 11.8 | 99.97 | 0.59 | <0.16 | 0.10 | 0.10 | 0.02 ⁷ | <0.02 |

Table 3-9. Total chemical composition (continued) of bulk materials and Na-exchanged clay fractions: minor and trace elements (all in ppm). All other elements after aqua regia extraction except Ba, Ni, Sr, Zr, Y, Nb and Sc from LiBO₂/Li₂B₄O fusion and nitric acid digestion.

| Sample | Mo | Cu | Pb | Zn | Ag | Ni | Co | As | U | Th | Sr | Cd | Sb | Bi | V | La | Ba | B | W | Tl | Hg | Ga | Zr | Y | Nb | Sc |
|-----------------|----|----|----|----|------|-----|----|----|----|----|----|------|----|----|----|----|----|-----|----|----|----|----|----|----|----|----|
| c65f8c, bulk | <1 | 2 | <3 | 4 | <0.3 | <20 | 10 | <2 | <8 | <2 | 26 | <0.5 | <3 | <3 | 6 | 19 | 24 | <20 | <2 | <5 | <1 | 7 | <5 | 20 | <5 | 1 |
| c65f8c, Na-clay | <1 | 14 | <3 | 9 | <0.3 | <20 | 2 | <2 | <8 | <2 | <2 | <0.5 | <3 | <3 | <1 | 3 | <5 | <20 | <2 | <5 | <1 | <5 | <5 | <3 | <5 | <1 |

Table 3-10. Occupation of tetrahedral, octahedral and interlayer positions, calculated molecular weight (MW), tetrahedral charge (TCh), octahedral charge (OCh), total charge (TotCh), beidellite content of the smectite (Beid), the minimum amount of silica impurities present in purified clay fractions (SiO₂) and calculated (calc) cation exchange capacity (CEC) after structural formula method (SFM) calculations and measured (obs) CEC of purified Na-exchanged clay fractions.

| Sample | For Na-exchanged smectite (from structural formula method) | | | | | | | | | | | | | | | | | | | For Na-exchanged clay fraction | |
|-----------------|--|-----------------------|------------------------|-----------------------|-------------------------------------|-------------------------------------|-----------------------|------------------------|-----------------------|-----------------------|------------------------|----------------------|------------------------|------------------------|--------------------------|----------|----------------------------|-------------------------------|----------------------|--------------------------------|--|
| | Tetrahedral positions | | | Octahedral positions | | | | | Interlayer positions | | | | Charges | | | | CEC obs Eqkg ⁻¹ | CEC obsStd Eqkg ⁻¹ | | | |
| | Si eqFU ⁻¹ | Al eqFU ⁻¹ | Sum eqFU ⁻¹ | Al eqFU ⁻¹ | Fe ³⁺ eqFU ⁻¹ | Fe ²⁺ eqFU ⁻¹ | Mg eqFU ⁻¹ | Sum eqFU ⁻¹ | Ca eqFU ⁻¹ | Na eqFU ⁻¹ | Sum eqFU ⁻¹ | MW gFU ⁻¹ | TCh eqFU ⁻¹ | OCh eqFU ⁻¹ | TotCh eqFU ⁻¹ | Beid w-% | | | SiO ₂ w-% | CEC calc Eqkg ⁻¹ | |
| c65f8c, Na-clay | 7.923 | 0.077 | 8.000 | 3.023 | 0.051 | 0.000 | 0.963 | 4.037 | 0.003 | 0.924 | 0.926 | 742 | -0.077 | -0.852 | -0.929 | 8 | 0 | 1.25 | 1.22 | ±0.008 | |

⁷ Value for sulphate-sulphur was used since it was higher than measured for the total sulphur.

The smectite in clay sample c65f8c has the composition of $(\text{Na}_{0.06}\text{Ca}_{0.37}\text{Mg}_{0.07})(\text{Al}_{3.02}\text{Fe}_{0.05}\text{Mg}_{0.96})$ $(\text{Al}_{0.08}\text{Si}_{7.92})\text{O}_{20}(\text{OH})_4$. The results in Table 3-10 show that the smectite in clay sample c65f8c is montmorillonite with a very low iron content but relatively high magnesium content in the octahedral layer. The smectite is also relatively highly charged, with a total charge of -0.93 , similar to values encountered in Sardinian bentonites (see Kiviranta et al. 2018). The calculated CEC (based on structural calculations, i.e. determined from chemical composition of smectite) of 1.25 eqkg^{-1} was in line with the measured CEC 1.22 eqkg^{-1} in the clay fraction.

Mineralogical composition

X-ray diffraction pattern of randomly oriented bulk sample is shown in Figure 3-3, together with peak assignments, and of oriented clay fraction in Figure 3-4. Mineralogical composition determined using the X-ray diffraction pattern of the bulk sample and information from qualitative mineralogical analyses of bulk sample and clay fraction, in addition to the chemical compositions, is given in Table 3-11.

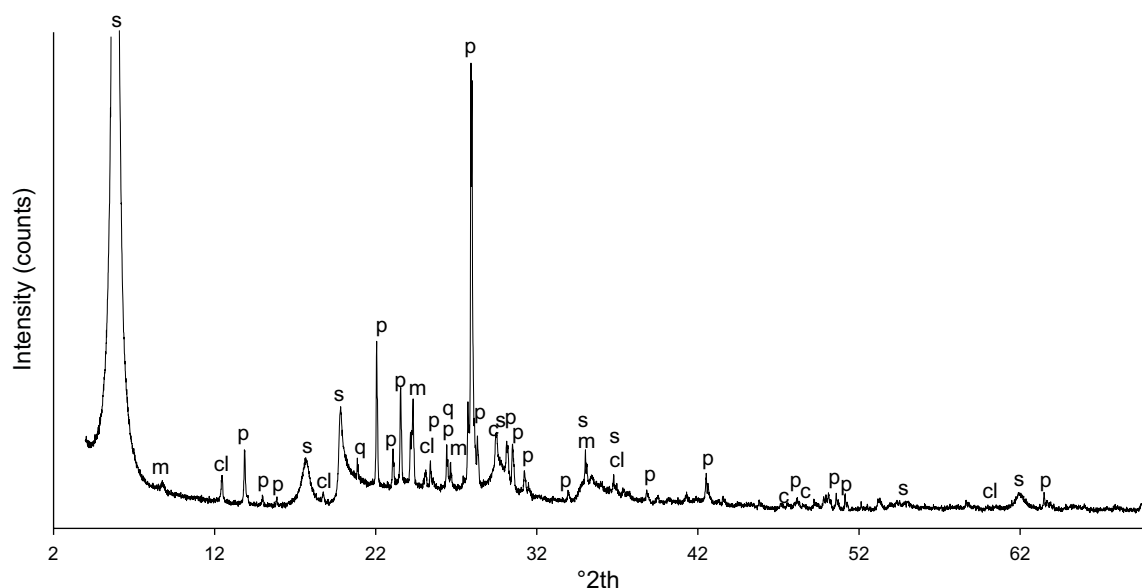


Figure 3-3. X-ray diffraction pattern of c65f8c bulk sample and identified minerals. Abbreviations: s=smectite, m=mica/illite, c=calcite, cl=chlorite, p=plagioclase and q=quartz.

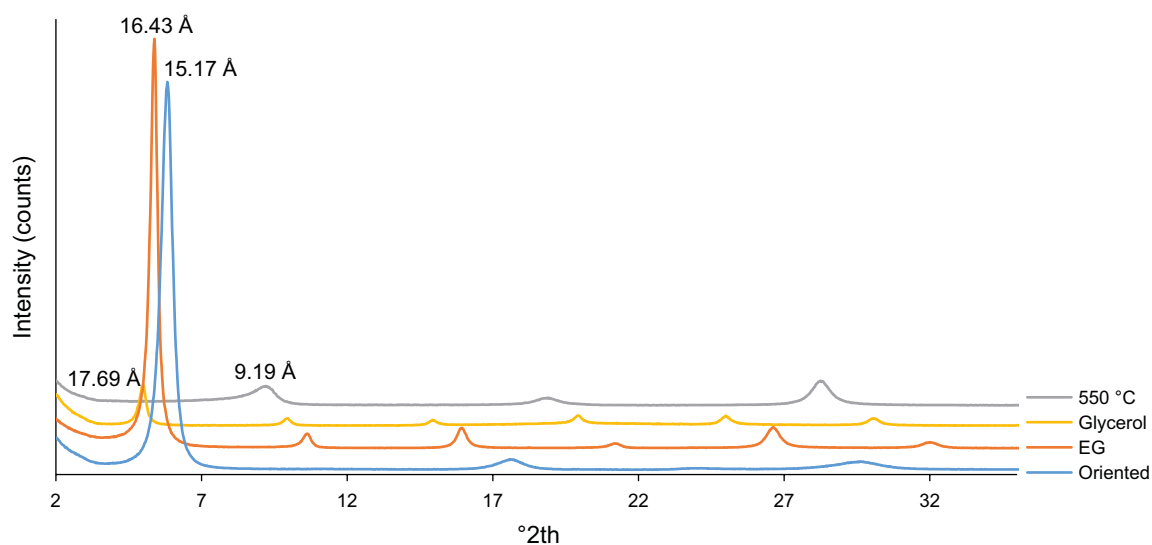


Figure 3-4. X-ray diffraction patterns of c65f8c clay-fraction and smectite $d[001]$ peak positions.

The analysis of the bulk samples indicated the presence of dioctahedral smectite since the $d[060]$ located approximately at 1.50 \AA (corresponding $^{\circ}2\theta$). Further analysis of the c65f8c clay fraction verified the presence of smectite, but also excluded the presence of vermiculite, which was tested with the additional glycerol treatment. Although chlorite was present in the c65f8c bulk sample, it was not present in the clay fraction ($<0.5 \text{ mm}$).

Table 3-11. Mineralogical composition of clay sample c65f8c. Values in brackets show smectite and mica/illite contents that are adjusted based on non-exchangeable K-content in the clay fraction.

| Sample | Smectite wt-% | Mica/ illite wt-% | Quartz wt-% | Chlorite wt-% | Plagioclase wt-% |
|--------------|---------------|-------------------|-------------|---------------|------------------|
| c65f8c, bulk | 61.2 (63.5) | 2.4 (0.1) | 0.3 | 2.4 | 33.6 |

Grain density

According to triplicate measurement, the grain density of clay sample c65f8c is $2.708 \pm 0.005 \text{ gcm}^{-3}$.

Swelling pressure and hydraulic conductivity

Swelling pressure and hydraulic conductivity sample properties, load cell properties and force measurement uncertainties are given in Table 3-12 and the results in Table 3-13.

Taking into account the dry density and smectite content (i.e. EMDD) the hydraulic conductivity of clay sample c65f8c is similar to those of bentonites (Figure 3-5), but among the samples with highest hydraulic conductivities. Likewise, comparison of swelling pressure with bentonites shows that clay sample c65f8c has similar swelling pressure to bentonites, but the values are among the highest for bentonites.

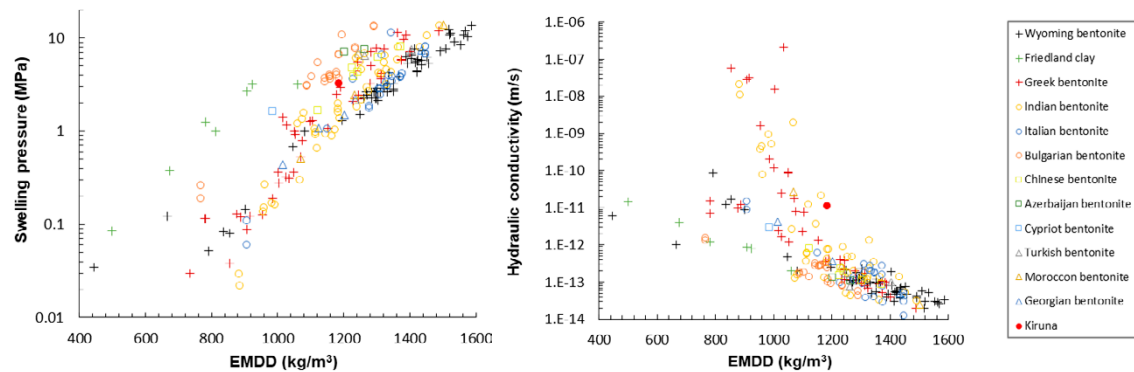


Figure 3-5. Comparison of swelling pressure and hydraulic conductivity of clay sample c65f8c (red dot) with bentonites and smectite clays of similar EMDD's and saturating solutions ($0\text{--}11 \text{ gL}^{-1} \text{ TDS}$). Data for other bentonites and smectite clays are taken from Kiviranta et al. (2018) and references therein.

Table 3-12. Details of swelling pressure and hydraulic conductivity samples and measurement set-up for clay sample c65f8c.

| Sample | Initial | Sample dimensions | | | Load cell | | | | Uncertainties for force measurements | | | Solution |
|--------------|---------|-------------------|-----------|----------------------------|-----------|--------------------------------------|--------------------------------------|----------------------------------|--------------------------------------|------------------------------|------------------------|--------------------------------------|
| | w % | Ø mm | Height mm | S _i (initial) % | Range kg | Cal F ₁ VKN ⁻¹ | Cal F ₂ VKN ⁻¹ | Cal.F. Average VKN ⁻¹ | ΔF _{transducer} kN | ΔF _{calibration} kN | ΔF _{total} kN | |
| c65f8c, bulk | 10.6 | 35 | 11.5 | 44 | 0–900 | 1.1283 | 1.1386 | 1.1335 | 0.080 | 0.014 | 0.081 | 10 gL ⁻¹ PRS ⁸ |

Table 3-13. Results of swelling pressure and hydraulic conductivity measurement, calculations and related uncertainties for clay sample c65f8c. EMDD was calculated using f=0.388.

| Material code | SP (after HC) | | HC at 20 °C | | Post-Mortem | | | | Calculations | | | | |
|---------------|---------------|---------|-------------------------|---------------------------|-------------|-------|----------------------------------|-----------------------------------|--------------------------------------|--------------------------------------|---------------------------------------|------------|----------------------------|
| | SP MPa | ΔSP MPa | k ms ⁻¹ | Δk ms ⁻¹ | w % | Δw % | ρ _b kgm ⁻³ | Δρ _b kgm ⁻³ | ρ _b (w) kgm ⁻³ | ρ _d (w) kgm ⁻³ | Δρ _d (w) kgm ⁻³ | Void ratio | EMDD (w) kgm ⁻³ |
| c65f8c, bulk | 3.25 | ± 0.09 | 1.1 × 10 ⁻¹¹ | ± 0.6 × 10 ⁻¹¹ | 29.0 | ± 1.9 | nd | nd | 1956 | 1516 | ± 43 | 0.79 | 1185 |

⁸ Posiva reference solution, Ca²⁺:Na⁺ mass ratio of 1:2

3.4 Mineralogy of Thirteen Samples from the Kiirunavaara mine, Sweden

Helen A. Pendlowski and Evelyne M. Delbos

3.4.1 Introduction

Thirteen samples were forwarded to the laboratory for whole rock mineralogical analysis by X-ray powder diffraction (XRPD). Additionally, two of the samples were selected for <2 µm clay fraction mineralogical analysis of oriented specimens, three samples for measurement of CEC and one sample for examination by SEM.

3.4.2 Sample description

The thirteen samples as supplied to James Hutton Ltd are listed in Table 3-14.

Table 3-14. Sample information as supplied to James Hutton Ltd, listed along with applied analytical methods. Locations in Appendix B.

| Job and Sample Information: | | | | | | |
|------------------------------|---|----------------|-----------|------------|-----|-----|
| Client No/ Reference: | Order | 20'674 (NAGRA) | | | | |
| Date Received: | Sample(s) | 16-July-2021 | | | | |
| | | SEM Plate | | | | |
| Hutton ID: | Client Sample code: | LKAB site code | Bulk XRPD | <2 µm XRPD | SEM | CEC |
| 1346794 | 1. 385-1165 | 385-1165 | X | | | |
| 1346795 | 2. 30-1108 | 30-1108-Y3085 | X | | | |
| 1346796 | 3. 381-1108 | 381-1108 | X | | | |
| 1346797 | 4. 378-1108 | 378-1108 | X | | | |
| 1346798 | 5. CHI-latitude 41 deg S | s. Chile | X | | | |
| 1346799 | 6. KU-L-2008-3 | 312.1-1165 | X | | | |
| 1346800 | 7. KUJ-L-2008-1 | 298-1194 | X | | | |
| 1346801 | 8. KU-L-2006-1 | 392-1194 | X | | | |
| 1346802 | 9. KUJ-L-2008-2 | 395-1194 | X | | | |
| 1346803 | 10. KUJ-L-2004-1 | 384-1194 | X | | | |
| 1346804 | 11. Kiruna 2018 c65ef8 (milled and homogenised) | 380-1194 | X | X | | X |
| 1346805 | 12. Kiruna 2019 c65f8d (milled and homogenised) | 306-1194 | X | X | | X |
| 1346806 | 13. Kiruna 2019 c65ff9 (solid, not milled) | 306-1194 | X | | X | X |

3.4.3 Methods

The methods employed are listed in Table 3-15 and are described in detail below.

Table 3-15. Methods employed on the samples.

| Methods | Accreditation Reference | Date Analysis Completed |
|---|-------------------------|-------------------------|
| Identification and Quantification of a polycrystalline material by XRPD | GM003 and GM004 | 31/08/2022 |
| Identification and Semi Quantification of Clay Minerals by XRPD | GM001 and GM002 | 31/08/2022 |
| CEC by Cobalt Hexammine Method | GM006 | 30/07/2021 |
| Examination of specimens by SEM | EM001 | 06/08/2021 |

X-ray powder diffraction (XRPD)

For bulk (whole sample) quantitative analysis, samples were wet ground for 12 minutes (in ethanol or water) in a McCrone mill and spray dried to produce random powder specimens (Hillier, 1999). XRPD patterns are typically recorded over a range of $65^{\circ}2\theta$ or more using either Cu or Co radiation, the actual range being instrument dependent, so is given on the individual scan plots (see appendix F⁹). Quantitative analysis was made by a normalised full pattern reference intensity ratio (RIR) method as described in Omotoso et al. (2006) and Butler and Hillier (2021). Unless stated otherwise, expanded uncertainty using a coverage factor of 2, i.e. 95 % confidence, is given by $\pm X0.35$, where X = concentration in wt.%, e.g. 30 wt.% \pm 3.3 (Hillier, 2003). Note also that, for phases present at the trace level (< 1 %), there may also be uncertainty as to whether the phase is truly present in the sample. This is both phase and sample dependent. It arises because, at trace levels, identification is often based on the presence of a single peak and the judgement of the analyst in assigning that peak to a likely mineral or phase.

For semi-quantitative analysis of clay minerals based on their basal reflections, clay fractions of $<2 \mu\text{m}$ were obtained by timed sedimentation, prepared as oriented mounts using the filter peel transfer technique and scanned from near 2 or $3^{\circ}2\theta$ to $45^{\circ}2\theta$ using either Cu or Co radiation. As the actual range is instrument dependent, it is also given on the individual XRDF scan plots in appendix E. Typically, three scans are made, one in the air-dried state, one after glycolation and one after heating to 300°C for one hour. Clay minerals identified were quantified using a mineral intensity factor approach based on calculated XRPD patterns (Hillier, 2003). Unless otherwise stated, for clay minerals present in amounts $> 10\text{wt.}\%$, uncertainty is estimated as better than $\pm 5\text{wt.}\%$ at the 95 % confidence level.

CEC

CEC was measured using a cobalt hexammine trichloride method (ISO, 2018), wherein the exchangeable cations on the sample are replaced by trivalent cobalt hexammine ions and the CEC of the sample is determined by absorption colourimetry.

SEM/EDS

A representative portion of the sample was mounted onto a standard SEM stub using a double-sided carbon tab as the adhesive. The prepared sample was analysed using a Carl Zeiss Sigma VP Field Emission Scanning Electron Microscope (FE-SEM). Characterisation of the material was aided by Energy Dispersive Spectroscopy (EDS) using a Bruker Quantax 400 Spectrometer and XFlash 5030 Silicon Drift Detector (SDD). EDS provides an elemental composition of the material analysed. The SDD detector is equipped with an ultra-thin window allowing detection of elements down to carbon. The analysis is qualitative. Prior to the analysis, the sample was coated with a thin layer of platinum to reduce charging under the electron beam. The analysis was conducted in variable pressure mode at an accelerating voltage of 15kV.

3.4.4 Results

XRPD whole rock results are presented in Table 3-16 (and the scan plots in appendix F), clay fraction results in Table 3-17, CEC data in Table 3-18 and SEM data in Figure 3-6. The EDS spectra of the smectite (Figure 3-6) appear to indicate that it is calcium saturated, which is consistent with the position of the peak in the clay fraction XRPD data at around 15 \AA .

⁹ Note that XRPD patterns are identified by a Hutton ID and by names based on KINA project supplied identifiers (see Table 3-14), plus the suffix 'A' for Air-Dried, 'G' for ethylene glycol treated, 'H3' for heated to 300°C and 'B' for bulk sample. The XRPD patterns, with the main non-clay phases identified in the bulk samples by reference to patterns from the International Centre for Diffraction Database (ICDD).

Table 3-16. XRPD Bulk Mineralogy (weight %) by RIR Method (see Section 3.4.3).

| Hutton ID | KINA sample ID | Quartz | Plagio- clase | K-feld- spar | Calcite | Amphibole | Pyroxene | Magnetite | Hematite | Pyrite | Rutile | Apatite | Gibbsite | Anatase | Mica (Tri) | Mica (Di) | Chlorite (Tri) | Kaolinite | Smectite (Di) | Total |
|-----------|---------------------------------|--------|------------------|-----------------|---------|-----------|----------|-----------|----------|--------|--------|---------|----------|---------|---------------|--------------|-------------------|-----------|------------------|-------|
| 1346794 | 1. 385-1165 | 1.0 | nd | 4.4 | 5.2 | 0.4 | nd | 11.8 | 0.3 | 0.6 | 0.5 | nd | nd | nd | 9.3 | 1.5 | nd | nd | 65.0 | 100.0 |
| 1346795 | 2. 30-1108 | 17.3 | 33.9 | 1.5 | 3.9 | 0.2 | 1.9 | nd | nd | 0.2 | 1.2 | nd | nd | nd | 0.3 | 1.2 | 1.2 | 0.9 | 36.3 | 100.0 |
| 1346796 | 3. 381-1108 | 7.0 | 40.5 | 0.5 | 3.3 | 1.2 | nd | 0.3 | 0.1 | nd | nd | 0.2 | nd | nd | 6.3 | 3.7 | 0.6 | 0.4 | 35.9 | 100.0 |
| 1346797 | 4. 378-1108 | 21.9 | 28.9 | 1.6 | 10.6 | 1.2 | nd | 4.1 | 0.3 | nd | nd | nd | nd | nd | 1.5 | 3.3 | nd | 0.5 | 26.1 | 100.0 |
| 1346798 | 5. CHI-latitude 41 deg S | 34.3 | 0.5 | 0.3 | 0.1 | nd | nd | nd | 0.1 | nd | nd | 0.2 | 31.6 | 0.3 | nd | 15.8 | 0.1 | 2.8 | 13.9 | 100.0 |
| 1346799 | 6. KUJ-L-2008-3 | 4.6 | 50.4 | 1.0 | 1.6 | 0.5 | nd | 0.5 | 0.1 | 0.3 | nd | nd | nd | nd | 1.4 | 1.0 | 2.4 | 0.5 | 35.7 | 100.0 |
| 1346800 | 7. KUJ-L-2008-1 | 9.6 | 4.6 | 2.3 | 37.7 | 1.0 | nd | 10.1 | 1.7 | nd | nd | nd | nd | nd | 4.3 | 1.5 | 5.7 | 1.5 | 20.0 | 100.0 |
| 1346801 | 8. KU-L-2006-1 | 4.8 | 27.9 | 4.4 | 7.5 | 0.1 | nd | 0.2 | 0.1 | nd | nd | nd | nd | nd | 0.1 | 1.3 | 1.2 | 0.8 | 51.6 | 100.0 |
| 1346802 | 9. KUJ-L-2008-2 | 1.0 | 53.2 | 22.5 | 1.1 | 0.2 | nd | 6.1 | 0.1 | nd | nd | 2.4 | nd | nd | 2.5 | 0.3 | nd | nd | 10.6 | 100.0 |
| 1346803 | 10. KUJ-L-2004-1 | 13.1 | 25.3 | 3.1 | 14.6 | 0.3 | nd | 3.9 | 0.2 | nd | nd | nd | nd | nd | 5.6 | 4.0 | 1.6 | 0.7 | 27.6 | 100.0 |
| 1346804 | 11. Kiruna 2018 c65ef8 | 2.8 | 0.1 | 3.4 | 13.8 | nd | nd | 0.2 | 0.2 | 0.1 | nd | 1.9 | nd | 0.1 | nd | 0.1 | 0.2 | 1.3 | 75.8 | 100.0 |
| 1346805 | 12. Kiruna 2019 c65f8d | 0.9 | 32.7 | 1.0 | 2.1 | 0.1 | nd | 1.0 | 0.2 | 0.2 | nd | nd | nd | nd | 0.2 | 1.3 | nd | 0.4 | 59.9 | 100.0 |
| 1346806 | 13. Kiruna 2019 solid c65ff9 | 3.6 | 50.5 | 0.6 | 1.8 | 0.4 | nd | 1.0 | 0.1 | 1.8 | nd | 0.1 | nd | nd | nd | 1.1 | nd | nd | 39.0 | 100.0 |

Di = Dioctahedral, Tri = trioctahedral, nd = not detected

Table 3-17. Relative percentage of clay minerals in the <2 µm clay size fraction.

| Hutton ID | KINA sample ID. | Trioctahedral Chlorite | Diocahedral Smectite | Percent Expandability |
|-----------|------------------------|------------------------|----------------------|-----------------------|
| 1346804 | 11. KIRUNA-2018-c65ef8 | trace | 100 | 100 |
| 1346805 | 12. KIRUNA-2019-c65f8d | trace | 100 | 100 |

Table 3-18, CEC measurements by the cobalt hexammine method.

| Hutton ID | KINA sample ID | CEC cmol(+)/kg ⁻¹ |
|-----------|------------------------------|------------------------------|
| 1346804 | 11. Kiruna 2018 c65ef8 | 77 |
| 1346805 | 12. Kiruna 2019 c65f8d | 70 |
| 1346806 | 13. Kiruna 2019 solid c65ff9 | 50 |

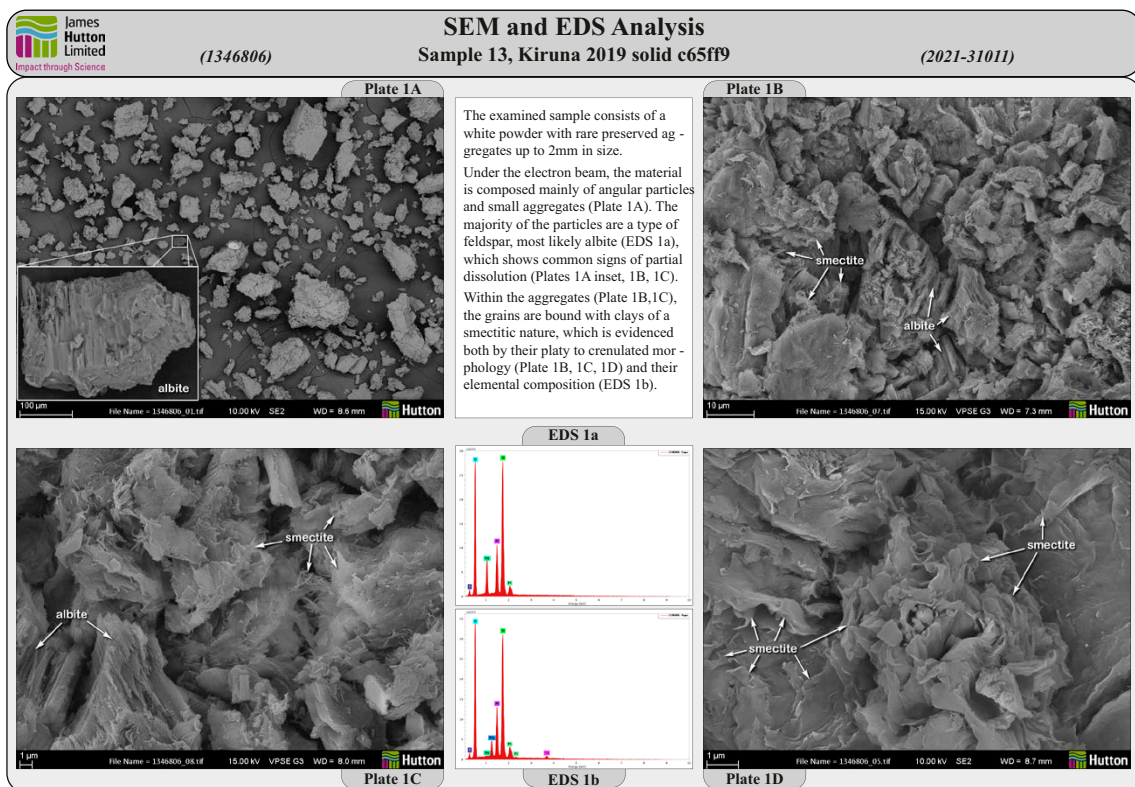


Figure 3-6. SEM images and EDS spectra of smectite-rich sample 134806 (KINA ID Kiruna 2019 solid c65ff9).

3.4.5 Discussion

Minerals identified and quantified in the bulk samples include quartz, plagioclase, K-feldspar, calcite, amphibole, pyroxene, magnetite, hematite, pyrite, rutile, apatite, gibbsite, anatase, trioctahedral mica, dioctahedral mica, chlorite, kaolinite and dioctahedral smectite. Note that pyroxene was only detected in one sample and there was some uncertainty about its presence. The presence of minor kaolinite is clear in sample 'CHI-latitude 41 deg S' but the presence of minor kaolinite in the other samples is less certain. The dioctahedral smectite content varies from around 10 to 75 wt.%. In all samples the plagioclase XRPD data are consistent with that of end, or near end, member albite, whilst the K-feldspar appears most consistent with a variety of microcline.

Analysis of the <2 µm clay-sized fractions of the two samples selected for this test confirmed that the smectite phase is a pure smectite i.e. there is no evidence of illitic interstratification (i.e. mixed layer illite-smectite). The only other phase detected in the <2 µm clay-sized fractions were traces of chlorite. It is also of note that the full width at half maximum of the main smectite peak in the glycolated trace is around $0.25 \Delta^2\Theta$. This is quite a narrow peak for a smectite and is suggestive of relatively large crystallite size and generally homogenous chemical composition. Additionally, there were some indications in the laboratory that the smectite rehydrates rapidly (and/or resists dehydration when heating), which can be indicative of relatively high layer charge (*S. Hillier, James Hutton Institute, pers. comm. June, 2024*).

The three CEC measurements indicated values ranging from around 50 to 77 cmol(+) kg⁻¹, and they correlate with the XRPD dioctahedral smectite content. Taken together they suggest that the pure smectite would have a CEC of around 110 cmol(+) kg⁻¹, though this should be regarded as tentative as it is only based on the three measurements and, if taken individually, they show a trend of decreasing 'pure smectite' CEC with increasing smectite content.

SEM images are provided in Figure 3-6. The sample examined was meant to be a large piece that could be fractured, but appeared to have disintegrated to a powder, presumably during transport. Nonetheless, examination of the larger fragments in the sample showed them to consist of clay particles, showing crenulated texture, typical of smectites, along with particles of plagioclase feldspar. The feldspar particles show chemical compositions consistent with albite, which is also as indicated by the XRPD data. The texture of the plagioclase is also suggestive of dissolution. The EDS spectra of the smectite appears to indicate that it is calcium saturated, which is consistent with the position of the peak in the clay fraction XRPD data at around 15 Å.

3.5 Potassium-Argon Geochronology of Clays from Northern Sweden

W. Crawford Elliott, J. Marion Wampler and Cyprian Ozigbo,

3.5.1 Introduction

This study was intended to determine the timing of alteration recorded by secondary phases formed from primary Palaeoproterozoic andesite and rhyodacite parent rocks in northern Sweden (Section 2.1 and Rieger, 2016). These primary rocks host the Kiruna iron ore deposits in the Kiirunavaara mine, northern Sweden. In addition, one sample from the nearby Malmberget area was also examined.

The present report includes a description of the methods used, a description of the main results and a brief discussion of those results with some possible interpretations of the wide-ranging K-Ar age values obtained. The results of a rather large number of complementary argon isotope analyses and K determinations, done throughout the study for quality assurance, are summarized within this report.

3.5.2 Sample description

The samples received from TUM are listed in Table 3-19.

Table 3-19. Clay samples as received from TUM (locations given in Appendix A).

| GSU sample code | Sample weight (g) | LKAB site code |
|-----------------|-------------------|---------------------------|
| MA-01 | 47.8 | Joh 635/2510 (Malmberget) |
| KI-01 | 46.2 | 332-1051 |
| KI-02 | 40.8 | Y3110-1022 |
| KI-03 | 51.1 | Y3090-1137 |
| KI-04 | 32.2 | 301-1194 |
| KI-05 | 19.6 | 384-1165 |

3.5.3 Methods

Chemical pre-treatment

The as-received samples were gently crushed by hand to pieces less than 5 mm across, soaked in deionised water for several days and then treated to remove carbonate and iron (III) oxide cements following established methods (cf. Jackson, 1979). Carbonate cements were removed with 1M Na-acetate-acetic acid buffer (NaOAc-HOAc, pH = 5) at 50 °C. The treated samples were then washed twice in this buffer solution. Iron (III) oxide cements were then removed by the citrate-bicarbonate-dithionate (CBD) method at 50 °C and the treated samples were again washed twice with the buffer solution. The removal of cements and amorphous matter permitted a better size separation. These treatments produced Na-exchanged clay for subsequent X-ray diffractometry and K-Ar age determinations.

Size separations

The sand (> 50 µm), silt (20–50 µm), fine silt (2–20 µm) and clay-sized fractions (<2 µm) were separated using timed settling methods based on Stokes's Law (Jackson, 1979). Submicron size fractions (1–2 µm, 0.25–1.0 µm, and <0.25 µm) were obtained using a Heraeus floor centrifuge. Except for Ki-02, the <0.25 µm fraction was sufficiently large for XRD and K-Ar geochronologic analyses. The 0.25-1.0 µm size fraction was the finest fraction studied for Ki-02.

Mineral identification

The minerals present in the clay-sized fractions were determined by XRD. Oriented mounts of the clay-sized fractions were scanned using Cu (Ni-filtered) X-radiation (Panalytical XPert Pro X-ray diffractometer). The XRD patterns were interpreted using a standard text (Moore and Reynolds, 1997) to identify minerals.

On seeing a 3.19 Å phase in the XRD spectrum of some samples, the Ki-01 and Ki-03 <2 µm clay-sized fractions were washed again in deionised water several times to exclude the possibility of remnant NaOAc-HOAc buffer in the clay fraction. The reflection at 3.19 Å was interpreted to be from the presence of feldspar.

K-Ar Geochronology

Age values of bulk (<2 µm) and fine (<0.25 µm or 0.25–1 µm) clay-sized fractions separated from the alteration products in the above tasks were calculated from amounts of Ar isotopes and K measured in the GSU K-Ar Geochronology Laboratory. A single-weigh out procedure (Stephens et al. 2007; De Man et al. 2010) is used at GSU for K-Ar measurements of clay-sized fractions to eliminate the effect of weighing error on the K-Ar age values. For smectite-rich clays, an important benefit of this procedure is that age values are not influenced by uncertainty in the moisture content of the clay at the time of weighing. Some of the clay-sized fractions had exceptionally low K contents, which called for special attention to factors that can affect the accuracy of K-Ar measurements when both K content and radiogenic Ar content are low. For this reason, the procedures used are described here in detail.

K-Ar Procedures

After preliminary K determinations had been used to estimate how much of each separated clay-sized fraction would be needed for isotopic analysis of the sample Ar content, three sets of clay-sized fraction test portions were prepared for K-Ar measurements. The first set, identified by the prefix NAG-2 (the prefix NAG-1 had been used for the preliminary K determinations), contained one test portion of each of the six separated bulk (<2 µm) clay-sized fractions and an empty copper-foil capsule included for procedural-blank measurements (see Table 3-20 for details). The second set, prefix NAG-3, contained larger test portions of each of the six <2 µm fractions. The need for larger test portions became evident after isotopic analyses of argon from the first set revealed that several of the clay-sized fractions had much less radiogenic Ar than had been anticipated. The third set, prefix NAG-5, was of fine clay-sized fractions of Ki-01, Ki-02 and Ma-01. Fine clay-sized fractions of Ki-03, Ki-04 and Ki-05 were not included because their K contents are too low for determination of their radiogenic-Ar content without a special, still to be proven, procedure to minimize their atmospheric-argon content.

Table 3-20. K-Ar test-portion masses and mass losses upon vacuum drying and upon argon extraction.

| Sample | Size fraction | Test portion | Initial weighing date | Relative humidity* (%) | Mass [†] (mg) | Drying time (days) | Mass loss upon drying (%) | Mass Loss upon argon extraction [‡] (%) | Total mass loss [§] (%) |
|--------------------------|---------------|--------------|-----------------------|------------------------|------------------------|--------------------|---------------------------|--|----------------------------------|
| Ma-01 | <2 µm | NAG-1A | 17-12-21 | 75 | 17.5 | | | | |
| Ki-01 | <2 µm | NAG-1B | 17-12-21 | 75 | 54.4 | | | | |
| Ki-02 | <2 µm | NAG-1C | 17-12-21 | 75 | 84.6 | | | | |
| Ki-03 | <2 µm | NAG-1D | 17-12-21 | 75 | 64.0 | | | | |
| Ki-04 | <2 µm | NAG-1E | 17-12-21 | 75 | 83.6 | | | | |
| Ki-05 | <2 µm | NAG-1F | 17-12-21 | 75 | 56.9 | | | | |
| Ma-01 | <2 µm | NAG-2A | 6-1-22 | 55 | 2.0 | 2 | 11 | 8 | 18 |
| Ki-01 | <2 µm | NAG-2B | 6-1-22 | 55 | 29.1 | 2 | 12.0 | 9.3 | 20.2 |
| Ki-02 | <2 µm | NAG-2C | 6-1-22 | 55 | 12.0 | 2 | 8.8 | 10.8 | 18.6 |
| Ki-03 | <2 µm | NAG-2D | 6-1-22 | 55 | 250.0 | 2 | 4.2 | 5.4 | 9.4 |
| Ki-04 | <2 µm | NAG-2G | 6-1-22 | 55 | 29.2 | 2 | 8.7 | 7.6 | 15.7 |
| Ki-05 | <2 µm | NAG-2F | 6-1-22 | 55 | 229.2 | 2 | 9.4 | 7.8 | 16.4 |
| Ma-01 | <2 µm | NAG-3A | 1-2-22 | 30 | 8.1 | 1 | 3.7 | 11.9 | 15.2 |
| Ki-01 | <2 µm | NAG-3B | 1-2-22 | 30 | 75.5 | 1 | 8.2 | 9.1 | 16.6 |
| Ki-02 | <2 µm | NAG-3C | 1-2-22 | 30 | 58.3 | 1 | 8.3 | 11.3 | 18.6 |
| Ki-03 | <2 µm | NAG-3D | 1-2-22 | 30 | 272.9 | 1 | 4.4 | 5.2 | 9.3 |
| Ki-04 | <2 µm | NAG-3E | 1-2-22 | 30 | 254.7 | 1 | 7.9 | 6.3 | 13.7 |
| Ki-05 | <2 µm | NAG-3F | 1-2-22 | 30 | 409.4 | 1 | 8.4 | 7.7 | 15.5 |
| Ma-01 | <0.25 µm | NAG-4A | 28-3-22 | 25 | 3.8 | | | | |
| Ki-01 | <0.25 µm | NAG-4B | 28-3-22 | 25 | 1.2 | | | | |
| Ki-02 | 0.25–1 µm | NAG-4D | 28-3-22 | 25 | 2.0 | | | | |
| Ki-03 | <0.25 µm | NAG-4E | 28-3-22 | 25 | 6.0 | | | | |
| Ki-04 | <0.25 µm | NAG-4F | 28-3-22 | 25 | 3.3 | | | | |
| Ki-05 | <0.25 µm | NAG-4G | 28-3-22 | 25 | 5.3 | | | | |
| Ma-01 | <0.25 µm | NAG-5A | 29-3-22 | 35 | 15.0 | | | | 10.3 |
| Ma-01 | <0.25 µm | NAG-5D | 29-3-22 | 35 | 30.1 | 4 | 3.2 | | |
| Ki-01 | <0.25 µm | NAG-5B | 29-3-22 | 35 | 36.6 | | | | 19.3 |
| Ki-02 | 0.25–1 µm | NAG-5C | 29-3-22 | 35 | 70.6 | | | | 20.5 |
| Reference samples | | | | | | | | | |
| GL-O | pellets | JMW-GL-O | 31-5-21 | | 27.8 | | | | 10.1 |
| GL-O | pellets | REF-1A | 21-2-22 | | 26.7 | | 3.1 | 7.6 | 10.5 |
| LP-6 Bio | 40–60# | REF-1B | 21-2-22 | | 29.9 | | 0.0 | | |
| LP-6 Bio | 40–60# | REF-2A | 9-3-22 | | 29.0 | | | | |

* Relative humidity represents afternoon values from Atlanta weather records (rounded to nearest 5 %).

[†] Mass values are of test portions as weighed in ambient air.

[‡] Mass loss upon argon extraction is relative to the mass of the vacuum-dried test portion.

[§] Total mass loss is relative to the mass of the test portion as weighed in ambient air.

Note: A blank cell indicates no determination.

To prepare a set of test portions, a portion of each clay-sized fraction to be dated was weighed into a copper-foil capsule using a Denver Instruments M-220 analytical balance. The open end of the capsule was then closed by folding to keep solid matter, but not gases, within the capsule. The closed capsules were then placed in the argon-extraction line and held under vacuum for at least 12 hours. The capsules were then removed from the extraction line and reweighed to obtain an approximate value of the adsorbed-moisture content of each clay-sized test portion at the time of original weighing. NAG-5A, -5B and -5C, however, were not removed from the extraction line and reweighed, because of concern that atmospheric Ar diffusing into clay interlayers upon removal from vacuum might become isotopically fractionated.

After the first set of test portions (NAG-2) had been returned to the argon-extraction line, they were held under vacuum at room temperature until each was heated for extraction of radiogenic Ar at about 1 000 °C. Heating was by a wire-wound resistance heater that surrounds a 5 cm length of 15 mm diameter fused-quartz tubing where each test portion was placed for heating. After overnight evacuation of the extraction line to remove all free air, each test portion of the second set (NAG-3) was preheated under vacuum at 150 °C (except the MA-01 portion, which was heated at 215 °C) to reduce its atmospheric Ar content before extraction of radiogenic Ar. During preheating, a valve was closed to isolate the extraction line so that the argon emitted during preheating could be collected and analysed. The test portions of <2 µm fractions having more than 0.1 % K₂O (from samples Ki-01, Ki-02, and Ma-01) were preheated for about one hour, but those having less than 0.1 % K₂O were preheated for two days. The test portions of the Ki-01 and Ki-02 fine clay-sized fractions in the third set of test portions (NAG-5) were each preheated at 150 °C for two days; the Ma-01 fine clay-sized fraction was not preheated because the relative amount of atmospheric argon therein was expected to be very small. The amount and isotopic composition of the argon released in each preheating phase was determined by mass spectrometry to confirm that no radiogenic argon had been extracted (see Table 3-21 for details).

Table 3-21. Argon accumulated in the extraction line when test portions were present at room temperature, during preheating of test portions, during blank argon extractions, and during reheating of test portions from which argon had been extracted.

| Test portion | Sample | Size fraction | Initial mass (mg) | Process | Temp. (°C) | Time | ⁴⁰ Ar (pmol) | Preheating* ³⁶ Ar/ ³⁶ Ar _{total} (%) | ⁴⁰ Ar/ ³⁶ Ar | Radiogenic argon (%) (pmol) | |
|--------------|--------------------------|------------------------|-------------------|------------------|------------|--------|-------------------------|---|------------------------------------|-----------------------------|------|
| NAG-2F | Empty capsule | | | Procedural blank | 1 000 | 12 min | 3.2 | | 270 ± 21 | -10 | -0.3 |
| NAG-3A | Ma-01 | <2 µm | 8.2 | Preheating | 215 | 1.3 h | 2.9 | 25 | 281 ± 17 | -5 | -0.2 |
| NAG-3A | Ma-01 | <2 µm | 8.2 | Reheating | 1 000 | 10 min | 3.3 | | 299 ± 16 | 1 | 0.0 |
| NAG-3B-F | Ki-01, ..., -05 | <2 µm | | No heating | 22 | 2 h | 1.4 | | 283 ± 35 | -4 | -0.1 |
| NAG-3B-F | Ki-01, ..., -05 | <2 µm | | No heating | 22 | 24 h | 7.9 | | 296 ± 8 | 0 | -0.1 |
| NAG-3B | Ki-01 | <2 µm | 75.6 | Preheating | 150 | 1 h | 1.0 | 14 | 309 ± 59 | 4 | 0.0 |
| NAG-3C | Ki-02 | <2 µm | 58.6 | Preheating | 150 | 1 h | 0.7 | 35 | 299 ± 75 | 1 | 0.0 |
| NAG-3D | Ki-03 | <2 µm | 272.9 | Preheating | 150 | 2 d | 8.2 | 44 | 291 ± 7 | -2 | -0.1 |
| NAG-3E | Ki-04 | <2 µm | 254.7 | Preheating | 150 | 2 d | 19.1 | 24 | 296 ± 3 | 0 | 0.0 |
| NAG-3F | Ki-05 | <2 µm | 409.6 | Preheating | 150 | 2 d | 143 | 39 | 295 ± 1 | 0 | -0.3 |
| NAG-5 set | Ma-01 (2), Ki-01, -02 | <0.25 µm, 0.25–1 µm | | No heating | 22 | 45 min | 0.6 | | 238 ± 54 | -25 | -0.2 |
| None | | | | Blank extraction | 1 000 | 12 min | 6.5 | | 291 ± 9 | -1 | -0.1 |
| NAG-5B | Ki-01 | <0.25 µm | 36.7 | Preheating | 150 | 2 d | 0.6 | 15 | 328 ± 76 | 10 | 0.0 |
| NAG-5C | Ki-02 | 0.25–1 µm | 70.6 | Preheating | 150 | 2 d | 1.1 | 5 | 285 ± 47 | -4 | 0.0 |

* The ratio of amount of ³⁶Ar extracted during preheating to the total amount of ³⁶Ar measured represents the percentage of atmospheric Ar extracted during preheating relative to the total amount present just before preheating, provided that no atmospheric Ar was lost during the interval between the end of preheating and extraction of radiogenic Ar. That interval was usually <30 min and in no case more than one hour. The <2 µm fractions of the Ki samples were under vacuum for from 7 days to 16 days before preheating began, while the fine-clay fractions of Ki-01 and Ki-02 were under vacuum for only 2 days and 5 days, respectively before preheating began.

To extract radiogenic Ar, each capsule was brought up slowly, over 10 minutes, to about 1 000 °C and held at that temperature for at least 10 minutes. A spike of virtually pure ^{38}Ar , of known amount and isotopic composition, was added to the extracted gases. Condensable vapours, mostly of water and CO_2 , were removed in a cold trap and other reactive gases were removed by reaction with heated Ti metal. The isotopic composition of the argon was determined with a modified MS-10 mass spectrometer operating in the static mode. Data were recorded in both chart and digital formats. A test portion of Ma-01 <2 μm size fraction was heated a second time for about 10 minutes at about 1 000 °C to see if any more radiogenic argon would be released.

After all the argon isotopic measurements for a set of test portions were done, the Cu-foil capsules were removed from the extraction line and weighed again to determine the mass of volatiles lost during argon extraction. Each capsule was then dissolved, and its included solid material digested, at ≤ 100 °C by a mixture (10:3 by mass) of concentrated hydrofluoric and nitric acids in a closed fluorocarbon container. After the container had been opened and remaining acid had been evaporated, the solid residue was dissolved in a nitric acid solution (0.1 molL^{-1}) containing CsCl (0.01 molL^{-1}) for K determination. The Cs was added to suppress ionization of K atoms during flame atomic absorption spectrophotometry (FAAS). After further dilution, if needed to bring K concentration below 2 mgL^{-1} , the K concentration of each test solution was determined with a Perkin Elmer Model 3110 AAS against reference solutions prepared from standard KCl (NIST SRM-999).

Microsoft Excel workbooks were used to calculate net argon-isotope ion currents from the digitally recorded data of each argon isotope analysis and to calculate the tabulated K-Ar analytical results and age values. The K-Ar age values were calculated with accepted values for the decay constants of ^{40}Ar and the isotopic abundances of terrestrial K and atmospheric Ar (Steiger and Jäger, 1977). The uncertainty of each $^{40}\text{A}_{\text{rad}}/\text{K}$ ratio was calculated by quadratic addition of 1σ analytical-error values (Dalrymple and Lanphere, 1969). The 2σ uncertainty of the corresponding age value was calculated from the uncertainty in $^{40}\text{A}_{\text{rad}}/\text{K}$ multiplied by a factor that accounts for the non-linearity of age value as a function of $^{40}\text{A}_{\text{rad}}/\text{K}$.

Calibration, precision and accuracy

The analytical balance has 0.1 mg sensitivity. Accuracy was gauged through measuring a calibrated weight (200 mg, Troemner Calibration Weights) when each set of test portions was prepared. Mass values for that weight were consistently $200.0 \pm 0.1 \text{ mg}$. Each capsule was weighed when empty, after the clay had been added, after being closed by folding, after vacuum drying of the clay (except most fine clay-sized fractions) and after argon had been extracted (except the NAG-4 set and NAG-5D). To ensure good precision and to avoid the effect of any mistake in transcription of mass values, each weighing was repeated one to three times.

The ^{38}Ar is stored in a large reservoir (volume about 8 dm^3) and released as individual spikes of about 1 cm^3 volume. The amount of ^{38}Ar in a spike was determined by comparison of the amount of ^{38}Ar in the spike to the amount of radiogenic argon released by melting a 30 mg portion of the interlaboratory reference biotite LP-6 Bio in a resistance-heated furnace (in a part of the argon-extraction line separate from the fused-quartz tube where argon was released from the clay). This calibration was checked by isotopic analyses of argon released from the interlaboratory reference glauconite GL-O by the same procedure described here for clay-sized fractions of Kiirunavaara and Malmberget samples.

The mass spectrometer was operated with a controlled direct current through the ion source's filament rather than the alternating current of the original MS-10 design, because of recent failure of the control circuit for the electron current through the mass spectrometer's ion source. Peak ion currents were recorded as a function of time so that each isotope ratio could be calculated from peak-current values that were corrected for any drift in sensitivity by interpolation or extrapolation to the central time of each scan. For isotopic analysis of argon with the MS-10 mass spectrometer, scanning across the mass spectrum from below $m/z = 36$ to above $m/z = 40$ is necessary to allow accurate interpolation of the curved baselines for the ion-current peaks of the less abundant isotopes, particularly ^{36}Ar . In the case of the samples examined here, such baselines were interpolated by fitting negative-exponential functions to the tails of large peaks – tails caused by scattering of ions from intense ion beams (of $^{40}\text{Ar}^+$ primarily, but also of $^{38}\text{Ar}^+$ in spiked runs and of CO_2^+). To ensure high precision of the argon-isotope ratios, each isotopic analysis included independent measurements of each ratio from at least six scans across the mass spectrum. Typically, the relative standard error of the mean for $^{40}\text{Ar}/^{38}\text{Ar}$ measurement

in spiked runs, which serves as a measure of short-term random variability of the ion-source electron current (over the ~15 minute course of the scanning), was a few tenths of a percent. To ensure accuracy of the isotope ratios, isotopic analysis of a reference argon mixture consisting of known proportions of atmospheric argon, virtually pure ^{38}Ar and isotopically fractionated atmospheric argon (which had leaked into the reference gas reservoir) was done at least once each day of operation to allow correction for mass discrimination in all other isotopic analyses for that day. For 14 runs of the reference argon mixture, the average value of the relative standard error of the mean for $^{40}\text{Ar}/^{38}\text{Ar}$ was 0.22 % and that for $^{40}\text{Ar}/^{36}\text{Ar}$ was 0.23 %. The uncertainty in K-Ar age values due to absence of control for the electron current through the mass spectrometer's ion source is minor relative to other sources of uncertainty.

In the argon isotopic analyses, small corrections were necessary for background ion currents due to hydrocarbons, HCl and isotopically fractionated atmospheric argon that leaked into the mass spectrometer. The hydrocarbon cracking pattern, the magnitude of the HCl signal, the rate at which atmospheric argon leaked in and the isotopic composition of the leaked-in argon were determined from background runs (where such a run begins by closure of a valve to isolate the mass spectrometer from vacuum pumping, but no gas from the extraction line is admitted). Frequent background runs showed that:

- argon memory effects were so small that no correction for them was needed,
- the HCl signals were very small, requiring minimal corrections,
- the hydrocarbon cracking pattern did not change appreciably over time,
- the incoming atmospheric argon was isotopically fractionated as expected for molecular flow (influx rate inversely proportional to the square root of molecular mass).

Given the hydrocarbon cracking pattern, corrections for hydrocarbon signals were based on the measured hydrocarbon signal at $m/z = 42$ (spiked argon) or $m/z = 37$ (unspiked argon). The only argon-isotope signal that needed appreciable correction for hydrocarbon and HCl signals was that for ^{36}Ar .

For K measurements by FAAS, ten one-second readings of absorbance due to the K from each solution were averaged by the instrument and the average was recorded manually. Occasional average values were rejected because the relative standard deviation of the ten readings was greater than 2 %. Such readings were taken sequentially for a set of test solutions and reference solutions, which had been arranged in order of increasing K concentration as determined in preliminary measurements. Readings were then taken in a reverse sequence, that is, from the solution with highest K content to that with the lowest. This procedure tends to average out the effect of instrumental drift, allows readings for each test solution to be closely bracketed in time by the reference solutions that are closest in K concentration and minimises the effect of cross contamination by liquid on the aspirator tube as it is moved from one solution to another. To ensure high precision of the K measurements, the described process was repeated twice for a total of six independent values of K concentration for each test solution. The relative standard error of the mean for such a set of measurements was typically between 0.2 % and 0.5 % for test solutions prepared from the K-Ar test portions of this study.

A decision was made to test the bulk clay fractions for the presence of K in water-soluble or exchangeable forms (forms from which radiogenic daughter ^{40}Ar would not have been retained), because the K_2O contents of three bulk-clay fractions (Ki-03, -04, and -05) were found to be extremely small (<0.10 % by mass). For this purpose, test portions of 0.5 g or 1 g were first mixed with 50 mL of deionised (DI) water in polypropylene centrifuge tubes. The tubes were shaken occasionally over three days and then centrifuged for one hour at 10 000 RCF. Most of the supernatant liquid in each tube was decanted off and saved for K determination. NaCl solution (0.5 molL^{-1}) prepared from purified NaCl was then added to each centrifuge tube to bring the volume to 50 mL. The tubes were again shaken occasionally, over two days, and then centrifuged for one hour at 10 000 RCF so that a portion of the supernatant liquid could be taken for determination of the dissolved K, most of which would have been released into solution by cation exchange with added Na. A portion of each supernatant solution (from the DI-water extraction and NaCl-solution exchange) was diluted with Cs-bearing HNO_3 solutions to make a test solution of 0.1 molL^{-1} in HNO_3 and 0.01 molL^{-1} in Cs for K measurement by FAAS. To find the amount of K released to solution by ion exchange, the amount of K found for each NaCl-extract solution was corrected for the K carried over in un-decanted supernatant liquid from the earlier DI-water extraction.

3.5.4 Results

Sample Mineralogy

The mineralogy of the clay-sized fractions (<2 μm) of five samples of altered rocks of the Kiruna iron deposits (Ki-01 to -05) and one sample of altered rock from Malmberget (Ma-01, Table 3-22) were determined and the resulting XRD plots are shown in Appendix G. Smectite or smectite-rich mixed layer Illite-smectite (I-S) was the predominant clay mineral found in the <2 μm fractions of the Kiirunavaara mine samples (Table 3-22). Illite was seen in Ki-02. Chlorite was noted in small amounts in Ki-01 (trace) and Ki-02, and quartz in Ki-03. Plagioclase peaks were observed in most of the <2 μm fractions (identified specifically as albite in Ki-03). The Malmberget Ma-01 sample contained mixed layer illite-smectite with a high percentage of illite layers (~90 %). The stacking order of this illite-smectite was R3 per the asymmetry noted on the high d -value side of the 10 Å peak (see appendix G, Figure MA-01 Combined (air dried, heated, glycol solvated) and Figure MA-01 bulk sample (glycol solvated)).

The intensity at $3-4^\circ 2\theta$ (saddle) was low for all these smectite-rich clays which signifies the presence of few, if any, illite layers. The difference between the peak positions of the two interstratified peaks can yield an estimate of the percentage of illite layers in I-S (i.e. the $\Delta 2\theta$ method of Moore and Reynolds, 1997). The $\Delta 2\theta$ values for the Kiirunavaara mine <2 μm fractions were <5.38° and signify the percentages of illite layers in I-S in these fractions were <10 %. (This measurement was less precise for Ki-03 and not possible for Ki-04 owing to these clays curling on the glass slide after drying.) These small percentages of illite in the mixed layer illite-smectite are consistent with the measured low K_2O values (below). Based on these $\Delta 2\theta$ values, the very low K_2O values and the low saddle intensities, the primary clay mineral in Ki-03, -04 and -05 is considered to be smectite rather than mixed layer illite-smectite with low percentages of illite layers. The $\Delta 2\theta$ value for the Ma-01 <2 μm fraction was 8.3° 2θ , which corresponds to about 90 % illite layers in I-S.

The submicron fractions (<0.25 μm for Ma-01, Ki-01, and Ki-03–Ki-05; 0.25–1.0 μm for Ki-02) were composed predominantly of smectite for the five Kiruna clays and mixed layer illite-smectite (~90 % I in I-S, R3) for the Malmberget sample. The diffraction patterns of the submicron fractions had better peak to background intensities. These clays did not curl on the slides. Diffraction peaks corresponding to feldspar were seen in the Ki-01 patterns and were barely visible in one other set of patterns (Ki-02). The $\Delta 2\theta$ values of the Kiruna fine clays were <5.38° 2θ , again indicating <10 % illite in mixed layer illite-smectite. The K_2O contents of the submicron clays are considered to be better indicators of the small presence of illite layers in these fractions. The fixed-K contents (as K_2O , Table 3-22) correspond to about 5 % illite layers in I-S within the Ki-01 and Ki-02 fine clay and virtually none in the other Kiruna fine clays.

K-Ar Geochronology

The K-Ar measurements and age values (Table 3-22) for bulk-clay fractions (<2 μm) are those obtained from the NAG-2 and NAG-3 sets of test portions (see Table 3-20 for test-portion identifiers). The age values from the second (NAG-3) of these sets are more accurate than those obtained from the first (NAG-2), because the NAG-3 test portions were larger and were preheated under vacuum to remove some of the atmospheric Ar (Table 3-21) before extraction of radiogenic Ar. Two of the three fine-clay fractions for which age values were obtained (Table 3-16) were also preheated to remove some of their atmospheric argon. The error given for each age value represents analytical uncertainty at the 95 % confidence level (2σ); it does not include the effects of uncertainty in decay constants and natural isotopic abundances, nor does it include any uncertainty due to failure of the clays to meet the assumptions of the conventional K-Ar dating method.

The fixed-K (as K_2O) contents of <2 μm fractions listed in Table 3-22 and used to calculate the age values for those fractions are based on the measured K contents of the test portions less a value for the amount of extraneous K, defined as K from which any associated radiogenic Ar would not have been retained. The amount of extraneous K in each test portion was calculated from the specific amounts of K extracted by deionised water and by 0.5 molL⁻¹ NaCl solution from larger test portions of the <2 μm fractions (Table 3-23) plus an estimate of the amount of exchangeable K remaining after the single extraction by NaCl solution. The latter was estimated on the basis of a set of experiments conducted on smectite-rich fine-clay separates in the last quarter of 2022, after laboratory work for the KiNA project had been completed.

A 10 % relative uncertainty in the amount of extraneous K in the <2 µm fractions Ki-01, Ki-02 and Ma-01 was assumed. For the three other <2 µm fractions, that uncertainty was assumed to be 15 %, because the smaller clay-water mass ratios used for extraction of exchangeable K from those separates meant the amount of exchangeable K remaining on the clay, which was estimated rather than measured, was relatively more than for the first three separates. The effect of that uncertainty on the relative uncertainty of the fixed-K contents listed in Table 3-22 ranges from negligible for Ma-01 <2 µm to 18 % for Ki-04 <2 µm; in the latter, extraneous K was about one-half of the original K present (Table 3-23).

Table 3-22. Clay mineralogy and K-Ar age values.

| Sample ID | Size fraction (µm) | Minerals identified | Fixed K as K ₂ O* (wt. %) | ⁴⁰ Ar _{rad} (% of ⁴⁰ Ar) | (nmolkg ⁻¹) | K-Ar age value (Ma) |
|-----------|--------------------|--|--------------------------------------|---|-------------------------|------------------------|
| Ki-01 | <2 | I-S (R0, <10 % I), Chlorite (tr.), Plagioclase | 0.27 0.28 | 45.2 60.7 | 110 122 | 268 ± 18 283 ± 11 |
| Ki-01 | <0.25 | I-S (R0, <10 % I), Feldspar | 0.50 | 49.3 | 75 | 102 ± 8 |
| Ki-02 | <2 | I-S (R0, <10 % I), Illite, Chlorite, Plagioclase | 0.41 0.40 | 58.6 72.5 | 404 463 | 581 ± 62 661 ± 66 |
| Ki-02 | 0.25–1.0 | I-S (R0, <10 % I) | 0.41 | 20.6 | 74 | 120 ± 9 |
| Ki-03 | <2 | Smectite, Quartz, Albite | 0.042 0.040 | 49.0 60.1 | 57 59 | 762 ± 33 817 ± 36 |
| Ki-03 | <0.25 | Smectite | (0.02) [†] | | | |
| Ki-04 | <2 | Smectite, Plagioclase | 0.043 0.039 | 2.7 8.7 | 13 22 | 185 ± 198 361 ± 122 |
| Ki-04 | <0.25 | Smectite | (0.05) | | | |
| Ki-05 | <2 | Smectite | 0.028 0.028 [‡] | 2.8 3.0 | 15 17 | 344 ± 130 366 ± 130 |
| Ki-05 | <0.25 | Smectite | (0.01) | | | |
| Ma-01 | <2 | I-S (R3, ~90 % I) | 7.98 [§] 7.97 | – 92.1 | – 13 133 | – 887 ± 16 |
| Ma-01 | <0.25 | I-S (R3, ~90 % I) | 8.13 | 98.6) | 12 759 | 853 ± 16 |

* For each <2 µm fraction except that of MA-01, two independent sets of K-Ar measurements are listed (except as noted below). A larger test portion (Table 3-23) was used for the second set in each case. Each listed value for fixed-K (as K₂O) content of a <2 µm fraction is based on the measured K content of the test portion less the extraneous K shown as K₂O in Table 3-23).

[†] The K₂O contents shown in parentheses, for the <0.25 µm fractions of Ki-03, -04, and -05, are from preliminary K determinations. No K-Ar determinations for these fractions were attempted because of the extremely small K contents.

[‡] There was no K determination for the second test portion of Ki-05 <2 µm (NAG-3F), so the fixed-K (as K₂O) content determined for NAG-2F was used in calculation of the age value for NAG-3F.

[§] There is no digital recording for the Ar-isotope analysis of the first test portion of Ma-01 <2 µm (NAG-2A), so the results of that isotopic analysis are not shown.

Errors considered, the duplicate age values for each the six <2 µm fractions are consistent with one another. In the following, only the more accurate results obtained from the NAG-3 test portions will be discussed.

Kiirunavaara mine samples. The <2 µm fractions showed a large range in the measured K-Ar ages (Table 3-22), from about 280 Ma to about 800 Ma. The fixed-K contents for these fractions were very small (0.03–0.4 wt. % K₂O). The small K₂O contents reflect the dominance of smectite in these clays and the presence of other non-K-bearing minerals (chlorite, quartz – see Table 3-22). The measured ⁴⁰Ar_{rad} contents of the Ki-04 and Ki-05 <2 µm fractions were extremely small and uncertain. The relatively large uncertainties (Table 3-22, last column) are due to an atmospheric Ar content in each more than ten times the radiogenic Ar content. Those large uncertainties in amount of radiogenic argon were not explicitly calculated, however, because the equation used for calculating the uncertainties (Dalrymple and Lanphere, 1969) is for the relative error in the ratio of radiogenic argon to potassium. These high uncertainties reflect the very low K₂O contents (<0.10 % by mass as already noted) of these clay-sized fractions.

The K-Ar age values for two fine-clay fractions from the Kiirunavaara mine samples, 102 ± 8 Ma for Ki-01 $<0.25 \mu\text{m}$ and 120 ± 9 Ma for Ki-02 $0.25\text{--}1.0 \mu\text{m}$, are considerably smaller than those for the corresponding $<2 \mu\text{m}$ fractions. The uncertainties are relatively a little larger than for the corresponding $<2 \mu\text{m}$ fractions, because atmospheric-Ar contamination was relatively more for the small amounts available of the submicron fractions. Nevertheless, those relative uncertainties are only about 8 % at the 95 % confidence level, so the age values are useful.

Malmberget sample. The K-Ar age values of the Ma-01 $<2 \mu\text{m}$ and $<0.25 \mu\text{m}$ fractions, 887 ± 16 Ma and 853 ± 16 , are close to K-Ar age values for $0.2\text{--}2 \mu\text{m}$ and $\leq 0.2 \mu\text{m}$ fractions of two Malmberget clay samples determined in this laboratory. Those size fractions had been prepared by Rieger (2016) from a portion of Ma-01 and another sample, identified by him as MAB01 and MP01, respectively. The age values were 884 ± 9 and 879 ± 8 Ma for the $0.2\text{--}2 \mu\text{m}$ fractions of MAB and MP, respectively, and 838 ± 8 and 837 ± 8 Ma for the respective $\leq 0.2 \mu\text{m}$ fractions. These values are close (the same within error) to those for the $<2 \mu\text{m}$ and $<0.25 \mu\text{m}$ fractions, respectively, of Ma-01 determined in the present study. The measured K_2O contents are consistent with the presence of mixed layer illite-smectite with a high percentage (~ 90 %) of illite layers. The relatively small uncertainties in K-Ar age values for the Malmberget clay reflect both the large K_2O content and the nonlinearity of the K-Ar age equation.

Table 3-23. Potassium extracted from $<2 \mu\text{m}$ fractions by deionised water and by 0.5 molL^{-1} NaCl solution and calculated values of remaining exchangeable K, total extraneous K, and fixed K, all as K_2O .

| Sample | Mass (g) | Original K content (% as K_2O) | K extracted by deionised water* | | K extracted by 0.5 molL^{-1} NaCl solution† | | Exchangeable K remaining‡ (% as K_2O) | Extraneous K total (% as K_2O) | Fixed K (% as K_2O) |
|--------|-------------|---|------------------------------------|------------------------------|---|------------------------------|--|---|---|
| | | | (μg) | (% as K_2O) | (μg) | (% as K_2O) | | | |
| Ma-01 | 0.521 | 8.10 8.09 | 134 | 0.031 | 298 | 0.069 | 0.014 | 0.114 | 7.98 7.97 |
| Ki-01 | 0.480 | 0.30 0.31 | 58 | 0.015 | 69 | 0.017 | 0.003 | 0.035 | 0.27 0.28 |
| Ki-02 | 0.611 | 0.64 0.64 | 553 | 0.109 | 519 | 0.102 | 0.020 | 0.232 | 0.41 0.40 |
| Ki-03 | 1.090 | 0.048 0.046 | 9 | 0.001 | 38 | 0.004 | 0.001 | 0.006 | 0.042 0.040 |
| Ki-04 | 1.054 | 0.088 0.084 | 74 | 0.008 | 269 | 0.031 | 0.006 | 0.045 | 0.043 0.039 |
| Ki-05 | 1.012 | 0.041 | 30 | 0.004 | 62 | 0.007 | 0.001 | 0.012 | 0.028 |
| Blank | | | 0 | | 1.5 | | | | |

* From a single extraction by DI water, water-clay mass ratio ~ 100 (Ma-01, Ki-01, and Ki-02) or ~ 50 (others).

† From a single extraction by 0.5 molL^{-1} NaCl solution, solution-clay mass ratio ~ 100 (MA-01, Ki-01, and Ki-02) or ~ 50 (others). Values were corrected for the K content of the NaCl as shown by the blank run.

‡ The amount of exchangeable K remaining after a single extraction by 0.5 molL^{-1} NaCl solution was calculated on the basis of a set of experiments conducted in the last quarter of 2022, after laboratory work for the present project had been completed.

3.5.5 Discussion

The most significant findings are:

- Smectite, or a smectite-rich mixed layer illite-smectite, was the predominant clay mineral in the Kiirunavaara mine samples. Two of the Kiirunavaara mine clay samples have a small but significant amount of illite in mixed layer illite-smectite. Only very small amounts of other phases were present in the finest separation fractions studied.
- The water-extraction and NaCl-exchange experiments conducted on the $<2 \mu\text{m}$ Kiirunavaara mine fractions showed that most of the K in four of those clays was fixed in structural sites and not exchangeable. (Table 3-23). Only about half of the K in $<2 \mu\text{m}$ Ki-04 was fixed, however. Wide-ranging age values of these fractions, from about 250 Ma to about 800 Ma, reflect the presence of variable amounts of inherited Proterozoic potassic phases in the clay.

- The K₂O measured values were very low for the submicron fractions of three of the Kiirunavaara mine samples studied – so low that their radiogenic Ar could not have been determined from the amounts of fine clay available. Age values for the two other fine-clay fractions suggest that most of their K is in a component, mixed layer illite-smectite, that is not older than about 100 Ma
- The measured K-Ar data for the Malmberget clay (Ma-01) were comparable to those reported elsewhere. The mineralogy of this illite-rich illite-smectite is consistent with hydrothermal alteration of pre-existing mica. In sharp contrast to the results for Kiruna samples, the K-Ar age values for the Malmberget clay were all greater than 800 Ma.

The results of this study have important implications for the character and the timing of the clay transformation at Kiruna and Malmberget. The presence of little or no illite in the smectite-rich clays from the Kiirunavaara mine and the predominance of illite-rich I-S in the Malmberget clay are consistent with transformation temperatures inferred from stable-isotope data. The K-Ar age values can be interpreted at first approximation as due to mixing of an older, coarser component with a finer, younger component. It is probable that all the studied clays have potassic material inherited from the Palaeoproterozoic parent rock and the age values for Ki-03 < 2 µm and both fractions of Ma-01 suggest that such inherited material has retained enough radiogenic Ar to have age values greater than 800 Ma. The discrete illite identified by XRD in Ki-02 < 2 µm (age value 661 ± 66 Ma) is probably mica inherited from the parent rock. The younger component in such a two-component model would then have arisen during clay transformation of the parent rock, for example by diagenetic processes perhaps associated with later orogenesis (Caledonian).

If the older component of Ki-01 and Ki-02 carries a K-Ar age > 800 Ma, as suggested by age values for Ki-03 and Ma-01 clays, then, by the two-component model, nearly all of the K in the Ki-01 and Ki-02 fine-clay fractions must be in the younger component. The age of that younger component is indeterminate but not more than the ~100 Ma age value of the fine-clay fractions of Ki-01 and Ki-02. Further K-Ar work on fine-clay fractions from the Ki-01 and Ki-02 samples would be useful to further clarify this point.

The younger component in the Ki-01 and Ki-02 fine-clay fractions is likely to be a small amount of illite in smectite-rich illite-smectite. If so, an important question that cannot be answered by K-Ar dating is whether smectite and illite formed concurrently, or if the clay transformation at Kiruna began with formation of pure smectite and illite was added later by smectite illitisation. If the former, then the K-Ar work puts the clay alteration within the last ~100 million years. If the latter, then the time when the original smectite formed cannot be inferred from the K-Ar work.

Extensive smectite formation required a large time-integrated volume of water to react with the bed-rock. The somewhat elevated temperature indicated by the stable-isotope data would have enhanced the reaction and could have promoted formation of some illite. These considerations, and Occam's razor, point to an expectation that illite formed concurrently with smectite at Kiruna, in which case the K-Ar age values indicate smectite not older than ~100 million years.

These new age values do not resolve the puzzle presented by the earlier K-Ar work on Malmberget clay fractions (Gilg et al. 2017). The narrow range of K-Ar age values (837–908 Ma) found across a wide range of particle size (from < 0.2 µm to 6.3–20 µm) in that earlier work suggests that the high-temperature clay alteration at Malmberget occurred in mid-Neoproterozoic time. Possibly the clay alteration at Malmberget is related to the beginning of the breakup of Rodinia just before 800 Ma (Koehl et al. 2018).

Finally, a working hypothesis is here offered for the cause of the relatively young illite (in I-S) in the Kiirunavaara mine. Kiruna is well to the north of the central area of the most recent Scandinavian continental ice sheet. Modelling by Lemieux et al. (2008a, b) of the effect of Wisconsinan glaciation on the groundwater flow system of North America indicated an enhanced hydraulic head in the rock below the central area of Wisconsinan ice sheets as each sheet grew and reached its maximum thickness. The increased hydraulic head in the crust below the thick sheet caused outward flow of groundwater toward the periphery. In the Canadian continental shield, the groundwater flow was mostly through fractures in the upper part of the crust. Clay transformation at Kiruna may have been caused by slow flow, relatively concentrated in fractured rock, of warm groundwater forced upward and outward by enhanced hydraulic head under the central areas of Scandinavian continental glaciers for long intervals during the Pleistocene.

3.6 Rb-Sr dating attempts on Kiruna clays

Igor M. Villa,

3.6.1 Introduction

The focus of the work performed at the University of Bern was to investigate the Sr isotopic compositions (Sr/C) of clay samples from the Kiirunavaara mine.

3.6.2 Sample description

Five grain size fractions were received from the Marek Szczerba of the Kraków laboratory (see appendix B) for five Kiruna samples, Ki-01 to Ki-05. From fine to coarse, the size fractions were:

- $<0.02\ \mu\text{m}$, labelled here VF
- $0.02\text{--}0.05\ \mu\text{m}$ (labelled F)
- $0.05\text{--}0.2\ \mu\text{m}$ (labelled M)
- $0.2\text{--}2\ \mu\text{m}$ (labelled C)
- $>2\ \mu\text{m}$ (labelled VC)
- One sample, Ki-03, was supplied both untreated (labelled “untr”) and treated by Na exchange following the method of Jackson (1979; labelled “Jack” here).
- One $<0.02\ \mu\text{m}$ (VF) sample from Malmberget (Ma-01) was also included.
- Finally, to obtain data on the interstitial matrix carbonates, the finely ground whole rock (wr) was leached for 15 minutes in very dilute, 0.01 molar HCl. The resulting leach solution is labelled wrL.

3.6.3 Methods

The samples were dissolved in screw-top Teflon beakers in a mixture of hot distilled concentrated HF+HNO₃. The solution was then dried and converted to nitrate using concentrated HNO₃, then dried once more and then taken up in a precisely known amount of dilute HNO₃. This solution was split 9:1; the smaller aliquot was spiked with an ⁸⁷Rb+⁸⁴Sr spike, dried, then taken up in concentrated HNO₃ to homogenise sample and spike. All solutions were dried and converted to chloride using concentrated distilled HCl and taken to dryness once again.

Chemical purification of Rb and Sr followed the routine procedure using Dowex cation resin and HCl as eluant. The Rb and Sr fractions thus obtained were further purified (after drying, converting to nitrate and drying again) using miniaturised columns and SrSpec resin with nitric acid as eluant. The Sr isotopic compositions on the large, unspiked aliquot and the Rb/Sr element ratios on the smaller spiked aliquot were measured on a NeptunePlus plasma source mass spectrometer.

For K, samples were dissolved in hot distilled concentrated HF+HNO₃, and the concentrations measured by atomic absorption. For Ar, the powder was melted in an ultra-high vacuum furnace connected to a NuInstruments Noblesseä rare gas mass spectrometer, using bracketing standards for the absolute intensity conversion to Ar amounts.

3.6.4 Results

The Rb-Sr results on the ten clay size fractions of “overdetermined” sample Ki-03 are presented in Table 3-24. Samples Ma-01, Ki-02, Ki-04 and Ki-05 are also presented in the table. The K and Ar concentrations were determined on dry aliquots of sample Ki-03 as received (see Section 3.6.2) and the results are presented in Table 3-25.

Table 3-24. The Rb-Sr results on the ten clay size fractions of “overdetermined” sample Ki-03 (and samples for Ma-01, Ki-02, Ki-04 and Ki-05).

| Sample ID | Rb ppm | 2SE % | Sr ppm | 2SE % | $^{87}\text{Rb}/^{86}\text{Sr}$ | 2SE abs. | $^{87}/^{86}\text{Sr}$ | 2SE abs. |
|---------------|--------|-------|--------|-------|---------------------------------|----------|------------------------|----------|
| Ki-03-Jack-VC | 1.71 | 0.22 | 11.53 | 0.009 | 0.4305 | 0.0010 | 0.733733 | 0.000036 |
| Ki-03-Jack-C | 1.09 | 1.47 | 17.91 | 0.003 | 0.1773 | 0.0026 | 0.733619 | 0.000019 |
| Ki-03-Jack-M | 54.92 | 0.71 | 21.40 | 0.005 | 7.4761 | 3.9569 | 0.777466 | 0.000019 |
| Ki-03-Jack-F | 13.69 | 0.12 | 33.36 | 0.001 | 1.1981 | 0.0015 | 0.798499 | 0.000012 |
| Ki-03-Jack-VF | 0.73 | 1.15 | 6.13 | 0.001 | 0.3442 | 0.0039 | 0.709542 | 0.000015 |
| Ki-03-untr-VC | 0.62 | 1.37 | 8.09 | 0.003 | 0.2242 | 0.2491 | 0.732257 | 0.000017 |
| Ki-03-untr-C | 0.83 | 0.14 | 13.81 | 0.002 | 0.1745 | 0.0002 | 0.733731 | 0.000013 |
| Ki-03-untr-M | 3.54 | 0.08 | 19.76 | 0.001 | 0.5212 | 0.0004 | 0.750485 | 0.000016 |
| Ki-03-untr-F | 14.78 | 0.19 | 25.13 | 0.003 | 1.7102 | 0.0033 | 0.760000 | 0.000016 |
| Ki-03-untr-VF | 6.38 | 1.10 | 34.52 | 0.005 | 0.5360 | 0.0059 | 0.730873 | 0.000019 |
| Ma-01 | 24.42 | 0.23 | 184.21 | 1.736 | 1.3448 | 0.0264 | 0.712539 | 0.000010 |
| Ki-02-wrL | 1.23 | 0.34 | 3.13 | 0.045 | 1.1366 | 0.0044 | 0.721098 | 0.000034 |
| Ki-02-VF | 20.45 | 0.84 | 5.13 | 0.052 | 11.5428 | 0.1029 | 0.722915 | 0.000083 |
| Ki-04-wrL | 0.56 | 0.62 | 0.93 | 0.123 | 1.7440 | 0.0130 | 0.733620 | 0.000134 |
| Ki-04-VF | 10.18 | 1.00 | 5.04 | 0.010 | 5.8594 | 0.0594 | 0.733068 | 0.000023 |
| Ki-05-wrL | nd | nd | nd | nd | nd | nd | 0.740936 | 0.000180 |
| Ki-05-VF | nd | nd | nd | nd | nd | nd | 0.738319 | 0.000028 |

Table 3-25. K and Ar concentrations in sample Ki-03.

| Sample ID | Mass (g) | [K] gg^{-1} | $^{40}\text{Ar}^*$ molg^{-1} | $^{40}\text{Ar}^*/^{40}\text{Ar}_{\text{tot}}$ | Age | Age uncertainty |
|---------------|----------|----------------------|---------------------------------------|--|--------|-----------------|
| Ki-03-Jack-VC | 0.0068 | 4.60E-05 | 4.15E-11 | 0.183 | 2445.7 | 48.9 |
| Ki-03-Jack-C | 0.0046 | 1.88E-04 | 1.42E-11 | 0.054 | 390.4 | 7.8 |
| Ki-03-Jack-VF | 0.0026 | 4.94E-04 | 1.47E-11 | 0.005 | 163.1 | 3.3 |
| Ki-03-untr-VC | 0.0044 | 5.20E-05 | 1.97E-10 | 0.633 | 4639.9 | 92.8 |
| Ki-03-untr-C | 0.0042 | 1.99E-04 | 1.15E-11 | 0.087 | 304.7 | 6.1 |
| Ki-03-untr-VF | 0.0014 | 7.81E-03 | 2.89E-09 | 0.900 | 1407.7 | 28.2 |

3.6.5 Discussion

It was immediately clear from the scatter of the Rb-Sr data points (summarised in Figure 3-7) that the results nullified the initial expectations of finding a system consisting of a binary mixture between an inherited component, expected to be hosted in the coarse clay fractions, and an authigenic component, expected to be hosted in the finest clay fractions. An idealised binary mixture would show the characteristic trend shown in Figure 3-8a: all mixtures of end-member 1 (EM1), the inherited component, and end-member 2 (EM2), the authigenic component, must lie on the tie-line between EM1 and EM2, whereby the VC size fraction would plot closest to EM1 and the F and VF size fractions would plot progressively closer to EM2.

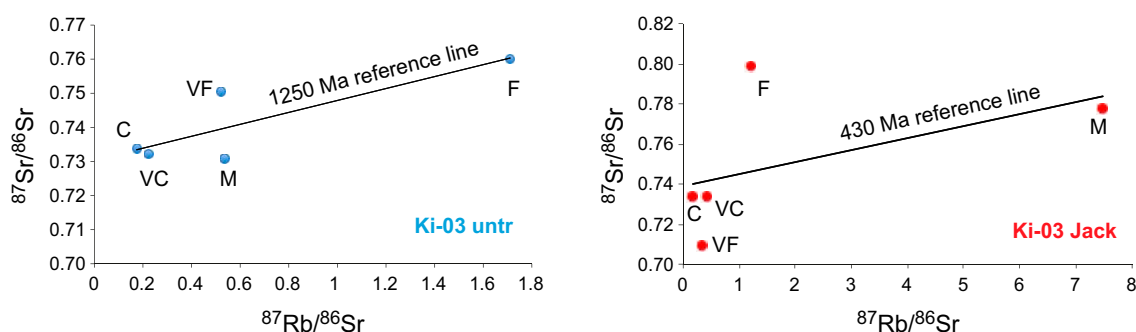


Figure 3-7. representative $^{87}\text{Rb}/^{86}\text{Sr}$ vs $^{87}\text{Sr}/^{86}\text{Sr}$ plots for sample Ki-03.

However, the measured values of the treated and untreated clay Ki-03 do not conform to this simple assumption (Figure 3-8b). The treated (red) and untreated (blue) fractions are significantly offset from each other. In both aliquots (apart from M), the trend from VC to C (i.e. coarser to finer) is horizontal towards the left (i.e. Sr mass fractions, [Sr], increase from VC to C, whereby [Sr] is reduced by the Jackson treatment; Jackson, 1979), then from C to F the trend is upward and to the left, with steadily increasing [Sr]. Finally, the VF fraction is totally erratic.

The implication that should be drawn is that perturbations of the Rb-Sr system, in addition to a likely multiphase geological history (see below), must have occurred. For example, plausible artefacts that cannot entirely be discounted may have occurred during sample preparation. End-member 3 in Figure 3-8c represents potential contamination from the solute (water) utilised in the clay separation process. The employed water was only deionised, not triply distilled, and the NaCl reagent was not checked for traces of Rb or Sr.

Even if the cation budget was likely low, the high surface/volume ratio of the clay, the intrinsically low Rb and Sr contents of smectitic clay, and the long exposure time to water in the separation system can have increased the Rb content of the clay and, at the same time, added Sr with a (presumable) isotopic composition close to environmental dust and marine aerosol. The dashed field marked EM3 in Figure 3-8c indicates the likely field of this potential aqueous contamination. A further process is incomplete removal of loosely bound interlayer cations (exchangeable cations) and/or excessive removal of true authigenic Rb. The Na exchange of the Jackson method (Jackson, 1979) is a common practice designed to remove exchangeable alkali ions. Since Na has a smaller ionic radius than K, it is thought that it forms tighter bonds with the smectite TOT¹⁰ framework and thus displaces the secondary exchangeable K ions; the tightly bound primary K ions are assumed to be unaffected.

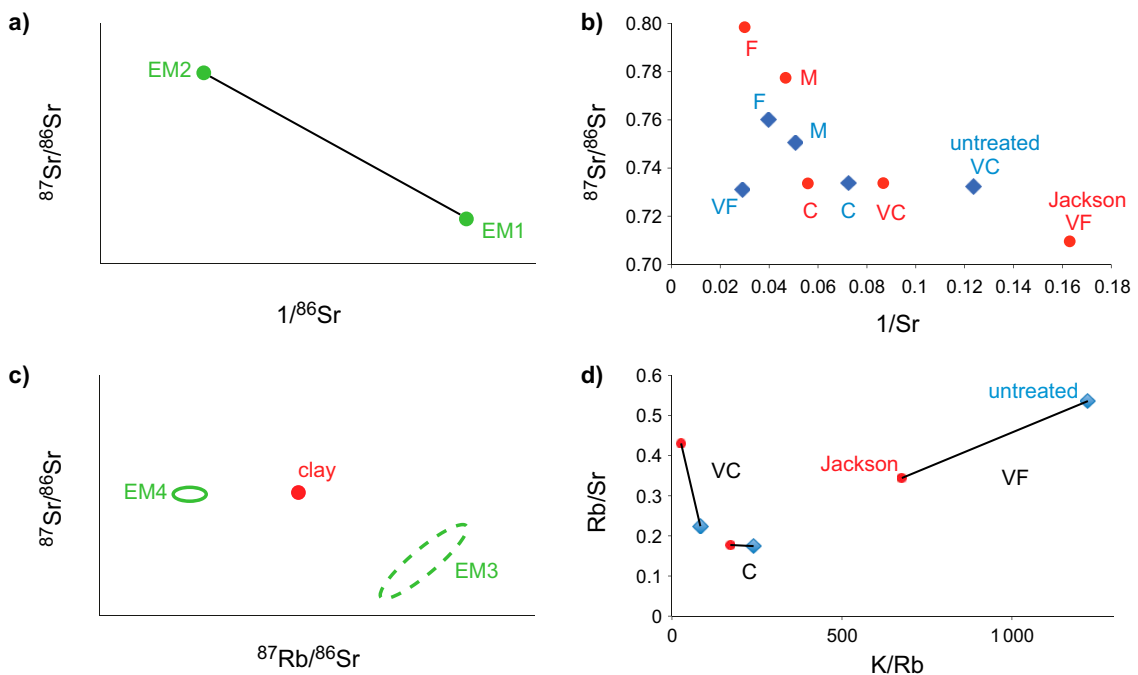


Figure 3-8. a) plot of $1/^{86}\text{Sr}$ vs $^{87}\text{Sr}/^{86}\text{Sr}$ for an idealised binary mixture between two end-members (EM1 and EM2). b) actual plot of $1/^{86}\text{Sr}$ vs $^{87}\text{Sr}/^{86}\text{Sr}$ for the measured values of the treated (red, Jackson) and untreated (blue) clay Ki-03. c) potential $^{87}\text{Rb}/^{86}\text{Sr}$ vs $^{87}\text{Sr}/^{86}\text{Sr}$ plot for a contaminated system. Clay (red) represents the proposed uncontaminated clay sample, end-member 3 (EM3, green dashed line) representing contamination from the solute used in the clay separation process, leading to uptake of Rb. End-member 4 (EM4, green solid line) is representative of a clay with unchanged Sr isotopic composition and a higher removal of Rb due to the separation process. d) plot of K/Rb vs Rb/Sr to illustrate the likely impact of the (Jackson) Na exchange treatment on the K/Rb and Rb/Sr ratios of sample Ki-03.

¹⁰ Tetrahedra-Octahedra-Tetrahedra. The 2:1 layer (TOT) structure consists of two silica (SiO_2) tetrahedral (T) layers which are electrostatically cross-linked via an Al_2O_3 (gibbsite), or Fe_2O_3 , octahedral (O) central layer.

In the present experiment, the likely exchange was not exacerbated by, for example, vigorous mixing or repeated rinsing of the samples and so it is suggested that it resulted in substantial, but only partial, removal of exchangeable K. For Rb, however, the exchange suffers from an additional complication: the Rb ion is much larger than both K and Na and therefore even primary interlayer Rb is very weakly bound. It is not clear how much secondary Rb has been retained and how much primary Rb has been removed due to its weaker bond with the smectite. The Sr ion has a higher charge but, at the same time, a larger ionic radius than Na. The Na-exchange behaviour of both primary and secondary Sr is unknown; because of the ionic charge, the retention of Sr is predictably higher than that of Rb. This is indicated by end-member EM4 in Figure 3-8c, which is assumed to have an unchanged Sr isotopic composition and a higher removal of Rb, i.e. a lower Rb/Sr ratio, and is therefore horizontally displaced to the left of the starting material (clay, in red).

These two latter processes act differently as a function of separation time and of the surface-volume area of the treated clay, so that $EM3(VF) \neq EM3(VC)$ and $EM4(VF) \neq EM4(VC)$. The result is a heavily under-determined system and primary Sr isotopic compositions can therefore only be semi-quantitatively estimated. The effect of the Na exchange treatment on the K/Rb ratio of sample Ki-03 is illustrated in Figure 3-8d and suggests a considerable lack of reproducibility on the Rb/Sr ratio. As for the K/Rb ratio, the predicted effect of Na substitution is that the Jackson treated clays should selectively lose more exchangeable Rb than exchangeable K, owing to the latter's smaller radius and stronger bond. Contrary to the original prediction, the C and VC size fractions show a moderate decrease of the K/Rb ratio, and the VF fraction a decrease by a factor 1.8. This is due to the increase of the Rb mass fraction, [Rb], by a factor 2.1 in the Jackson treated VF aliquot. Such a large increase can only be explained by a significant secondary contamination by the combination of reagents and vessels in the Jackson treatment.

How has this likely to have impacted the apparent formation age of the clay samples analysed here? Considering the negative effects of natural inheritance on the larger grain sizes (VC to F), it is assumed that the VF size, being mostly authigenic, would give the least biased age. A credibility test was performed on sample Ma-01 from Malmberget, for which K-Ar age values of 853 ± 16 to 887 ± 16 Ma (clay fraction size dependent) were obtained (Table 3-22). These age values and ones obtained earlier for three size fractions each of Ma-01 and another, similar sample, provide a strong constraint that the Malmberget clay was formed in the Proterozoic and has suffered very little disturbance since. The Rb-Sr analyses on Ma-01 were performed on the VF clay fraction. As the clay provides only one point, it is necessary to analyse a second mineral phase in order to calculate an isochron. This is shown in Figure 3-9a, using data for stilbite from sample Ma-04 as reported by Romer (1996) and Romer and Rocholl (2004). The coarse-grained calcite from Ma-01 is in disequilibrium with the Ma-01 clay, which may point to the fact that the calcite analysed by Romer (1996) and the clay were not cogenetic. The Rb-Sr apparent age thus obtained, 231 Ma, is a factor of 3.5 younger than the K-Ar age. It should be noted that the Ma-01 clay is highly enriched in Sr and this may point to admixture of an EM3-type contamination (cf. Figure 3-8c). As was noted above, an external Rb addition of a factor 2 can occur during the Jackson treatment. The discrepancy with the robustly established K-Ar ages of the Malmberget samples is proof that the apparent Rb-Sr age of the Kiirunavaara mine samples is a strictly lower limit.

The K-Ar results for Ki-03 (Table 3-25) broadly confirm the insight discussed above, that the Jackson treatment reduces the K concentration of the samples by removing exchangeable K. The ages of the coarsest fractions carry a large inheritance of Proterozoic detritus; none of the obtained ages is younger than Mesozoic, particularly not the VF fractions. The K-Ar ages for the Ki-01 to Ki-05 samples reported in Section 3.5 were obtained after extensive Jackson treatment. In that respect, those results are not directly comparable to the present study (Table 3-25) in which VC, C and VF fractions of untreated and moderately treated clays were analysed. Nevertheless, it is a quite robust observation that apparent K-Ar ages range between Proterozoic and Phanerozoic, with none of the samples younger than Mesozoic.

Before the extent of the laboratory artefacts was realised, it was decided to attempt Rb-Sr isochron dating. Based on geological arguments, two mineral phases were thought to be cogenetic: the VF clay fraction ("authigenic") and carbonates, assumed to have been precipitated from the same fluid responsible for the late-stage clay diagenesis. This was attempted on samples Ki-02, Ki-04 and

partly Ki-05¹¹ (Table 3-24). To obtain the carbonate, the finely ground whole rock (wr) was leached for 15 minutes in very dilute, 0.01 molar HCl¹². The resulting leach solution, wrL, was pipetted off from the residuum and dried; as it visually contained very little material, presumably only calcium and trace elements, it was converted to nitrate and directly purified on SrSpec columns.

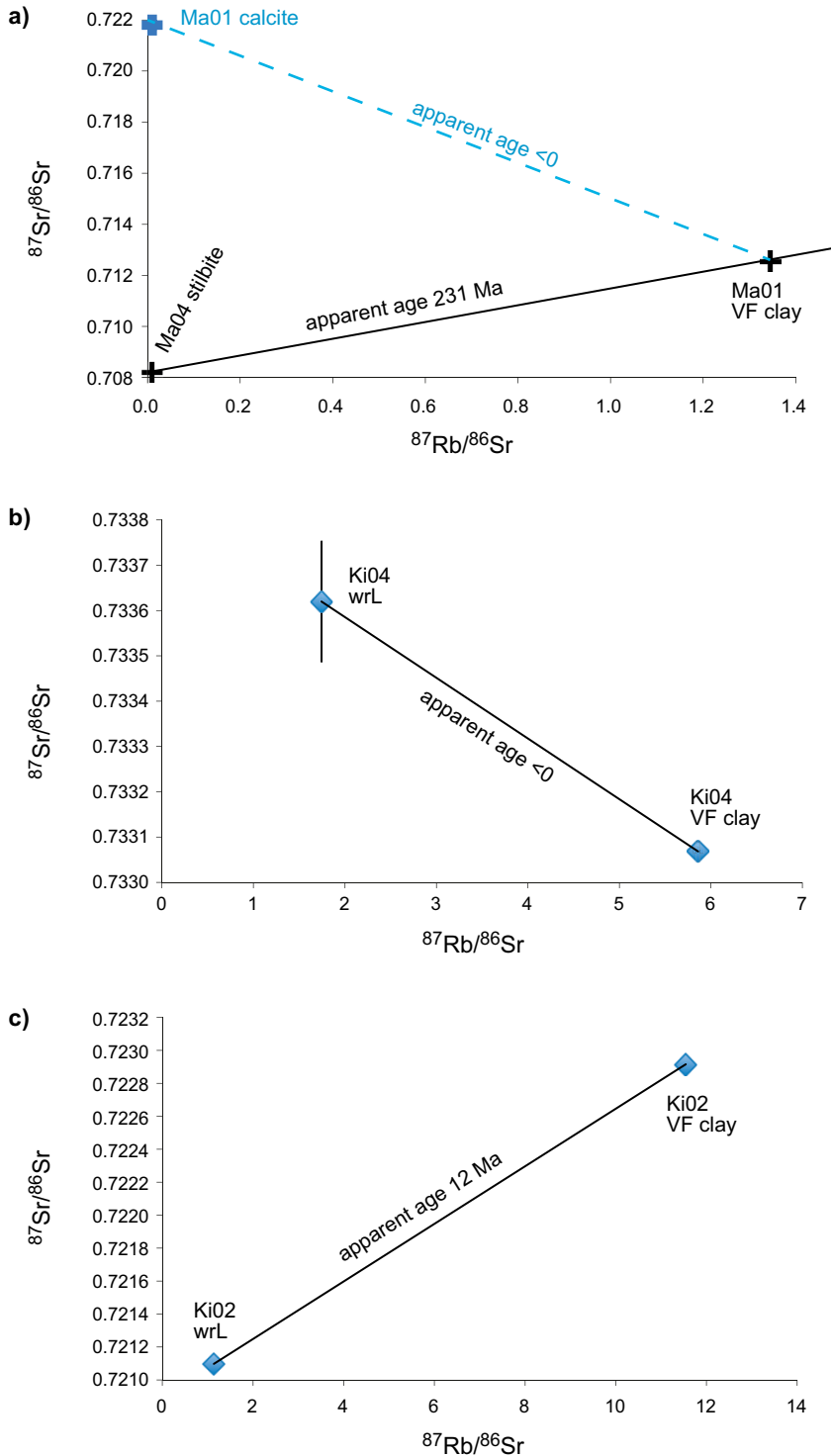


Figure 3-9. $^{87}\text{Rb}/^{86}\text{Sr}$ vs $^{87}\text{Sr}/^{86}\text{Sr}$ plots for carbonate (i.e. wrL) extracts and VF samples for Ma-01, Ki-04, Ki-02 and Ma-04.

¹¹ Note that no Rb data were obtained for sample Ki-05 (Table 3-24).

¹² Note that this treatment will also release exchangeable cations from the clays.

The results are summarized in Figure 3-9. It can be noted that in three of four cases (Ma-01, Ki-02 and -04) the carbonate (i.e. wrL) data are in disequilibrium with the VF clay (Figure 3-9a and 3-9b). This may suggest that the whole rock matrix usually contains minute relicts of a mineral phase that existed prior to the formation of the clay and that was as soluble as calcite in dilute HCl. The only sample that gives an apparent isochron with a positive slope is Ki-02 (Figure 3-9c). However, this positive slope is most likely affected by the same artefact evident in the other three instances: namely, the presence of non-cogenetic relict minerals that must not be regressed with the clay. Indeed, the Miocene apparent wrL-VF age of Ki-02 contrasts with all the chronological constraints discussed above and with the context provided by the K-Ar determinations (cf. Section 3.5).

An alternative approach to circumvent the plausible Proterozoic inheritance of the wrL extracts is referring the Rb-Sr isochron to an arbitrarily assumed SrIC of the circulating aqueous fluid equal to the SrIC of the stilbite in Ma-04, namely 0.7082 (Romer, 1996; Romer and Rocholl 2004). This value is close to the apatite in Ma-02 (0.7094; Romer, 1996). Even if the Jackson-treated Ki03-VF fraction has a similarly low SrIC, this is not decisive because of the possible external contamination in the laboratory. In that assumption, shown in Figure 3-10, the apparent ages of Ki-02, and Ki-04 produce a better agreement with the K-Ar ages provided in Section 3.5. In particular, the apparent age of Ki-02 is moved from the Miocene to the Mesozoic (although a Mesozoic metamorphic event in northern Sweden is not documented).

In conclusion, the present study identifies a multiphase history of the Kiruna samples, starting in the Proterozoic (ca. 2 500–540 Ma) and ending in the Mesozoic (ca. 250–66 Ma). After the Mesozoic no further water circulation event was recorded by the Kiruna clay analysed here.

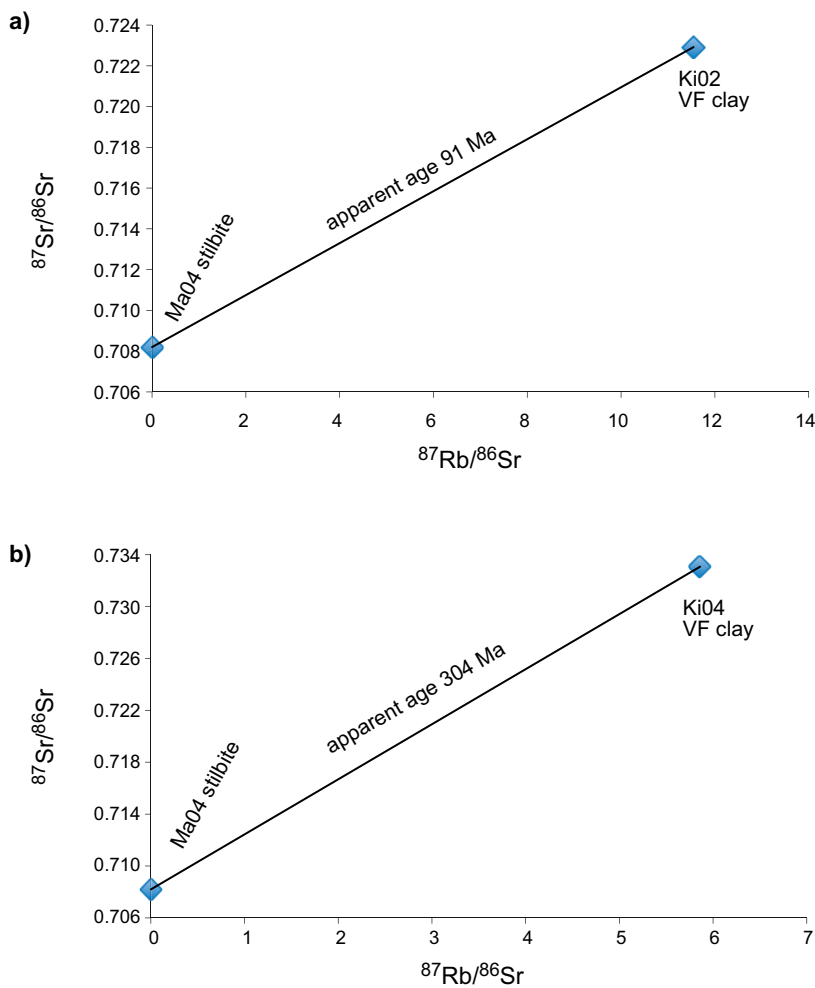


Figure 3-10. $^{87}\text{Rb}/^{86}\text{Sr}$ vs $^{87}\text{Sr}/^{86}\text{Sr}$ plots for an arbitrarily assumed SrIC for samples Ki-02 and Ki-04.

3.7 Kiruna clay: Relevant properties and processes

Patrik Sellin and Daniel Svensson

3.7.1 Introduction

The clay in the Kiirunavaara mine can be viewed as a natural analogue for a bentonite buffer in a radioactive waste repository since:

- The clay consists mainly of montmorillonite, which is the same mineral as in the benefacted bentonite in many repository designs
- The environment is rather similar to that of a repository (depth, hydrogeology, hydrogeochemistry, host rock characteristics etc.)
- The dimensions of the clay layers range from the centimetres to tens of metres. The size of most barriers (e.g. borehole seals, canister buffer, tunnel seals, shaft seals) in a repository fit well within this range

One objective of the studies in the KINA project is to investigate the state of the properties of the clay and to compare those to what is expected in the clay barriers in the assessment of repository evolution. Another objective is to try to identify which processes have been going on in the clay layers and, if possible, quantify the extent of those process.

3.7.2 Mineral composition

The mineral composition of the Kiruna clay is of prime importance. It needs to be reasonably similar to that of a commercial (benefacted) bentonite to be useful as a NA (cf. comments in sections 1.2–1,4). The elemental composition of the Kiruna smectite has been determined with XRF, the mineralogical composition has been determined with XRD (both detailed in Svensson et al. 2019) and the CEC has been determined with exchange with a Cu^{2+} -triethylenetetramine complex (Meier and Kahr, 1999).

The elemental composition of the first sample batch (Kiruna, 2018) collected in the Kiirunavaara mine can be seen in Table 3-26. It is clear that the clay is in a pure calcium form of smectite. The iron content is surprisingly low considering the proximity to the iron ore body.

Table 3-26. Elemental composition by XRF from the first batch of Kiruna smectite (wt%). Three separate analyses taken from the same batch.

| Ident | Na ₂ O | MgO | Al ₂ O ₃ | SiO ₂ | P ₂ O ₅ | SO ₃ | Cl | K ₂ O | CaO | TiO ₂ | MnO | Fe ₂ O ₃ |
|--------------------------------------|-------------------|-------|--------------------------------|------------------|-------------------------------|-----------------|-------|------------------|-------|------------------|-------|--------------------------------|
| Kiruna smectite sample 30-1137-F3032 | 0 | 4.656 | 21.048 | 63.407 | 0 | 0.016 | 0.004 | 0.202 | 6.887 | 1.14 | 0.237 | 2.403 |
| Kiruna smectite sample I | 0 | 4.63 | 20.99 | 63.194 | 0 | 0.025 | 0.004 | 0.201 | 7.099 | 1.207 | 0.244 | 2.408 |
| Kiruna smectite sample II | 0 | 4.625 | 21.036 | 63.309 | 0 | 0.032 | 0.004 | 0.205 | 6.872 | 1.302 | 0.236 | 2.38 |

An XRD spectrum of the first batch from Kiruna can be seen in Figure 3-11 and the interpretation of the results from both batches in Table 3-27. It is clear that the variability in composition between different locations can be rather substantial (cf. Sections 3.2-3.6). The accessory minerals are mainly carbonates and albite.

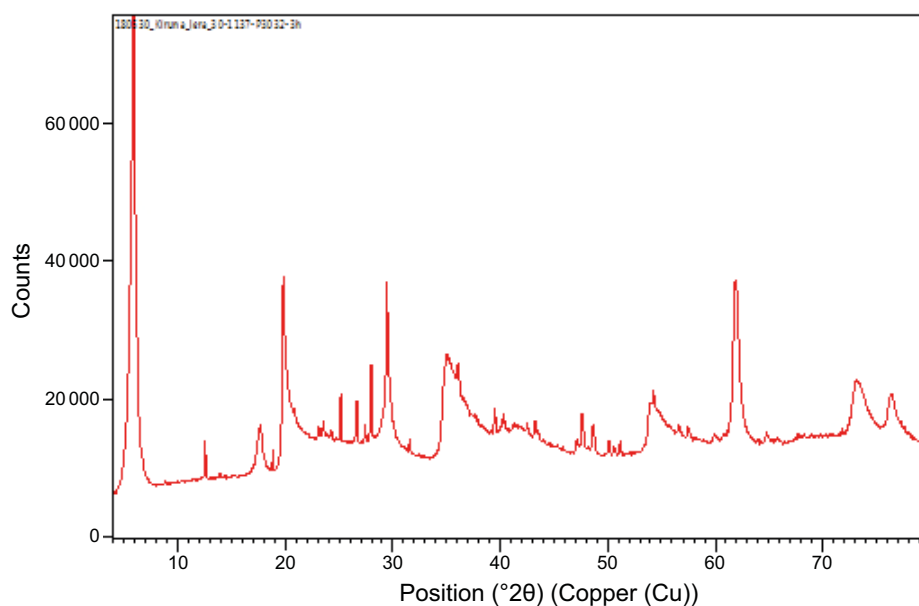


Figure 3-11. XRD pattern from a dry sample of the first batch of the Kiruna smectitic clay.

Table 3-27. Mineralogical composition (wt%) from XRD analyses.

| Sample | Quartz | Calcite | Magnetite | Albite | Smectite | Mica |
|-------------|--------|---------|-----------|--------|----------|------|
| Kiruna 2018 | 1.1 | 17.4 | 0.8 | 0 | 80.7 | ? |
| Kiruna 2019 | 0.1 | 1.1 | 0.2 | 40.1 | 58 | ? |

The measured CEC can be found in Table 3-28 together with calculated values for the CEC of the montmorillonite fraction. The CEC corresponds fairly well with a variation in montmorillonite content. The difference may possibly be due to the uncertainty in the mica content due to difficulties with the background treatment in the software in the vicinity of the 001 mica reflection, or other phases not yet identified.

Table 3-28. CEC (cmolk⁻¹) and calculated values for montmorillonite CEC.

| Sample | CEC | Montmorillonite (XRD) | CEC_Montmorillonite_calc |
|-------------|------|-----------------------|--------------------------|
| Kiruna 2018 | 85.7 | 81 | 105.8 |
| Kiruna 2019 | 70.8 | 58 | 122.1 |

It is clear that the Kiruna clay consists mainly of montmorillonite which makes it suitable as a NA for the bentonite barrier in the EBS. The variability between sampling locations can be rather large regarding the content and composition of the associated minerals. This is not a problem for the usefulness of the material, but needs to be considered in the interpretation of results.

3.7.3 Hydraulic conductivity and swelling pressure

The swelling pressure and the hydraulic conductivity are key parameters that determine the performance of a bentonite barrier. It is of interest to confirm that these properties in the Kiruna clay are in the same range to that what is expected in the repository material.

The hydraulic conductivity and the swelling pressure of two sampling batches from Kiruna has been measured with the standard method that is used at SKB (Svensson et al 2019). The results can be seen in Figure 3-12 and Figure 3-13 and in Appendix J. As, comparison, measured hydraulic conductivity and swelling pressure for a number of industrial bentonites are shown in Figure 3-14 and Figure 3-15.

There is a rather large difference in the hydraulic conductivity between the two different batches of the Kiruna material. This could, however, be explained by a lower montmorillonite content in the 2019 batch as seen in Table 3-27. The hydraulic conductivity of both batches seems to be largely unaffected by the salinity and composition of the external solution in the tests. The hydraulic conductivity of the 2018 batch is $\sim 10^{-13}$ m/s at a dry density of 1500 kgm^{-3} . The conductivity of the 2019 batch is higher, but still in the range of benefacted industrial bentonites.

The relative difference in swelling pressure between the two batches is smaller than the hydraulic conductivity. The swelling pressure is, however, more affected by the salinity of the external solution. The swelling pressure in de-ionised water at a dry density of 1500 kgm^{-3} is around 4 MPa for both batches (cf. the other natural bentonites presented in Figure 3-13). Most industrial bentonites have a swelling pressure of 6–9 MPa for the same density. The reason for this difference is currently unknown (see Figure 3-15).

In conclusion, the hydraulic conductivity of the Kiruna clay is similar to that of a industrial bentonite with the same smectite content. The swelling pressure is, however, lower for reasons currently unknown.

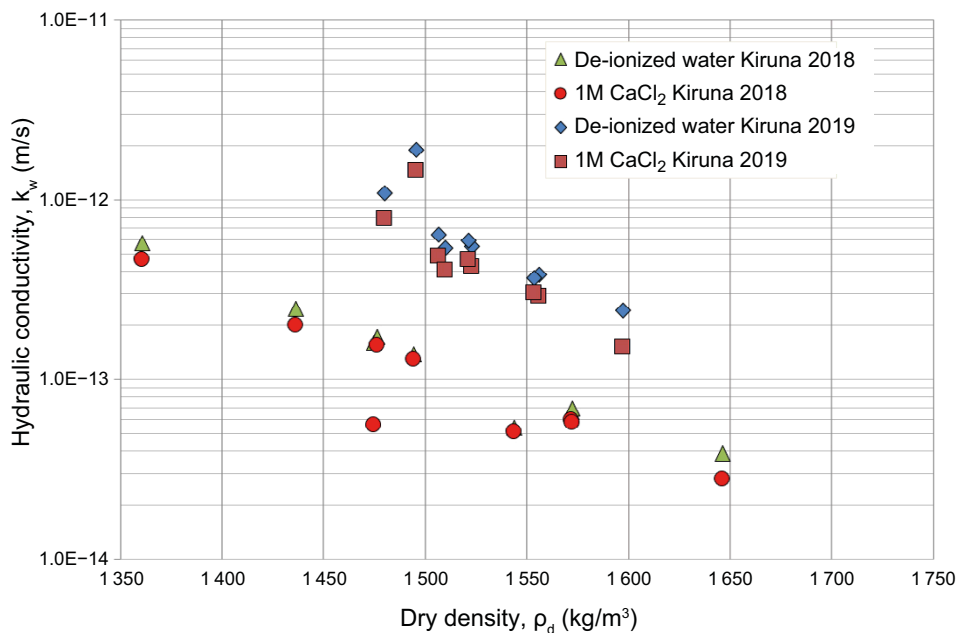


Figure 3-12. Hydraulic conductivity in two sample batches (Kiruna 2018 and Kiruna 2019) of Kiruna clay.

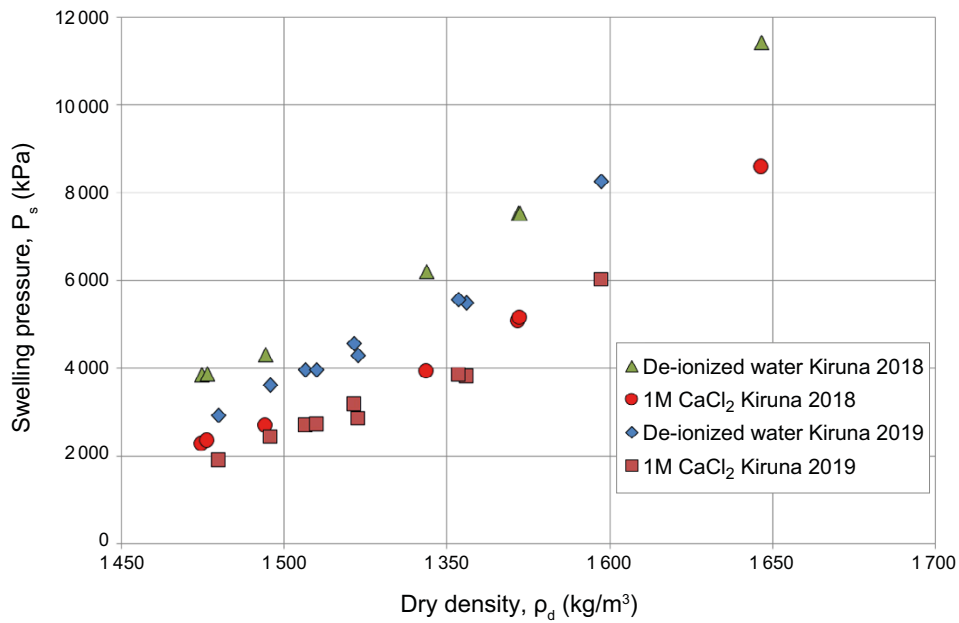


Figure 3-13. Swelling pressure in two sample batches (Kiruna 2018 and Kiruna 2019) of Kiruna clay.

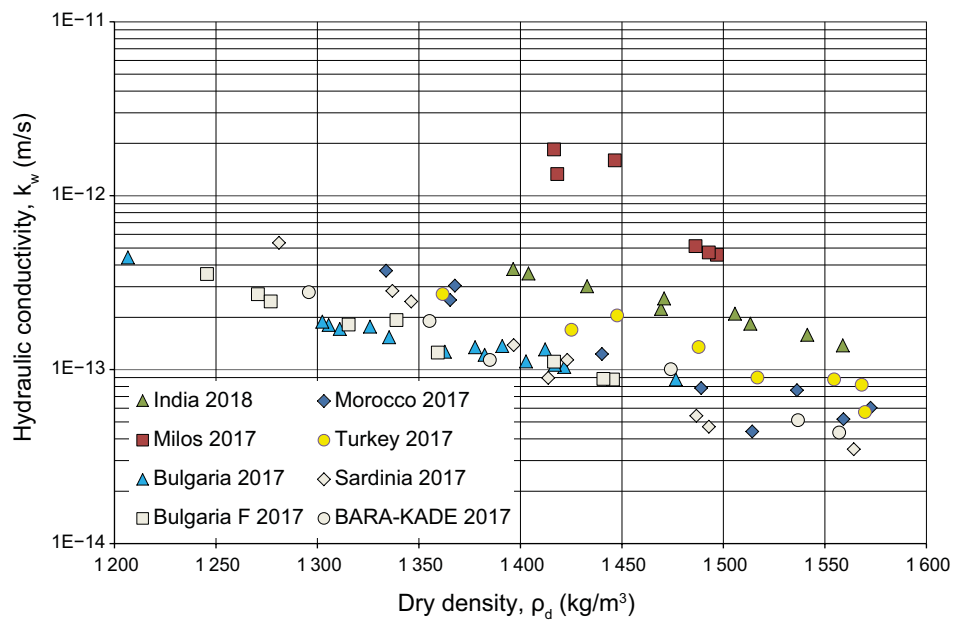


Figure 3-14. Determined hydraulic conductivity, measured with deionised water, as function of dry density for eight previously investigated bentonites (Svensson et al. 2019).

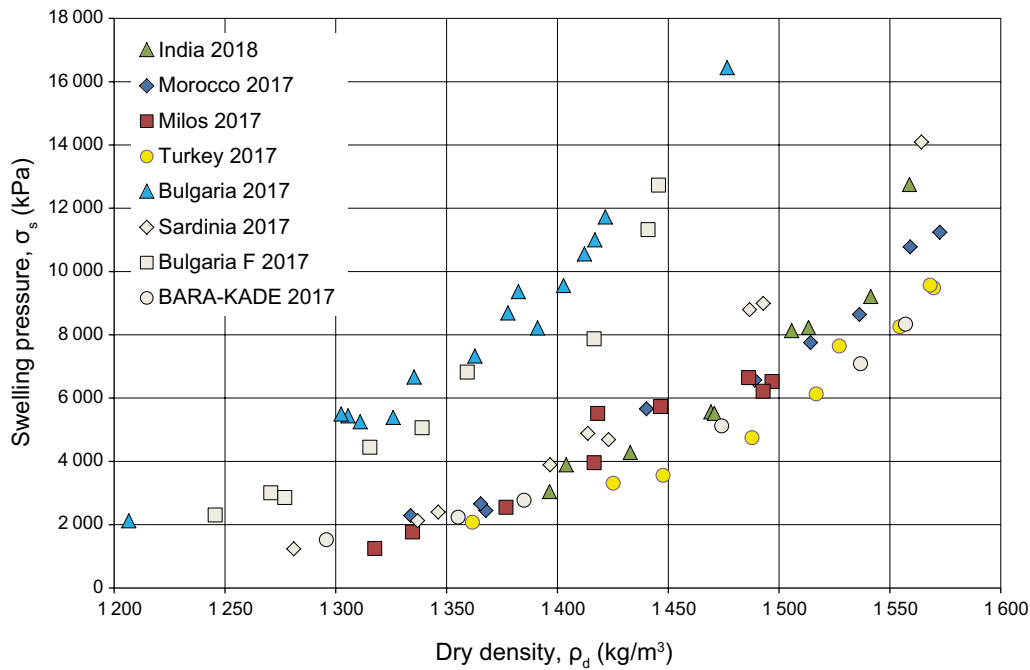


Figure 3-15. Determined swelling pressure, measured with deionised water, as function of dry density for 8 investigated bentonites (Svensson et al. 2019).

3.7.4 Mineral stability

A bentonite buffer should resist mineral transformation, even over time scales of hundreds of thousands to a million years. Based on the investigations presented in other chapters of this report, it seems clear that the Kiruna clay samples studied here have been stable in the environment in the Kiirunavaara mine, at least close to the sampling site. The material described in Section 3.6 appears to have been stable since the Mesozoic (ca. 250–66 Ma), further supporting the conclusions for the material studied here (but note this is discussed further in Section 8.3). Additionally, no signs of any alteration products, such as illite, have been found.

This conclusion must however be further supported with an understanding of the genesis of the Kiruna clay.

3.7.5 Interaction with other repository components

A special case of the mineral stability issue is the interaction between bentonite and other repository components. The most important are the interactions with metals and cement. Neither of those interactions can be studied in Kiruna. It is however possible to investigate the interaction between bentonite and magnetite, which is expected to be the predominant corrosion product of iron in many repository designs (e.g Smart et al. 2002). Figure 3-16 shows the smectite-magnetite interface in sample Kiruna 2018 c65ef8.

The elemental composition of the smectite presented in Table 3-26 shows that the iron content is relatively low. While this indicates that the interaction between magnetite and Kiruna clay is weak, little more can be said for the moment as the degree of saturation of the clay and the likely Eh/pH conditions at the magnetite/clay interface are unknown (see further the discussions in chapters 4 and 7). The magnetite must be able to dissolve to provide a source of iron and the environment should be low pH and high Eh, otherwise the amount of [Fe] in equilibrium with the magnetite would be very small and so the source of Fe for uptake by the clay would be limited in the first place.



Figure 3-16. Smectite-magnetite interface in sample “Kiruna 2018” from the Kiirunavaara mine.

3.7.6 Sulphate reduction

One safety function assigned to the bentonite buffer in the KBS-3 (and some other) concept is the ability to suppress microbial sulphate reduction. This ability requires a certain minimum density of the bentonite. At this stage, the in-situ density of the Kiruna smectite has not been determined, but it is very likely that it is too low to suppress microbial activity (see Chapter 5). There are sulphide minerals present in the clay as well as on the interfaces (Figure 3-17). How and when these were formed remains open (but please see the comments in appendix H).

Suppression of microbial sulphate reduction has not yet been addressed in the Kiruna mine (see Chapter 6), but has been assessed in both natural (e.g. Beaver et al. 2022) and industrial (e.g. Maanoja et al. 2020) bentonites by studies of microbial systems, indicating the viability of such an approach.



Figure 3-17. Kiruna smectite-pyrite interface (pyrite confirmed by XRD).

4 Description of the iron-clay interface in the Kiirunavaara mine (and assessment of potential iron-clay interaction)

Tsubasa Otake¹, Ryosuke Kikuchi¹, Tatsuya Fujimura², Tsutomu Sato¹, Satoru Suzuki³, Takahiro Goto³ and Shuhei Nemoto³

4.1 Introduction

The safety functions of the clay buffer in a radioactive waste repository are predominantly due to the properties of the main constituent mineral, smectite. These may be affected by alteration of smectite, cementation of the clay by precipitation of secondary minerals and changes in the interlayer cations of smectite (Sellin and Leupin, 2013).

In addition, there are materials such as carbon steel and cement in contact with the clay in the repository EBS. If alteration of the clay occurs due to the interaction between these materials and the clay, this may also lead to degradation of the safety functions.

The purpose of this chapter is to present the preliminary results of an examination of samples from the Kiirunavaara mine, Kiruna, northern Sweden. The samples consist of magnetite, an expected corrosion product of a carbon steel waste container, which has been in contact with smectite for geological time periods so the detailed observations on the interface between magnetite and smectite should show evidence of long-term interaction of the two materials. Some additional data can be found in Appendix I.



Figure 4-1. Image of the sampling site of the University of Hokkaido samples (LKAB site code LKAB site code 395-1194). Photo: U.B. Andersson

4.2 Sample details

The samples labelled as KINA1-1 (with a clearly visible magnetite-silicate interface), KINA1-2 and KINA1-3 were collected on 17th September, 2019 in the Kiirunavaara Mine (LKAB site code 306-1194 also referred to as “Kiruna 2019”) – see Appendix B. The samples labelled KINA2-1 to 2-7 were collected by U.B. Andersson in November 2020 at location 395-1194. samples KINA3-1 and 3-2 were collected by NUMO at the sites noted in Table 4-1. All sample locations are shown in Appendix B.



KINA sample 1-1



KINA sample 1-2



KINA sample 1-3



KINA sample 2-1



KINA sample 2-2



KINA sample 2-3



KINA sample 2-4



KINA sample 2-5



KINA sample 2-6



KINA sample 2-7



KINA sample 3-1



KINA sample 3-2

Figure 4-2. Photographs of all hand specimens supplied to the University of Hokkaido (please see Table 4-1 for sample information).

Table 4-1. Sample details and applied analytical methods.

| University of Hokkaido sample ID | Lithology | LKAB site code | XRD | Thin section | SEM-EDS | FE-EPMA | LA-ICP-MS | K-Ar dating |
|----------------------------------|-------------------------|----------------|-----|--------------|---------|---------|-----------|---------------------|
| 1-1 | Magnetite and andesite? | 306-1194 | x | x | x | | | |
| 1-2 | White bentonite | 306-1194 | x | x | x | | x | |
| 1-3 | White bentonite | 306-1194 | x | x | x | | | |
| 2-1 | Magnetite > bentonite | 395-1194 | x | x | x | | x | |
| 2-2 | Magnetite = bentonite | 395-1194 | x | x | x | x | x | |
| 2-3 | Magnetite < bentonite | 395-1194 | x | x | x | | x | |
| 2-4 | Magnetite = bentonite | 395-1194 | x | x | x | x | x | Biotite |
| 2-5 | Magnetite > bentonite | 395-1194 | x | x | x | | | |
| 2-6 | Magnetite < bentonite | 395-1194 | x | x | x | | | |
| 2-7 | Magnetite > bentonite | 395-1194 | x | x | x | | x | |
| 3-1 | Black bentonite | 307-1137 | x | x | x | | x | |
| 3-2 | Grey bentonite | 384-1137 | x | x | x | x | x | Biotite Smectite |

4.3 Analytical methods

4.3.1 Microscopy

An optical microscope (OLYMPUS BX60®) was used to observe thin sections of the samples under plain and polarised light.

A SEM from JEOL (JSM-IT200®) was used to observe carbon-coated thin and polished sections. Energy dispersive spectroscopy (EDS) was also used to obtain information about chemistry on observed points in the samples.

4.3.2 X-ray diffraction (XRD)

In order to identify the minerals contained in the samples, powder XRD analyses were performed. The equipment used was a desktop XRD analyser RINT1200® (Rigaku Corporation, Tokyo, Japan) and a desktop XRD analyser Mini Flex (also manufactured by the Rigaku Corporation). As copper radiation for iron-containing materials leads to a high background, a cobalt source was used to produce high quality diffractograms, making phase identification unambiguous (see, for example, Mos et al. 2018, for details). Identification of smectite in the samples was based on the change in basal spacing before and after treatment of ethylene glycol (EG treatment) using the stereotaxic method.

Minerals in the bulk samples were identified from XRD patterns for powder samples. The powder samples were scanned from 3 to 90° in 2 θ at scanning speed of 3°min⁻¹. For identification of clay minerals, preferred orientation samples were prepared with and without ethylene glycol treatment as mentioned below. The preferred orientation samples were scanned from 3 to 40° in 2 θ at a scanning speed of 1°min⁻¹.

Preparation of preferred orientation samples

Clay mineral fraction with 0.2 to 2 μ m size in diameter were used for the preferred orientation method. The preferred orientation sample was prepared as follows:

- 10 mg of the clay fraction is placed into a 2 mL microcentrifuge tube.
- 200 μ L of distilled water was added to the tube.
- Disperse ultrasonically for 10~15 minutes.
- The supernatant was taken with a dropper, spread it over a 20 mm \times 28 mm area on a glass slide and put to dry naturally.

Ethylene glycol (EG) treatment

For EG treatment, the preferred orientation samples were placed in a container containing ethylene glycol stock solution and exposed to evaporated EG in an oven at 65 °C. After about 12 hours, the preferred orientation samples were immediately measured by XRD.

4.3.3 SEM-EDS

To investigate the morphology and potential alteration state of the magnetite-clay contact in the sample, the morphology and mineralogy were observed using a scanning electron microscope (SEM, JEOL Ltd., JSM-IT200) and the chemical composition of the mineral was analysed by EDS.

4.3.4 FE-EPMA

To examine the potential alteration state of the magnetite-clay contact of the samples based on mineral chemical composition, observation and analysis were conducted using a field emission electron probe micro analyser (FE-EPMA) manufactured by JEOL Ltd (JXA-8530F).

4.3.5 LA-ICP-MS

To investigate the formation environment of magnetite in the sample, trace constituents of the magnetite were analysed by laser ablation inductively coupled plasma mass spectrometry (LA-ICP-MS) in an attempt to estimate the temperature at which the magnetite was formed. The analysis was performed by ICP-MS (Agilent Technologies, Agilent 7850) at the Department of Earth Sciences, Kanazawa University, Japan. The laser used was the UP-213 (New Wave Research, Nd-YAG wavelength 213 nm).

4.3.6 K-Ar dating

To estimate the contact period between magnetite and clay, K-Ar dating was performed on smectite and biotite in contact with magnetite. K-Ar dating was conducted at the Hiruzen Institute for Geology and Chronology, Japan. Samples with magnetite and biotite as major components and a small amount of smectite (KINA 2-1) and samples with smectite as major component and a small amount of magnetite and biotite (KINA 3-2) were analysed. Biotite and smectite were separated and concentrated by the elutriation method and K and Ar isotope ratios were measured.

Smectite dating could not be performed on sample KINA 2-1 because too little smectite was present. In addition, smectite in sample KINA 3-2 was determined by the very low blank method (Itaya et al. 1996) due to the K content being at the limit of detection (<0.2 wt.%).

4.4 Results

4.4.1 Morphological observation of samples and chemical analysis of major constituent minerals

Optical observation

Figure 4-3 and Figure 4-4 show the results of observations of the KINA 2-2 and KINA 2-3 thin sections, respectively. In Figure 4-3, smectite is in contact with magnetite in sample KINA 2-2. In Figure 4-4, the presence of magnetite particles in the smectite in sample KINA 2-3 can be observed. From these results the contact conditions between magnetite and smectite in the Kiirunavaara mine can be broadly classified into the following two cases:

Case A: Thin sections which exhibit the interface between iron ore (as magnetite aggregates) and clay (e.g., sample KINA 2-2, cf. Figure 4-3)

Case B: Thin sections in which magnetite particles are dispersed in clay (e.g., sample KINA 2-3, cf. Figure 4-4)

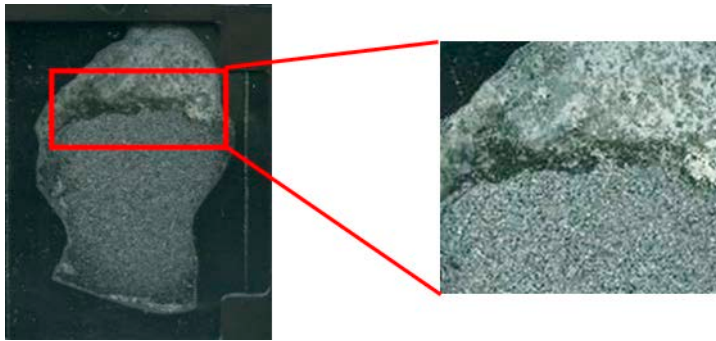


Figure 4-3. KINA 2-2 thin section photomicrograph. Note that the iron ore (bottom half of the thin section, right) occurs as an aggregate.

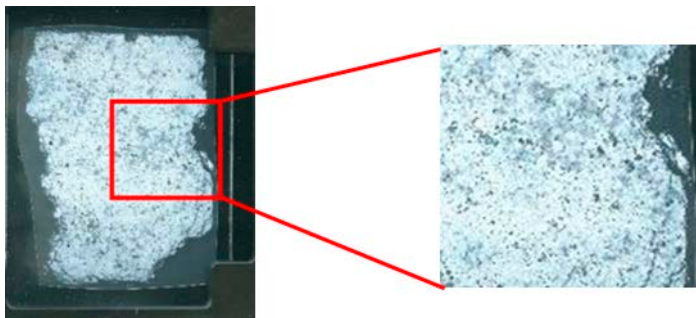


Figure 4-4. KINA 2-3 thin section photomicrograph.

In Case A, the magnetite surface was often covered with biotite grains as described later in Section 4.4.3 and interfaces between magnetite aggregates and clay were rarely found. In contrast, in Case B, clay minerals directly contact with magnetite and such interfaces were easily found in thin section as discussed below. As such, in this study, the interaction between magnetite and clay is discussed mainly for Case B.

4.4.2 XRD Analysis

The results of the random oriented method for KINA 3-1 and the results of the oriented method before and after EG treatment are shown in Figure 4-5 and Figure 4-6, respectively. In addition, Table 4-2 shows the mineral composition determined from powder XRD analysis for each KINA sample. Figure 4-5 shows peaks of smectite, chlorite, quartz, magnetite, biotite and talc in sample KINA 3-1. For the peak identified around 8° in Figure 4-5, Figure 4-6 shows that the peak moved from 13.18 \AA to 16.59 \AA after EG treatment, suggesting this peak was smectite.

Table 4-2. Powder XRD results for each KINA sample.

| KINA sample No. | Identified Minerals |
|-----------------|---|
| 1-1 | Albite, Biotite, Calcite, Chlorite, Magnetite, Smectite, Quartz |
| 1-2 | Smectite, Albite, Magnetite |
| 1-3 | Smectite, Albite, Magnetite |
| 2-1 | Biotite, Smectite, Quartz, Magnetite, Calcite, Chlorite |
| 2-2 | Biotite, Magnetite, Chlorite, Smectite, Calcite, Quartz |
| 2-3 | Smectite, Quartz, Magnetite, Chlorite, Biotite |
| 2-4 | Smectite, Quartz, Chlorite, Magnetite, Biotite |
| 2-5 | Biotite, Magnetite |
| 2-6 | Smectite, Magnetite, Chlorite |
| 2-7 | Biotite, Quartz, Chlorite, Magnetite |
| 3-1 | Smectite, Calcite, Chlorite, Quartz, Magnetite, Biotite, Talc |
| 3-2 | Chlorite, Smectite, Quartz, Calcite, Biotite, Magnetite |

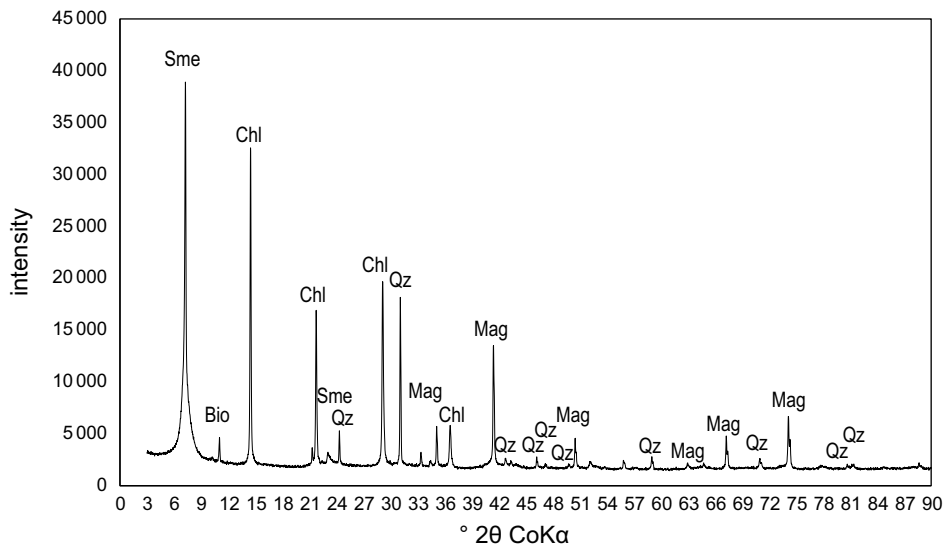


Figure 4-5. XRD results (random oriented sample) for KINA 3-1.
 Bio: Biotite, Ca: Calcite, Chl: Chlorite, Mag: Magnetite, Qz: Quartz, Sme: Smectite

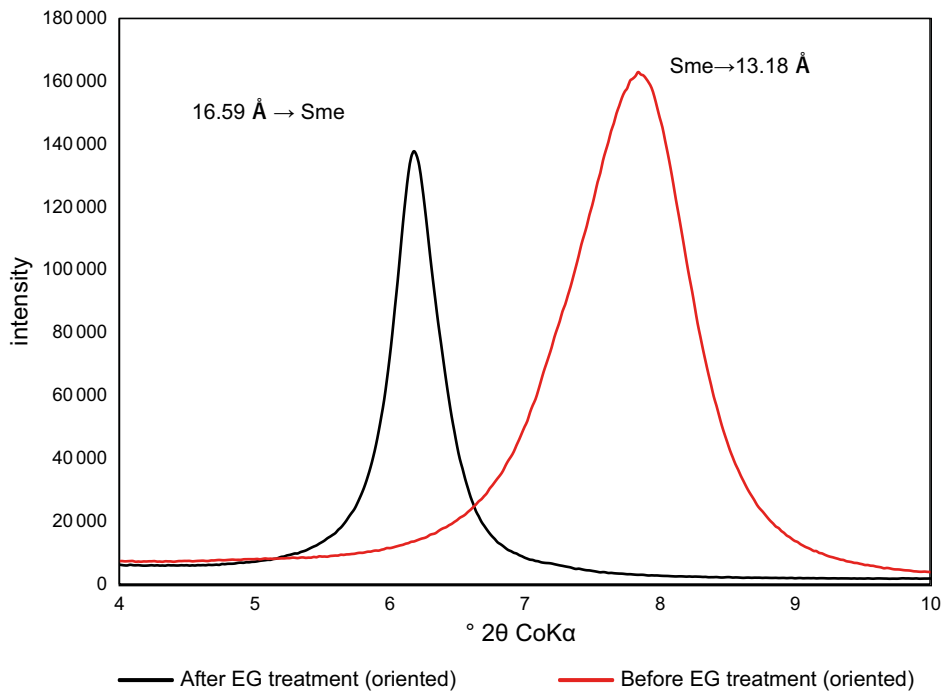


Figure 4-6. XRD results before and after EG treatment (oriented sample) for KINA 3-1.

4.4.3 SEM-EDS observation and analysis

Figure 4-7 presents SEM images of sample KINA 2-2, showing that the magnetite is present as an agglomerate of individual particles or grains. Figure 4-8 shows SEM images of sample KINA 2-3 (magnetite particles in smectite) and Figure 4-9 shows the results of elemental mapping analysis by EDS (carried out on the area framed in red and confirming the smectite identification). Figure 4-7 shows that, in the sample measured in this study, the surface of the magnetite was covered with biotite, and there were few interfaces where the smectite and magnetite were in direct contact. In addition, as is evident in Figure 4-9, despite the direct contact between magnetite and smectite, the iron content in the smectite was low and no significant changes were observed in the clays.

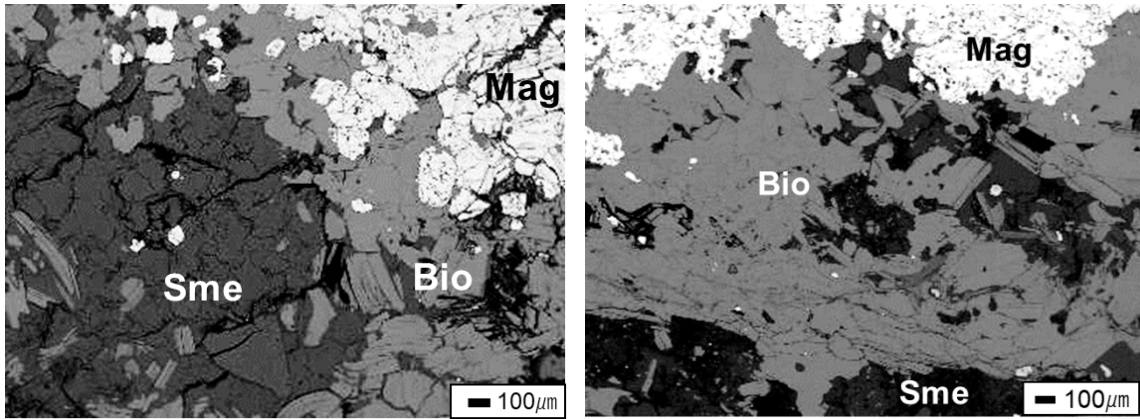


Figure 4-7. SEM observation image for case A (sample KINA 2-2). Mag: Magnetite, Sme: Smectite, Bio: Biotite.

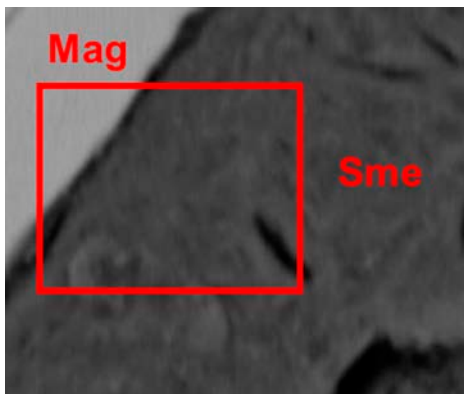


Figure 4-8. SEM observation image for case B (sample KINA 2-3). Mag: Magnetite, Sme: Smectite.

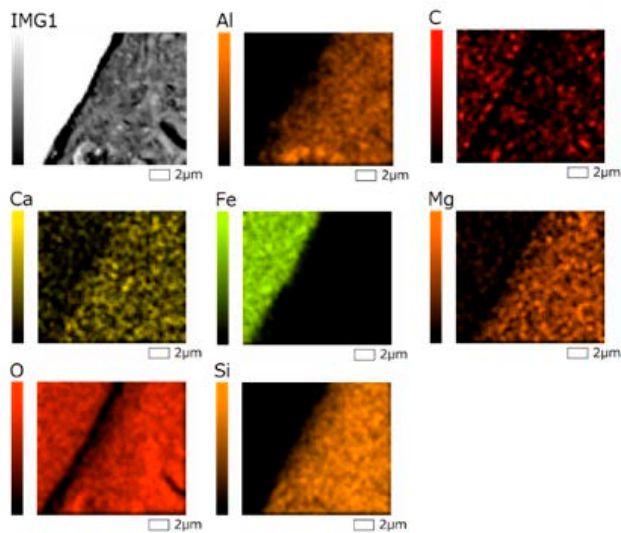


Figure 4-9. Elemental mapping analysis Results for case B (sample KINA 2-3).

4.4.4 FE-EPMA observation and analysis

Figure 4-10 shows an example FE-EPMA image of sample KINA 2-3 which confirms the presence of smectite and magnetite. Elemental mapping analysis by EPMA was carried out on the area framed in red and the results are shown in Figure 4-11. As with the observations in Section 4.4.3, the iron content in the smectite was low and no change was observed in the smectite, despite the direct contact between magnetite and smectite. Other similar interfaces were investigated and all indicated a low iron content in the smectite.

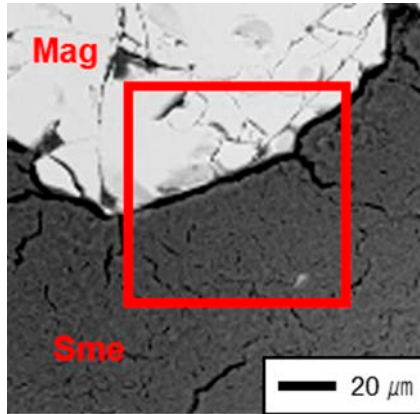


Figure 4-10. FE-EPMA observation image for case B (sample KINA 2-3).

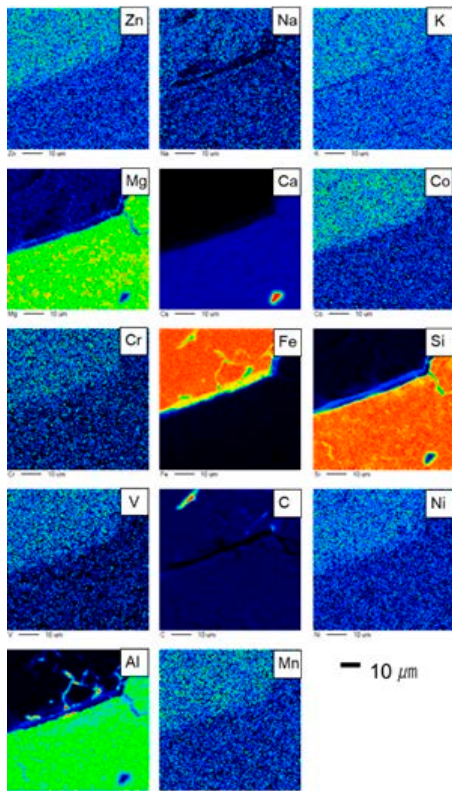


Figure 4-11. Elemental mapping analysis results for case B (sample KINA 2-3). Sme: Smectite, Mag: Magnetite.

4.4.5 Trace Element Analysis of Magnetite

The total Al and Mn content in magnetite is plotted against the total Ti and V content in Figure 4-12. The majority of the analytical results for magnetite grains in clay plot in the fields of IOGC (iron oxide gold copper), Kiruna and Porphyry types. Approximate formation temperatures of the magnetite are indicated in Figure 4-12b: some samples plot in the light green zone at 200-300 °C, but most of them plot in the region of 300–500 °C (orange symbols) and a few over 500 °C (brown symbols).

4.4.6 Dating of major minerals

Table 4-3 shows the K-Ar dating results for smectite and biotite in contact with magnetite. In the present measurement range, the K-Ar age of biotite in sample KINA 2-1 was 812 ± 15 (Ma). In addition, the K-Ar age of the smectite in sample KINA 3-2 is 352 ± 17 (Ma) and the biotite is 1012 ± 17 (Ma).

Table 4-3. K-Ar dating results for samples KINA 2-1 and KINA 3-2.

| KINA sample No. | Minerals (Elutriation particle size) | K content (wt. %) | Radiogenic ^{40}Ar (10^{-8}cc STP/g) | Age (Ma) | Non-radiogenic ^{40}Ar (%) |
|-----------------|--------------------------------------|-------------------|--|---------------|-------------------------------------|
| 2-1 | Biotite (50–120 μm) | 7.648 ± 0.153 | 30451 ± 301 | 812 ± 15 | 0.02 |
| 3-2 | Biotite (75–120 μm) | 5.720 ± 0.114 | 30140 ± 297 | 1012 ± 17 | 0.03 |
| | Smectite (0.2–2.0 μm) | 0.066 ± 0.003 | 99.6 ± 1.7 | 352 ± 17 | 35.7 |

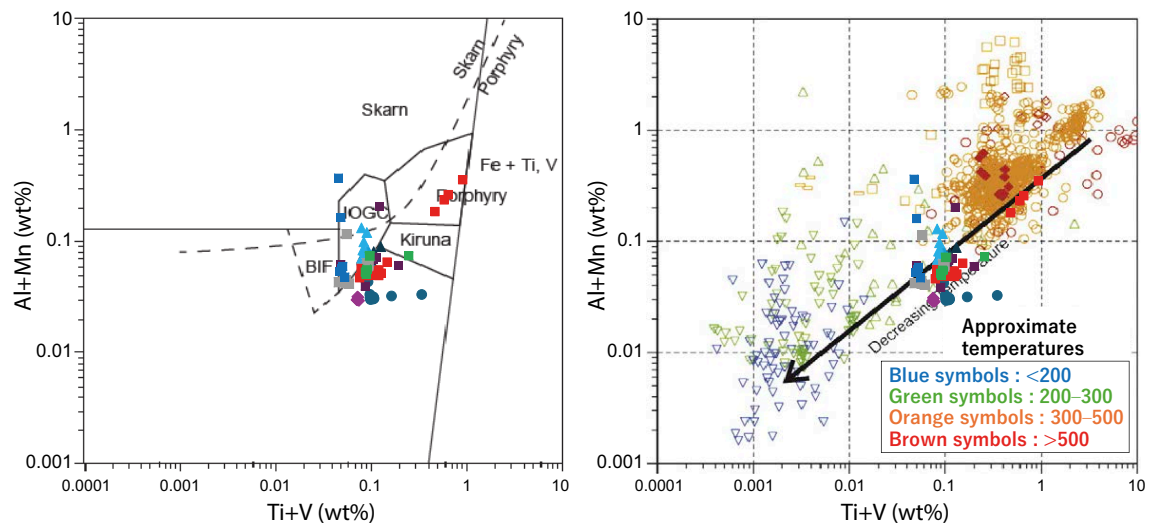


Figure 4-12. Discrimination diagram using trace element composition of magnetite with the trace element analysis results plotted in $(\text{Ti} + \text{V})$ vs $(\text{Al} + \text{Mn})$. After Nadoll et al. (2014). Note that the solid circles are the analytical results from this study, all other symbols are from Nadoll et al. (2014).

4.5 Discussion on magnetite-smectite interaction

4.5.1 Estimation of formation age of magnetite and clay

The formation age of the iron ore is thought to be c. 1.88 Ga (Westhues et al. 2016). From Section 4.4.6, the K-Ar age of biotite in sample KINA 2-1 is estimated to be 800 Ma, that of biotite in sample KINA 3-2 to be 1 Ga and that of smectite to be 350 Ma.

According to Armstrong et al. (1966), the K-Ar ages of biotite indicate a time when the temperature of the biotite-bearing rocks was around 325 to 350 °C. Smectite, however, generally forms at temperatures below 150 °C (Inoue, 1995), indicating a period of such hydrothermal activity. Several hydrothermal alteration events have been reported in the area where the samples were collected (see Section 2.1 and Yan et al. 2023b), and the present samples may also have been subjected to repeated hydrothermal alteration events.

Although it is necessary to increase the number of dated samples (of magnetite-smectite interfaces) in the future, at least biotite is considered to have formed before the smectite and not to have been formed during the reaction which produced the smectite.

4.5.2 Estimation of magnetite formation environment

(Ti + V) vs (Al + Mn) contents in magnetite grains in clay plot at approximate temperatures of 200–300 °C in the diagram after Nadoll et al. (2014), suggesting the formation temperature of the smectite-associated magnetite might be 200–300 °C. The formation temperature of magnetite in IOA (iron-oxide-apatite) ore deposits, similar to Kiirunavaara, is approximately 400 °C or higher (Troll et al. 2019; Palma et al. 2021). There are three possible reasons for the discrepancy of the formation temperature of magnetite calculated here and as reported for IOA deposits:

1. The here analysed magnetite was not present during the formation of andesite or rhyolite (the country rock and smectite source rocks), but may have been newly formed by hydrothermal activity during smectite formation.
2. The magnetite was originally contained in the andesite/rhyolite country rock (as is observed in places in the mine) but may have been altered by the hydrothermal activity involved in the smectite formation.
3. The method of estimating temperatures by using the method of Nadoll et al. (2014) is inappropriate.

To determine which of these is most likely, additional analysis of the trace element content of magnetite grains in the iron ore is required, as well as using additional methods to that of Nadoll et al. (2014). If smectite formed before magnetite formation, illitisation of smectite could occur (Inoue, 1995). If so, it could be concluded that smectite was formed after formation of magnetite or post-alteration of magnetite. However, without any further information, the precise sequence of formation currently remains unclear.

4.5.3 Formation environment and time transition of magnetite-smectite and discussion on formation process of magnetite-smectite

Based on the above discussion, the thermal history of the clay samples analysed here is illustrated in Figure 4-13. Magnetite in the iron-ore deposit formed at 400 °C or higher, while the magnetite grains dispersed in the clay formed at lower temperatures, 200–300 °C. The temperature of the samples containing biotite decreased to 300 °C, the closure temperature of biotite (Armstrong et al. 1966), at around 0.8 Ma to 1 Ga. Clay may be formed by hydrothermal fluids below 150 °C around 350 Ma based on the K-Ar dating of smectite reported here (but see also Chapter 3). After the formation of smectite, hydrothermal activity is considered to have never exceeded 150 °C. Note that this compares with the existing work of Gilg et al. (2022) where, based on combined stable H and O isotopic compositions of montmorillonites from Kiruna, an equilibration temperature of 20 to 40 °C is indicated and this is assumed to have occurred with waters on the GMWL that are significantly isotopically heavier than present-day and Tertiary meteoric water compositions.

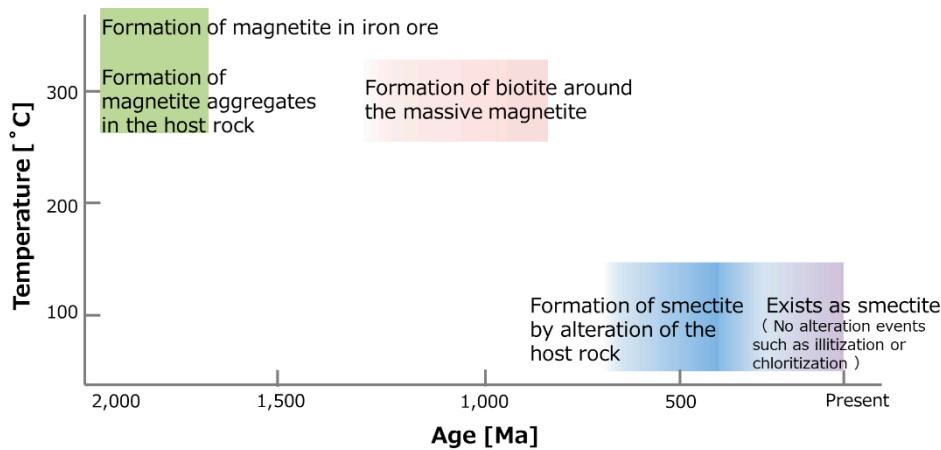


Figure 4-13. Formation environment and time transition of magnetite-smectite.

4.6 Discussion on the formation process of the magnetite-smectite interface

The formation process of the two different magnetite-smectite interfaces in the Kiirunavaara mine can be broadly classified into the following two cases:

Case A: the magnetite aggregates in the iron ore were probably pre-existing in this case, and then the clay may have formed by hydrothermal alteration of the trachyandesite or rhyolite, at temperatures as low as 150 °C. The magnetite aggregates and clay might be then be physically in contact. However, what kind of physical events such as fluid fracturing or faulting is unknown.

Case B: the magnetite aggregate existed in the original host rock (trachyandesite or rhyolite) and then clay formation occurred later by altering the host rock by low-temperature (lower than 150 °C) hydrothermal activity. The magnetite aggregates and clay would then be physically in contact as the secondary clays formed around the existing magnetite aggregates.

The formation processes of these interfaces need to be considered further in future with additional observation and analysis of the interfaces in addition to detailed outcrop observations.

4.7 Conclusion

4.7.1 Overview

These preliminary results suggest that magnetite and smectite have been in direct contact at a temperature of less than 150 °C for an extended period of time (ca. 350 Ma). However, since these conclusions are based on a limited number of samples and analyses, further examination of the contact zone between the iron minerals (e.g. pyrite in addition to magnetite) and smectite in samples newly collected from the Kiruna mine on 4–5th May 2023 is ongoing and will be reported in due course. Nevertheless, it is remarkable that the clays examined to date are effectively iron-free.

4.7.2 How to proceed with future studies

The interface between magnetite and clay can be classified into at least two types. Although this study was mainly concerned with Case B in Section 4.6, in which magnetite is dispersed in smectite, it is planned to conduct further research on

- the interface in Case A,
- the interface between smectite and other iron-bearing minerals such as pyrite and biotite,
- the duration of contact between iron minerals and smectite,
- further define the environment during the reaction of magnetite-smectite,
- the relationship between geological structures and the ages of smectite, biotite and magnetite (including a detailed consideration of the existing data in Chapter 3),
- the site hydrogeochemistry¹³, including the composition of hydrothermal water by analysis of fluid inclusions,
- the temperature history of the site using additional geothermometer phases,
- reaction mechanisms at the magnetite-smectite interface by geochemical modelling of the so produced data.

¹³ Unpublished preliminary LKAB data make it clear that, as in most mines the current groundwaters represent a mixture of groundwaters and meteoric waters in a system which has been disturbed for the last 120 years. As such, a detailed study of the site hydrogeochemistry would be a significant future use of resources.

5 Microbial metabolic potential in a natural clay analogue for deep geological radioactive waste repositories

Rizlan Bernier-Latmani and Natalia Jakus

5.1 Introduction

Generally, it is assumed (cf. King et al. 2023) that microbial activity in the EBS bentonite can be excluded on the basis that it will be suppressed by the highly compacted nature of the buffer. Nevertheless, it is well documented (e.g. Bagnoud et al. 2016; Beaver et al. 2022; Mitzscherling et al. 2023) that clays, including natural bentonites, contain microorganisms but there is little information about whether these microorganisms would survive in the clay for the extended period of time (thousands to hundreds of thousands of years) of relevance to a repository safety case.

The Kiirunavaara mine includes clays (dominated by smectites, see chapters 3 and 4 formed *in situ* as transformation and neof ormation products within the magnetite ore and the country rock. They occur to depths of more than 1 000 m below surface and appear to have formed > 100 Ma ago (see Chapters 2–4). As a direct natural analogy of the industrial (benefacted) EBS bentonite, this ancient smectite-rich clay provides an opportunity to investigate the microbial community, its metabolic potential and thus the potential long-term role microorganisms could have in the repository EBS (see also the discussion in Stroes-Gascoyne, 1989).

As such, the goals of this chapter are threefold:

- characterise the microbial community using DNA-based approaches (that access all microorganisms, live, dead, active and inactive),
- characterise the cultivable microbial community (present but not necessarily active),
- use tools which can assess ancient DNA to evaluate whether some of the community represents thousands or millions of years-old DNA (preserved in the clay) and evaluate their metabolic potential.

5.2 Methods

5.2.1 Drilling

The standard drilling methods applied to sampling clays for petrography and chemical analysis are unsuitable for microbiological applications. This limitation arises from the risk of losing the core integrity and introducing microbial contamination during the drilling process. This includes using drilling fluid and non-sterile equipment, which can carry microbial cells into the sampled material. This issue is particularly concerning in the case of the Kiirunavaara clays, given the already likely low biomass in the rock. In a test phase, drilling was initially performed by conventional methods and was unsuccessful (see also the discussion in Reijonen and Alexander, 2024 on appropriate methods for bentonite sampling). As such, Nagra (Rene Dorrer and Raphael Schneeberger) developed in collaboration with EPFL a hand drilling method to collect intact clay cores with minimal disturbance (Figure 5-1a). In addition, in an attempt to track drilling-induced microbial contamination, fluorescent particles (0.25–0.45 μm) were applied to the surface of the clay prior to drilling (Figure 5-1b).

The short cores (of three different coloured clays, see Figure 5-2) were collected under the most sterile conditions possible in the working mine. Drilling rods and the core barrels were sterilised, the drillers wore gloves and masks (Figure 5-1a), the cores were processed quickly by placing them in sterile bags and preserved under anoxic conditions and stored at less than 4 °C. Samples were shipped maintaining anoxic conditions and at a recommended temperature of 4 °C to the laboratory immediately after all the material was collected (maximum 4 days after the collection of the first sample).



Figure 5-1. a) hand drilling short cores for clay samples, b) fluorescent tracer applied to the surface of the clay at the drilling location.

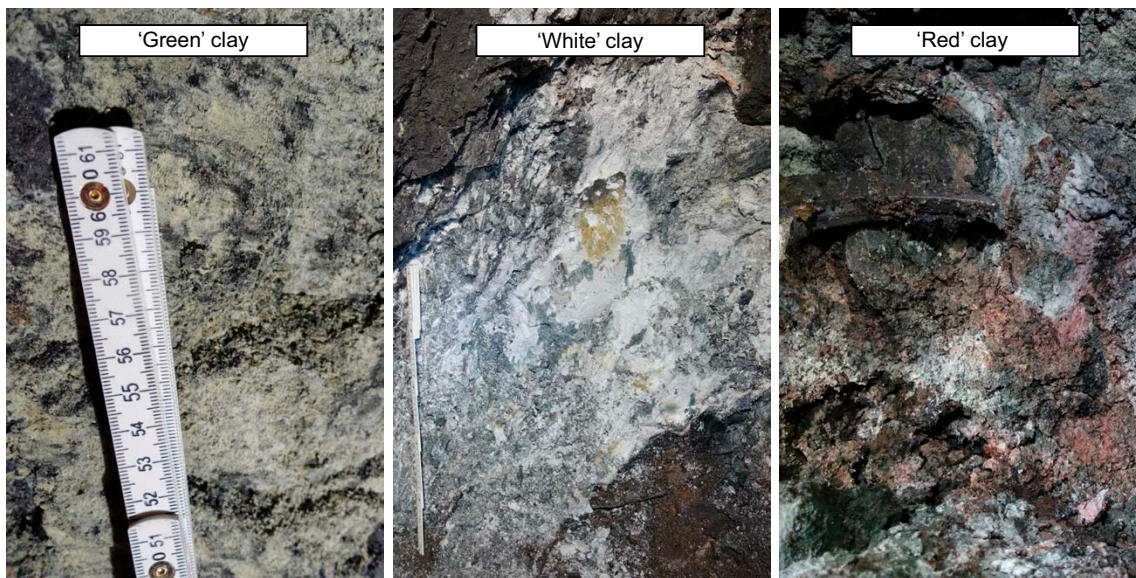


Figure 5-2. Three sites were sampled: 307-1165 (green clay), 405-1194 (white clay), and 307-1223 (red clay).

5.2.2 Sample handling

Following transport of the drillcores, the clay cores were removed from the core barrels under sterile conditions in the lab using a lever press and a custom designed plunger that allowed for core extraction while maintaining the intact structure of the core. In a sterile laminar flow hood, the extracted cores were sectioned and only the inner part of the core was collected to target only the microorganisms associated with the undisturbed clay. All samples were carefully checked for contamination by assessing the spatial distribution of the fluorescent particles using flow cytometry (see McKinnon, 2018, for details). The use of cytometry for separating clay particles from the fluorescent tracer was developed for this project and is a novel strategy that required significant optimisation of the entire workflow.

5.2.3 Microbial cultivation

Microbial cultivation was initiated for sample 307-1223. 2.9–3.2 g of clay (as obtained) were suspended in 25 mL of artificial freshwater medium modified after Ehrenreich and Widdel (1994) containing 0.6 gL⁻¹ potassium phosphate (KH₂PO₄), 0.3 gL⁻¹ ammonium chloride (NH₄Cl), 0.5 gL⁻¹ magnesium sulphate (MgSO₄·7H₂O) and 0.1 gL⁻¹ calcium chloride (CaCl₂·2H₂O). The medium was buffered at pH 7.0–7.1 with 22 mmolL⁻¹ bicarbonate and with addition of 1 mL⁻¹ trace element solution (Tschech and Pfennig, 1984), 0.1 mL⁻¹ selenate–tungstate solution (Widdel, 1980) and 1 mL⁻¹ sterile filtered vitamin solution (Widdel and Pfennig, 1981). Bottles were closed with butyl-rubber stoppers and crimped, and the headspace was flushed with N₂/CO₂ (90:10).

Based on knowledge of the site, conditions were selected for autotrophic and heterotrophic growth (Table 5-1). In particular, the electron donors selected for autotrophic growth were H₂ and CH₄ (presumed to be from geogenic origins at the site), sulphide and ferrous iron (potentially present in the clay, see Chapter 5). The serum bottles were stopped and crimped and allowed to incubate at room temperature in the dark and transferred to fresh medium every 2 to 3 weeks. Heterotrophic growth was stimulated with acetate as the electron donor (and carbon source) including H₂, Fe(II), or no amendment and lactate.

Table 5-1. Combinations of electron donors and acceptors used in the enrichment cultures.

| | | Autotrophic | | | | Heterotrophic | | | |
|----------------|-------------------------------|-------------------|-----------------|-------------------|------------------|-------------------|--------------------------|----------------------------|---------|
| | | electron acceptor | | | | electron acceptor | | | |
| | | H ₂ | CH ₄ | Na ₂ S | Fe ²⁺ | acetate | acetate + H ₂ | acetate + Fe ²⁺ | lactate |
| electron donor | CO ₂ | | | | | | | | |
| | SO ₄ ²⁻ | | | | | | | | |
| | Fe(III) | | | | | | | | |
| electron donor | C _{org} | | | | | | | | |
| | SO ₄ ²⁻ | | | | | | | | |
| | Fe(III) | | | | | | | | |
| electron donor | NO ₃ ⁻ | | | | | | | | |
| | | | | | | | | | |

5.2.4 Ancient DNA extraction

To extract DNA from clay samples, a protocol that was originally designed for recovering ancient DNA from dental calculus (Dabney et al. 2013) was used and adapted for work with extracellular DNA from deep limestone aquifer (Wegner et al. 2023). Here, the protocol was further modified to allow for working with smectite-rich clays which, due to their swelling properties, differ in from processing non-swelling rock samples such as carbonates. First, to target microorganisms associated strictly with clays and reduce the possibility of modern environmental DNA contamination, 2.0 g of rock powder was extracted using a sterile stainless-steel cylinder from the inside of the core collected in the field. Clay sub-samples were then decalcified to liberate all DNA fragments that could be trapped by carbonates (2.1–5.8 wt% in these samples) present in the clays by immersing samples in EDTA (pH 8.0) and rotating them for 7 days at room temperature until the carbonates were dissolved. Samples were then concentrated using Amicon® ultra centrifuge filter units (MWCO 30 kDa and 10 kDa) and DNA was extracted by adding 1 mL of extraction buffer (EDTA pH 8.0, 0.45 M; Proteinase K 0.025 mgmL⁻¹) and then rotated overnight. Over the few next days, samples were centrifuged and subsequently mixed with binding buffer (guanidine hydrochloride, 4.77 M; isopropanol, 40 % [v/v]) and 400-µL sodium acetate (3 M, pH 5.2). After that, the samples were transferred to a high pure extender assembly from the High Pure Viral Nucleic Acid Large Volume kit (Roche, Mannheim, Germany). DNA was purified using the column assembly and tubes together with the wash buffer provided with the kit. Finally, DNA was eluted into a silicon tube by adding elution buffer (containing 0.04 % Tween 20 in 1 × Tris–EDTA [pH 8.0]). The elution step was repeated once and the pooled eluate was stored at –20 °C until further processing. All outlined steps were carried out in a sterile laminar flow hood using sterile clean-room grade disposable plasticware. Additionally, protective sleeves and mask were worn throughout the process to further minimise the risk of contamination. Blank extractions were carried out alongside the sample extractions, using identical steps, with the exception that water instead of clay was used as the input material. DNA concentrations were determined using a Qubit® fluorometer and the DNA high-sensitivity assay (ThermoFisher, Schwerte, Germany).

5.2.5 Mineralogical and microscopic characterisation

Sub-samples were sent to the James Hutton laboratory in Scotland and the results are presented in sections 3.4. Samples reported in Table 5-3 analysed by H.A. Gilg.

5.2.6 Organic matter content

Several sub-samples were analysed by the University of Toronto Scarborough, Canada, using the methods described in Usman and Simpson (2021) and Huan Tong et al. (2023) for natural organic matter (NOM), but with limited success. As the results (Table 5-2) show, some of the samples contained very little organic carbon (TC, TIC or TOC) and that was an issue for further analyses. For solid-state ¹³C NMR, the samples were digested to concentrate the organic matter so that it was detectable. This process, which uses both HCl and HF, works well for secondary clay minerals and evaporites but was much less successful in these clay-rich samples (cf. Section 3.2).

Some lipids were detected by gas chromatography – mass spectrometry (GC-MS) but very few and not enough to indicate the source of the NOM (terrestrial or aquatic, etc) as is generally the case when the organic carbon content is below trace level.

Table 5-2. Samples obtained by U.B. Andersson and EPFL in September 2021 and sent to NWMO for organic carbon analysis (TC, TIC and TOC data from University of Toronto Scarborough). Sample locations in Appendix B.

| Sample Description, LKAB ID and sampling date | Listed mass (kg) | Actual mass received (kg) | TC (%) | TIC (%) | TOC (%) |
|---|------------------|---------------------------|--------|---------|---------|
| Clay + Ore, 307-1165, 14/09/21 | 1.94 | 1.85 | 0.69 | 0.59 | 0.099 |
| Unconsolidated clay, 383-1165, 14/09/21 | 1.70 | 1.60 | 0.33 | 0.32 | 0.005 |
| Unconsolidated clay, 306-1165, 14/09/21 | 0.72 | 0.69 | 1.51 | 1.51 | 0.005 |
| 9.95 kg Clay, 302-1165, 14/09/21 | 3.10 | 2.92 | 1.04 | 1.03 | 0.011 |
| Clay vein 1 (white), 386-1194, 16/09/21 | 1.00 | 0.88 | 1.08 | 1.05 | 0.024 |
| Clay vein 2 (red), 386-1194, 16/09/21 | 1.36 | 1.28 | 3.77 | 3.53 | 0.241 |
| Clay vein 3 (black), 386-1194, 16/09/21 | 1.37 | 1.30 | 1.51 | 1.47 | 0.036 |

5.2.7 Iron content

The clay samples were subjected to chemical extraction to differentiate and quantify iron pools based on their reactivity and crystallinity following a digestion protocol after Moeslund et al. (1994). Briefly, less crystalline and, in general, more bioavailable mineral phases like Fe(III) (oxyhydr)oxides were extracted by incubation of the clay in 0.5 M HCl at room temperature for 1 hour. To extract more crystalline iron phases, such as poorly reactive sheet silicate Fe, Fe_xS_x species or magnetite, clay samples were subjected to 6 M HCl extraction at 70 °C for 24 hours. Both incubations were carried out under anoxic conditions using degassed acid and acid-washed glass vials closed with butyl septa in a glovebox purged with 100 % N₂ gas. Dissolved Fe(II) and Fe(III) were quantified using the ferrozine protocol (Stookey, 1970). The purple ferrozine-Fe(II) complex was quantified at 562 nm using a microtiter 96-well plate reader; all ferrozine measurements were done in triplicate. The data were then normalised to 1.0 g of dry clay.

5.3 Results and discussion

5.3.1 Solid phase characterisation

The three clay types were characterised with respect to their morphology, organic carbon content and mineralogy (with only the latter noted in Table 5-3). The mineralogy was surprisingly different for the three clay samples. Sample 405-1194 (40-white) contained, in addition to the dominant montmorillonite, 22.8 % of phlogopite, 10.7 % magnetite and 5.8 % calcite and less quartz than the other two clays. Sample 307-1223 (30-red) was characterised by a high titanite content (34.1 %), in addition to montmorillonite (47.1 %). Sample 307-1165 (30-green) included the most montmorillonite (67.6 %), but also the most chlorite (4.2 %) and some fluorapatite (1.5 %). Total organic carbon was very low in all cases (0.039–0.050 %) and total carbon (0.12–1.2 %) roughly reflected the calcite content. Both sample 405-1194 (40-white) and sample 307-1165 (30-green) are dominated mineralogically, by far, by clay (total clay content ~80 %). The sample 307-1223 (30-red) includes a substantial amount of titanite. But all three contain more than 50wt% of clay.

Table 5-3. Mineralogical content of the three analysed clay samples (in wt%). Sample locations in Appendix B.

| | | 405-1194 (white clay) | 307-1223 (red clay) | 307-1165 (green clay) |
|-----------------------------------|-----------------|--------------------------|------------------------|--------------------------|
| Phyllosilicates (clays, micas) | Montmorillonite | 56.3 | 47.1 | 67.6 |
| | Chlorite | 2.2 | 0.8 | 4.2 |
| | Phlogopite | 22.8 | 6.1 | 7 |
| Silicates | Quartz | 2.3 | 7.6 | 6.7 |
| | Titanite | - | 34.1 | 1.9 |
| Iron minerals | Magnetite | 10.7 | <1 | 7.0 |
| | Pyrite | - | <1 | - |
| Carbonates | Calcite | 5.8 | 2.3 | 2.1 |
| Phosphates | Fluoroapatite | - | - | 1.5 |

In addition, characterisation of iron content and speciation was performed (Figure 5-3). The extracted iron content was low when bioavailable iron was assessed (0.5 M HCl) with mostly reduced iron in sample 307-1165 (30-green) and more oxidised iron in sample 307-1223 (30-red). As expected, extraction of total iron (6 M HCl) confirmed the presence of more ferrous iron in sample 307-1165 (30-green) and more ferric in sample 307-1223 (30-red). Sample 405-1194 (40-white) contains the least iron and it is mostly in ferrous form.

The ferric iron content of sample 307-1223 (30-red) suggests the potential for iron reduction as a microbial metabolism.

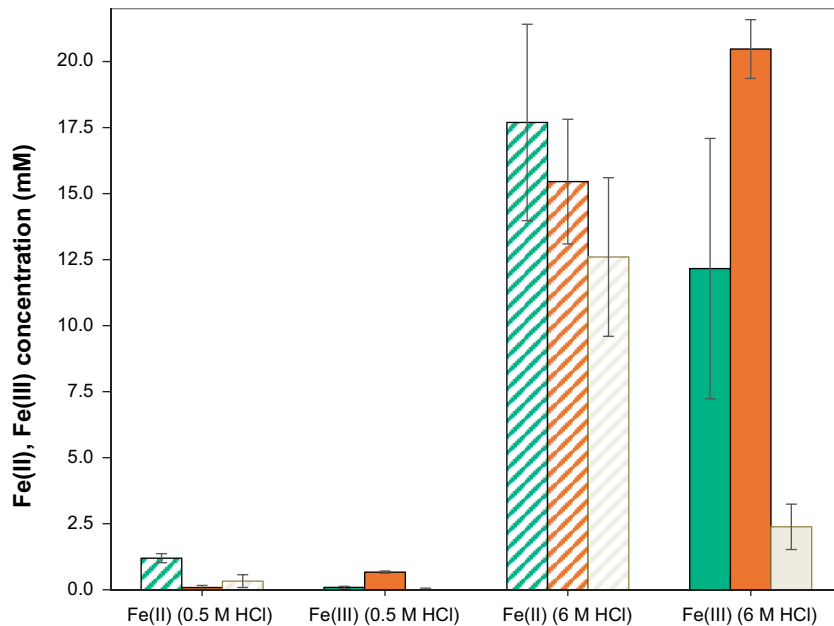


Figure 5-3. HCl extractable Fe (0.5M and 6M measured as ferrous or ferric Fe for the three types of clays. Figure colour coding is grayish white for sample 405-1194 (white clay), brown for 307-1223 (red clay) and green for 307-1165 (green clay).

However, the extractable iron results do not match with the mineralogy. Sample 405-1194 (40-white) contains the most iron (as magnetite) but, as expected, it appears that this mineral is not readily dissolved in 6 M HCl. Similarly, sample 307-1165 (30-green) has the next most magnetite but exhibits less extractable Fe than sample 307-1223 (30-red).

SEM images (Figure 5-4) show the characteristic structure of montmorillonite from sample 307-1223 (30-red) sample.

5.3.2 Microbial characterisation

Contamination of the cores was assessed using flow cytometry. Flow cytometry is a technique that works on the principle of light scattering and fluorescence emission by the specific fluorescent probe-labelled objects (e.g. particles or cells) as they pass through a laser beam. This approach allows the detection of the fluorescent particles (tracer) added to the rock surface prior to drilling (see Figure 5-1b). Only samples determined to be free of the tracer were considered free from any contamination and further processed. Figure 5-5 shows an example of the data for an uncontaminated sample (left) and a sample spiked with particles (positive control, right). It is very clear that the sample does not contain any fluorescent particles.

The microbial community was grown under the conditions detailed in Table 5-1. Growth was found under several heterotrophic conditions with sulphate, Fe(III) and nitrate as electron acceptors, suggesting that viable microorganisms are present in the clay. Activity of microbes was indicated by chemical analysis, namely: 3 mM of acetate and 4.5 mM of nitrate was depleted in nitrate-containing cultures, 3 mM of acetate was removed by cultures simultaneously grown on sulphate and H₂ and 2 mM of lactate was consumed by cultures incubated with Fe(III) in a form of synthetic ferrihydrite. The presence of viable and living cells was then additionally confirmed by microscopy observation. Figure 5-6 shows SYTO9-stained cells in a lactate and Fe(III) culture.

DNA was extracted using an ultra-pure protocol described in detail in the method section derived from the ancient DNA research field (modified from Mann et al. 2018 after Dabney et al. 2013) and is compared to that in MX-80 industrial bentonite in Table 5-4.

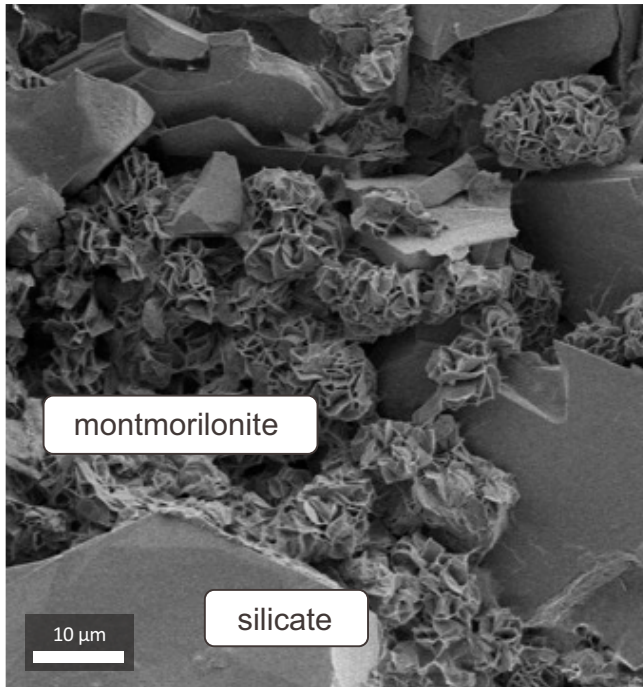


Figure 5-4. SEM of subsample from sample 307-1223 (30-red).

Table 5-4. Amount of DNA extracted from Kiruna sample 405-1194 (40-white) in comparison to the negative control (to check for contamination) and MX-80 industrial bentonite.

| Sample | DNA content (ngµl ⁻¹) |
|------------------------------|-----------------------------------|
| Negative control | <0.05 |
| MX-80 industrial bentonite | 0.151 |
| Kiruna 405-1194 (white clay) | 0.336 |

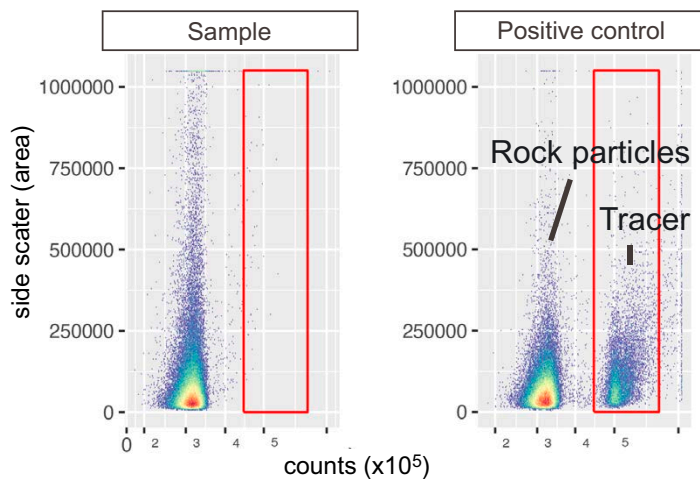


Figure 5-5. Flow cytometry results showing side scattering of a laser beam from all particles present in the sample against the count of the particles exhibiting fluorescence specific to the tracer used. The gate (red rectangle) indicates the area in which tracer particles could be detected (see the positive control spiked with the tracer in the figure on the right). No signal in the gate (left figure, sample) indicates that the sample is not contaminated.

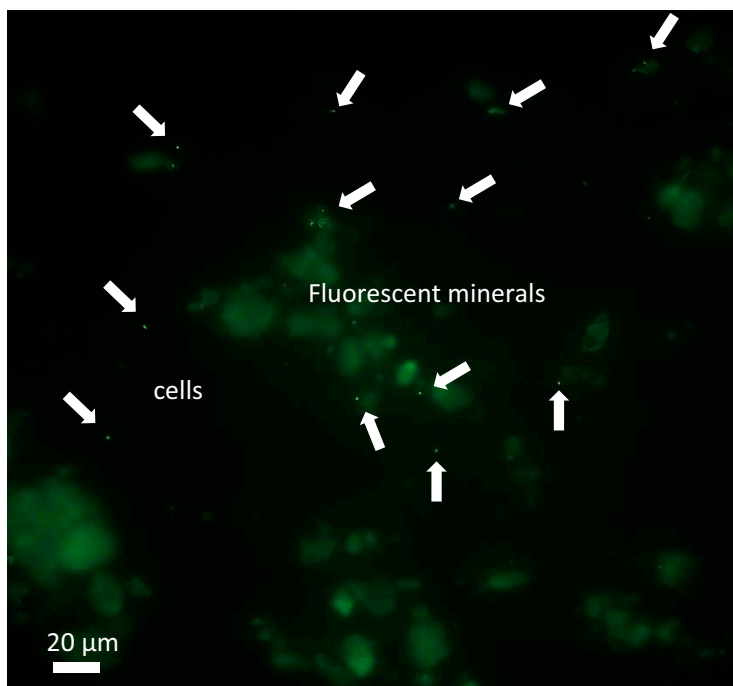


Figure 5-6. Optical microscopy of sample 405-1194 (40-white) incubated with Fe(III) and lactate and stained with SYTO 9. Arrows indicate cells stained with SYTO 9, indicating live cells.

5.4 Conclusions and future work

Extracting meaningful microbiological data from the Kiruna clay proved to be challenging and required the development of customised tools for the core drilling and handling and for DNA extraction. As such, the majority of the time to date was used developing these tools. Nonetheless, it was possible to establish the appropriateness of the methods and demonstrate the extraction of DNA and the cultivation of microorganisms. Ultra-pure DNA extraction provides the first evidence for the presence of biomolecules in clays from the Kiirunavaara area. Additionally, the cultivation-dependent study supports the existence of active microbial life related to Fe(III), NO_3^- and SO_4^{2-} metabolism with low molecular weight organic acids (acetate and lactate). These organic carbon-based metabolic pathways could be supported by the traces of organic carbon detected in the clay.

The data collected to date form the basis for additional work to extract DNA from more samples and for characterisation of DNA damage patterns that would allow estimation of the proportion of contemporary vs. ancient DNA. Amplicon sequence analysis for marker genes (16 S rRNA) and functional genes will allow quantification of the microbial community composition and to obtain insight into the metabolic potential of the community.

Furthermore, using a combination of NanoSIMS and FISH (fluorescence in situ hybridisation), it is intended to identify which organisms are active under heterotrophic conditions and, if the autotrophic cultures show activity, under autotrophic conditions.

6 Erosion properties of the clay from the Kiirunavaara mine

Patrik Sellin and Daniel Svensson

Colloid formation and subsequent erosion and mass loss during conditions when very dilute groundwaters enters the repository is a safety relevant issue in repositories in fractured rock (Sellin and Leupin, 2013). Here, in an attempt to better understand bentonite erosion processes (in particular clay stability versus colloid formation), the behaviour of Kiruna clay is compared to that of industrial bentonite.

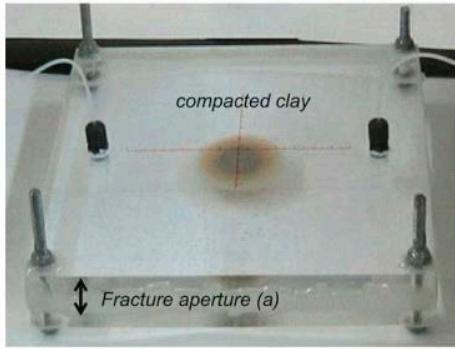
The expansion and erosion properties of the Kiirunavaara clay have been tested in a laboratory set-up with artificial fractures (Figure 6-1). The samples used were from the same batch as those denoted “Kiruna 2018” in Section 3.7. Results from an expansion test can be seen in Figure 6-2. The Kiirunavaara clay shows almost no expansion into the artificial fracture and no erosion/sedimentation behaviour whatsoever. This is in sharp contrast to all tested industrial (i.e. benefacted) bentonites – as shown for the BaraCade bentonite in Figure 6-1. As seen in Table 6-1, these Kiruna clay samples contain no sodium. A pure Ca-smectite should be resistant to colloid formation. Prior to the erosion tests, the Kiruna clay was ion-exchanged with sodium. The ion-exchange may, however, have been incomplete or insufficient, which may explain the unexpected behaviour.

Additional attempts were made to ion-exchange these smectite samples into a sodium form (see Table 6-1). Samples of the clay were washed three times with a 3 M NaCl solution (dispersed-centrifuged-decanted; each dispersion step > 1 h), dried and dialysed to remove excess salt. Elemental composition of the treated samples with XRF showed that there was no sodium at all in the clay (below detection limit). It appears that it was impossible to ion-exchange these Kiruna clay samples into even a partial sodium form in a dispersed system. A possible explanation for this could be the relatively high content of calcite in the material. The smectite exchanges as expected with the Cu-Trien in the determination of cation exchange capacity.

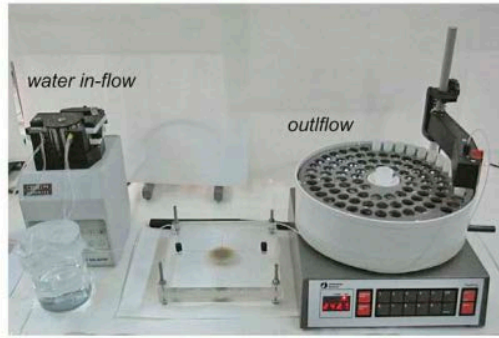
Table 6-1. Results of the ion-exchange experiments carried out on sample “Kiruna 2018 c65ef8” (methods described in Svensson et al. 2019). Note that the sample in row 1 is Kiruna montmorillonite 30-1138-F3032 (which was supplied by LKAB). Locations in Appendix B.

| Ident | Time | Na ₂ O | MgO | Al ₂ O ₃ | SiO ₂ | Cl | K ₂ O | CaO |
|--|------------|-------------------|-------|--------------------------------|------------------|-------|------------------|--------|
| Kiruna montmorillonit 30-1137-F3032 | 5/31/2018 | 0.000 | 4.656 | 21.048 | 63.407 | 0.004 | 0.202 | 6.887 |
| Kiruna repeat | 5/31/2018 | 0.000 | 4.630 | 20.990 | 63.194 | 0.004 | 0.201 | 7.099 |
| Kiruna II | 5/31/2018 | 0.000 | 4.625 | 21.036 | 63.309 | 0.004 | 0.205 | 6.872 |
| Kiruna bentonit ion-exchanged dialysed 190314 – I | 3/15/2019 | 0.011 | 3.196 | 20.542 | 54.308 | 0.001 | 0.945 | 15.852 |
| Kiruna bentonit ion-exchanged dialysed 190314 – II | 3/15/2019 | 0.006 | 3.300 | 21.459 | 56.582 | 0.005 | 0.777 | 13.443 |
| Kiruna bentonit raw 38/1165m 190314 – I | 3/15/2019 | 0.000 | 3.331 | 21.824 | 58.755 | 0.050 | 3.163 | 9.504 |
| Kiruna bentonit raw 38/1165m 190320 – I | 3/21/2019 | 0.000 | 3.365 | 21.925 | 58.789 | 0.042 | 3.128 | 9.399 |
| Kiruna Erosion Project c65ef8 #9 | 10/25/2022 | 0.000 | 3.492 | 22.440 | 58.044 | 0.004 | 0.749 | 11.536 |
| Kiruna Erosion Project c65ef8 B #9 | 10/25/2022 | 0.000 | 3.580 | 22.489 | 58.410 | 0.007 | 0.747 | 11.033 |
| Kiruna Na2 exchanged | 12/14/2022 | 0.574 | 2.918 | 19.021 | 50.072 | 0.022 | 1.237 | 21.593 |
| Kiruna Na1 exchanged | 12/14/2022 | 1.095 | 3.233 | 22.245 | 57.834 | 0.234 | 0.820 | 11.318 |
| Kiruna Sr exchanged | 12/14/2022 | 0.000 | 2.547 | 18.978 | 52.769 | 0.080 | 0.770 | 5.630 |
| Kiruna Li exchanged | 12/14/2022 | 0.798 | 3.045 | 21.411 | 56.383 | 0.052 | 0.855 | 13.738 |
| Kiruna K exchanged | 12/15/2022 | 0.000 | 2.480 | 16.116 | 41.875 | 0.020 | 5.288 | 29.192 |
| Kiruna 2018 Na dialysed c66039 210614 | 12/15/2022 | 0.000 | 3.274 | 22.071 | 57.993 | 0.015 | 0.923 | 12.346 |

a) Artificial narrow fracture

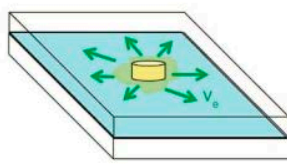


b) Experimental set-up



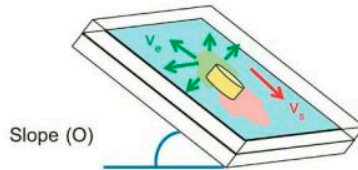
c) Erosion tests

1) Expansion



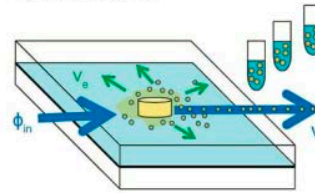
v_e : expansion rate

2) Sedimentation



v_s : sedimentation rate

3) Erosion by flow



ϕ_{in} : Flow, v_e : eluted mass rate

Figure 6-1. Experimental set-up of the erosion tests.

The overall conclusion is that no chemical erosion through colloid formation, or sedimentation, will take place in the Kiruna smectite samples analysed here. Another possible conclusion is that it is unlikely that the in-situ smectites analysed here have ever been exposed to Na-rich dilute groundwaters. The amount of calcite present in the material has been sufficient to buffer the composition of the exchanger to a 100 % calcium form for as long as the clay was (possibly last) transformed¹⁴. However, as noted in Section 3.2.4, some Kiruna clay samples may have been exposed to shallow weathering processes. Further, as noted in Section 3.2.5, some of the Kiruna clays (e.g. sample KI-02 from the shallowest alteration zone investigated in the footwall trachy-andesite), "...has an unusual Na-K-dominated interlayer cation composition that can only be explained by a local cation exchange reaction with Na- and K-rich waters."

In any case, there are a few remaining questions:

1. Are the ion-exchange properties of the Kiruna smectite samples examined here, especially regarding sodium, different than that of other smectites? Or is the difficulty to exchange it into a sodium form only related to the calcite content? According to Itälä (2018) and Kaufhold et al. (2023), it is likely the latter.
2. If the calcite content is the reason for the lack of sodium exchange, has the role of calcite as an accessory mineral been underestimated in the erosion estimates in the past? The results produced here may simply be an artefact of the particular samples examined, but soil erosion studies suggest that calcite may have a role to play in reducing bentonite erosion (cf. Shourijeh et al. 2020).
3. Can the calcium content in the smectite in Kiruna actually indicate anything about the evolution of the groundwater composition over time at the Kiirunavaara site?

¹⁴ As noted in Section 3.2.5, the ancillary calcites in the clays are extremely fine-grained and, with one exception, sample KI-04 from the ore zone, not residual phases from the altered country rock, nor co-genetic with smectitisation. They probably formed by a relatively late secondary process that has overprinted most clays in the Kiirunavaara mine.

In conclusion, on the basis of the examination of the few samples analysed here, the Kiruna smectite seems to be more stable than industrial bentonites with regards to colloid formation/erosion. The reason for this is not yet understood, it could be a function of the smectite itself, or it may be due to the high intrinsic calcite content of these particular samples, and further analyses are needed to define this point.

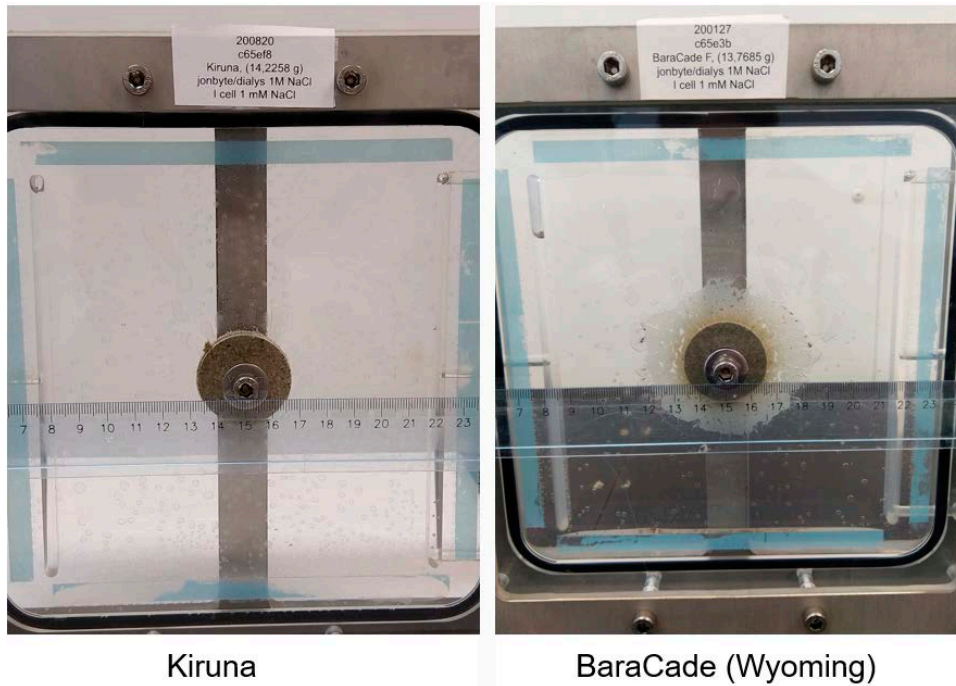


Figure 6-2. Expansion into an artificial fracture by Kiruna clay (left) and BaraCade bentonite (right).

7 Conclusions

W. Russell Alexander

7.1 Introduction

As introduced at the beginning of the report (Section 1.1.2), the aims of the project were:

- examination of potential long-term iron oxide minerals – bentonite interaction (as may occur in a repository EBS),
- understanding the very long-term behaviour of bentonite under conditions of direct relevance to deep geological disposal of radioactive waste,
- the potential for erosion of the bentonite barrier by groundwater in a deep geological repository,
- the potential impact of microbial populations in bentonite under repository conditions.

Here, these are examined one-by-one. However, before moving on to the particulars, it is worth mentioning a major external influence on the project, namely the COVID pandemic. It is important to note here that the results produced to date have been significantly affected by the severe constraints imposed on sample availability by the travel and work restrictions imposed due to the pandemic just as the KINA project was launched. In the first instance, this meant that the only samples available for most of the project duration were those collected during a reconnaissance campaign in the mine in September, 2019. As these were simply meant to provide background information and prove if the site was fit-for-purpose, they were by no means collected with the project-specific aims in mind and this has had an undeniable impact on the project output (see further comments below). Second, the two, focussed, sampling campaigns¹⁵ carried out in the mine post-pandemic clearly post-date the main period of analytical effort and this means that the data subsequently produced will only be available post-project reporting.

Keeping these points in mind, the project output to date will now be examined.

7.2 Examination of potential long-term iron oxide minerals – bentonite interaction

The mineralogical and chemical studies presented in Section 3.2 show that the clay transformation (and, in places, probably neof ormation) in the Kiirunavaara mine is related to the formation of significant amounts (44 to 81 wt%) of a high-charge, predominantly cis-vacant, Fe-poor, montmorillonite with a generally Ca-rich exchangeable interlayer composition. No interstratifications with illite were detected by XRD analysis. The <0.02 µm fractions of the material from the clay transformation zones consist of smectite while coarser fractions (0.02 to 0.2 µm) may contain ancillary feldspar, mica or chlorite. The smectite compositions are similar in the transformation zone of the footwall and hanging wall volcanic rocks as well as within the ore.

In Section 3.3.4, smectite compositions calculated from results of the chemical composition of the Na-exchanged clay (<0.5mm) fraction, citrate-bicarbonate-dithionite extractable elements and mineralogical analyses from the clay fraction are all presented. The results in Table 3-10 show that the smectite in clay sample c65f8c is montmorillonite with a very low iron content but relatively high magnesium content in the octahedral layer and has the composition of $(\text{Na}_{0.06}\text{Ca}_{0.37}\text{Mg}_{0.07})(\text{Al}_{3.02}\text{Fe}_{0.05}\text{Mg}_{0.96})(\text{Al}_{0.08}\text{Si}_{7.92})\text{O}_{20}(\text{OH})_4$. The smectite is also relatively highly-charged, with a total charge of -0.93, similar to values encountered in Sardinian bentonites (see Kiviranta et al. 2018).

As noted in Section 3.2.5, based on previous general studies of the mine clay bodies, “The iron contents of the dioctahedral smectites show minor variations with Fe_2O_3 ranging from 0.93 to 2.46 wt.-% that are not related to the presence or absence of residual magnetite in the altered rocks or to proximity to magnetite ores.”

¹⁵ In May, 2022, for samples for microbiological analyses (see Chapter 6) and in May, 2023 for samples to assess iron-clay interaction (see Chapter 5).

In addition, although based on only a few samples, the preliminary results presented here suggest that the magnetite has not been destabilised during transformation of the host rock.

Further examination of the magnetite-clay interface is presented in Section 3.7.5 where it is noted that “While this indicates that the interaction between magnetite and Kiruna clay is weak, little more can be said for the moment as the degree of saturation of the clay and the likely Eh/pH conditions at the magnetite/clay interface are unknown.” And these points should be addressed in any further studies at the site.

Further, detailed, study of magnetite-clay interfaces presented in Chapter 4, fully support the above conclusions. Here, the preliminary results suggest that magnetite and smectite have been in direct contact at a temperature of less than 150 °C for an extended period of time (probably in the order of hundreds of Ma) and little or no uptake of Fe in the clay has been observed. Nevertheless, as noted above, as the samples analysed in the project to date were collected for broader assessment, this study currently continues, examining the material collected in the recent focussed sampling campaign of May, 2023. This information will subsequently be published elsewhere, but an example of the ongoing work is provided in appendix J. Finally, the presence of biotite in many samples has yet to be addressed. It is possible that magnetite has reacted with smectite to form a non-swelling phase (i.e. biotite) at relatively high temperature so preventing smectite incorporating iron.

7.3 Understanding the very long-term behaviour of bentonite under conditions of direct relevance to deep geological disposal of radioactive waste

7.3.1 Introduction

Although this may seem obvious in hindsight, one of the first targets of the project was to assess if the clays present in the mine were of relevance to repository safety cases. Of prime importance was the question ‘how closely analogous are the clays in the mine to the industrial bentonites which will be used in the buffer, backfill and seals in a repository?’ Are the mineralogy, general physico-chemical characteristics and age of the Kiirunavaara clay(s) directly relevant?

7.3.2 Mineralogy

As noted in Section 1.5 “...much is already known about the ore itself but, as the clay has no monetary value, it has been largely ignored to date.” As above, the existing evidence based on previous general studies of the mine clay bodies noted in Section 3.2.5 showed that “The mineralogical and chemical studies presented here show that deep clay transformation in the Kiirunavaara mine is related to the formation of significant amounts (44 to 81 wt%) of a high-charge, predominantly cis-vacant, Fe-poor, montmorillonite with a generally Ca-rich exchangeable interlayer composition. No interstratifications with illite were detected by XRD analysis.”

Further, as noted by GSU in Section 3.5.5:

- “Smectite (or a smectite-rich mixed layer illite-smectite for the fine fraction clay-sized separation) is the predominant clay in the Kiirunavaara mine samples. The Kiirunavaara mine smectites do not appear to have converted to significant amounts of illite-smectite (or to illite) since their formation.”
- Indicating the overall very long-term stability of the smectite in the deep Kiirunavaara mine.

With respect to the actual amount of smectite present, the results of new analyses reported in Chapter 3 are summarised in Tables 7-1a and 7-1b. Four analytical groups produced mineralogical data and here the TUM data are shown in red, Mitta in blue, SKB in purple and James Hutton in green.

Table 7-1a. Selected mineralogical data (wt %) from the TUM, Mitta and SKB analytical groups.

| Sample ID | KI-01 | KI-02 | KI-03 | KI-04 | KI-05 | c65f8c, bulk | Kiruna 2018 | Kiruna 2019 |
|--------------------|-------|-------|-------|-------|-------|--------------|-------------|-------------|
| Smectite | 46 | 44 | 47 | 62 | 79 | 61.2 | 80.7 | 58 |
| Calcite | 4 | 12 | 3 | 8 | 12 | | 17.4 | 1.1 |
| Quartz | 6 | 8 | 16 | 6 | 3 | 0.3 | 1.1 | 0.1 |
| Albite | 36 | 19 | 29 | 14 | | 33.6 | | 40.1 |
| Microcline | | 3 | | | | | | |
| Magnetite | 1 | 1 | <1 | 1 | | | 0.8 | 0.2 |
| Haematite | | | | | | | | |
| Pyrite | | <1 | | <1 | | | | |
| Rutile | | <1 | 1 | 1 | 3 | | | |
| Chlorite | <1 | 2 | | 1 | | | | |
| R3 I-S + Muscovite | | | | | | 2.4 (0.1) | | |

Table 7-1b. Selected mineralogical data (wt %) from the James Hutton analytical group.

| Hutton ID | 1346794 | 1346795 | 1346796 | 1346797 | 1346798 | 1346799 | 1346800 | 1346801 | 1346802 | 1346803 | 1346804 | 1346805 | 1346806 |
|----------------|-------------|------------|-------------|-------------|--------------------------|-----------------|-----------------|----------------|-----------------|------------------|------------------------|------------------------|------------------------------|
| KINA sample ID | 1. 385-1165 | 2. 30-1108 | 3. 381-1108 | 4. 378-1108 | 5. CHI-latitude 41 deg S | 6. KU-L-20.09-J | 7. KUJ-L-2008-1 | 8. KU-L-2006-1 | 9. KUJ-L-2008-2 | 10. KUJ-L-2004-1 | 11. Kiruna 2018 c65ef8 | 12. Kiruna 2019 c65f8d | 13. Kiruna 2019 solid c65ff9 |
| Smectite(Di) | 65 | 36.3 | 35.9 | 26.1 | 13.9 | 35.7 | 20 | 51.6 | 10.6 | 27.6 | 75.8 | 59.9 | 39 |
| Calcite | 5.2 | 3.9 | 3.3 | 10.6 | 0.1 | 1.6 | 37.7 | 7.5 | 1.1 | 14.6 | 13.8 | 2.1 | 1.8 |
| Quartz | 1 | 17.3 | 7 | 21.9 | 34.3 | 4.6 | 9.6 | 4.8 | 1 | 13.1 | 2.8 | 0.9 | 3.6 |
| Albite | nd | 33.9 | 40.5 | 28.9 | 0.5 | 50.4 | 4.6 | 27.9 | 53.2 | 25.3 | 0.1 | 32.7 | 50.5 |
| Microcline | 4.4 | 1.5 | 0.5 | 1.6 | 0.3 | 1 | 2.3 | 4.4 | 22.5 | 3.1 | 3.4 | 1 | 0.6 |
| Magnetite | 11.8 | nd | 0.3 | 4.1 | | 0.5 | 10.1 | 0.2 | 6.1 | 3.9 | 0.2 | 1 | 1 |
| Haematite | 0.3 | | 0.1 | 0.3 | 0.1 | 0.1 | 1.7 | 0.1 | 0.1 | 0.2 | 0.2 | 0.2 | 0.1 |
| Pyrite | 0.6 | 0.2 | | | | 0.3 | | | | | 0.1 | 0.2 | 1.8 |
| Rutile | 0.5 | 1.2 | | | | | | | | | | | |
| Chlorite (Tri) | nd | 1.2 | 0.6 | | 0.1 | 2.4 | 5.7 | 1.2 | | 1.6 | 0.2 | | |
| Mica(Tri) | 9.3 | 0.3 | 6.3 | 1.5 | n | 1.4 | 4.3 | 0.1 | 2.5 | 5.6 | | 0.2 | |
| Mica(Di) | 1.5 | 1.2 | 3.7 | 3.3 | 15.8 | 1 | 1.5 | 1.3 | 0.3 | 4 | 0.1 | 1.3 | 1.1 |

While it is clear from Appendix B that the samples represent a rather heterogeneous selection from across the mine, it is obvious that the majority are smectite-rich, reaching a maximum of 80.7 wt % smectite. Interestingly, in those samples with the markedly lower smectite contents (e.g. KINA-5, -7 and -9 in Table 7-1b), the residual phases represent a mix of quartz, calcite and albite (and dioctahedral mica in KINA-5). However, any future sampling campaigns can use this background information to collect wholly appropriate samples.

Care will, however, have to be taken during future clay sampling due to the seemingly ubiquitous calcite:

- in those cases when magnetite-bentonite reactions are the focus, care should be taken to avoid those clay zones particularly enriched with calcite (cf. sample Kiruna 2018 analysed in Chapter 6) as this would not be the case in most industrial bentonites considered as potential material for a deep geological repository. As noted in Section 3.2.5, the ancillary calcites in the clays are extremely fine-grained, are not residual phases from the country rock, nor co-genetic with the smectitisation process. They were probably formed by a relatively late secondary process that appears to have overprinted most clays in the Kiirunavaara mine to some degree
- in those cases where bentonite erosion is the focus, the results presented in Chapter 7 appear to indicate a possible relationship between bentonite erosional resistance and calcite content and this must be addressed during sampling

To place the current Kiirunavaara samples in context, it is worth noting that Posiva require a minimum smectite content of 65 wt% in their repository buffer and backfill, with a preferred level of 75–90 wt% (Posiva, 2021).

As it currently stands, 4 of the 21 reported analyses, above, would pass the criterion for the smectite content (of > 65 wt%) for the (benefacted) repository buffer (as set out in Ahonen et al. 2008 and Posiva, 2021, for example) and an additional three samples lie just below this criterion.

7.3.3 Age of the natural Kiirunavaara clay

All data presented here on the smectite-rich natural clays indicate that they are significantly older than any timescales of relevance to a repository safety case. Further, there is evidence (cf. sections 3.5.4, 3.6.4 and 3.7.4) that, since formation, the natural bentonite in Kiruna has been perturbed several times but has nevertheless retained the basic physico-chemical properties required of the industrial bentonite in a repository. This fact alone increases confidence in the long-term stability of the industrial bentonites to be utilised in repository buffers, backfill and seals.

As noted in Section 3.5.4, ““The K-Ar age values for two fine-clay fractions from the Kiirunavaara mine samples, 102 ± 8 Ma for Ki-01 $< 0.25 \mu\text{m}$ and 120 ± 9 Ma for Ki-02 $0.25\text{--}1.0 \mu\text{m}$, are considerably younger than those for the corresponding $< 2 \mu\text{m}$ fractions. The age values can be interpreted at first approximation as due to mixing of an older, coarser component with a finer, younger component. If the older component of Ki-01 and Ki-02 carries a K-Ar age near 800 Ma, as suggested by age values for Ki-03 and Ma-01 clays then, by the two-component model, most of the K in the Ki-01 and Ki-02 fine-clay fractions must be in the younger component. The age of that younger component is indeterminate but not more than the ~ 100 Ma age value of the fine-clay fractions of Ki-01 and Ki-02.”

Clearly this is of direct relevance to the repository safety case and further K-Ar work on fine-clay fractions from the Ki-01 and Ki-02 samples would be useful to further clarify this point.

7.3.4 Further considerations

A comparison of the hydraulic conductivity and swelling pressure of the available natural Kiirunavaara clays with data for several industrial bentonites (from Kiviranta and Kumpulainen, 2011) is presented in Table 7-2 and Appendix J.

Table 7-2. Values for swelling pressure and hydraulic conductivity from the Kiirunavaara clay compared with several industrial bentonites which are under consideration in the Finnish SF programme (NB values are for ‘at emplacement’).

| Sample (laboratory or reference) | Swelling pressure (MPa) in deionised water | Hydraulic conductivity $\times 10^{-14}$ (ms^{-1}) in deionised water |
|--|--|--|
| Natural bentonites | | |
| Kiruna clay bulk sample (James Hutton, Section 3.4) | 3.25 \pm 0.09 | |
| Kiruna 2018-9, highest dry density (SKB, Appendix J) | 11.42 | 3.9 |
| Kiruna 2018-1, lowest dry density (SKB, appendix J) | 1.47 | 57 |
| Kiruna 2019 mald 9, highest dry density (SKB, Appendix J) | 8.25 | 24 |
| Kiruna 2019 mald 1, lowest dry density (SKB, Appendix J) | 2.93 | 1.1 |
| Industrial Na-bentonites (Kiviranta and Kumpulainen 2011) | | |
| BT1 | 13.56 | 3.27 |
| BT2 | 10.83 | 2.92 |
| BT3 | 10.90 | 3.02 |
| Ibeco 1 | 11.47 | 9.25 |
| Ibeco 2 | 9.66 | 9.84 |
| Ibeco 3 | 10.76 | 8.84 |
| 1-1-Sa | 8.44 | 3.00 |
| 1-1-Sar | 10.49 | n/a |
| 1-2-Sa | 5.31 | 4.78 |

Of the four SKB samples presented here, the two highest dry density samples (Kiruna 2018-9 and Kiruna 2019 mald 9) show similar swelling pressures and hydraulic conductivities to the industrial bentonites. The two lowest dry density samples (Kiruna 2018-1 and Kiruna 2019 mald 1) show much lower swelling pressures and much higher hydraulic conductivities. As noted in Svensson et al. (2019), a drop in the montmorillonite content of MX-80 lowered the swelling pressure and increased the hydraulic conductivity of the samples and it is suggested that this may be the explanation here.

Comparison of the swelling pressure of Kiirunavaara clay sample c65f8c with the natural bentonites assessed in Section 3.3.4 shows that the clay sample has similar swelling pressure to the natural bentonites with among the highest values for the material examined (see Figure 3-5 and Section 3.7.3). Further, as was also noted in Section 3.3.4, taking into account the effective montmorillonite dry density and smectite content, the hydraulic conductivity of Kiirunavaara clay sample c65f8c is similar to those of a range of natural bentonites (Figure 3-5).

7.4 Potential impact of microbial populations in bentonite under repository conditions

The information presented in Chapter 5 is preliminary, but it can be stated that ultra-pure DNA extraction has provided the first evidence for the presence of biomolecules in clays from the Kiirunavaara area. In addition, the study supports the existence of active microbial life related to Fe(III), NO_3^- and SO_4^{2-} metabolism with low molecular weight organic acids. These organic carbon-based metabolic pathways could be supported by the traces of organic carbon which were also detected in the clay.

Suppression of microbial sulphate reduction has not yet been addressed in the Kiruna mine, but has been assessed elsewhere (e.g. Maanoja et al. 2020; Beaver et al. 2022), indicating the viability of such an approach.

7.5 Potential for erosion of the bentonite barrier by groundwater in a deep geological repository

The very limited amount of work on clay erosion which proved possible to conduct during the project lifetime (see Chapter 6) indicates that the particular smectite-rich clay examined is relatively stable compared to the industrial bentonites intended for use in the repository environment. However, as was noted above, this result may have also been influenced by the restricted sample availability, leading to the choice of a calcite-rich sample, Kiruna 2018 (see Table 7-1a).

The overall conclusion of the chapter is that no chemical erosion through colloid formation, or sedimentation, will take place in this particular Kiruna smectite sample analysed here. It was noted that this is possibly because it is unlikely this sample has ever been exposed to Na-rich dilute groundwaters and that the amount of calcite present in the material has been sufficient to buffer the composition of the exchanger to a 100 % calcium form. However, as noted in Section 3.2.4, some Kiruna clay samples may have been exposed to shallow weathering processes. Further, some of the Kiruna clays (e.g. sample KI-02 from the shallowest alteration zone investigated in the footwall trachy-andesite), "...has an unusual Na-K-dominated interlayer cation composition that can only be explained by a local cation exchange reaction with Na- and K-rich waters." Rather, it seems likely that sample Kiruna 2018 was more heavily influenced by the late-stage calcite overprint discussed in Section 3.2.5 and that the role of calcite in bentonite erosion be assessed in future (cf. Shourijeh et al. 2020).

As such, the conclusions should be treated as preliminary until a wider range of samples from the mine (including those like sample KI-02) can be assessed under the same laboratory conditions as reported here. Similarly, focussed sampling and analysis of local groundwaters would provide a better context in which to place these laboratory erosion results (but see also footnote 16 in Section 4.7.2 which points out that this would be a significant use of resources).

7.6 Final comments

As noted in Posiva (2021) "A drawback of most natural analogues is the lack of knowledge of the geochemical conditions....making straightforward extrapolation to repository conditions difficult". Indeed, in their critical review of existing NA data, Alexander and Reijonen (2024) reject many existing NA studies for just those reasons.

However, when the existing information on the Kiirunavaara natural clays (Chapter 2 is combined with the novel data presented here in Chapter 3 it would be unreasonable to make such a claim about these natural clays. Indeed, if anything, the new information has made it very clear that the natural clays in the Kiirunavaara mine represent a complex, multi-phase system which has experienced various degrees of transformation and neof ormation over more than a Ga and this will, once again, make straightforward extrapolation to repository conditions difficult. However, that would ignore the main, safety case-relevant messages which can already be taken from this study, namely:

- The smectite-rich Kiirunavaara natural clays have survived relatively unscathed for periods several hundred times longer than will be required for the industrial bentonites in a repository.
- With respect to their smectite content, swelling pressure and CEC values, these natural clays are, indeed, excellent analogues of the industrial bentonites which will be used in repository buffers, backfill and seals.
- Historical and novel data presented here indicate that Fe uptake by the natural, smectite-rich clays under repository-relevant conditions (i.e. not at the higher temperatures alluded to in Section 7.2) is minimal, even when the clays are in close proximity to the magnetite for extended periods of time.
- Very careful sampling and subsequent sample handling have produced artefact-free samples for microbial analysis and the full results of this work will be available at a later date.
- The question of clay age(s) has been addressed here with the novel data produced in the project indicating that the system is, not surprisingly, complex. Nevertheless, it is clear that all historical and novel data on the smectite-rich natural clays presented here indicate that they are significantly older than any timescales of relevance to a repository safety case.

Nevertheless, some open questions remain (can they be tackled?):

- Can careful, focussed sampling in future routinely access Kiirunavaara natural clays which are directly comparable to the industrial bentonite which will be employed in repository buffer, backfill and seals? This seems more than likely.
- Could the *in situ* redox conditions in and around the Kiirunavaara natural clays and iron ore be assessed to define the degree of relevance to a repository near-field (see Muñoz et al. 2024, for details)? Not easily, but yes, beginning with thermodynamic modelling to guide future sampling and analytical work at the site.
- Could the analogy between the Kiirunavaara natural clays and the industrial bentonites foreseen for repository EBS be strengthened if a wider range of physico-chemical parameters were available for the clays, so allowing a more detailed comparison (cf. Alexander and Milodowski, 2014, Alexander et al. 2017) than has been the case here? Most certainly yes.
- Similarly, could the analogy be strengthened by a fuller understanding of the overall site, including a detailed assessment of the current hydrogeochemistry? Most certainly, yes, but see the comments in footnote 16.
- Microbial sulphate reduction has not yet been addressed here, but has been assessed elsewhere (e.g. Maanoja et al. 2020; Beaver et al. 2022), indicating the viability of such an approach.
- Although the bulk (and clay fraction) CEC values of unaltered clay remain in the repository-relevant range, would it be possible to analyse any clays which have clearly reacted with iron-oxides to assess if this induces any CEC decrease? Definitely.
- Will it be possible to more closely examine the potential (lower temperature) reaction between magnetite and the natural, smectite-rich clays? This is currently ongoing and the full results will be reported in due course.
- What is the role of biotite in minimising apparent iron uptake by smectite in Kiruna? Is this an indication of a higher temperature reaction between magnetite and smectite to form non-swelling biotite at relatively high temperature so preventing smectite incorporating iron? This could also be assessed (guided by thermodynamic modelling).
- What is the influence of the calcite content on bentonite erosion? This could be assessed in the laboratory.

8 Acknowledgements

First and foremost, the KINA project team would like to thank LKAB and all their staff who were involved with us for their unstinting support over the rather longer-than-planned duration of the work, it is greatly appreciated. The KINA project was financed by Andra (F), Nagra (CH), NUMO (J), NWMO (CA), NWS (UK), Posiva (FI) and SKB (S) with in-kind contributions from LKAB (S).

The COVID pandemic also rather interrupted the planned progress of KINA and this led to some difficulties with sample provenance etc., so many thanks to the LKAB personnel, particularly Joaquim Otero Johansson and Jonathan Sumelius (both LKAB) and Daniel Svensson (SKB) for all their efforts post-pandemic in establishing the facts.

HAG would like to thank the mine geology department at LKAB in Kiruna for access and support in sampling. Special thanks also go to Adrian Hall, Philip Rieger, Frank Friedrich and Marek Szczerba. Holly Stein acknowledges the assistance of Aaron Zimmerman.

RB-L and NJ would like to thank Manon Frutschi (EPFL). Maja-Stina Bransfjell, Josefin Fors (both LKAB), Rene Dorrer and Raphael Schneeberger (both Nagra) are thanked for support during the microbiological sampling campaign. Thanks also to Mehran Behazin (NWMO) for providing additional organics analyses.

Finally, many thanks to the anonymous external reviewer for a thorough, thoughtful and helpful review.

References

SKB's (Svensk Kärnbränslehantering AB) publications can be found at www.skb.com/publications.

AECL 1994. Environmental Impact Statement on the concept for disposal of Canada's nuclear fuel waste. AECL-10711, COG-93-1. AECL, Chalk River, Canada.

Ahonen L, Korkeakoski P, Tiljander M, Kivikoski H, Laaksonen R, 2008. Quality Assurance of the Bentonite Material. Posiva Working Report WR2008-33, Posiva, Finland.

Alexander W R, 2018. Sealing site investigation boreholes: Phase 2. The use of natural, commercial and archaeological analogues in support of the borehole sealing project, Amec Foster Wheeler Report 202580/07 for RWM Ltd. NWS, Harwell, UK.

Alexander W R, Neall F B, 2007. Assessment of potential perturbations to Posiva's SF repository at Olkiluoto caused by construction and operation of the ONKALO facility. Posiva Working Report 2007-35, Posiva, Finland.

Alexander W R, Reijonen H M, 2024. Natural Analogues – a catalogue. GTK Research Report to client (NWS Ltd) GTK/175/03.02/2020 November 13 2023. GTK, Finland.

Alexander W R, Arcilla C A et al. 2008. A new natural analogue study of the interaction of low-alkali cement leachates and the bentonite buffer. *Sci Basis Nucl Waste Manag XXXI*, 493-500.

Alexander W R, Berry J A, Kelly M J, Swanton S, 2011. Review of colloids in the geosphere and their treatment in performance assessment. Report to NDA-RWMD. Serco/TAS/002924/01, Serco, Didcot, UK.

Alexander W R, Milodowski A E, Pitty A F (eds), 2012. Cyprus Natural Analogue Project (CNAP) Phase III Final Report. Posiva Working Report WR 2011-77, Posiva, Finland.

Alexander, W.R, Milodowski, A E, 2014. Cyprus Natural Analogue Project (CNAP) Phase IV Final Report; Posiva Working Report WR 2014-02; Posiva, Finland.

Alexander W R, Reijonen H M, MacKinnon G, Milodowski AE, Pitty A F, Siathas A, 2017. Assessing the long-term behaviour of the industrial bentonites employed in a repository for radioactive wastes by studying natural bentonites in the field. *Geosciences Special Issue on Geological Disposal of High Level Radioactive Waste – The Relationship between Engineered and Natural Barriers*, eds. R.Lunn, S.Harley, S.Norris & J.Martinez-Frias. *Geosciences* 7, 5.

Alexander W R, Reijonen H M, Norris S, 2024. Assessing the performance of a radioactive waste repository over geological timescales: past experience and the way forward. *in Sustainable geological disposal and containment of radioactive waste*, Norris, S and Cooke, A (eds). *Geoenergy* v2, <https://doi.org/10.1144/geoenergy2023-046>

Anderson M W, 1989. Basement-cover evolution during Caledonian orogenesis, Troms, N. Norway. In Gayer (ed.) *The Caledonian geology of Scandinavia*. Kluwer Academic Publications, Norwell, MA, USA.

Andersson U B, 2013. Coeval iron oxide and silicate magmas; structural evidence for immiscibility and mingling at Kiirunavaara and Luossavaara, Sweden. *Proc. 12th SGA Biennial Meeting, Uppsala, Sweden*, pp 1635-1638. Geological Survey of Sweden, Sweden.

Andersson U B, Berglund J, 2024. Interpretations of structures related to two areas of lithological breaks in Kiirunavaara. *LKAB Investigation 2024-0028*, 38 pp. + 2 App. 58 pp.

Andersson U B, Rutanen H, 2016. Geological features in and around the Kiirunavaara ore body, northernmost Sweden, and some implications. *International Geological Congress, Kapstadén, 2016-08-27–09-04, Paper Nr. 2989*.

Andersson J, Riggare P, Skagius K, 1998. Project Safe. Update of the SFR-1 safety assessment – Phase 1. SKB R-98-43, Svensk Kärnbränslehantering AB.

Andersson J B H, Bauer T E, Lynch E P, 2020. Evolution of structures and hydrothermal alteration in a Palaeoproterozoic supracrustal belt: Constraining paired deformation–fluid flow events in an Fe and Cu–Au prospective terrain in northern Sweden. *Solid Earth* 11, 547–578.

- Andersson J B H, Bauer T E, Martinsson O, 2021.** Structural evolution of the central Kiruna area, northern Norrbotten, Sweden: implications on the geologic setting generating iron oxide-apatite and epigenetic iron and copper sulfides, *Economic Geology*, vol. 116: 1981–2009.
- Andersson J B H, Logan L, Martinsson O, Chew D, Kooijman E, Kielman-Schmitt M, Kampmann T C, Bauer T E, 2022a.** U-Pb zircon-titanite-apatite age constraints on basin development and basin inversion in the Kiruna mining district, Sweden. *Precambrian Research* 372, 106613, 17 pp.
- Andersson U B, Segovia Menard D, Majka J, 2022b.** Uranium mineralizations at Kiirunavaara, Sweden. Geological Society of Sweden, 150 Year Anniversary Meeting, Uppsala, Sweden, Abstract Volume pp. 348–349.
- Andersson U B, Pihl J, Bäckström A, Fröjdö S, Eklund O, 2024.** Dyke porphyries in Kiirunavaara: feeders of the hanging wall volcanism. 36th Nordic Geological Winter Meeting, Gothenburg, Jan. 10–12, 2024. Geol. Soc. of Sweden, Special Publ. 5, p.123.
- Armstrong R L, Jäger E, Eberhardt P, 1966.** A comparison of K-Ar and Rb-Sr ages on Alpine biotites. *Earth Planet. Sci. Lett.* 1, 13–19.
- Augustsson C, 2017.** Trace element geochemistry of magnetite from the Kiirunavaara iron-apatite ore, as determined by LA-ICP-MS. Unpubl. Master thesis B965, University of Gothenburg, Sweden.
- Aupers K, 2014.** Gangue mineralogy and deportment of deleterious elements in the iron ore of the Kiirunavaara deposit, Sweden. Unpubl. Master thesis, TU Bergakademie Freiberg, Freiberg, Germany.
- Bagnoud A, Chourey K, Hettich R L, de Bruijn I, Andersson A F, Leupin O X, Schwyn B, Bernier-Latmani R, 2016.** Reconstructing a hydrogen-driven microbial metabolic network in Opalinus Clay rock. *Nat Commun.* 14, 12770. doi: 10.1038/ncomms12770. PMID: 27739431; PMCID: PMC5067608.
- Bailey S W, 1982.** Nomenclature for regular interstratifications. *American Mineralogist* 67, 394–398.
- Bauer T E, Andersson J B, Sarlus Z, Lund C, Kearney T, 2018.** Structural controls on the setting, shape, and hydrothermal alteration of the Malmberget iron oxide-apatite deposit, Northern Sweden. *Economic Geology* 113, 377–395.
- Beaver R C, Engel K, Binns W J, Neufeld J D, 2022.** Microbiology of barrier component analogues of a deep geological repository. *Can J Microbiol.* 68, 73–90.
- Beaver R C, Vachon M A et al. 2024.** Impact of dry density and incomplete saturation on microbial growth in bentonite clay for nuclear waste storage. *Journal of Applied Microbiology*, 2024, 135, lxae053. <https://doi.org/10.1093/jambio/lxae053>.
- Berglund J, Andersson U B, 2013.** Kinematic analysis of geological structures in Block 34, Kiirunavaara. LKAB Investigation 13-746, 48 sid. + 2 Appendices.
- Bergman S, 2018.** Regional Geology of the northern Norrbotten County. *Geology of the Northern Norrbotten ore province, northern Sweden. SGU Rapport och Meddelanden* 141, 9–18. Geological Survey of Sweden, Sweden (*in Swedish*).
- Bergman S, Weihed P, 2020.** Archean (> 2.6 Ga) and Paleoproterozoic (2.5–1.8 Ga), pre-and syn-orogenic magmatism, sedimentation and mineralisation in the Norrbotten and Överkalix lithotectonic units, Svecofennian orogen. *Memoirs of the Geological Society of London*, 50, 27–81.
- Bergmann J, Friedel P, Kleeberg R, 1998.** BGMN – a new fundamental parameters-based Rietveld program for laboratory X-ray sources; its use in quantitative analysis and structure investigations. *International Union of Crystallography, Commission on Powder Diffraction Newsletter* 20, 5–8.
- Bergman S, Kübler L, Martinsson O, 2001.** Description of regional geological and geophysical maps of northern Norrbotten county (east of the Caledonian orogen). *Sveriges Geologiska Undersökning, Ba* 56, 1–110. Geological Survey of Sweden, Sweden (*in Swedish*).
- Bernal N F, Gleeson S A, Smith M P, Barnes J D, Pan Y, 2017.** Evidence of multiple halogen sources in scapolites from iron oxide-copper-gold (IOCG) deposits and regional NaCl metasomatic alteration, Norrbotten County, Sweden. *Chemical Geology* 451, 90–103.

- Billström K, Evins P, Martinsson O, Jeon H, Weihed P, 2019.** Conflicting zircon vs. titanite U-Pb age systematics and the deposition of the host volcanic sequence to Kiruna-type and IOCG deposits in northern Sweden, Fennoscandian shield. *Precambrian Research* 321, 123–133.
- Björnell T, Andersson U B, Eriksson P, Faber M, Larsson, C F, 2015.** Structural mapping and 3-D photographing, in and around block 34, levels 1079–1137, in the Kiirunavaara mine. LKAB Investigation 15-820, 90 pp. + 3 Appendices, 34 pp.
- Blomgren H, 2015.** U-Pb dating of monazites from the Kiirunavaara and Rektorn ore deposits – hydrothermal events affecting the Kiruna main ore. Unpubl. Masters thesis, B891, University of Gothenburg, Sweden.
- Brindley G W, 1966.** Ethylene glycol and glycerol complexes of smectites and vermiculites. *Clay Minerals* 6, 237–259.
- Broughm S G, Hanchar J M, Tornos F, Westhues A, Attersley S, 2017.** Mineral chemistry of magnetite from magnetite-apatite mineralisation and their host rocks: examples from Kiruna, Sweden, and El Laco, Chile. *Mineralium Deposita* 52, 1223–1244.
- Butler B M, Hillier S, 2021.** Automated full-pattern summation of x-ray powder diffraction data for high-throughput quantification of clay-bearing mixtures. *Clays Clay Miner.* 69, 38–51.
- Bygdén A, 1902.** Analysen einiger Mineralien von Gellivare Malmberg. *Bull. Geol. Inst. Upsala*, 6, 92–100 (*in Swedish*).
- Carlson L, Karnland O, Olsson S, Rance A, Smart N, 2008.** Experimental studies on the interactions between anaerobically corroding iron and bentonite. SKB R-08-28, Svensk Kärnbränslehantering AB.
- Chapman N A, McKinley I G, Smellie J A T, 1984.** The Potential of Natural Analogues in Assessing Systems for Deep Disposal of High-Level Radioactive Waste; Nagra Technical Report NTB 85-41, Nagra, Wettingen, Switzerland.
- Cleveland G B, 1960.** Geology of the Otay bentonite deposit, San Diego County, California. California Division of Mines (CDM) Special Report 64. CDM, San Francisco, USA.
- Cliff R A, Rickard D, 1992.** Isotope systematics of the Kiruna magnetite ores, Sweden; Part 2, Evidence for a secondary event 400 Ma after ore formation. *Economic Geology*, 87, 1121–1129.
- Cliff R A, Rickard D, Blake K, 1990.** Isotope systematics of the Kiruna magnetite ores, Sweden; Part 1, Age of the ore. *Economic Geology* 85, 1770–1776.
- Colella C, Gualtieri A F, 2007.** Cronstedt's zeolite. *Microporous and Mesoporous Materials* 105, 213–221.
- Cronstedt A F, 1756.** Rön och beskrifning om en obekant bärg art, som kallas Zeolites. (Observation and description of an unknown kind of rock to be named zeolites). *Kungl. Svenska vetenskapsakademiens handlingar (Stockholm)* 17, 120–123 (*in Swedish*).
- Dabney J, Knapp M et al. 2013.** Complete mitochondrial genome sequence of a Middle Pleistocene cave bear reconstructed from ultrashort DNA fragments. *Proceedings of the National Academy of Sciences* 110, 15758–15763.
- Dalrymple G B, Lanphere M A, 1969.** Potassium-argon dating. W.H. Freeman Ltd, New York, USA.
- De Man E, Van Simaey S, Vandenberghe N, Harris W B, Wampler J M, 2010.** On the nature and chronostratigraphic position of the Rupelian and Chattian stratotypes in the southern North Sea basin. *Episodes*, 33, 3–13.
- Döbelin N, Kleeberg R, 2015.** Profex: a graphical user interface for the Rietveld refinement program BGMN. *Journal of Applied Crystallography* 48, 1573–1580.
- Eberl D D, 1983.** Clay mineral formation and transformation in rocks and soils. *Philosophical Transactions of the Royal Society A: Mathematical, Physical and Engineering Sciences* 311, 241–257. Doi 10.1098/rsta.1984.0026
- Ehrenreich A, Widdel F, 1994.** Anaerobic oxidation of ferrous iron by purple bacteria, a new type of phototrophic metabolism. *Applied and Environmental Microbiology* 60, 4517–4526.

- Elo O, Hölttä P, Kekäläinen P, Voutilainen M, Huittinen N M, 2019.** Neptunium(V) transport in granitic rock : a laboratory scale study on the influence of bentonite colloids Appl. Geochem. 103, 31–39.
- Er-ramly A, Ider A, 2014.** Physico-chemical and mineralogical characterisation of a Moroccan bentonite (Azzouzet) and determination of its nature and chemical structure. Int. J. Mats. Sci. and Appl. 3, 42–48.
- Forsell P, 1987.** The stratigraphy of the Precambrian rocks of the Kiruna district, northern Sweden. Sveriges geologiska undersökning C 812, 1–36. Geological Survey of Sweden, Sweden.
- Frietsch R, 1960.** En zon av kaolinlera och vittrad blodsten vid Svappavaara, Norrbotten. Sveriges Geologiska Undersökning, C 572, 1–45. Geological Survey of Sweden, Sweden (*in Swedish*).
- Frietsch R, 1966.** Geology and ores of the Svappavaara area, northern Sweden. Sveriges Geologiska Undersökning C 604. Geological Survey of Sweden, Sweden (*in Swedish*).
- Frietsch R, 1970.** Trace elements in magnetite and haematite mainly from northern Sweden. Sveriges geologiska undersökning C 646. Geological Survey of Sweden, Sweden.
- Frietsch R, 1978.** On the magmatic origin of iron ores of the Kiruna type. Economic Geology 73, 478–485.
- Frietsch R, Tuisku P, Martinsson O, Perdahl J A, 1997.** Early Proterozoic Cu-(Au) and Fe ore deposits associated with regional Na-Cl metasomatism in northern Fennoscandia. Ore Geology Reviews 12, 1–34.
- Fujii N, Yamakawa M et al. 2015.** Alkaline alteration processes of bentonic sediment in the Philippines natural analogue and perspective on the survey of the active type. In Alexander, W.R., Ruskeeniemi, T. and Reijonen, H.M. (eds) (2015). Proceedings NAWG-14 Workshop, Rauma, Finland, 9–11 June, 2015. Geological Survey of Finland (GTK) Guide 61. GTK, Finland. http://tupa.gtk.fi/julkaisu/opas/op_061.pdf
- Fujita K, Sato T, Nakabayashi R, Yamakawa M, Fujii N, Namiki K, Pascua C, Arcilla C A, Alexander W R, Yoneda T, 2010.** Natural analogue study of the interaction between hyperalkaline groundwater and bentonite at the ophiolite of the Philippines. Proc. Japan Geoscience Union Meeting 2010, 23–28 May, 2010, Makuhari, Japan, JGU, Tokyo, Japan (*in Japanese*).
- Fukushi K, Sugiura T, Morishita T, Takahashi Y, Hasebe N, Ito H, 2010.** Iron–bentonite interactions in the Kawasaki bentonite deposit, Zao area, Japan. Appl. Geochem., 25, 1120–1132.
- Gee D G, Stephens M B, 2020.** Regional context and tectonostratigraphic framework of the early–middle Paleozoic Caledonide orogen, northwestern Sweden. Memoirs of the Geological Society of London 50, 481–494.
- Geijer P, 1910.** Igneous rocks and iron ores of Kiirunavaara, Luossavaara and Tuolluvaara. Scientific and practical researches in Lapland. In Igneous rocks and iron ores of Kiirunavaara, Luossavaara and Tuolluvaara, Geology of the Kiruna District 2. Aktie Bolag, Sweden.
- Geijer P, 1930.** Gällivare malmfält: geologisk beskrivning. Sveriges geologiska undersökning, Ca 22, 1–115. Geological Survey of Sweden, Sweden (*in Swedish*).
- Gilg H A, Andersson U B, 2020.** Geology of deep clay alteration in the Kiirunavaara and other iron ore deposits, northern Norrbotten, Sweden. LKAB Investigation 2020-0053, 30 pp.
- Gilg H A, Hall A M, Ebert K, Fallick A E, 2013.** Cool kaolins in Finland. Palaeogeography, Palaeoclimatology, Palaeoecology 392, 454–462.
- Gilg H A, Rieger P, Wampler J M, Andersson U B, 2017.** Origin of clays in Kiruna-type iron ore deposits, Sweden. In Living Clays: Clay Minerals Society Meeting, June 5th, 2017, NAIT, Edmonton, Alberta, Canada. Conference abstracts p. 22.
- Gilg H A, Bindeman I, Andersson U B, 2022.** A mineralogical and stable H-O-C-isotope study of clay-rich alteration zones in the Fennoscandian Shield, Norrbotten, Sweden. 10th Jubilee Mid- European Clay Conference, Kliczków, Polen, September 11–15th 2022, Book of Abstracts p. 37.

Gilmour K, Davie C T, Gray N, 2022. Survival and activity of an indigenous iron-reducing microbial community from MX80 bentonite in high temperature / low water environments with relevance to a proposed method of nuclear waste disposal. *Science of the Total Environment*, 814. p. 152660. ISSN 0048-9697

Gleeson S A, Smith M P, 2009. The sources and evolution of mineralising fluids in iron oxide–copper–gold systems, Norrbotten, Sweden: Constraints from Br/Cl ratios and stable Cl isotopes of fluid inclusion leachates. *Geochimica et Cosmochimica Acta* 73, 5658–5672.

Gray W, 2016. Genesis of the Kiirunavaara nodular porphyry and Kiruna-type iron deposits: clues from titanite geothermometry and magnetite trace element composition. Unpubl. BSc. Honours thesis, University of St. Andrews, St. Andrews, Scotland, UK.

Grigull S, Berggren R, Jönberger J, Jönsson C, Hellström F A, Luth S, 2018. Folding observed in Palaeoproterozoic supracrustal rocks in northern Sweden. In: Bergman, S. (ed) *Geology of the Northern Norrbotten ore province, northern Sweden*. Sveriges geologiska undersökning Rapporter och Meddelanden 141 (paper 5, 13). Geological Survey of Sweden, Sweden.

Guillaume D, Neaman A et al. 2004. Experimental study of the transformation of smectite at 80 and 300 °C in the presence of Fe oxides. *Clay Minerals* 39, 17–34.

Huan Tong H, Behazin M, Simpson M J, 2023. Assessment of heat and radiation impacts on natural organic matter composition in bentonite for used nuclear fuel disposal. *Applied Clay Science* 232, 106808.

Hallsworth C R, Knox R W O'B, 1999. BGS Rock Classification Scheme. Volume 3: Classification of Sediments and Sedimentary Rocks. British Geological Survey Research Report, RR99-03. British Geological Survey, Keyworth, Nottingham, UK.

Harlov D E, Andersson U B, Förster H J, Nyström J O, Dulski P, Broman C, 2002. Apatite–monazite relations in the Kiirunavaara magnetite–apatite ore, northern Sweden. *Chemical Geology* 191, 47–72.

Hedrich S, Schlömann M, Johnson D B, 2011. The iron-oxidizing proteobacteria. *Microbiology* 157, 1551–1564.

Hendriks B W H, 2003. Cooling and denudation of the Norwegian and Barents Sea margins, Northern Scandinavia: constrained by apatite fission track and (U-Th)/He thermochronology. Unpubl. PhD thesis, Vrije universiteit, Amsterdam, The Netherlands.

Hendriks B W, Andriessen P A, 2002. Pattern and timing of the post-Caledonian denudation of northern Scandinavia constrained by apatite fission-track thermochronology. *Geological Society of London Special Publication* 196, 117–137.

Hillier S, 1999. Use of an air brush to spray dry samples for X-ray powder diffraction: *Clay Minerals*, 34, 127–135.

Hillier S, 2003. Quantitative analysis of clay and other minerals in sandstones by X-ray powder diffraction (XRPD), in R.H. Worden and S. Morad eds., *Clay Mineral Cements in Sandstones: International Association of Sedimentologists, Special Publication* 34, 213–251.

Hossack J R, Cooper M A, 1986. Collision tectonics in the Scandinavian Caledonides. *Geological Society of London Special Publication* 19, 285–304.

Inoue A, 1995. Formation of clay minerals in hydrothermal environments: in Velde, B., *Origin and mineralogy of clay, clays in the environment*. Springer Berlin, Heidelberg, Germany.

ISO 2018. Soil quality – Determination of effective cation exchange capacity (CEC) and exchangeable cations using a hexamminecobalt(III)chloride solution. ISO Standard 23470:2018, ISO, Geneva, Switzerland.

Itaya T, Doi M, Ohira T, 1996. Very low potassium analysis by flame photometry using ultra low blank chemical lines: an application of K-Ar method to ophiolites. *Geochemical Journal*, 30, 31–39.

Itäla A, 2018. Chemical behaviour of bentonite in the near field of the KBS-3V concept. PhD. Thesis, University of Helsinki, Helsinki, Finland. ISBN 978-951-38-8669-1 (URL: <http://www.vttresearch.com/impact/publications>).

- JAEA, 2007.** Second Progress Report on Research and Development for TRU Waste Disposal in Japan – Repository Design, Safety Assessment and Means of Implementation in the Generic Phase. JAEA/FEPCO joint report, JAEA-Review 2007-010, JAEA, Tokai, Japan.
- Jackson M L, 1979.** Soil chemical analyses – advanced course (3rd ed.). Prentice Hall Inc, Madison, USA.
- Jakus N, Schneeberger R, Andersson U B, Gilg A, Leupin O, Bernier-Latmani R, 2023.** Microbial metabolic potential in a natural clay analogue for deep geological radioactive waste repositories. *Goldschmidt Conference 2023, Lyon, France, July 9–14th*.
- Jansson M, 2009.** Bentonite erosion, laboratory studies. SKB TR-09-33, Svensk Kärnbränslehantering AB.
- Jensen S, Grant S W, 1998.** Trace fossils from the Dividalen Group, northern Sweden: implications for Early Cambrian biostratigraphy of Baltica. *Norsk Geologisk Tidsskrift* 78, 305–317.
- JNC, 2000.** H12: Project to Establish Technical Basis for HLW Disposal in Japan, Project Overview Report and three Supporting Reports, JNC TN1410 2000-001-004. JAEA, Tokai, Japan.
- Kaufhold S, Dohrmann R, Wallis I, Weber C, 2023.** Chemical and mineralogical reactions of bentonites in geotechnical barriers at elevated temperatures: review of experimental evidence and modelling progress. *Clay Minerals*. 58, 280–300. doi:10.1180/clm.2023.26
- King F, Behazin M, Keech P, 2023.** Natural and archaeological analogues for corrosion prediction in nuclear waste systems. *Materials and Corrosion* 74, 1811–1822.
- Kiviranta L, Kumpulainen S, 2011.** Quality Control and Characterisation of Bentonite Materials. Posiva Working Report WR 2011-84, Posiva, Finland.
- Kiviranta L, Kumpulainen S, Pintado X, Karttunen P, Schatz T, 2018.** Characterisation of bentonite and clay materials 2012–2015. Posiva Working Report WR 2016-05. Posiva, Finland.
- Knight W C, 1898.** Bentonite. *Engineering & Mining Journal*, 66, 491.
- Koehl J B P, Bergh S G, Wemmer K, 2018.** Neoproterozoic and post-Caledonian exhumation and shallow faulting in NW Finnmark from K–Ar dating and P/T analysis of fault rocks. *Solid Earth* 9, 923–951.
- Kremer E P, Alexander W R, 2015.** Long-term durability of shaft sealing materials under highly saline groundwater conditions. In Alexander, W.R., Ruskeeniemi, T. and Reijonen, H.M. (eds.) (2015). Proceedings NAWG-14 Workshop, Rauma, Finland, 9–11 June, 2015. Geological Survey of Finland (GTK) Guide 61. GTK, Finland. http://tupa.gtk.fi/julkaisu/opas/op_061.pdf
- Kuligiewicz A, Derkowski A, Szczerba M, Gionis V, Chryssikos G D, 2015a.** Revisiting the infrared spectrum of the water–smectite interface. *Clays and Clay Minerals* 63, 15–29.
- Kuligiewicz A, Derkowski A, Emmerich K, Christidis G E, Tsiantos C, Gionis V, Chryssikos G D, 2015b.** Measuring the layer charge of dioctahedral smectite by O–D vibrational spectroscopy. *Clays and Clay Minerals* 63, 443–456.
- Kulling O, 1964.** Översikt över norra Norrbottensfjällens Kaledonberggrund. Sveriges Geologiska Undersökning Ba 19, 1–166. Geological Survey of Sweden, Sweden (*in Swedish*).
- Laine H M, Karttunen P, 2010.** Long-Term Stability of Bentonite: A Literature Review. Posiva Working Report WR 2010-53, Posiva, Finland.
- Lemieux J-M, Sudicky E A, Peltier W R, Tarasov L, 2008a.** Dynamics of groundwater recharge and seepage over the Canadian landscape during the Wisconsinian glaciation. *Journal of Geophysical Research* 113, F01011.
- Lemieux J-M, Sudicky E A, Peltier W R, Tarasov L, 2008b.** Simulating the impact of glaciations on continental groundwater flow systems: 2. Model application to the Wisconsinian glaciation over the Canadian landscape. *Journal of Geophysical Research* 113, F03018.
- Leupin O X, Smith P A et al. 2016.** High-level waste repository-induced effects. Nagra Technical report NTB14-03. Nagra, Wettingen, Switzerland.

- Loberg B E, Horndahl A K, 1983.** Ferride geochemistry of Swedish Precambrian iron ores. *Mineralium Deposita* 18, 487–504.
- Lundkvist A, 1998.** The process water geochemistry of the Kiirunavaara magnetite ore. Luleå University of Technology. Unpubl. Masters thesis, Luleå University of Technology, Sweden.
- Lynch E P, Hellström F A, Huhma H, Jönberger J, Persson P O, Morris G A, 2018.** Geology, lithostratigraphy and petrogenesis of c. 2.14 Ga greenstones in the Nunasvaara and Masugnsbyn areas, northernmost Sweden. pp19–77 *In* Bergman, S. (ed) *Geology of the Northern Norrbotten Ore Province, Northern Sweden*. Sveriges Geologiska Undersökning, Rapporter och meddelanden, 141. Geological Survey of Sweden, Sweden.
- McKinnon K M, 2018.** Flow Cytometry: An Overview. *Curr Protoc Immunol.* 120, 5.1.1–5.1.11. doi: 10.1002/cpim.40.
- Maanoja S, Lakaniemi A-M, Lehtinen L, Salminen L, Auvinen H, Kokko M, Palmroth M, Muuri E, Rintala J, 2020.** Compacted bentonite as a source of substrates for sulfate-reducing microorganisms in a simulated excavation-damaged zone of a spent nuclear fuel repository. *Appl. Clay Sci.* 196, 105746. <https://doi.org/10.1016/j.clay.2020.105746>.
- Mann A E, Sabin S et al. 2018.** Differential preservation of endogenous human and microbial DNA in dental calculus and dentin *Scientific Reports* 8, Article number 9822 (doi: <https://doi.org/10.1038/s41598-018-28091-9>).
- Marcos N, 2004.** Results of the Studies on Bentonite Samples from Serrata de Nijar, Almería, Spain. Posiva Working Report 2004-24. Posiva, Finland.
- Martinsson O, 1997.** Paleoproterozoic greenstones at Kiruna in northern Sweden: a product of continental rifting and associated mafic-ultramafic volcanism. In O. Martinsson: *Tectonic setting and metallogeny of the Kiruna greenstones*. Unpubl. PhD. thesis, Luleå University of Technology, Sweden.
- Martinsson O, 2004.** Geology and metallogeny of the northern Norrbotten Fe-Cu-Au province. In *Svecofennian Ore-Forming Environments Field Trip Volcanic-associated Zn-Cu-Au-Ag and magnetite-apatite, sediment-hosted Pb-Zn, and intrusion-associated Cu-Au deposits in northern Sweden*. Society of Economic Geologists Guide Book Series 33, 131–148.
- Martinsson O, Perdahl J-A, 1993.** Paleoproterozoic extensional and compressional magmatism in northern Sweden. *In* Perdahl, J.-A., *Svecofennian Volcanism in Northernmost Sweden*. Unpubl. PhD. thesis, Luleå University of Technology, Sweden.
- Martinsson O, Vaasjoki M, Persson P-O, 1999.** U-Pb ages of Archaean to Palaeoproterozoic granitoids in the Torneträsk-Råstojaure area, northern Sweden. In S. Bergman (ed.): *Radiometric dating results 4*. Sveriges geologiska undersökning C 831, 70–90. Geological Survey of Sweden, Sweden.
- Martinsson O, Billström K, Broman C, Weihed P, Wanhainen C, 2016.** Metallogeny of the northern Norrbotten ore province, northern Fennoscandian Shield with emphasis on IOCG and apatite-iron ore deposits. *Ore Geology Reviews*, 78, 447–492.
- Meier L P, Kahr G, 1999.** Determination of the cation exchange capacity (CEC) of clay minerals using the complexes of copper(II) ion with triethylenetetramine and tetraethylenepentamine. *Clays and Clay Minerals* 47, 386–388.
- Miller W M, Alexander W R, Chapman N A, McKinley I G, Smellie J A T, 2000.** *Geological disposal of radioactive wastes and natural analogues*. Waste management series, vol. 2, Pergamon, Amsterdam, The Netherlands.
- Milodowski A E, Alexander W R, 2024.** Natural analogues of long-term steel canister stability: two novel examples from Scotland. *Inter. J. corrosion (in prep.)*.
- Milodowski A E, Cave M R, Kemp S J, Taylor H, Green K, Williams C L, Shaw R A, Gowing C J B, Eatherington N D, 2009.** Mineralogical investigations of the interaction between iron corrosion products and bentonite from the NF-PRO Experiments (Phase 2). SKB TR-09-03, Svensk Kärnbränslehantering AB.
- Milodowski A E, Norris S, Alexander W R, 2016.** Minimal alteration of montmorillonite following long-term reaction in natural alkali solutions: implications for geological disposal of radioactive waste. *Appl. Geochem.* 66, 184–197.

- Mining-technology, 2010.** “Kiruna Iron Ore Mine, Sweden”. mining-technology.com. 2010. Retrieved 02 November, 2023.
- Missana T, Alonso U, Fernández A M, Lopez T, García-Gutiérrez M, 2018.** Analysis of stability behavior of colloids obtained from different raw bentonites for its implications on erosion processes in the frame of high-level waste repositories. *Appl. Geochem.* 92, 180–187.
- Mitzscherling J, Genderjahn S, Schleicher A M, Bartholomäus A, Kallmeyer J, Wagner D, 2023.** Clay-associated microbial communities and their relevance for a nuclear waste repository in the Opalinus Clay rock formation. *Microbiologyopen* 12, e1370. doi:10.1002/mbo3.1370
- Moeslund L, Thamdrup B, Jørgensen B B, 1994.** Sulfur and iron cycling in a coastal sediment: radiotracer studies and seasonal dynamics. *Biogeochem.* 27, 129–152.
- Moore D M, Reynolds R C, 1997.** X-Ray Diffraction and the Identification and Analysis of Clay Minerals, 2nd ed. Oxford University Press, Oxford, UK.
- Mos Y M, Vermeulen A C, Buisman C J N, Weijma J, 2018.** X-Ray Diffraction of Iron Containing Samples: The Importance of a Suitable Configuration, *Geomicrobiology Journal*, 35, 511–517. doi: 10.1080/01490451.2017.1401183
- Müller B, Axelsson M D, Öhlander, B, 2003.** Trace elements in magnetite from Kiruna, northern Sweden, as determined by LA-ICP-MS. *Geologiska Föreningen i Stockholm Förhandlingar* 125, 1–5.
- Muñoz A G, Abdelouas A et al. 2024.** WP15 ConCorD state-of-the-art report (container corrosion under disposal conditions). *Front. Nucl. Eng.* 3:1404739. doi: 10.3389/fnuen.2024.1404739
- Möri A, Schild M, Siegesmund S, Vollbrecht A, Adler M, Mazurek M, Ota K, Haag P, Ando T, Alexander W R, 2003.** The Nagra-JNC in situ study of safety relevant radionuclide retardation in fractured crystalline rock IV: The in situ study of matrix porosity in the vicinity of a water-conducting fracture. Nagra Technical Report NTB 00-08, Nagra, Wettingen, Switzerland.
- Nadoll P, Angerer T, Mauk J L, French D, Walshe J, 2014.** The chemistry of hydrothermal magnetite: a review. *Ore Geology Reviews.* Elsevier, Amsterdam, The Netherlands.
- Nagra, 1985.** Project Gewähr 1985 – Nuclear waste management in Switzerland -Feasibility studies and safety analyses. Nagra Project Gewähr Report series, NGB 85-09, Nagra, Wettingen, Switzerland.
- Nagra, 1994.** Kristallin-1. Safety assessment report. Nagra Technical Report Series NTB 93-22, Nagra, Wettingen, Switzerland.
- Nagra, 2002.** Project Opalinus Clay Safety Report. Nagra Technical Report 02-05, Nagra Wettingen, Switzerland.
- Niiranen K, 2006.** The Deep Parts of the Kiirunavaara Apatite-magnetite Ore Body in Kiruna, Northern Sweden and the Impact of Future mining on the Township of Kiruna. p p. 57–67, Proceedings, 6th International Mining Geology Conference, Darwin, Australia. The Australasian Institute of Mining and Metallurgy, Melbourne, Australia.
- Nordstrand J, 2012.** Mineral chemistry of gangue minerals in the Kiirunavaara iron ore. Unpubl. Masters thesis, Luleå University of Technology, Sweden.
- NRC IPA, 1995.** Availability of NRC Iterative Performance Assessment Phase 2: Development of Capabilities for Review of a Performance Assessment for a High-Level Waste Repository. USNRC Report 60 FR 57026, USNRC, Washington, USA.
- NUMO, 2021.** NUMO safety case report – Development of Pre-siting SDM-based Safety Case. NUMO TR21-01, NUMO, Tokyo, Japan.
- Nyström J O, Henríquez F, 1994.** Magmatic features of iron ores of the Kiruna type in Chile and Sweden; ore textures and magnetite geochemistry. *Economic Geology* 89, 820–839.
- Nyström J O, Billström K, Henríquez F, Fallick A E, Naslund H R, 2008.** Oxygen isotope composition of magnetite in iron ores of the Kiruna type in Chile and Sweden. *Geologiska Föreningen i Stockholm Förhandlingar* 130, 177–188.

- Omotoso O, McCarty D K, Hillier S, Kleeberg R, 2006.** Some successful approaches to quantitative mineral analysis as revealed by the 3rd Reynolds Cup contest: *Clays and Clay Minerals*, 54, 748–760.
- Palm P, 2015.** Footwall porphyry nodules of the Kiirunavaara and Luossavaara apatite-iron ores: Mineralogy and mineral chemistry of magnetite, amphibole and mica. Unpubl. BSc thesis B849, University of Gothenburg, Sweden.
- Palm P, 2016.** Laser ablation in-situ Rb-Sr and U-Pb dating of the footwall porphyry nodules of the Kiirunavaara apatite-iron ore deposit. Master thesis, Gothenburg University, 46 pp.
- Palma G, Reich M, Barra F, Ovalle J T, Del Real I, Simon A C, 2021.** Thermal evolution of Andean iron oxide–apatite (IOA) deposits as revealed by magnetite thermometry, *Scientific Reports* 11, 18424.
- Paolillo L, Giapis C, 2021.** A preliminary assessment of hydrothermal alterations in the giant Kiruna IOA deposit, Kiruna, Sweden. *LITHOSPHERE 2021 Symposium, January 19–20. pp. 107–110.*
- Parák T, 1975.** Kiruna iron ores are not intrusive-magmatic ores of the Kiruna type. *Economic Geology* 70, 1242–1258.
- Pihl J, 2024.** The dyke porphyries in Kiirunavaara – geology, geochemistry, mineralogy and age. Master thesis, Åbo Akademi Univ., 62 pp.
- Posiva, 2012a.** Safety case for the disposal of spent nuclear fuel at Olkiluoto – Complementary Considerations 2012. POSIVA 2012-11, Posiva, Finland.
- Posiva, 2012b.** Safety case for the disposal of spent nuclear fuel at Olkiluoto – Features, Events and Processes 2012. POSIVA 2012-07, Posiva, Finland.
- Posiva, 2021.** Buffer, backfill and closure evolution. Posiva Working Report 2021-08. Posiva, Finland.
- Posiva, 2022.** Palaeohydrogeochemical data, concepts and interpretation for the Olkiluoto site. Posiva Report 2021-13. Posiva, Finland.
- Posiva, 2023a.** Safety Case for the Operating Licence Application – Synthesis (SYN). Posiva Report 2021-01. Posiva, Finland.
- Posiva, 2023b.** Safety Case for the Operating Licence Application – Complementary Considerations (CC). Posiva Report 2021-02. Posiva, Finland.
- Posiva, 2023c.** Safety Case for the Operating Licence Application – Olkiluoto Site Description (OSD 2018). Posiva Report 2021-10. Posiva, Finland.
- Rehnström E F, Torsvik T H, 2003.** Cambrian sediments and Proterozoic granites in the Dividalen-Torneträsk area, northern Scandinavia: palaeomagnetism and U-Pb geochronology. *Geologiska Föreningen i Stockholm Förhandlingar* 125, 131–138.
- Reijonen H M, Alexander W R, 2015.** Bentonite analogue research related to geological disposal of radioactive waste – current status and future outlook. *Swiss Journal of Geosciences* 108, 101–110.
- Reijonen H, Marcos N, 2016.** Chemical erosion of bentonite buffer – do we observe it in nature? *in* Norris, S., Bruno, J., Van Geet, M. and Verhoef, E. (eds). *Radioactive Waste Confinement: Clays in Natural and Engineered Barriers*. Special Publications 443, pp. 307–317. The Geological Society of London, UK.
- Reijonen H M, Alexander W R, 2024.** Sealing deep site investigation boreholes: Phase 3 International Bentonite Longevity (IBL) Project Report – Phase A. NWS Contractor Report NWS-CR-23-004. NWS, Harwell, UK.
- Reijonen H M, Alexander W R, Norris S, 2023a.** Resilience in knowledge management – the case of natural analogues in radioactive waste management. *J. Process Safety Environ. Protection* 180, 205–222.
- Reijonen H, Elminen T, Heikkilä P, Kuva J, Jolis E, 2023b.** Enhanced identification of fracture smectites and other alteration minerals via short wave infrared reflectance at two Finnish crystalline sites, Olkiluoto and Hyrkkölä. *Rock Mechanics and Rock Engineering* <https://doi.org/10.1007/s00603-024-03764-2>.

- Reijonen H, Al-ani T, Elminen T, Kuva J, Issukka K, Lamminmäki R, 2024.** Fracture smectite in bedrock at Kivetty and Romuvaara sites, Finland as natural analogues for nuclear waste repository buffer. *Geoenergy* 2024 doi: <https://doi.org/10.1144/geoenergy2023-053>.
- Rieger P, 2016.** Low-temperature alteration in the iron ore deposits of Norrbotten, Sweden. Unpubl. Masters thesis, Lehrstuhl für Ingenieurgeologie, Technical University of Munich, Munich, Germany.
- Ritter W, Kronthaler F, Girstmair A, Vartanian R, Koark H J, Purtscheller F, Märk E, Märk T D, 1984.** Fission-track temperature ages. *Nuclear Tracks and Radiation Measurements* 8, 391–394.
- Romer R L, 1996.** U-Pb systematics of stilbite-bearing low-temperature mineral assemblages from the Malmberget iron ore, northern Sweden. *Geochimica et Cosmochimica Acta*, 60, 1951–1961.
- Romer R L, Wright J E, 1993.** Lead mobilization during tectonic reactivation of the western Baltic Shield. *Geochimica et Cosmochimica Acta* 57, 2555–2570.
- Romer R L, Rocholl A, 2004.** Activity disequilibrium of ^{230}Th , ^{234}U and ^{238}U in old stilbite: effects of young U mobility and α -recoil. *Geochimica et Cosmochimica Acta*, 68, 4705–4719.
- Romer R L, Martinsson O, Perdahl J-A, 1994.** Geochronology of the Kiruna iron ores and hydro-thermal alterations. *Economic Geology* 89, 1249–1261.
- Sandberg H, 2018.** A petrological investigation of the host rocks for the Kuj-Kiirunavaara ore. Unpublished BSc thesis, Dept. of Earth Sciences, Uppsala University, Sweden.
- Sarlus Z, Andersson U B, Bauer T E, Wanhainen C, Martinsson O, Nordin R, Andersson J B, 2018.** Timing of plutonism in the Gällivare area: implications for Proterozoic crustal development in the northern Norrbotten ore district, Sweden. *Geological Magazine* 155, 1351–1376.
- Sarlus Z, Andersson U B, Martinsson O, Bauer T E, Wanhainen C, Andersson J B, Whitehouse M J, 2020.** Timing and origin of the host rocks to the Malmberget iron oxide-apatite deposit, Sweden. *Precambrian Research* 342, 105652.
- Schaeffer T, Huber F, et al. 2012.** Nanoparticles and their influence on radionuclide mobility in deep geological formations. *Appl. Geochem.* 27, 390–403.
- Sellin P, Leupin O X, 2013.** The use of clays as an engineered barrier in radioactive-waste management: a review. *Clay Clay Miner.* 61, 477–498.
- Shourijeh P T, Soroush A, Daneshi-Sadr A H, 2020.** The effects of lime, bentonite and nano-clay on erosion characteristics of clay soils. *European Journal of Environmental and Civil Engineering*, 26, 3762–3787. <https://doi.org/10.1080/19648189.2020.1818629>
- Sidborn M, Marsic N, Crawford J, Joyce S, Hartley L, Idiart A, de Vries L M, Maia F, Molinero J, Svensson U, Vidstrand P, Alexander R, 2014.** Potential alkaline conditions for deposition holes of a repository in Forsmark as a consequence of OPC grouting. Revised final report after review SKB R-12-17, Svensk Kärnbränslehantering AB.
- SKB, 1983.** Final storage of spent nuclear fuel – KBS-3. Svensk Kärnbränslehantering AB.
- SKB, 1992.** SKB 91 – Final disposal of spent nuclear fuel, Importance of the bedrock for safety. SKB TR-92-20, Svensk Kärnbränslehantering AB.
- SKB, 1999.** Deep repository for spent nuclear fuel. SR 97 – Post-closure safety. Main Report – Volume I, Volume II and Summary. SKB TR-99-06, Svensk Kärnbränslehantering AB.
- SKB 2010.** Fuel and canister process report for the safety assessment SR-Site. SKB TR-10-46, Svensk Kärnbränslehantering AB.
- SKB, 2011.** Long-term safety for the final repository for spent nuclear fuel at Forsmark. Main report of the SR-Site project. SKB TR-11-01, Svensk Kärnbränslehantering AB.
- Skelton A, Mansfeld J, Ahlin S, Lundqvist T, Linde J, Nilsson J, 2018.** A compilation of metamorphic pressure–temperature estimates from the Svecofennian province of eastern and central Sweden. *Geologiska Föreningen i Stockholm Förhandlingar* 140, 1–10.
- Skiöld T, 1986.** On the age of the Kiruna Greenstones, northern Sweden. *Precambrian Research* 32, 35–44.

- Skiöld T, 1987.** Aspects of the Proterozoic geochronology of northern Sweden. *Precambrian Research* 35, 161–167.
- Skiöld T, 1988.** Implications of new U-Pb zircon chronology to early Proterozoic crustal accretion in northern Sweden. *Precambrian Research* 38, 147–164.
- Smart N R, Blackwood D J, Werme L, 2002.** Anaerobic corrosion of carbon steel and cast iron in artificial groundwaters: Part 1 – Electrochemical aspects. *Corrosion* 58, 547–559.
- Smith M P, Storey C D, Jeffries T E, Ryan C, 2009.** In situ U–Pb and trace element analysis of accessory minerals in the Kiruna district, Norrbotten, Sweden: new constraints on the timing and origin of mineralisation. *Journal of Petrology* 50, 2063–2094.
- Smith M P, Gleeson S A, Yardley B W D, 2013.** Hydrothermal fluid evolution and metal transport in the Kiruna District, Sweden: Contrasting metal behaviour in aqueous and aqueous–carbonic brines. *Geochimica et Cosmochimica Acta* 102, 89–112.
- Smith P A, Schatz T, Reijonen H M, Hellä P, 2017.** Chemical erosion and mass redistribution of bentonite in a KBS-3H repository. Posiva report 2016-12, Posiva, Finland.
- Środoń J, 1980.** Precise identification of illite/smectite interstratifications by X-ray powder diffraction. *Clays and Clay Minerals*, 28, 401–411.
- Steiger R H, Jäger E, 1977.** Sub-commission on Geochronology: Convention on the use of decay constants in geo- and cosmochronology. *Earth and Planetary Science Letters*, 36, 359–362.
- Stein H J, Morgan J W, Scherstén A, 2000.** Re-Os dating of low-level highly-radiogenic (LLHR) sulfides: the Harnäs gold deposit, southwest Sweden records continental scale tectonic events: *Economic Geology*, 95, 1657–1671. <https://doi.org/10.2113/gsecongeo.95.8.1657>
- Stephens E C, Anderson J R, Gullett-Young C, Wampler J M, Elliott W C, 2007.** Age of the Ocmulgee Limestone (Georgia Coastal Plain) based on revised methodology for the K-Ar age of glaucony. *Southeastern Geology*, 45, 15–24.
- Stookey L L, 1970.** Ferrozine – a new spectrophotometric reagent for iron. *Anal Chem* 42, 779–781. <https://doi.org/10.1021/ac60289a016>
- Storey C D, Smith M P, Jeffries T E, 2007.** In situ LA-ICP-MS U–Pb dating of metavolcanics of Norrbotten, Sweden: Records of extended geological histories in complex titanite grains. *Chemical Geology* 240, 163–181.
- Stroes-Gascoyne S, 1989.** The Potential for Microbial Life in a Canadian High Level Fuel Waste Disposal Vault: A Nutrient and Energy Source Analysis. Atomic Energy of Canada Limited (AECL) Report, AECL-9574. AECL, Chalk River, Canada.
- Stroes-Gascoyne S, 2010.** Microbial occurrence in bentonite-based buffer, backfill and sealing materials from large-scale experiments at AECL's Underground Research Laboratory. *Applied Clay Science*, 47, 36–42.
- Stroes-Gascoyne S, Hamon C J, Maak P, Russell S, 2008.** The effects of the physical properties of highly compacted smectite clay (bentonite) on the culturability of indigenous microorganisms. *Appl. Clay. Sci.* doi:10.1016/j.clay.2008.06.010
- Svensson D, Eriksson P, Johannesson L-E, Lundgren C, Bladström T. 2019.** Development and testing of methods suitable for quality control of bentonite as KBS-3 buffer and backfill. SKB TR-19-25, Svensk Kärnbränslehantering AB.
- Takagi T, Koh S M, Song S, Itoh M, Mogi K, 2005.** Geology and properties of the Kawasaki and Dobuyama bentonite deposits of Zao region in northeastern Japan. *Clay Minerals*, 40, 333–350.
- Talbot C J, Koyi H, 1995.** Palaeoproterozoic intraplating exposed by resultant gravity overturn near Kiruna, northern Sweden. *Precambrian Research* 72, 199–225.
- Troll V R, Weis F A, Jonsson E, Andersson U B, Majidi S A, Högdahl K, Harris C, Millet M-A, Chinnasamy S S, Koojiman E, Nilsson, K P, 2019.** Global Fe–O isotope correlation reveals magmatic origin of Kiruna-type apatite-iron-oxide ores. *Nature communications* 10, 1712.

- Tschech A, Pfennig N, 1984.** Growth yield increase linked to caffeine reduction in *Acetobacterium woodii*. *Archives of Microbiology*, 137, 163–167.
- Usman M O, Simpson M J, 2021.** Assessment of the molecular-level compositional heterogeneity of natural organic matter in bentonites intended for long-term used nuclear fuel storage. *Organic Geochemistry* 152, 104166
- USNRC, 1957.** The disposal of radioactive waste on land. Publication 519, USNAS-National Research Council, Washington, USA.
- Vieno T, Nordman H, 1999.** Safety assessment of spent fuel disposal in Hästholmen, Kivetty, Olkiluoto and Romuvaara – TILA-99. POSIVA 99-07, Posiva, Finland.
- Vieno T, Hautajärvi A, Koskinen L, Nordman H, 1992.** TVO-92 safety analysis of spent fuel disposal. YJT-92-33E. Nuclear Waste Commission of Finnish Power Companies (YJT), Finland.
- Vieno T, Lehikoinen J, Löfman J, Nordman H, Mészáros, F. 2003.** Assessment of disturbances caused by construction and operation of ONKALO. Posiva Report 2003-06, Posiva, Finland.
- Vollmer F W, Wright S F, Huddleston P J, 1984.** Early deformation in the Svecokarelian greenstone belt of the Kiruna district, northern Sweden. *Geologiska Föreningens i Stockholm Förhandlingar* 106, 109–118.
- Wegner C E, Stahl R et al. 2023.** A glimpse of the paleome in endolithic microbial communities. *Microbiome* 11, 210. <https://doi.org/10.1186/s40168-023-01647-2>
- Welin E, 1980.** Tabulation of recalculated radiometric ages published 1960–1979 for rocks and minerals in Sweden. *Geologiska Föreningen i Stockholm Förhandlingar* 101, 309–320.
- Welin E, 1987.** The depositional evolution of the Svecofennian supracrustal sequence in Finland and Sweden. *Precambrian Research* 35, 95–113.
- Welin E, Christiansson K, Nilsson Ö, 1971.** Rb-Sr radiometric ages of extrusive and intrusive rocks in northern Sweden. *Sveriges geologiska undersökning C* 666, 1–38. Geological Survey of Sweden, Sweden
- Wersin P, Birgersson M, Olsson S, Karnland, O, Snellman, M, 2008.** Impact of corrosion-derived iron on the bentonite buffer within the KBS-3H disposal concept. The Olkiluoto site as case study. SKB R-08-34, Svensk Kärnbränslehantering AB.
- Wersin P, Hadi J et al. 2023.** Unravelling the corrosion processes at steel/bentonite interfaces in in situ tests. *Materials and Corrosion* 74, 1716–1727.
- Westerstrand M, 2009.** The process water geochemistry at the Kiirunavaara iron mine, northern Sweden. Unpubl. Masters thesis, Luleå University of Technology, Sweden.
- Westhues A, Hanchar J M, Whitehouse M J, Martinsson O, 2016.** New constraints on the timing of host rock emplacement, hydrothermal alteration, and iron oxide-apatite mineralisation in the Kiruna district, Norrbotten, Sweden. *Economic Geology* 111, 1595–1618.
- Westhues A, Hanchar J M, Voisey C R, Whitehouse M J, Rossman G R, Wirth R, 2017a.** Tracing the fluid evolution of the Kiruna iron oxide apatite deposits using zircon, monazite, and whole rock trace elements and isotopic studies. *Chemical Geology* 466, 303–322.
- Westhues A, Hanchar J M, LeMessurier M J, Whitehouse M J, 2017b.** Evidence for hydrothermal alteration and source regions for the Kiruna iron oxide-apatite ore (northern Sweden) from zircon Hf and O isotopes. *Geology* 45, 571–574.
- Widdel F, 1980.** Anaerober Abbau von Fettsäuren und Benzoesäure durch neu isolierte Arten. Ph.D. thesis, Universität Göttingen, Göttingen, Germany (*in German*).
- Widdel F, Pfennig N, 1981.** Studies on dissimilatory sulfate-reducing bacteria that decompose fatty acids. I. isolation of a new sulfate-reducer enriched with acetate from saline environments. description of *Desulfobacter postgatei* gen. nov. sp. nov. *Archives of Microbiology*, 129, 395–400.
- Wilson J, Alexander W R, Hedström M, Jefferies N, 2016.** Sealing Site Investigation Boreholes: Phase 2. Aspects of longevity of bentonite seals. Amec Foster Wheeler Report 202580/09 Issue P1 for RWM Ltd. NWS, Harwell, UK.

Wright S F, 1988. Early Proterozoic deformational history of the Kiruna district, northern Sweden. Unpubl. Ph.D. thesis, University of Minnesota, Twin Cities of Minneapolis and Saint Paul, Minnesota, USA.

Yan S, Wan B, Andersson U B, 2023a. Apatite age and composition: a key to the geological history of the Malmberget Iron-Oxide-Apatite (IOA) deposit and the region. *J. Geochem. Expl.*, Vol. 252, paper 107267, 12 pp + Suppl.

Yan S, Wan B, Andersson U B, 2023b. Hydrothermal circulation at 1.8 Ga in the Kiruna area, northern Sweden, as revealed by apatite geochemical systematics. *Prec. Res.*, Vol. 395, Article 107151, 12 pp + Suppl.

Appendices

Sample sites

U.B. Andersson and W.R. Alexander, editors

Maps (courtesy of LKAB) of all sample sites in the mine are shown in appendix A. Where possible, sample ID numbers as provided by the authors have been reformulated and are now expressed in the LKAB standard format (of block-mine level).

TUM samples (Chapter 3.2)

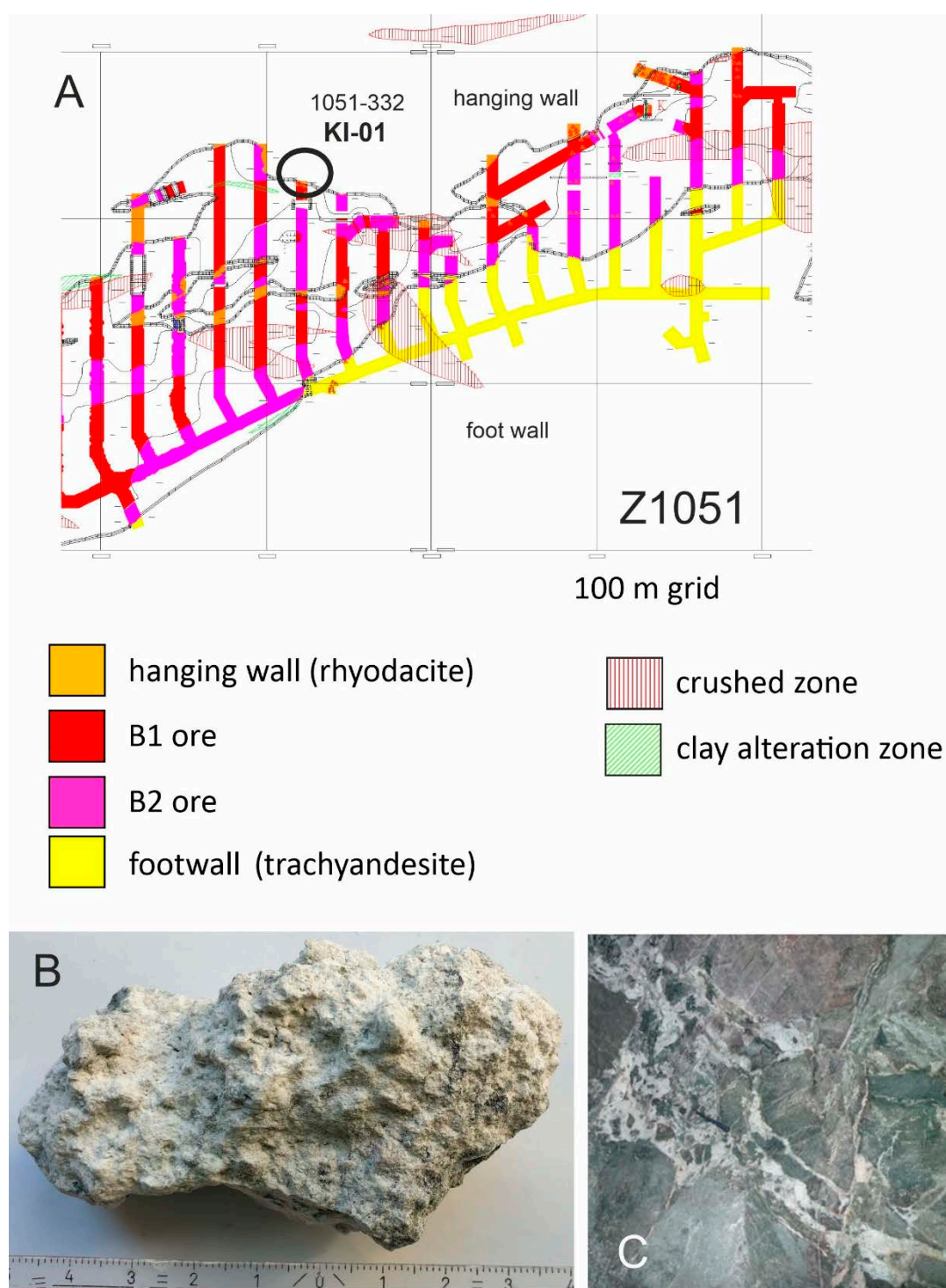


Figure A-1. Sample KI-01, a clay-altered hanging wall meta-rhyodacite a) location, b) hand specimen and c) outcrop (all images H.A. Gilg).

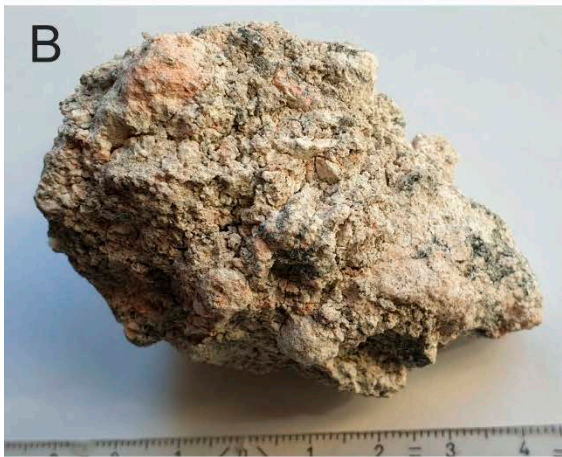
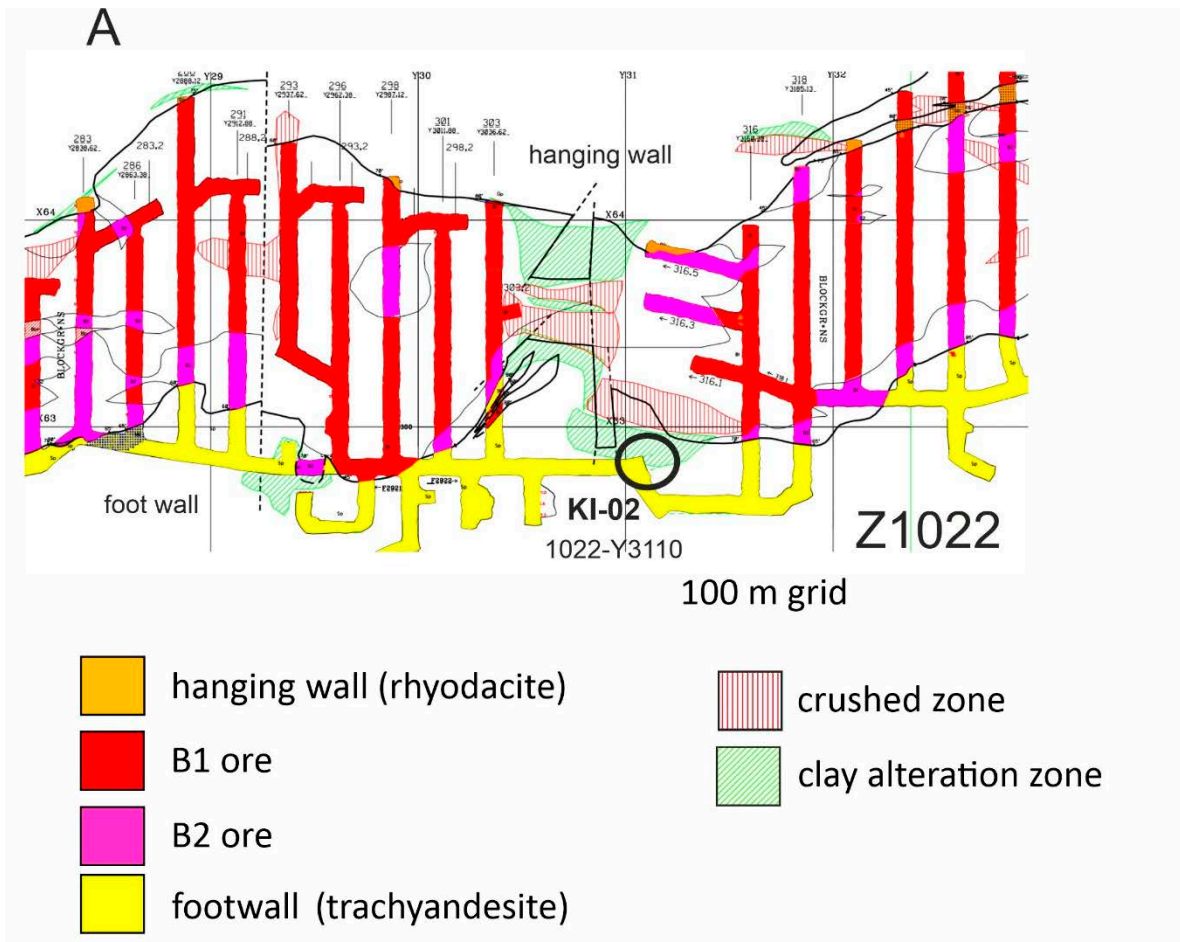


Figure A-2. Sample KI-02, a clay-altered footwall trachyandesite a) location, b) hand specimen (image H.A. Gilg) and c) outcrop (image P. Rieger).

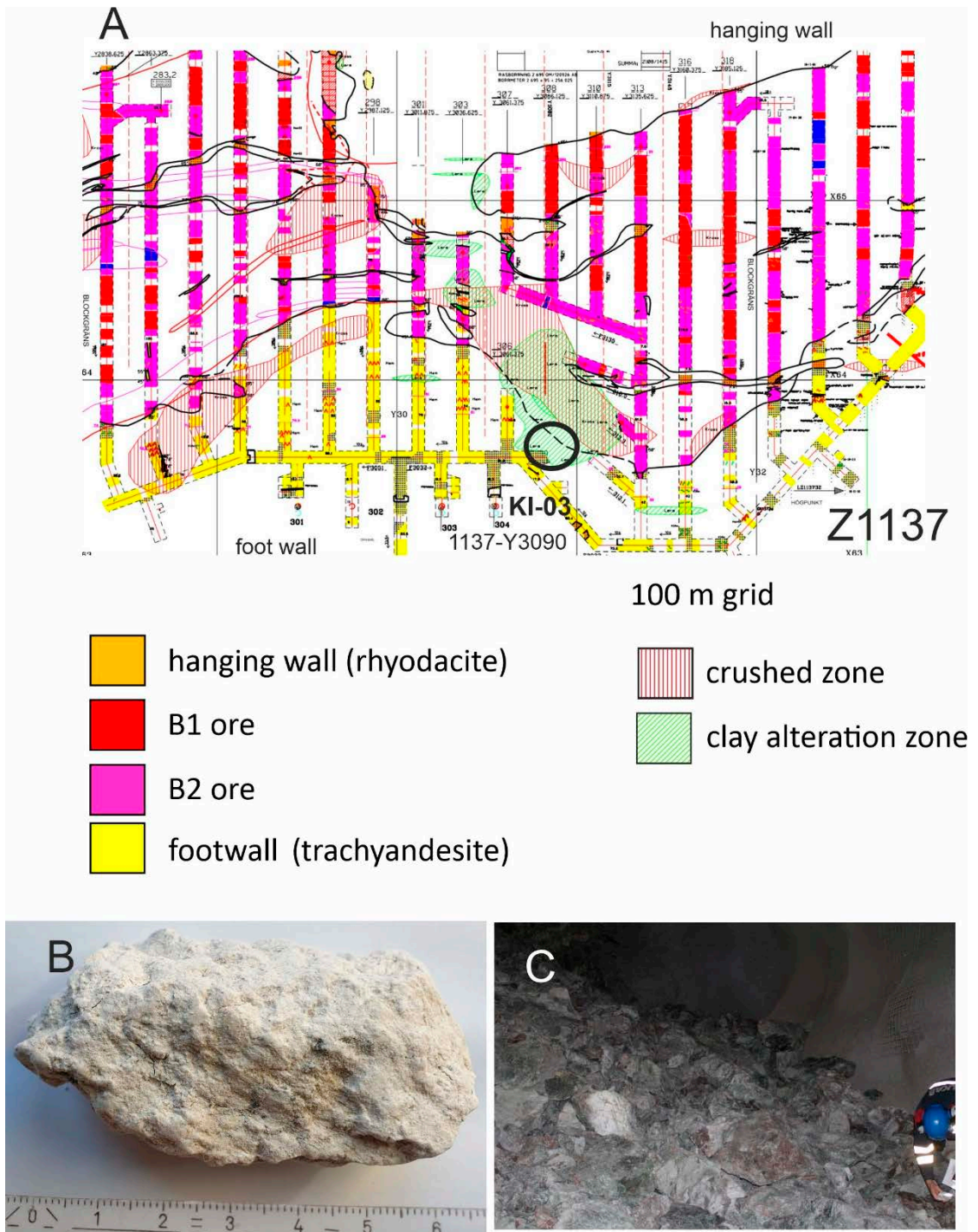


Figure A-3. Sample KI-03, a clay-altered footwall trachyandesite a) location, b) hand specimen and c) outcrop (images H.A. Gilg).

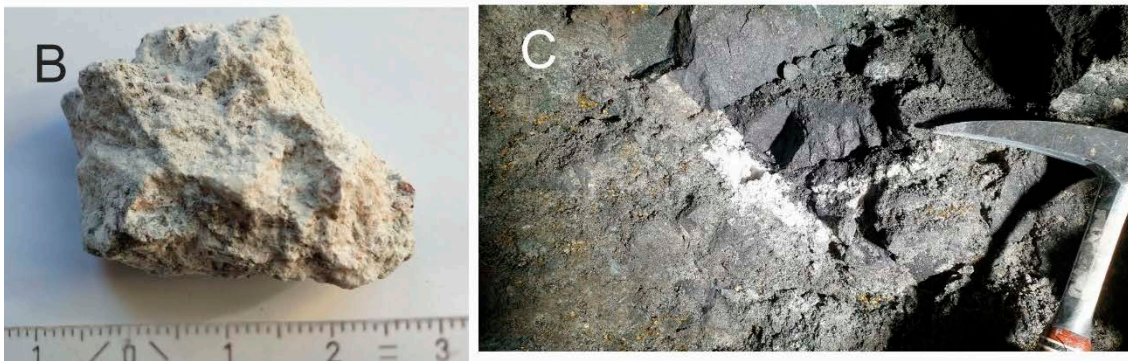
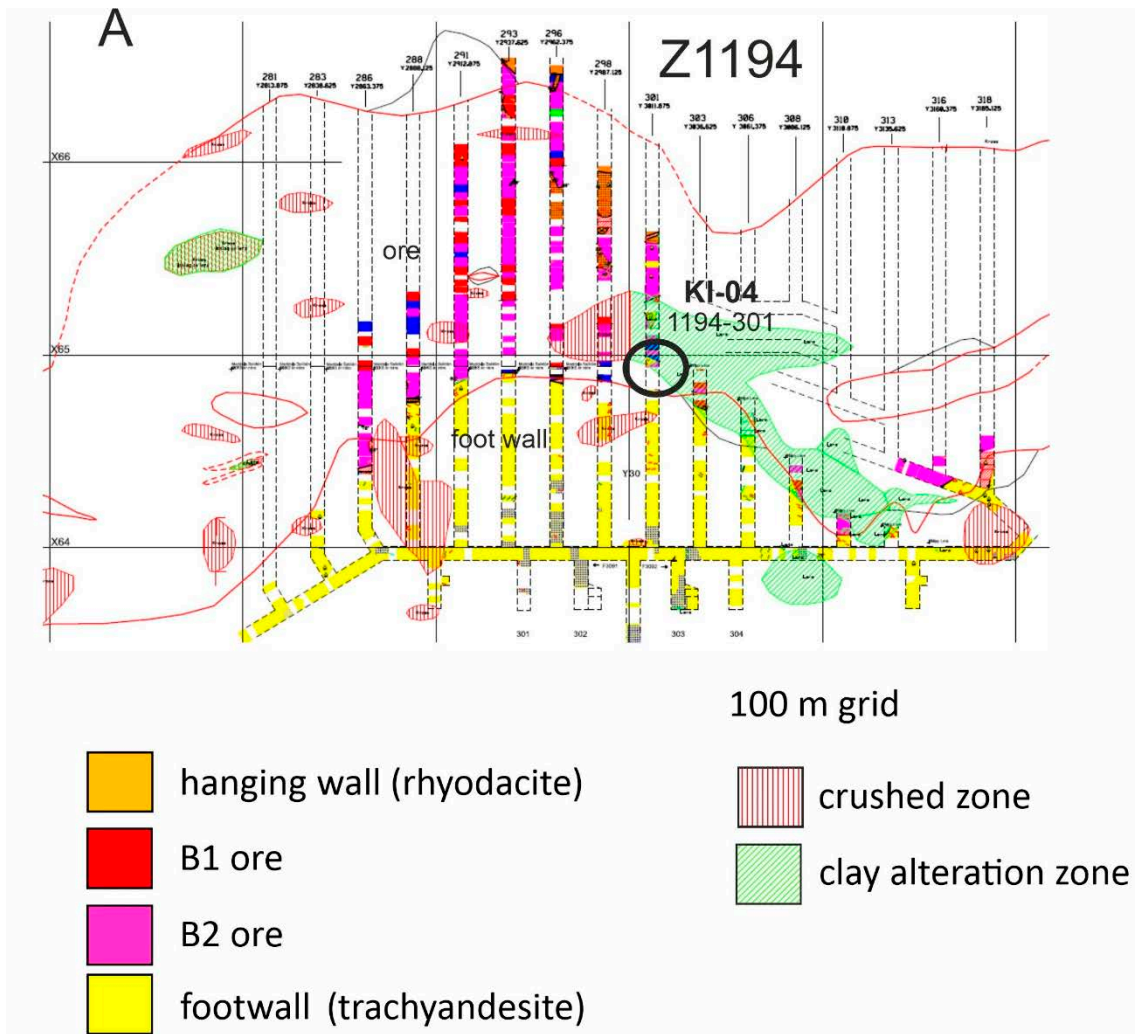


Figure A-4. Sample KI-04, a clay-altered footwall trachyandesite at contact to magnetite ore a) location, b) hand specimen and c) outcrop situation of (images H.A. Gilg).

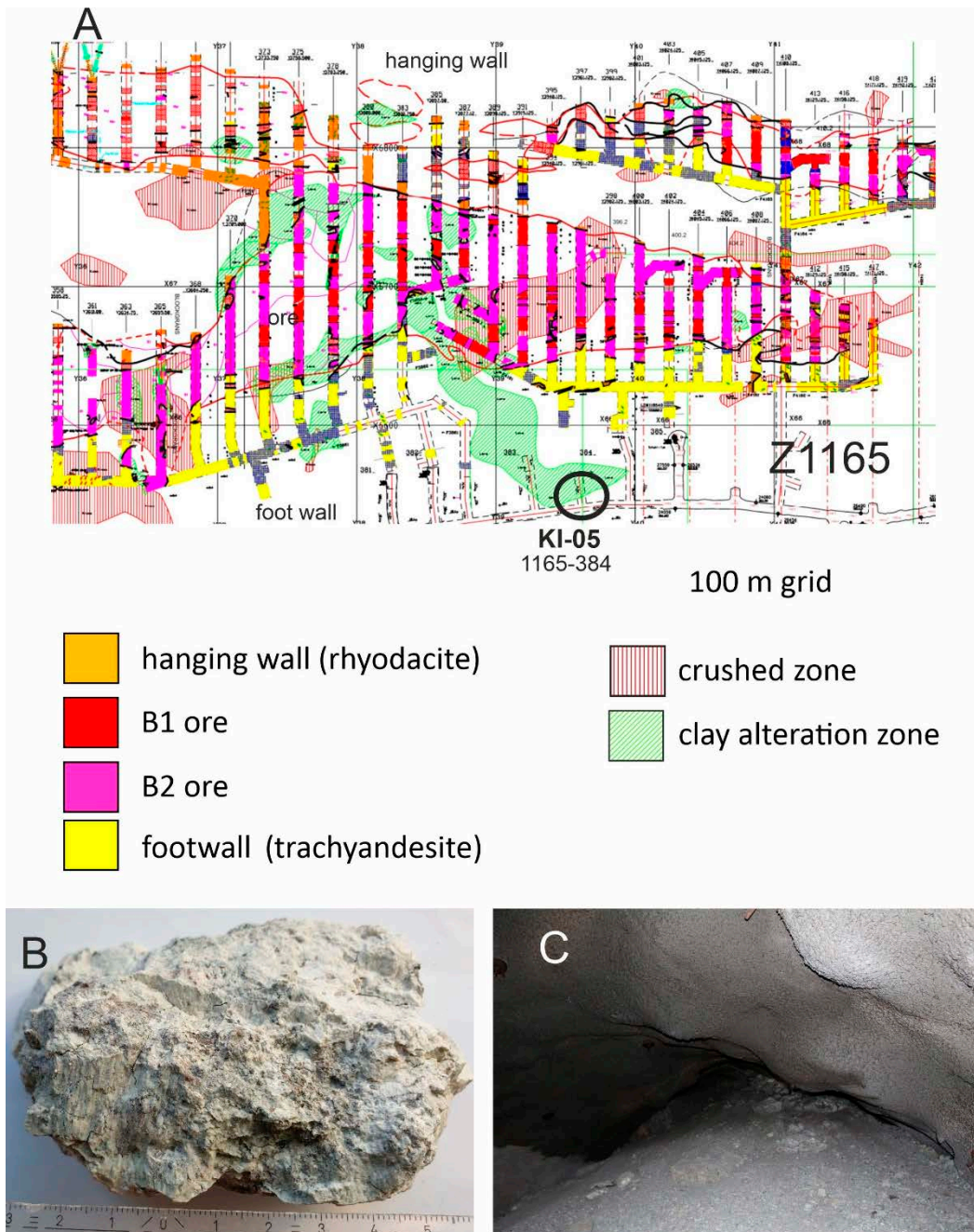


Figure A-5. Sample KI-05, a clay-altered footwall trachyandesite a) location, b) hand specimen and c) outcrop (images H.A. Gilg).

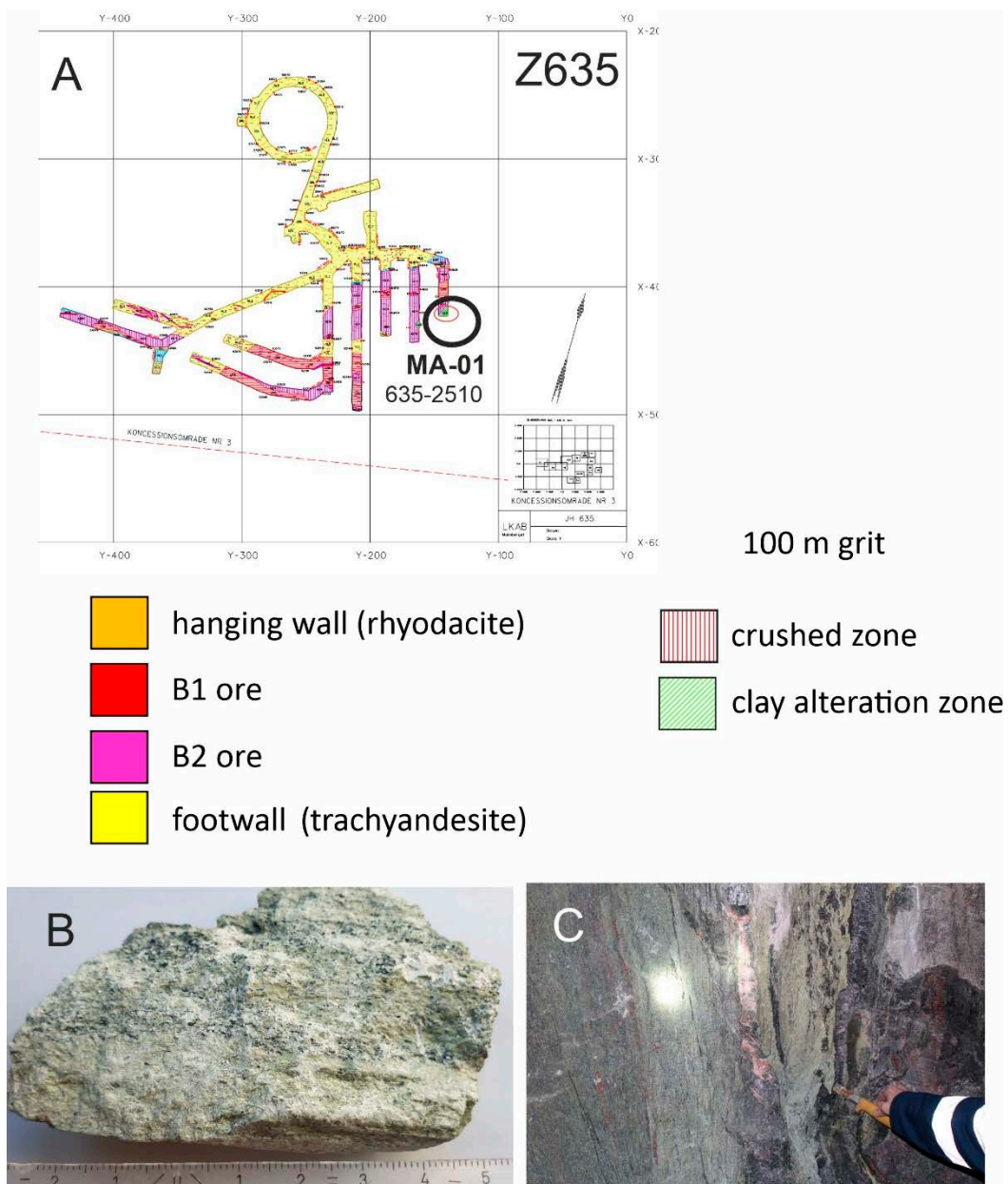


Figure A-6. Sample MA-01, a clay-altered gneiss from the Johannes ore body, Malmberget mine a) location, b) hand specimen and c) outcrop (images H.A. Gilg).

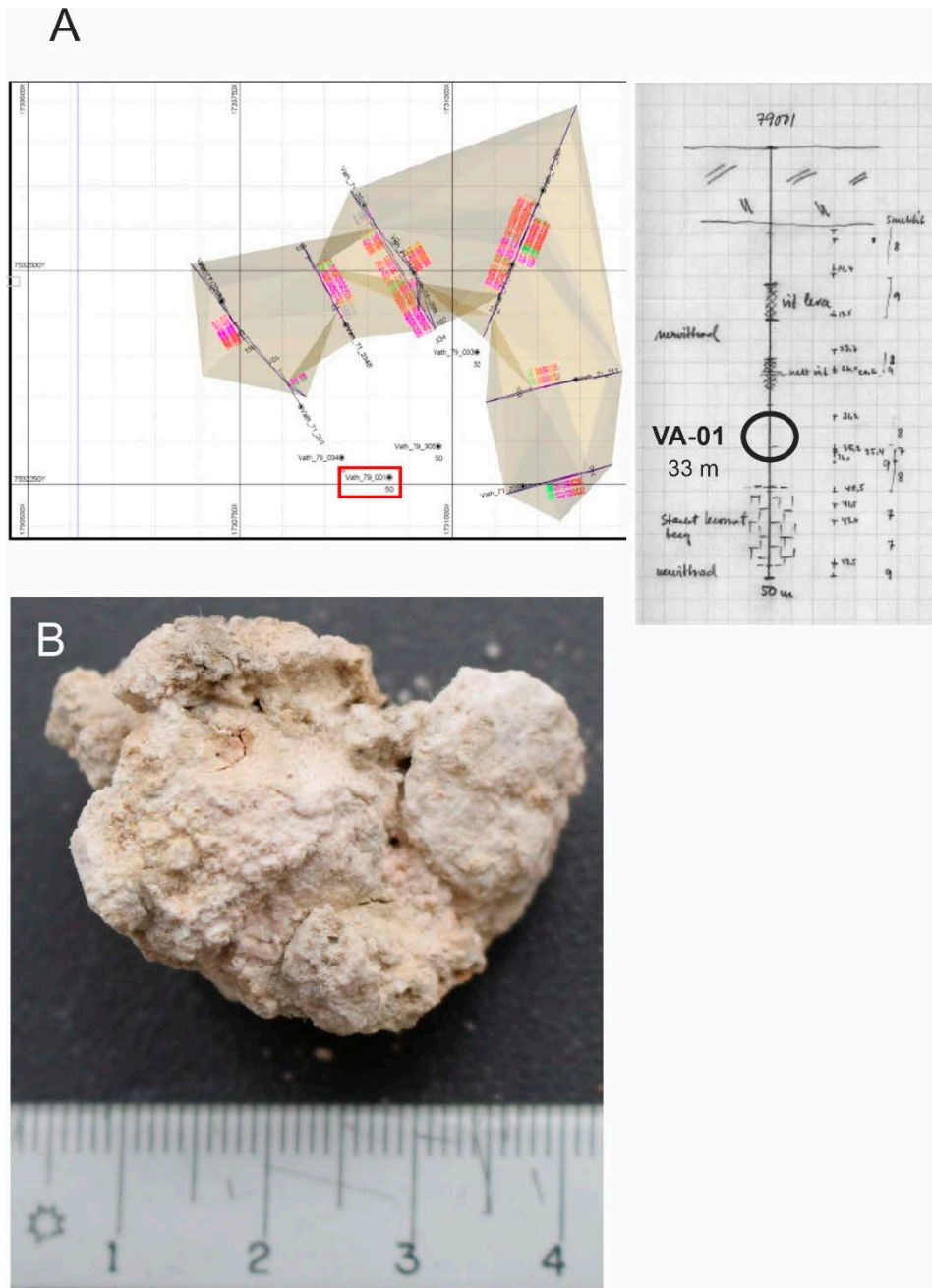


Figure A-7. Sample VA-01, a clay-altered metaandesite from the drill core 79001, Vahtanvaara prospect a) location and b) hand specimen (image H.A. Gilg).

Sample locations of samples from the Kiirunavaara mine described in the various chapters (all maps courtesy of LKAB)

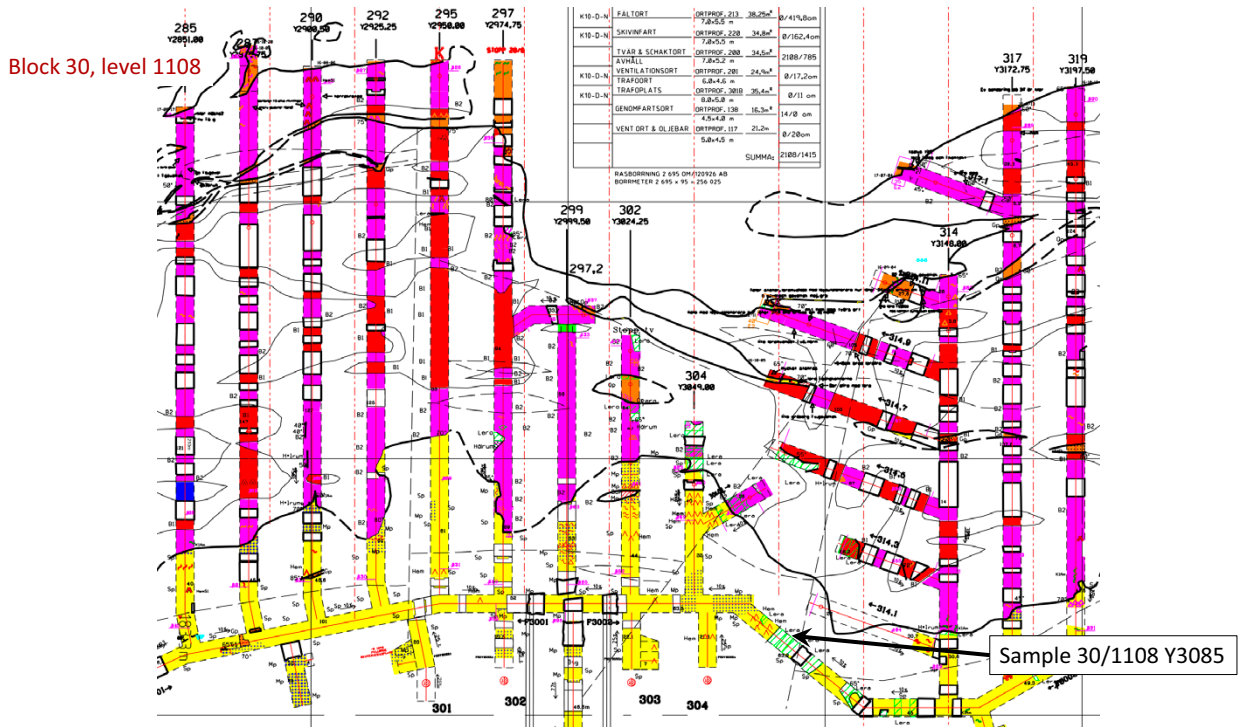


Figure B-1. Block 30, level 1108.

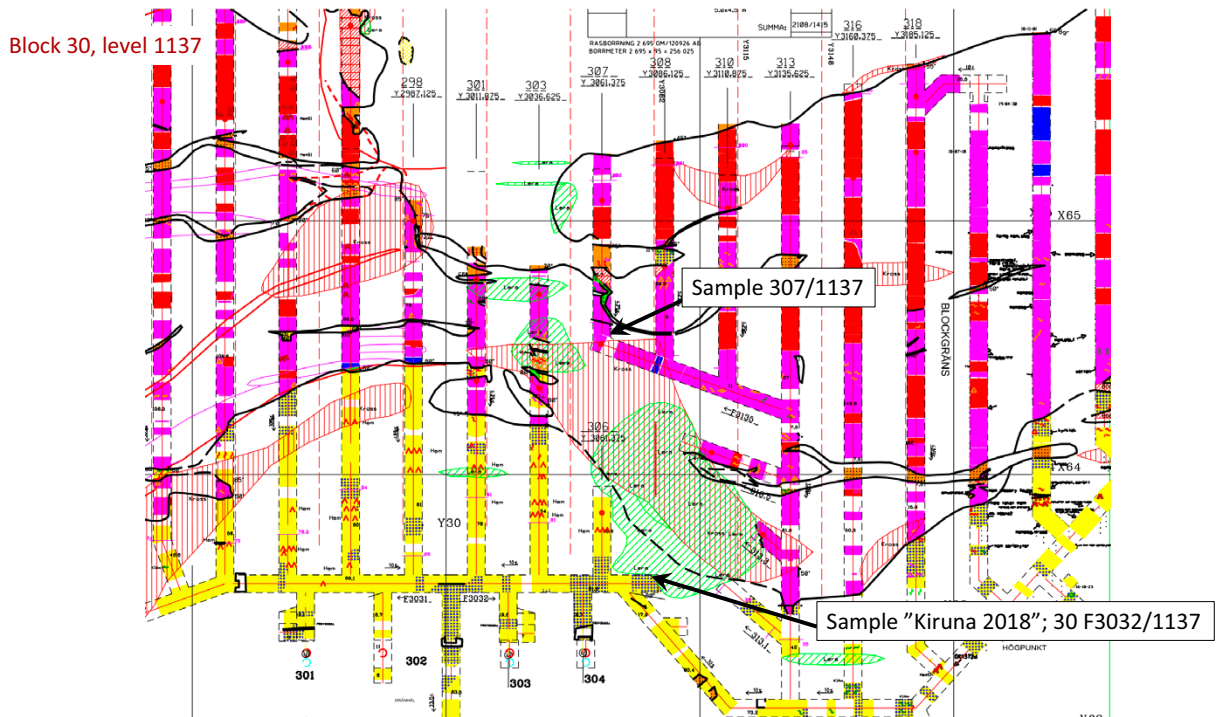


Figure B-2. Block 30, level 1137.

Block 30, level 1165

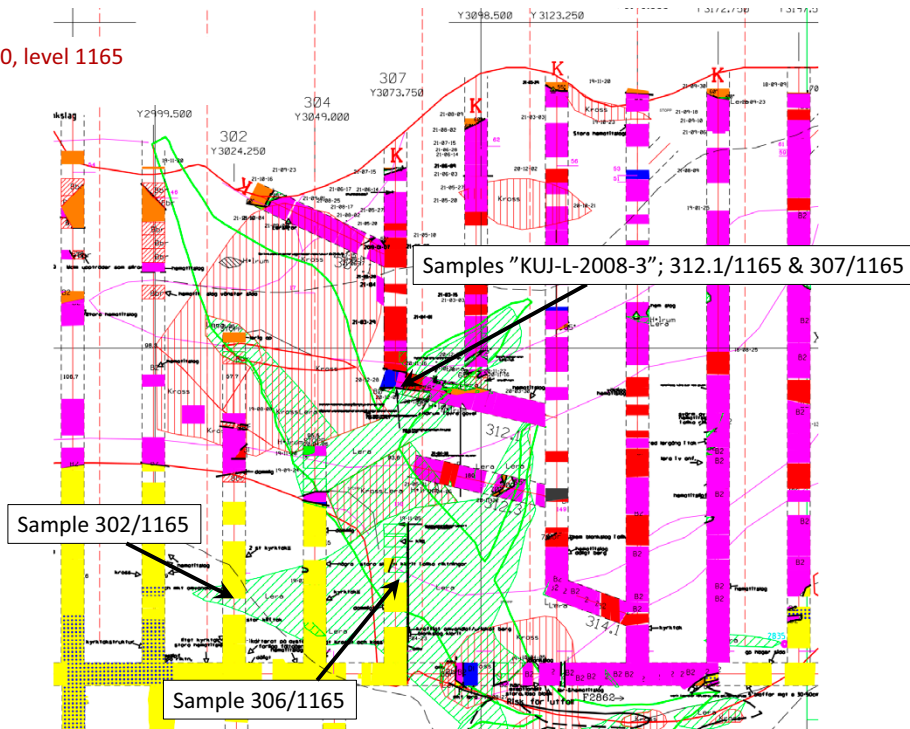


Figure B-3. Block 30, level 1165.

Block 30, level 1194

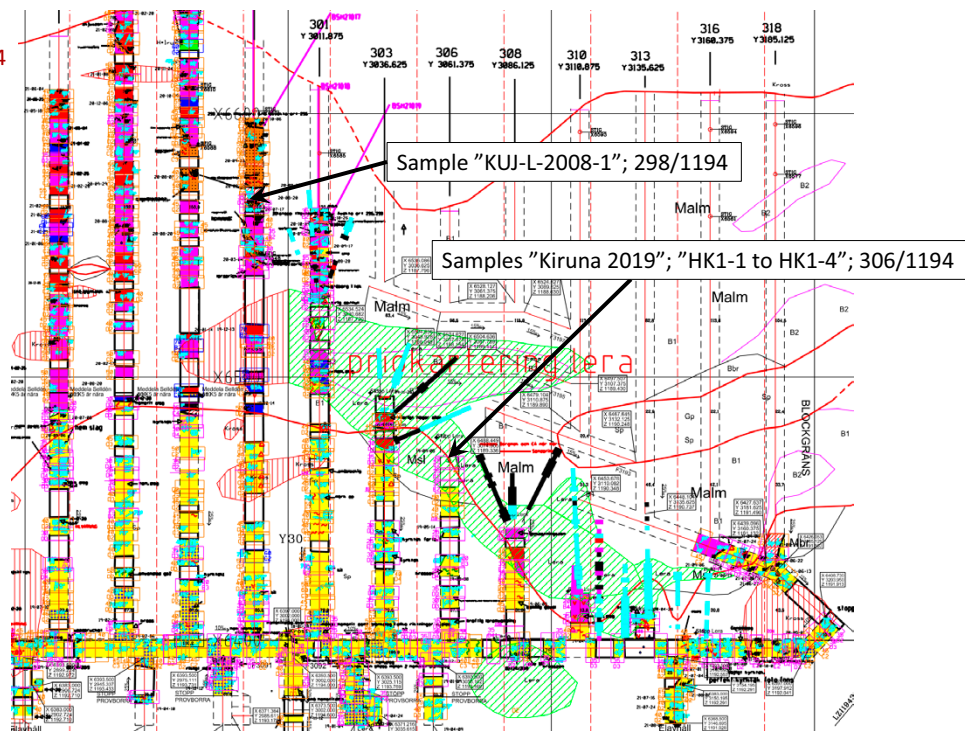


Figure B-4. Block 30, level 1194.

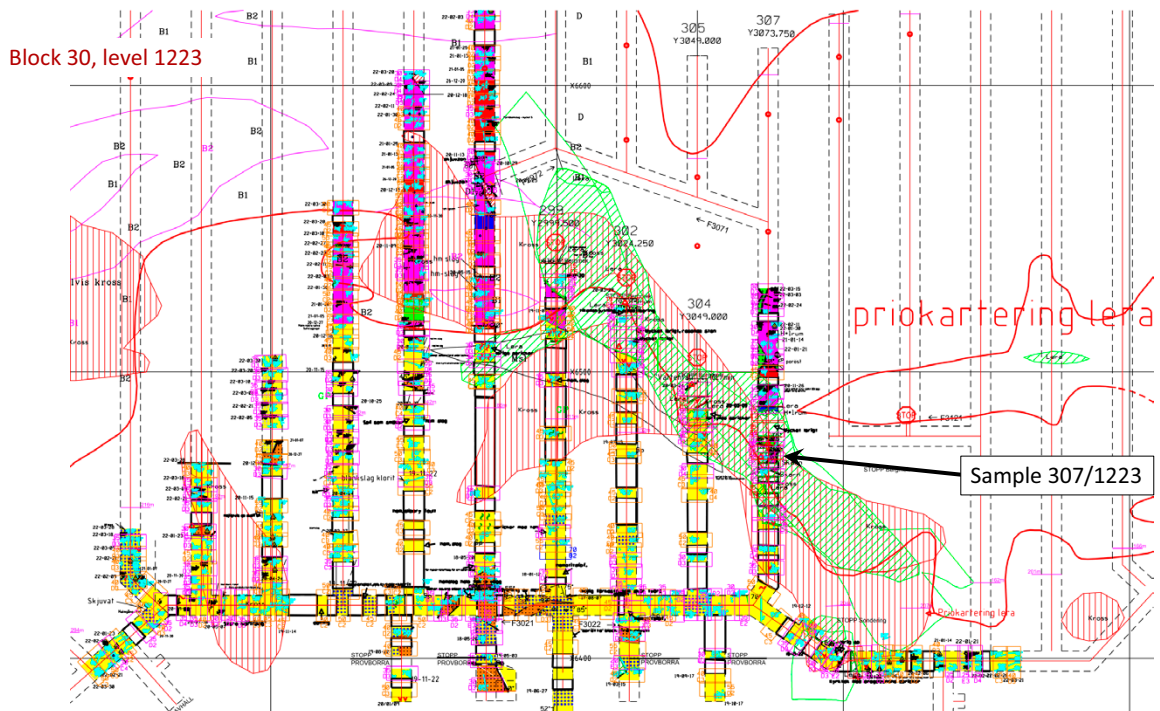


Figure B-5. Block 30, level 1223.

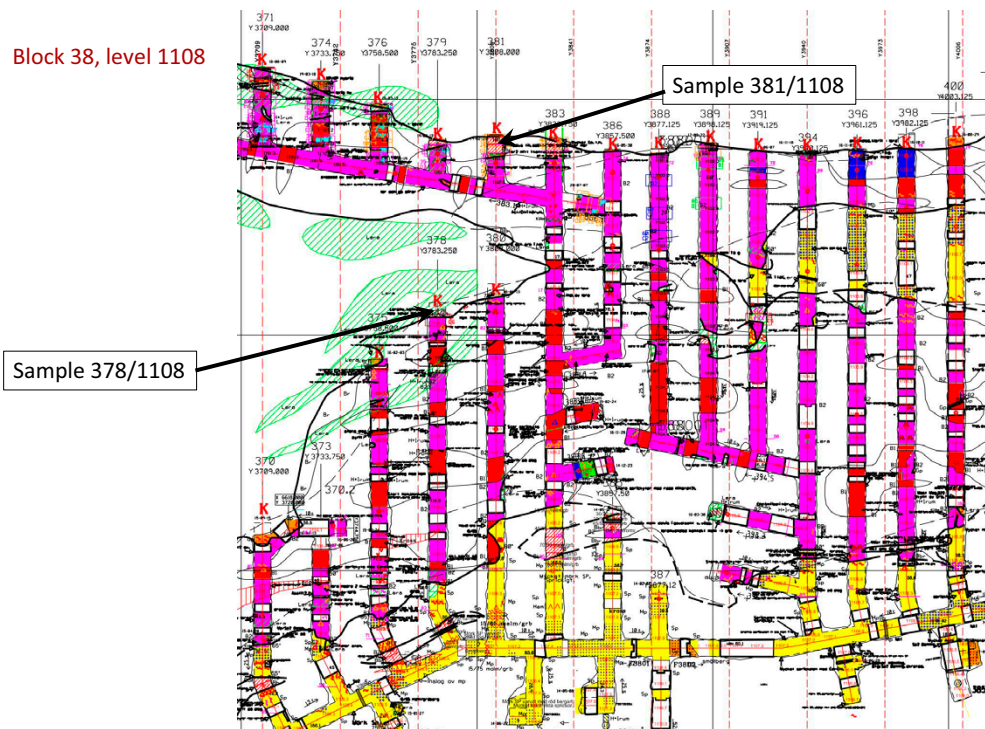


Figure B-6. Block 38, level 1108.

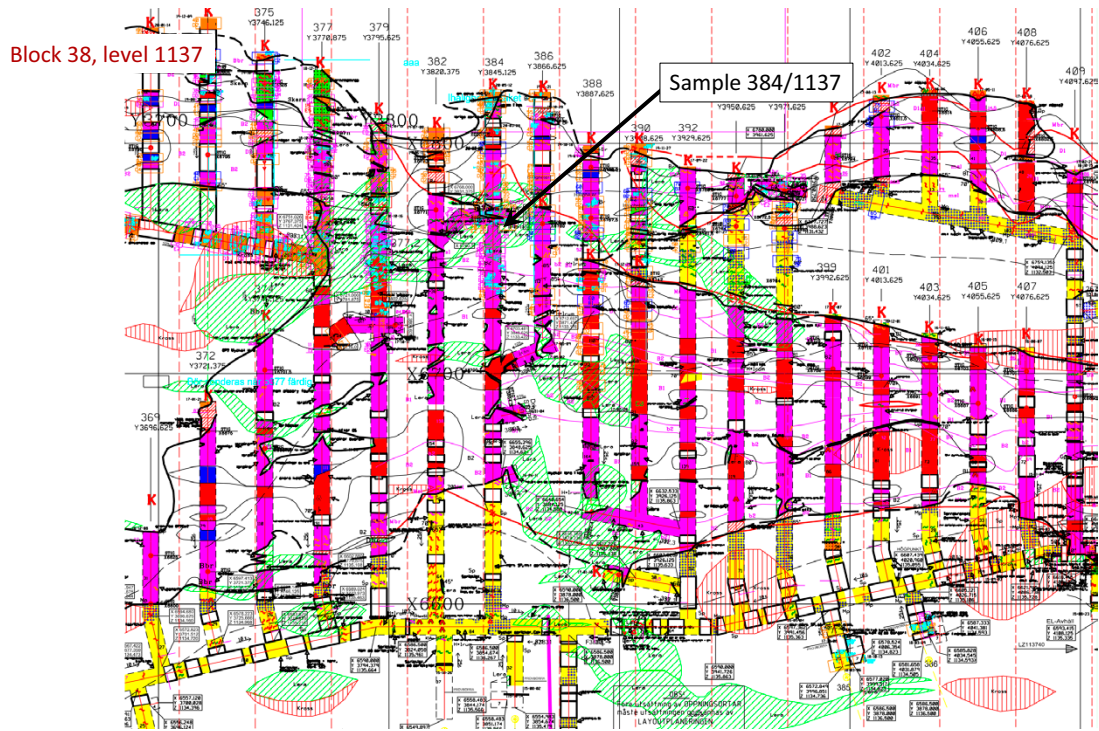


Figure B-7. Block 38, level 1137.

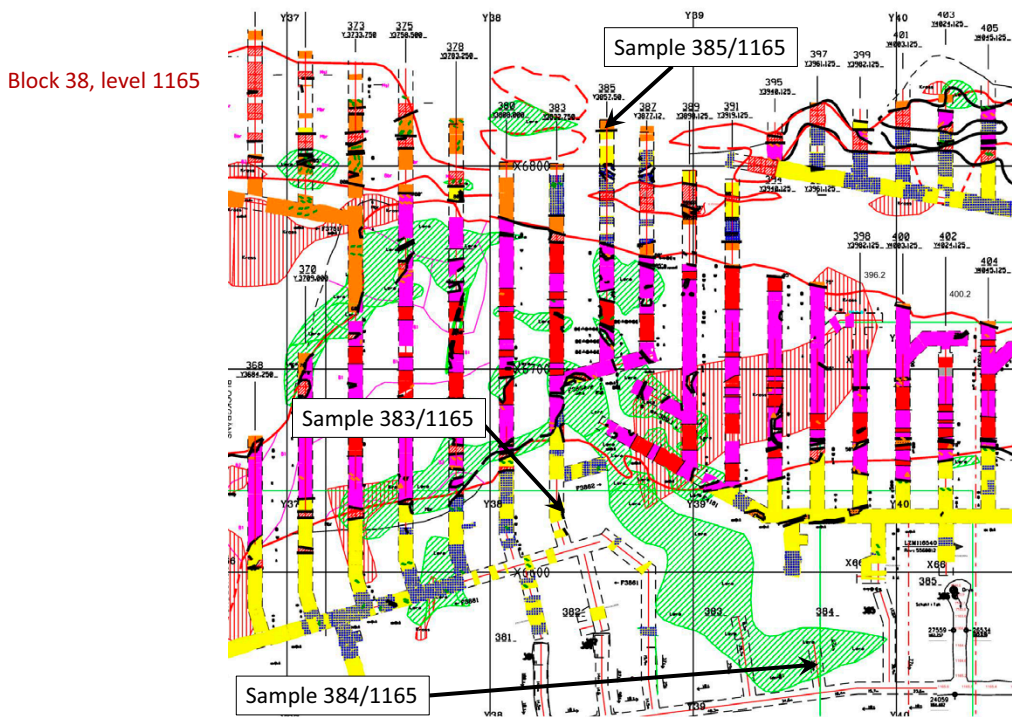


Figure B-8. Block 38, level 1165.

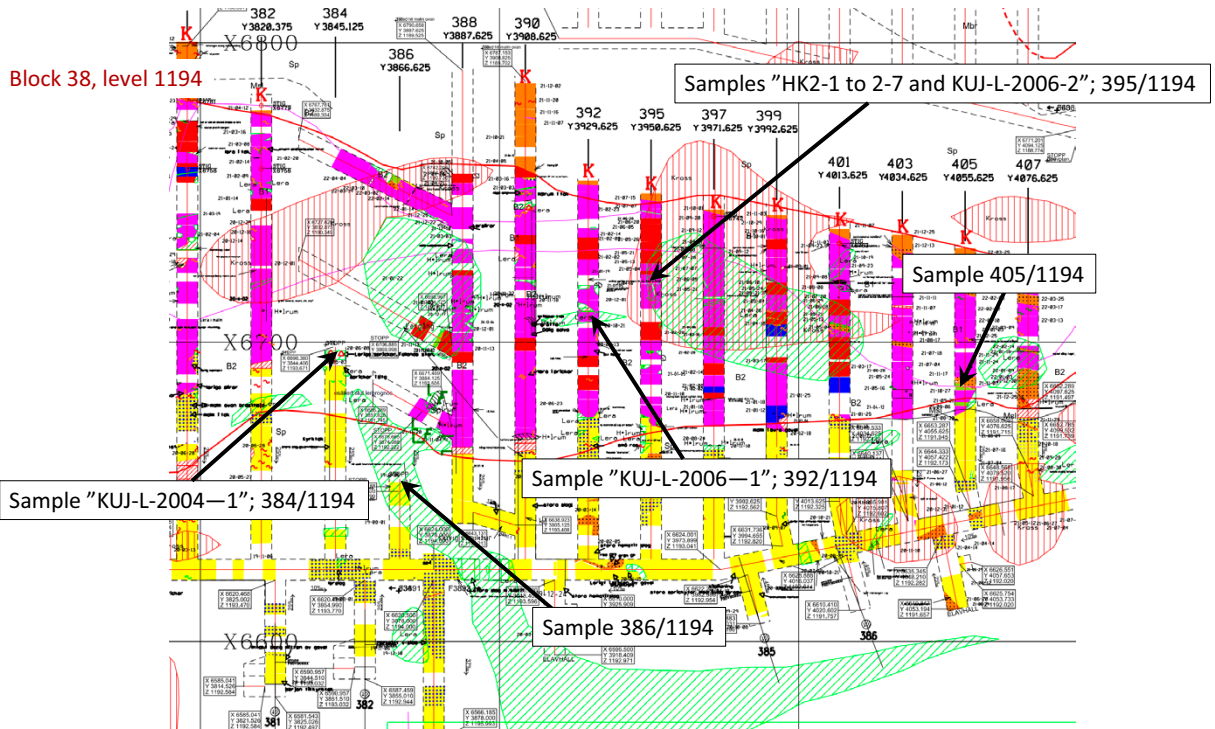


Figure B-9. Block 38, level 1194.

Procedures of separation of clay minerals (M. Szczerba, Polish Academy of Sciences)

C.1 Carbonate removal

1. Reagents:
 - acetate buffer (82 g of sodium acetate and 27 mL of acetic acid, dilute to 1L with deionised water)
 - deionised water
2. Pour 5 g of the sample with deionised water, leave it overnight, and then break it with ultrasounds for 5 min. Centrifuge at 2000 RPM for 15 minutes. Transfer the sample to beakers and pour 50 mL of acetate buffer. Heat up to boiling point and keep on magnetic mixers for 30 min. Then centrifuge at 2000 RPM for 15 min. Repeat the operations 2–4 times (depending on the content of carbonates).

C.2 Removal of organic matter

1. Reagents:
 - mixture of NaOCl (13 %) and HCl – pH ~8–9.
 - deionised water
2. The material is transferred from centrifuge containers to beakers using NaOCl mixture and H₂O and set on magnetic mixers. Add 100 mL of NaOCl mixture and mix until foaming stops (when there is too much of foam production add deionised water). When it is not foamy, add another 100 mL of NaOCl mixture. Keep temperature at 80–85 °C and leave overnight. Spin at 2000 RPM for 15 minutes. After centrifuging, wash the sample with 2x acetate buffer and centrifuge again.

C.3 Removal of iron oxides

1. Reagents:
 - citrate-bicarbonate buffer (88 g of sodium citrate, part / 1L of H₂O; 84 g of sodium bicarbonate, part 1 / H₂O; mixed in a 40: 5 ratio)
 - deionised water
 - sodium dithionite
 - saturated sodium chloride solution,
2. The material is transferred from centrifuge containers to beakers with a buffer citrate – bicarbonate (45 mL of buffer/sample). Raise the temperature of the solution up to 75–80 °C (no more – check with a thermometer in each beaker). Add a teaspoon of sodium dithionite. Stir for 6 minutes. Add another teaspoon of sodium dithionite, stir for 5 minutes, add a third, if there is still the colour of iron oxides (red, brown), do not mix for another 10 minutes. Add 10 mL of saturated sodium chloride solution. Clean by centrifugation.

NOTE to item I.–III. Whenever balancing the centrifuge containers, use the reagent that was used for the operation.

C.4 Separation of fractions

Divide the sample in 1/3: 2/3. Extract a fraction of 2 µm from a 1/3 volume 500 RPM, s/15 min. / in 1L H₂O Repeat the operation twice. From a 2/3 volume, extract a 0.2 µm fraction at 3000 RPM, s/42 min. / in 1L of H₂O. Repeat the operation three times. The 2 µm and 0.2 µm slurries are collected in beakers and coagulated with saturated sodium chloride solution and left to stand overnight. Then levitate the water from the sludge of the fractions. The material remaining on the bottom is transferred with deionised water for centrifuge containers and centrifuge at 2000 RPM, s for 10 min. After centrifugation, transfer the material to dialysis bags and place them in large beakers containing deionised water. Dialyze the samples until they obtain the purity of deionised water (checked with a conductometer).

TUM X-ray diffractograms for bulk samples

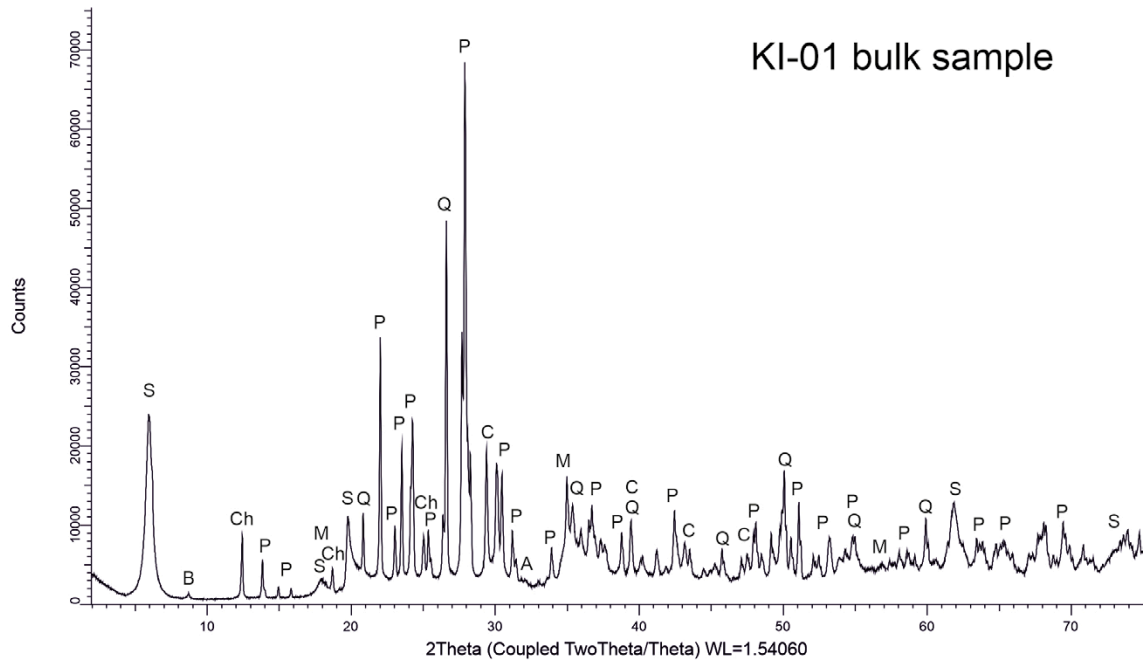


Figure D-1. XRD pattern of bulk sample KI-01. A: fluor-apatite, B: phlogopite, C: calcite, Ch: chlorite, M: magnetite, P: albite, Q: quartz, S: montmorillonite.

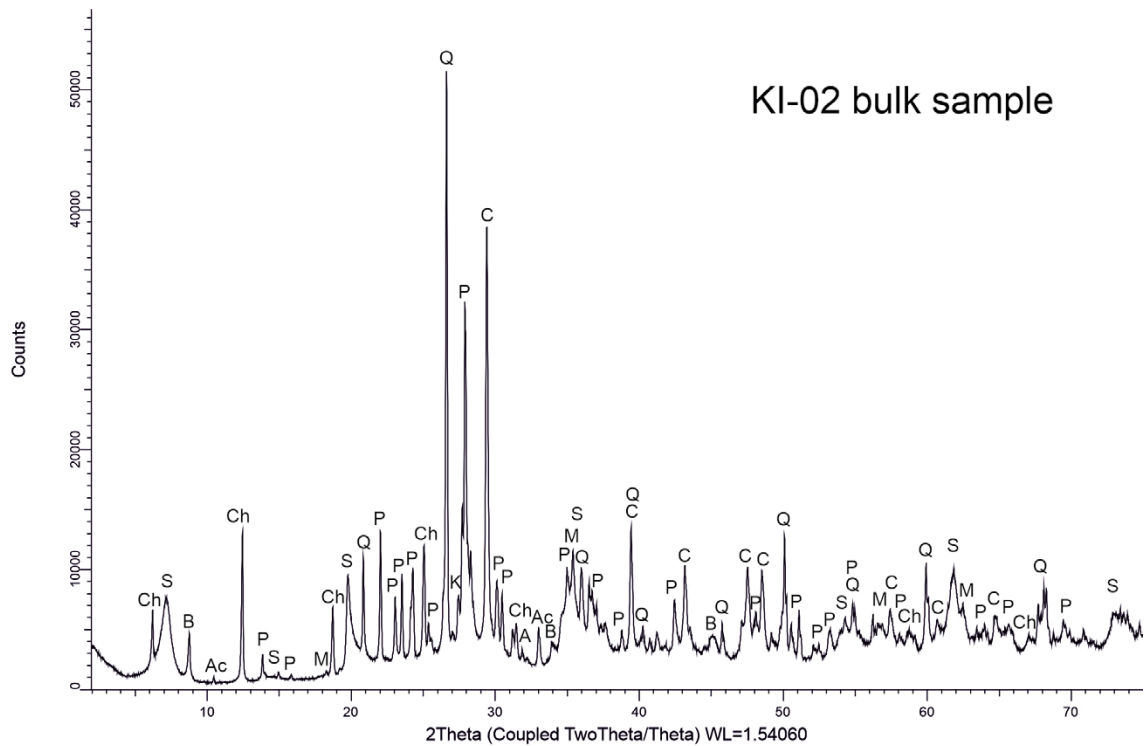


Figure D-2. XRD pattern of bulk sample KI-02. A: fluor-apatite, Ac: actinolite, B: phlogopite, C: calcite, Ch: chlorite, K: microcline, M: magnetite, P: albite, Q: quartz, S: montmorillonite.

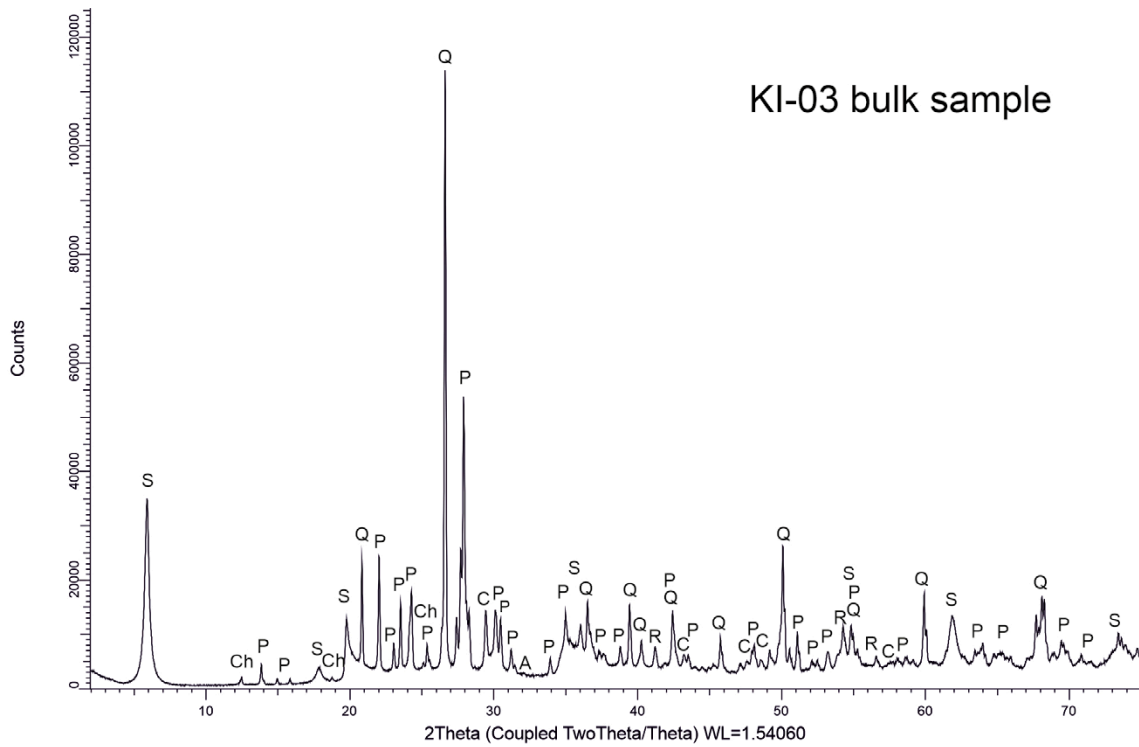


Figure D-3. XRD pattern of bulk sample KI-03. A: fluor-apatite, C: calcite, Ch: chlorite, P: albite, Q: quartz, R: rutile, S: montmorillonite.

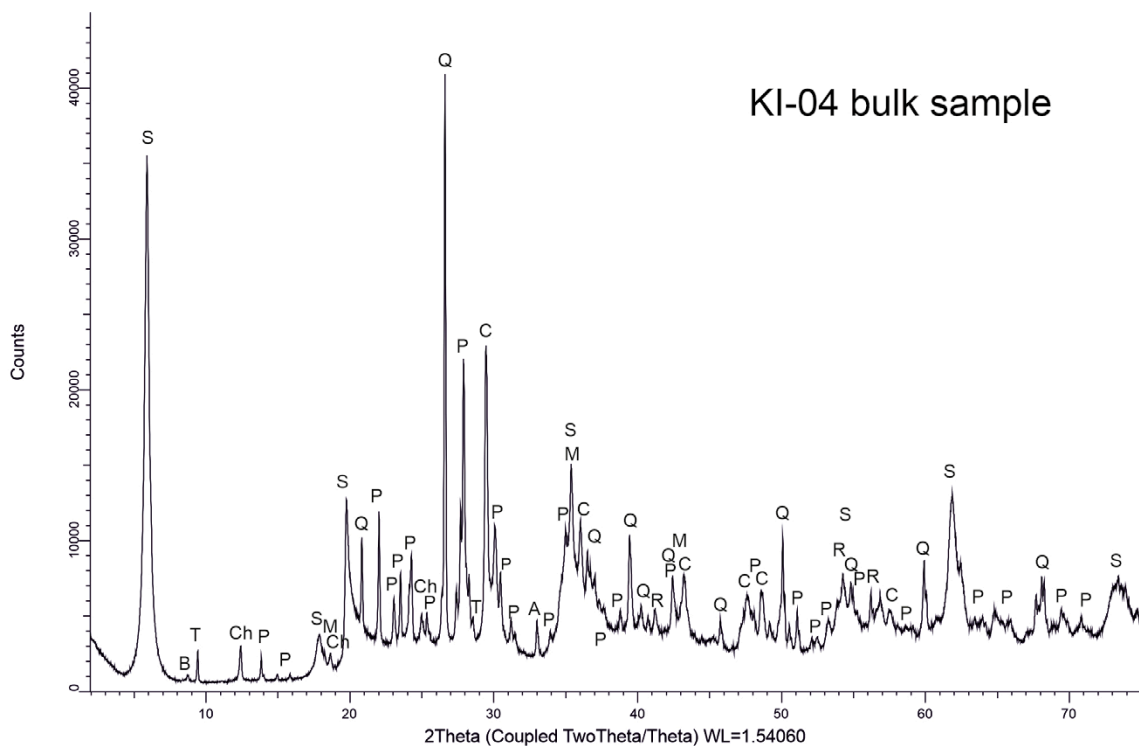


Figure D-4. XRD pattern of bulk sample KI-04. A: fluor-apatite, B: phlogopite, C: calcite, Ch: chlorite, M: magnetite, P: albite, Q: quartz, S: montmorillonite, T: talc.

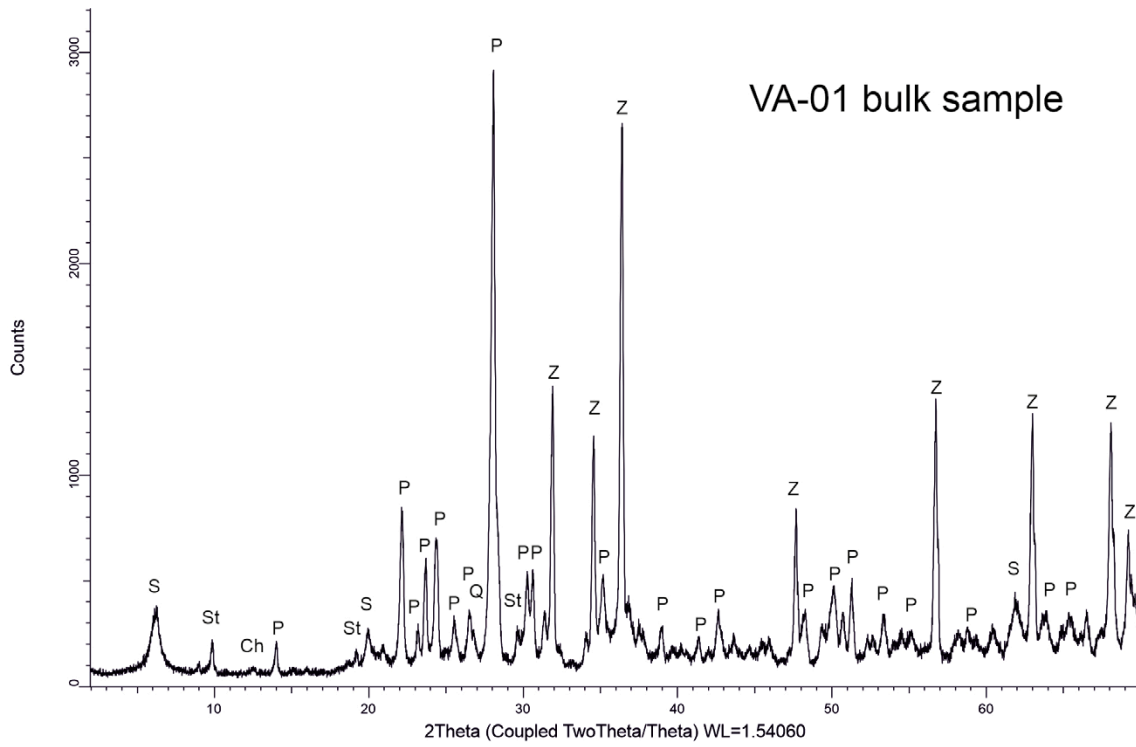


Figure D-7. XRD pattern of bulk sample VA-01. Ch: chlorite, P: albite, Q: quartz, S: montmorillonite, St: Stilbite, Z: zincite (added as internal standard at 20 wt%).

TUM X-ray diffractograms for separated ultrafine fractions

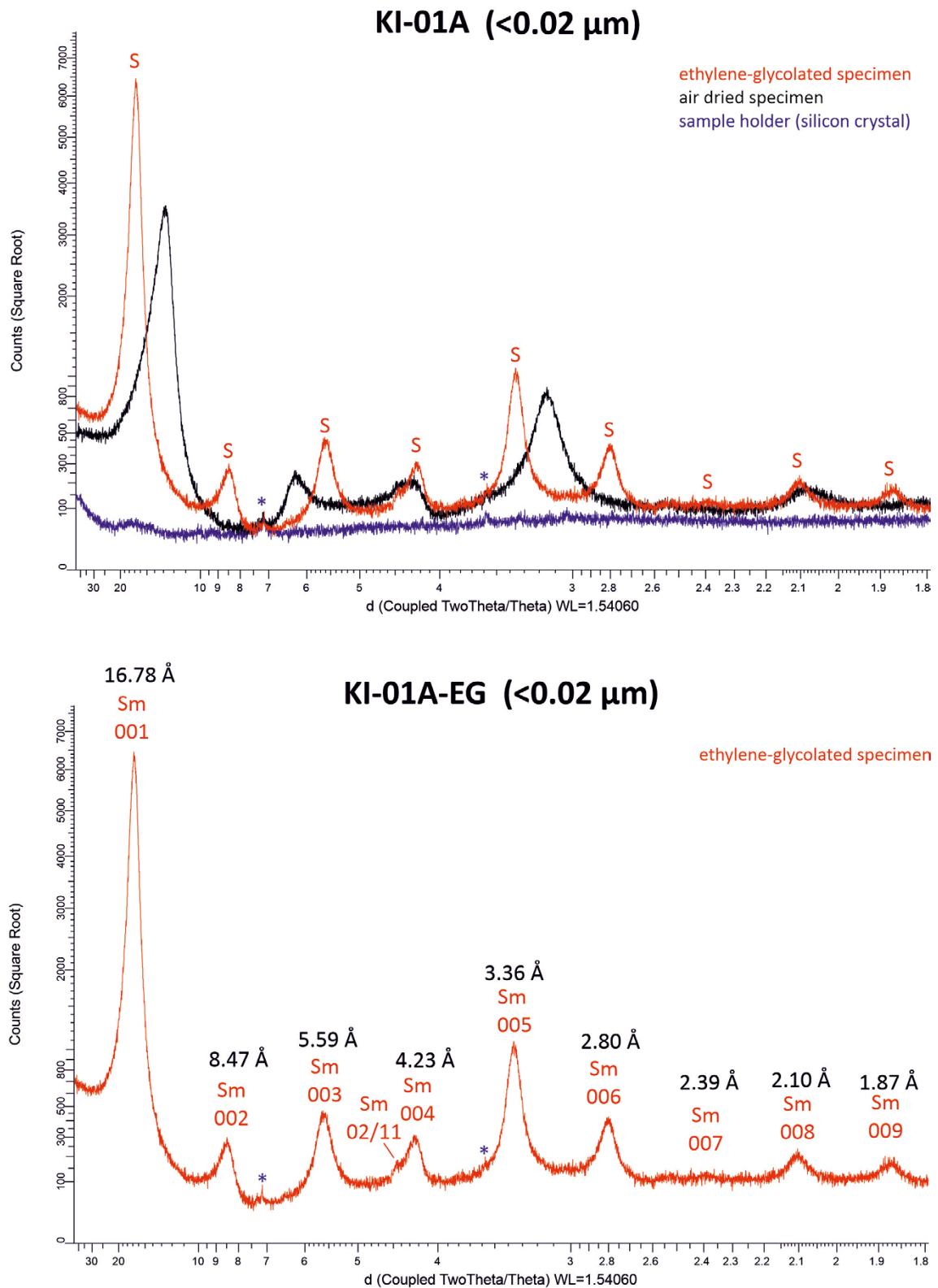
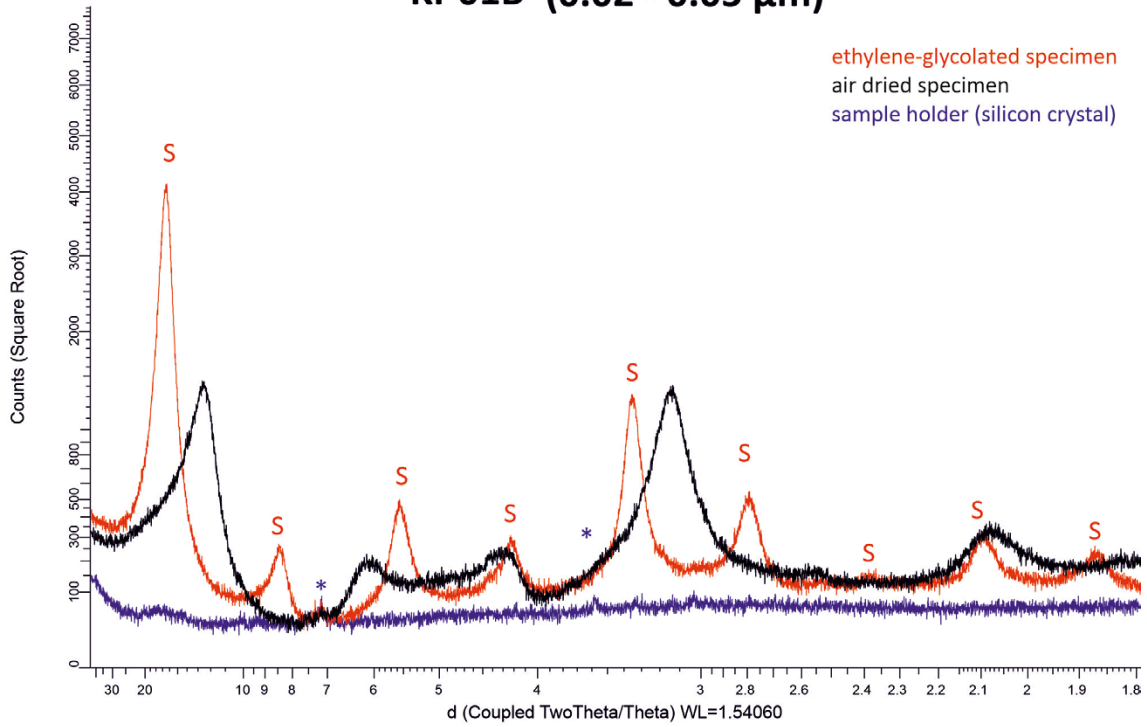


Figure E-1. X-ray diffractogram of air-dried and ethylene-glycolated oriented specimen of sample KI-01A and d-value of 00l peaks of montmorillonite (S, Sm). * = peaks from sample holder.

KI-01B (0.02 - 0.05 μm)



KI-01B-EG (0.02 - 0.05 μm)

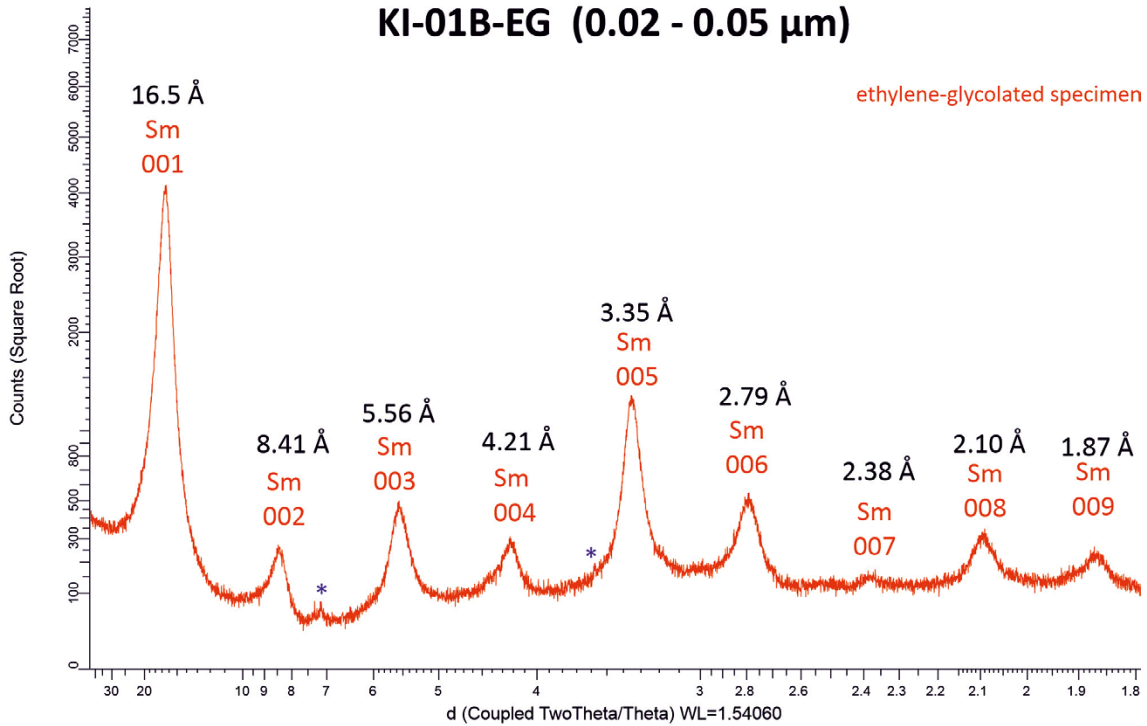
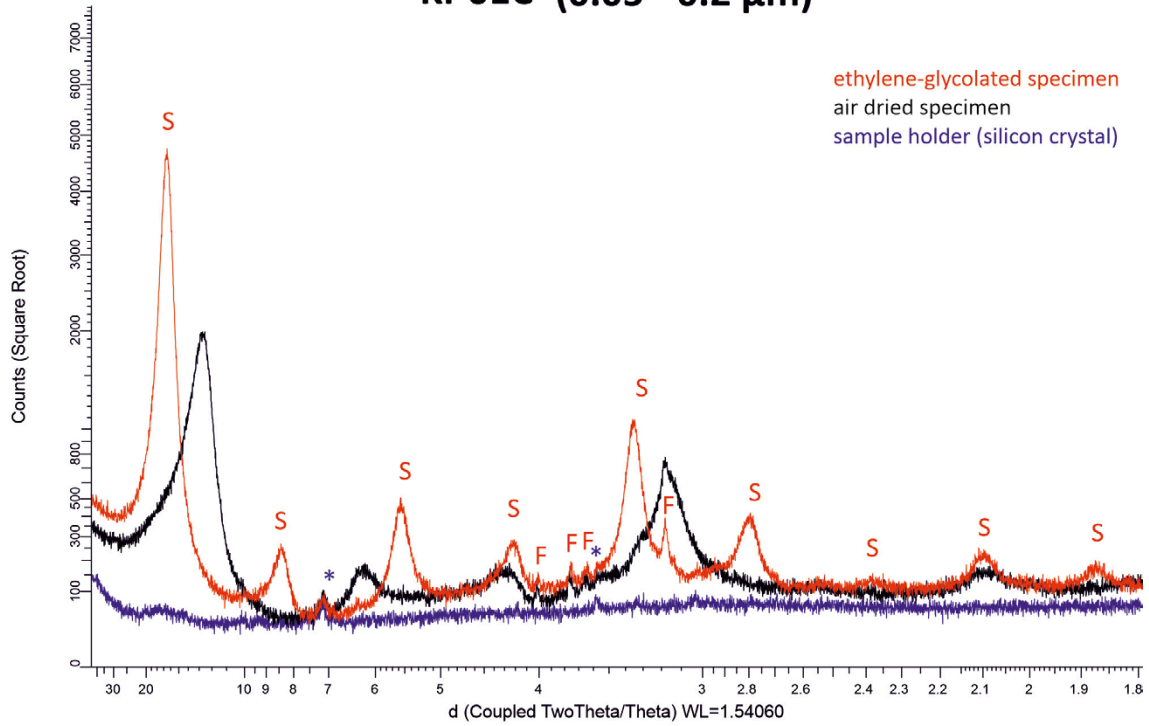


Figure E-2. X-ray diffractogram of air-dried and ethylene-glycolated oriented specimen of sample KI-01B and d-value of 00l peaks of montmorillonite (S, Sm). * = peaks from sample holder.

KI-01C (0.05 - 0.2 μm)



KI-01C-EG (0.02 - 0.05 μm)

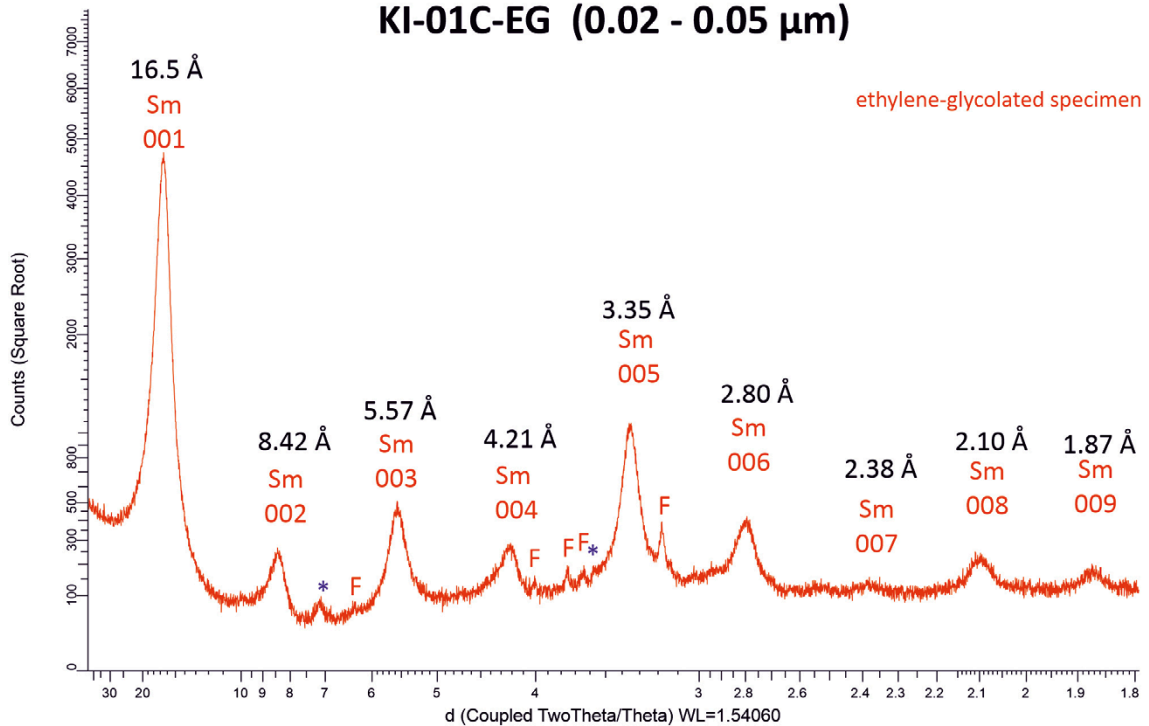
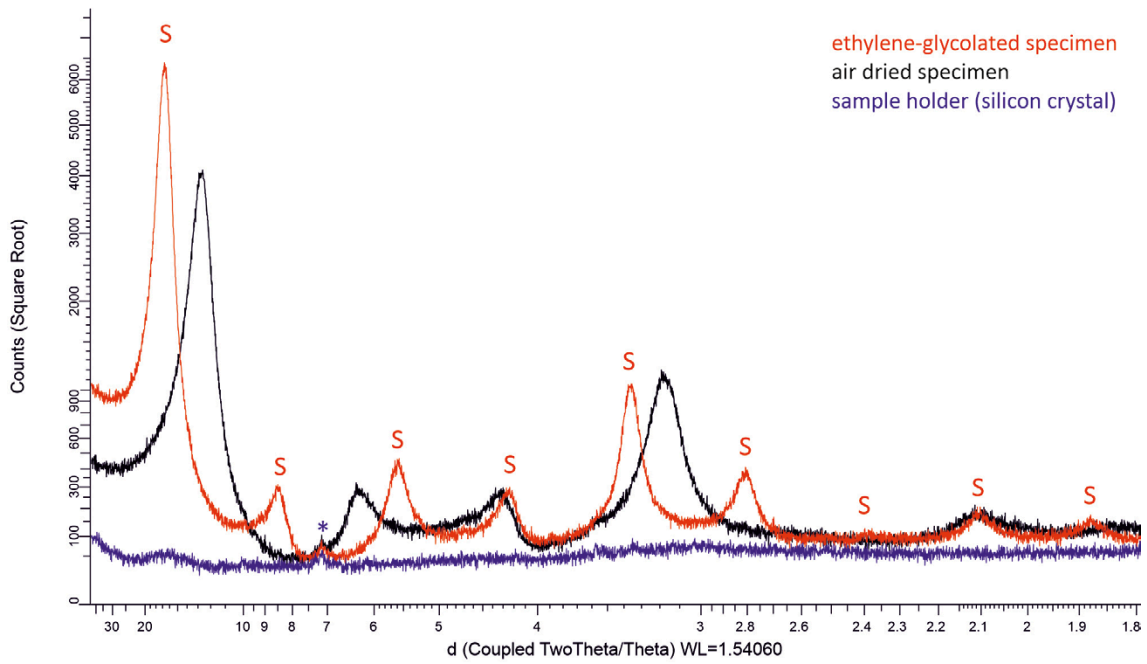


Figure E-3. X-ray diffractogram of air-dried and ethylene-glycolated oriented specimen of sample KI-01C and d-value of 00l peaks of montmorillonite (S, Sm). F = feldspar, * = peaks from sample holder.

KI-02A (<0.02 μm)



KI-02A-EG (<0.02 μm)

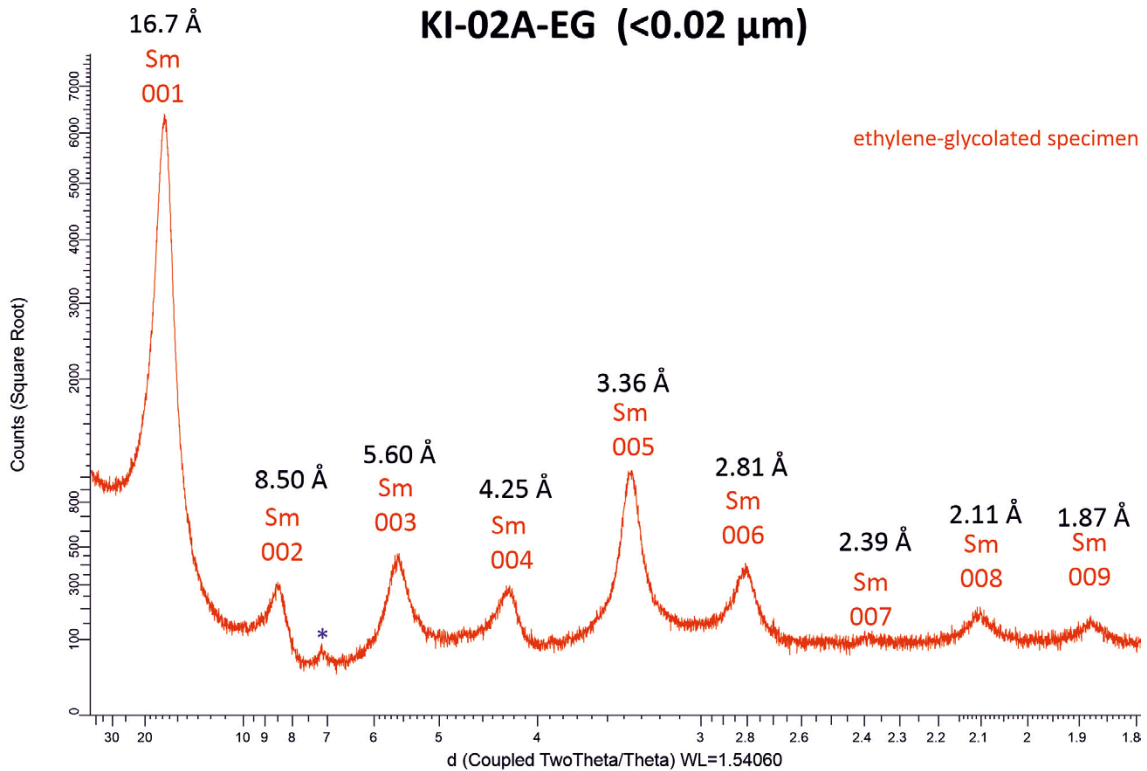


Figure E-4. X-ray diffractogram of air-dried and ethylene-glycolated oriented specimen of sample KI-02A and d-value of 00l peaks of montmorillonite (S, Sm). * = peak from sample holder.

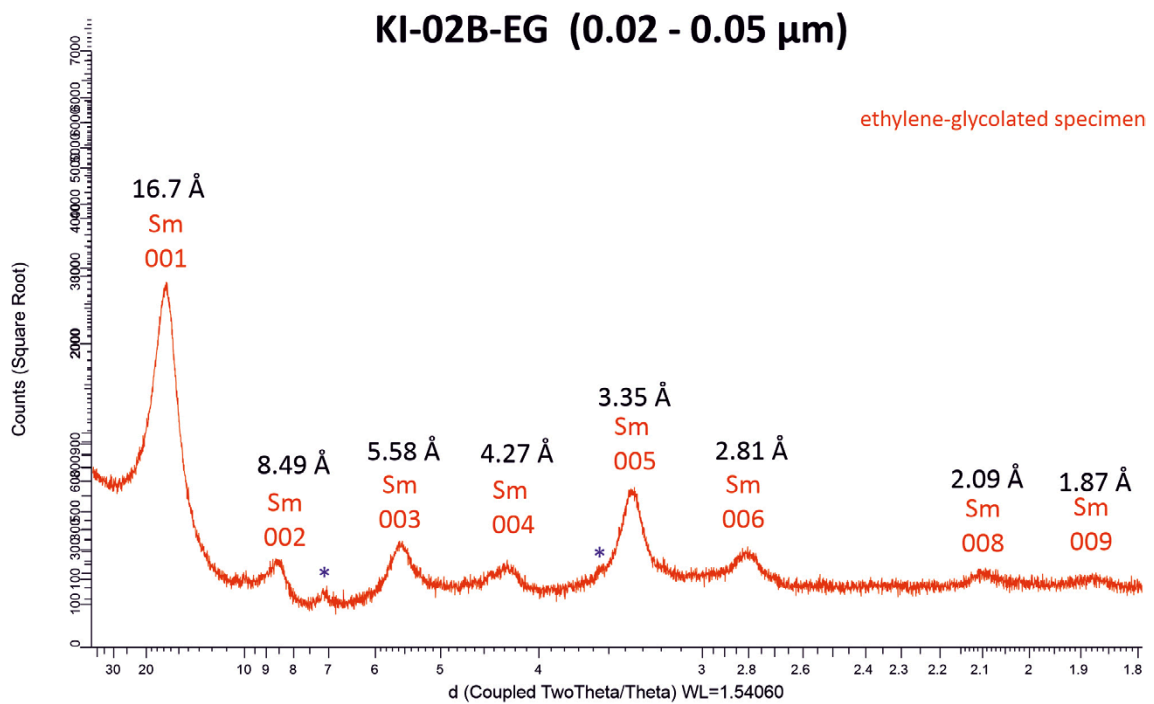
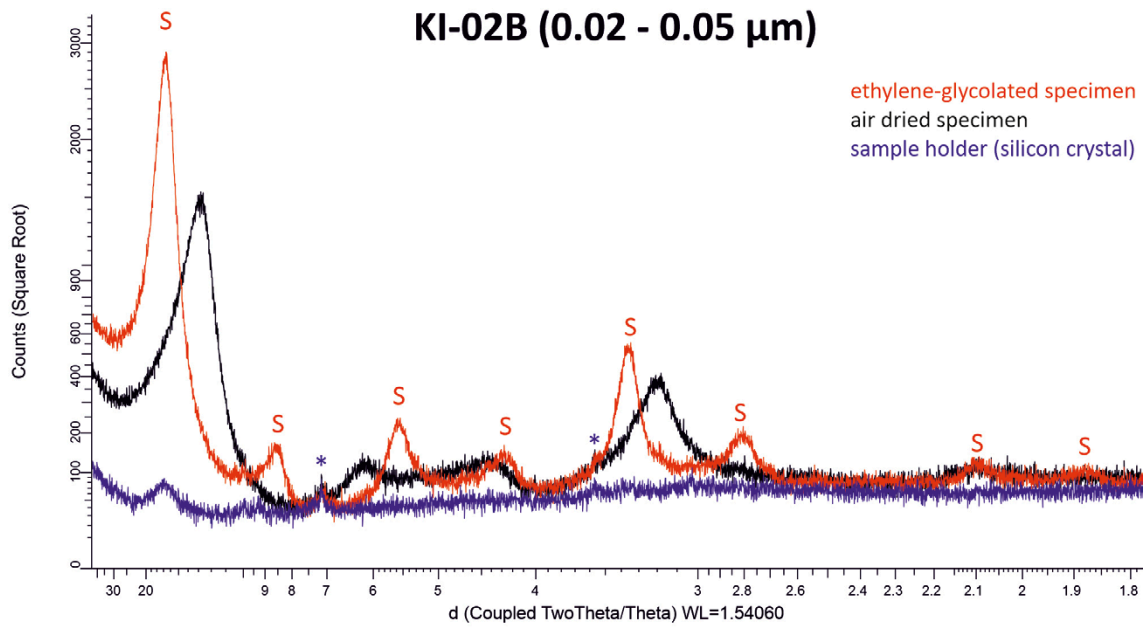
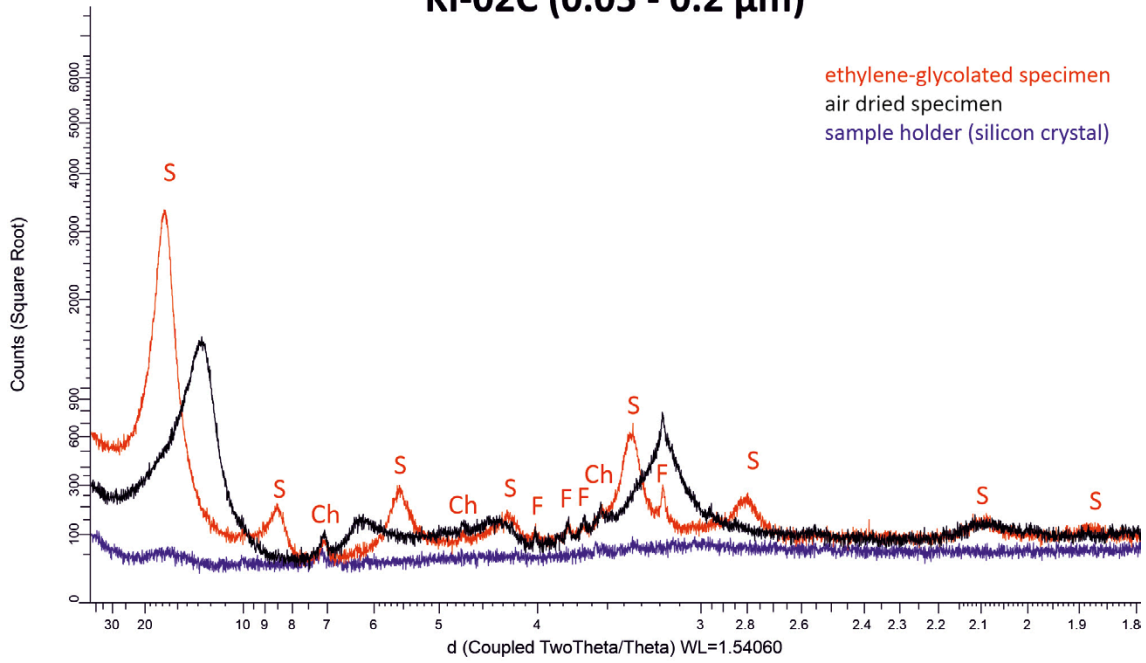


Figure E-5. X-ray diffractogram of air-dried and ethylene-glycolated oriented specimen of sample KI-02B and d-value of 00l peaks of montmorillonite (S, Sm). * = peaks from sample holder.

KI-02C (0.05 - 0.2 μm)



KI-02C-EG (0.02 - 0.05 μm)

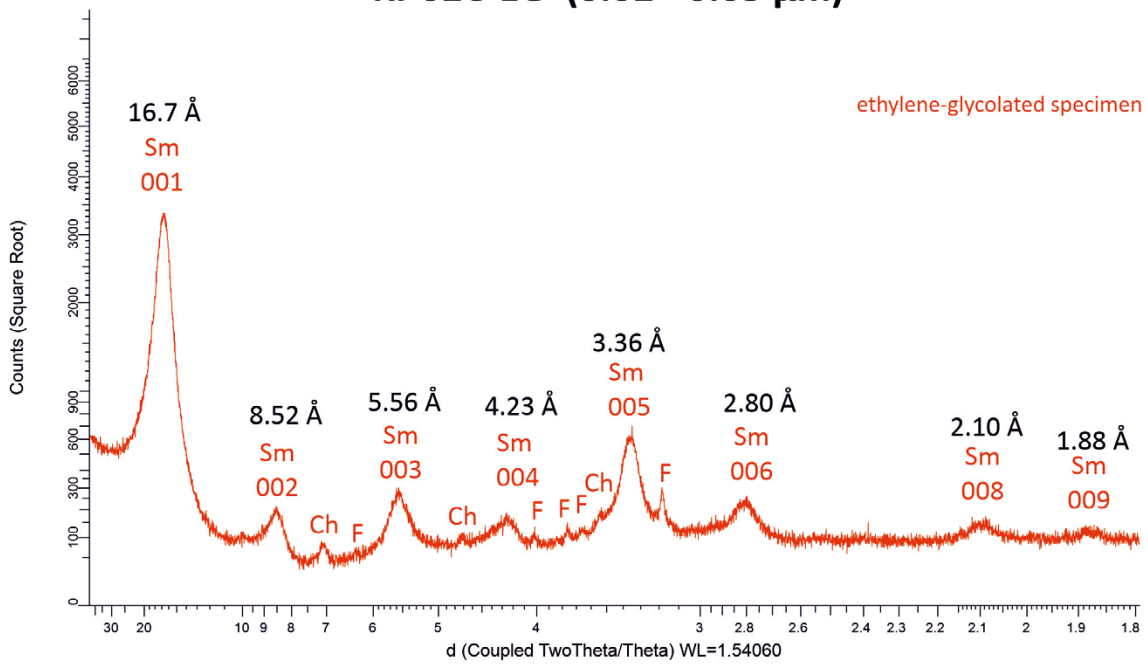
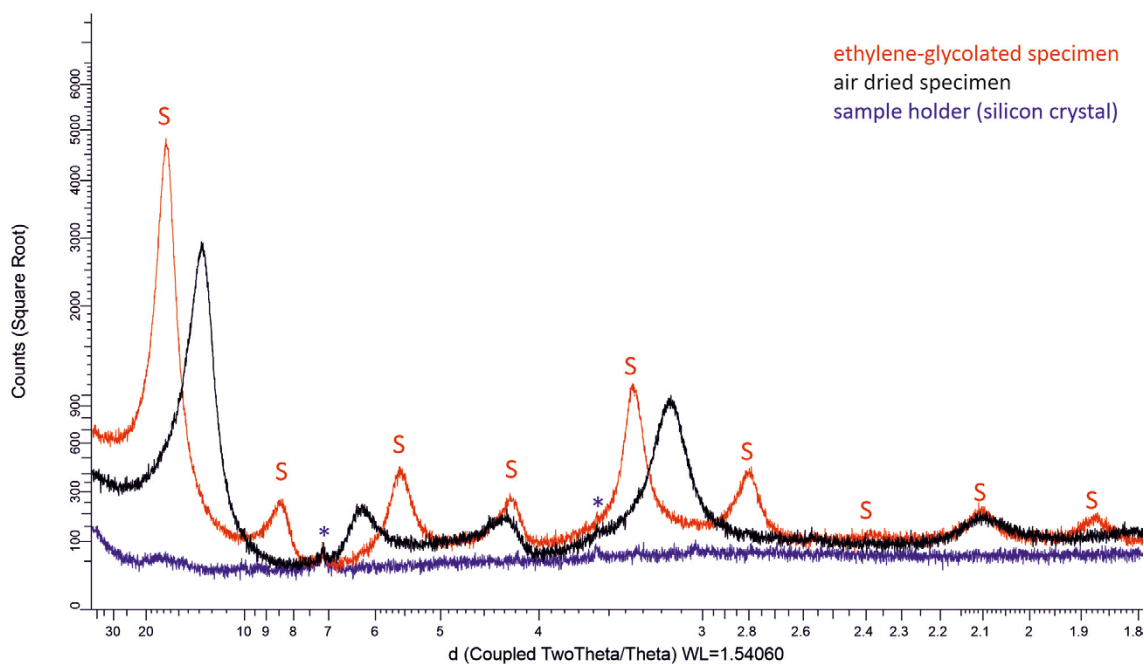


Figure E-6. X-ray diffractogram of air-dried and ethylene-glycolated oriented specimen of sample KI-02C and d-value of 00l peaks of montmorillonite (S, Sm). Ch = chlorite, F = feldspar.

KI-03A (<0.02 μm)



KI-03A-EG (<0.02 μm)

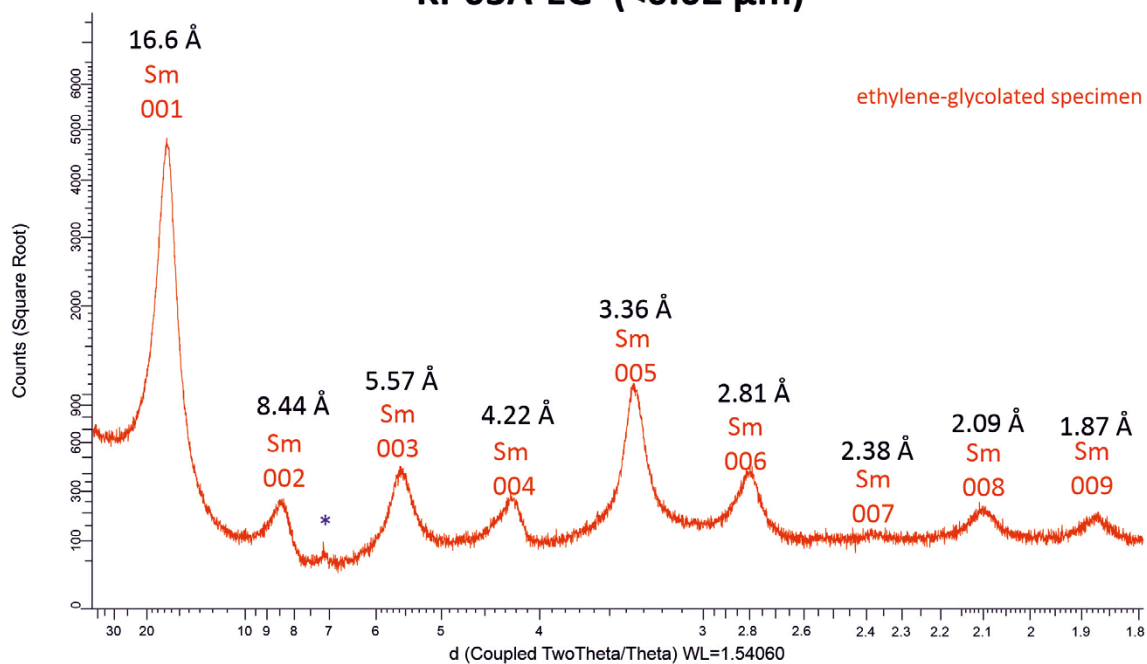


Figure E-7. X-ray diffractogram of air-dried and ethylene-glycolated oriented specimen of sample KI-03A and d-value of 00l peaks of montmorillonite (S, Sm). * = peak from sample holder.

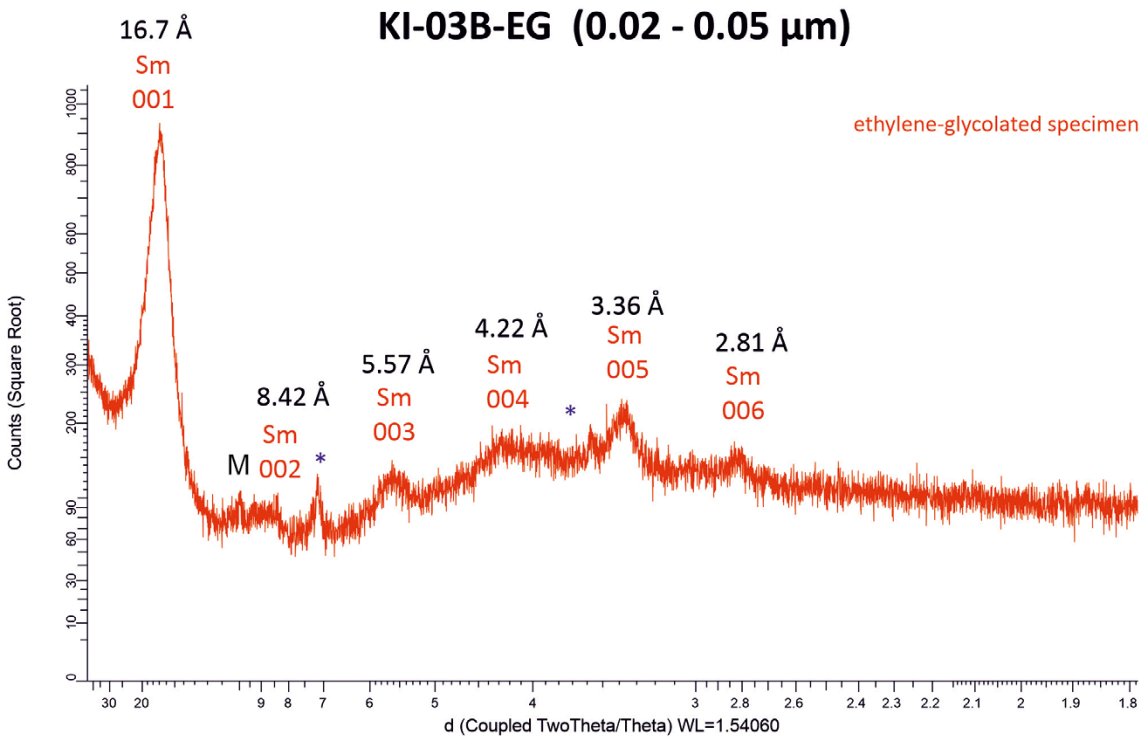
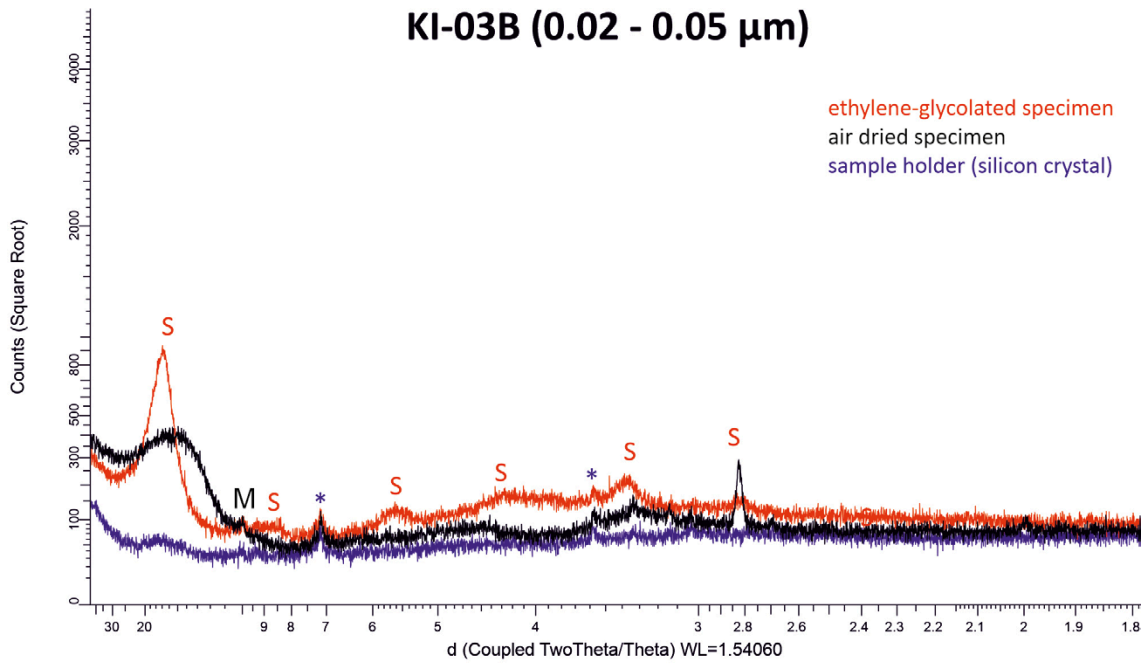


Figure E-8. X-ray diffractogram of air-dried and ethylene-glycolated oriented specimen of sample KI-03B and d-value of 00l peaks of montmorillonite (S, Sm). M = mica, * = peaks from sample holder.

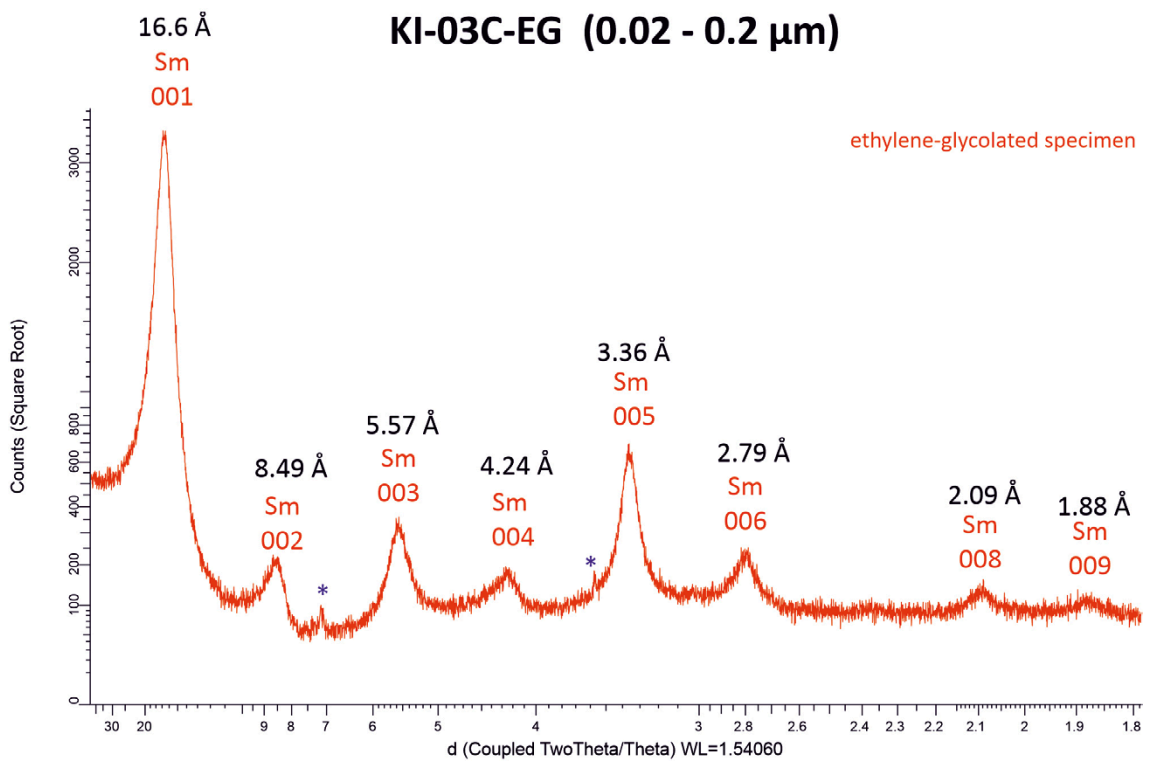
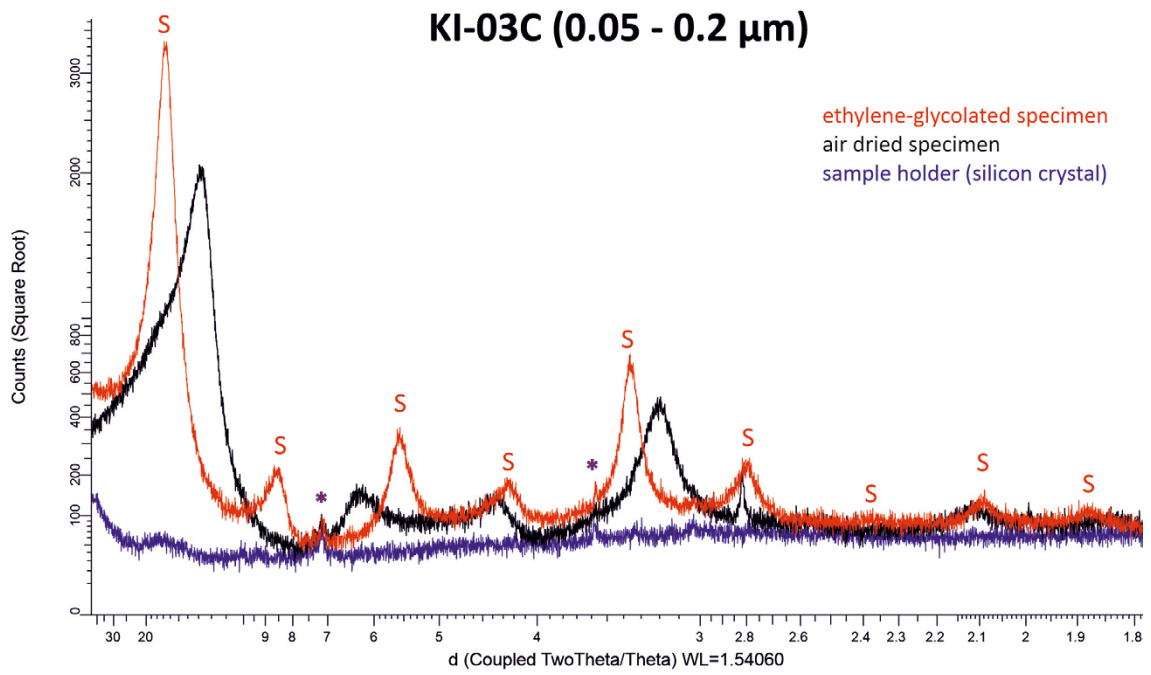


Figure E-9. X-ray diffractogram of air-dried and ethylene-glycolated oriented specimen of sample KI-03C and d-value of 00l peaks of montmorillonite (S, Sm). * = peaks from sample holder.

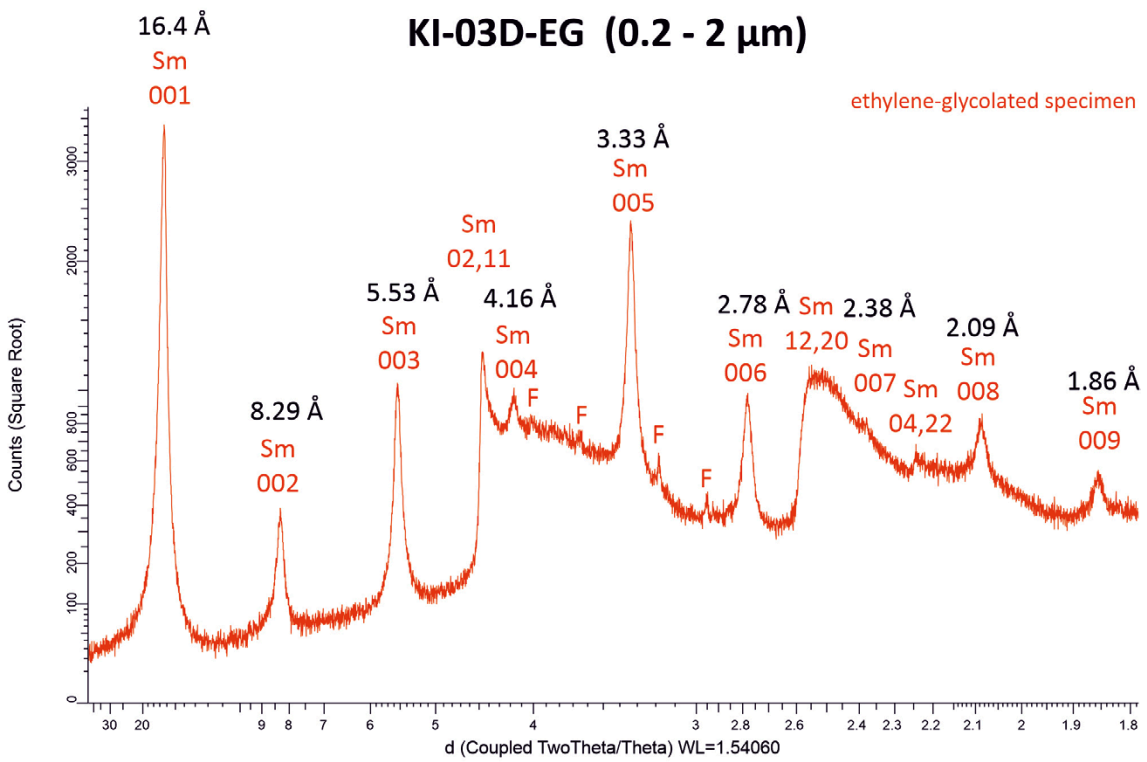
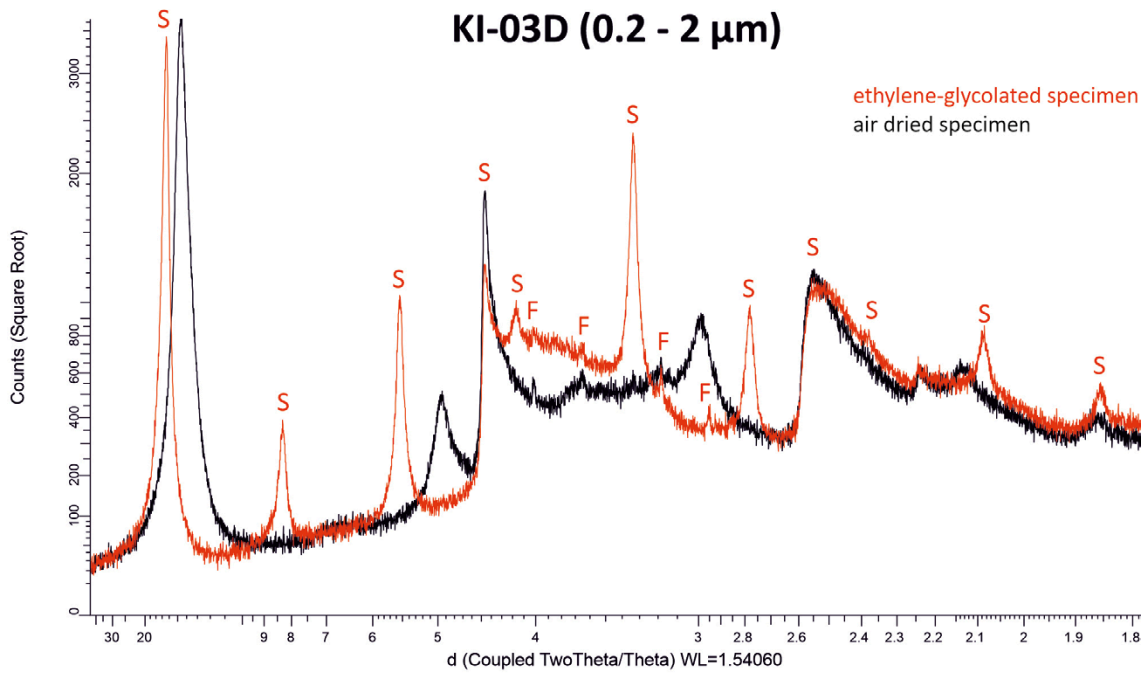
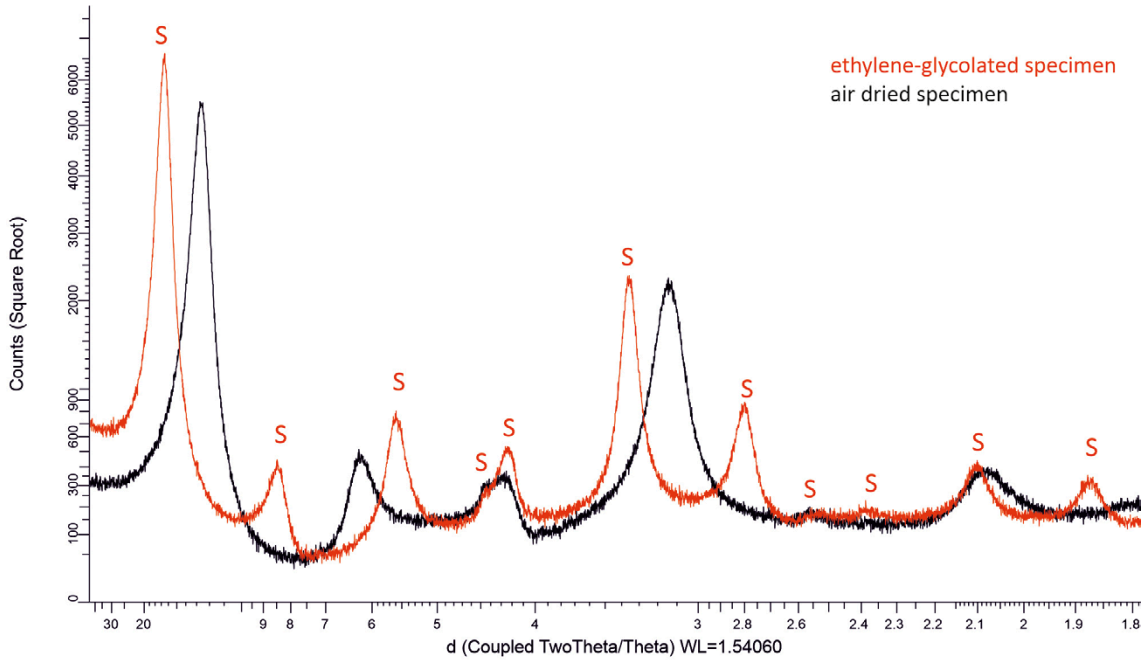


Figure E-10. X-ray diffractogram of air-dried and ethylene-glycolated oriented specimen of sample KI-03D and d-value of 00l peaks of montmorillonite (S, Sm). F = feldspar.

KI-04A (<0.02 μm)



KI-04A-EG (<0.02 μm)

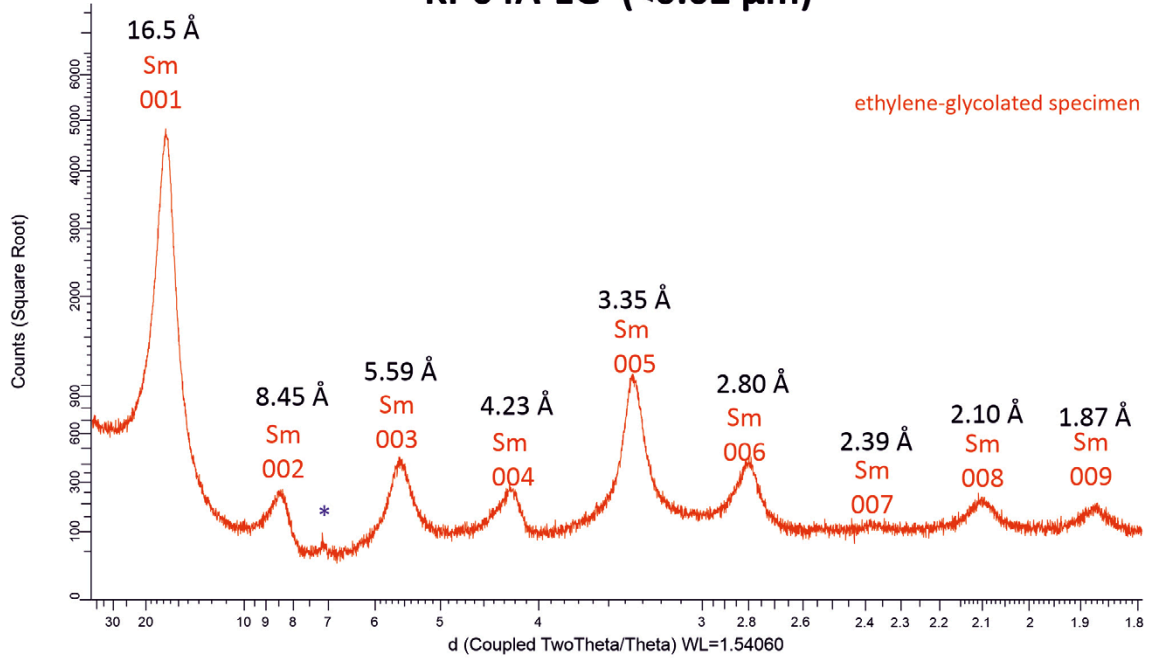


Figure E-11. X-ray diffractogram of air-dried and ethylene-glycolated oriented specimen of sample KI-04A and d-value of 00l peaks of montmorillonite (S, Sm). * = peak from sample holder.

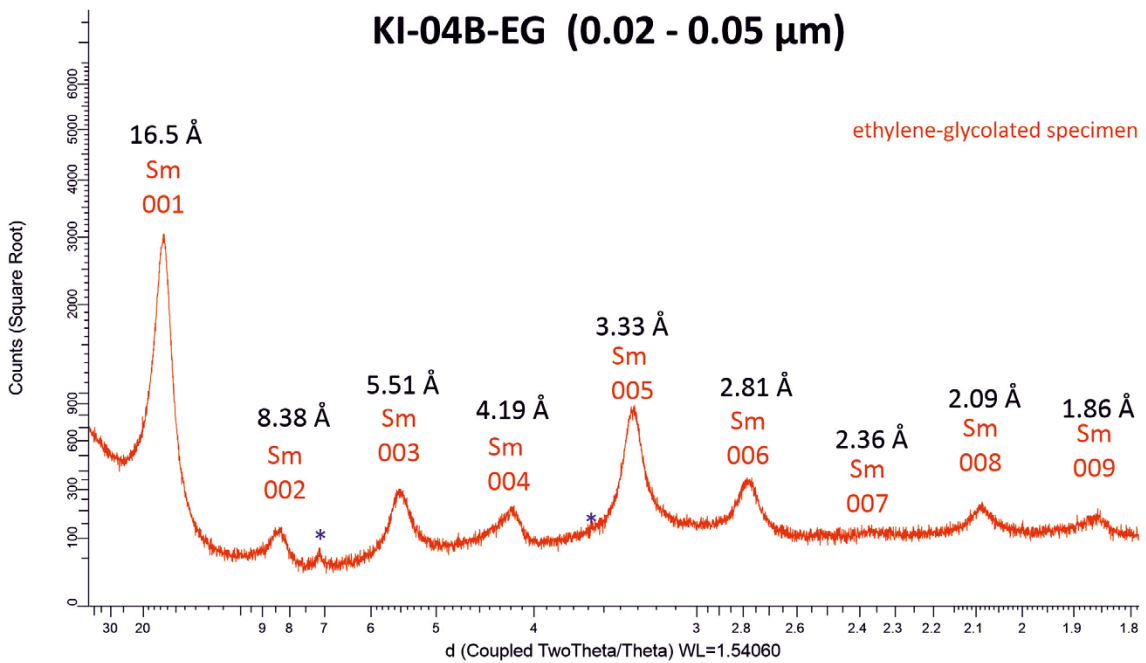
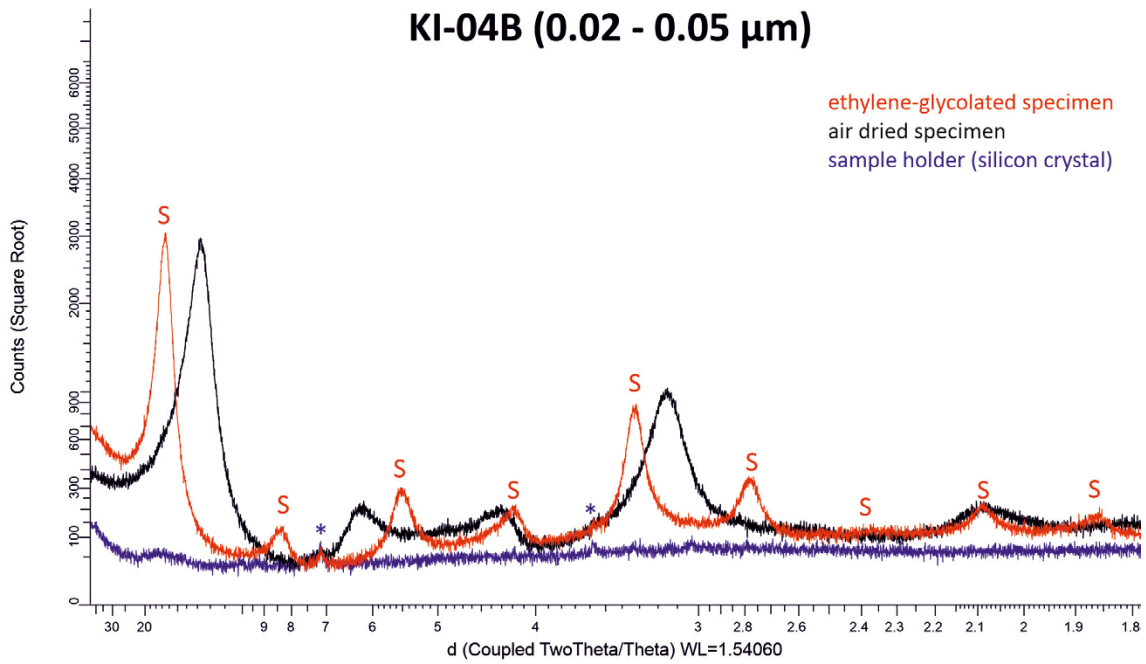


Figure E-12. X-ray diffractogram of air-dried and ethylene-glycolated oriented specimen of sample KI-04B and d-value of 00l peaks of montmorillonite (S, Sm). * = peaks from sample holder.

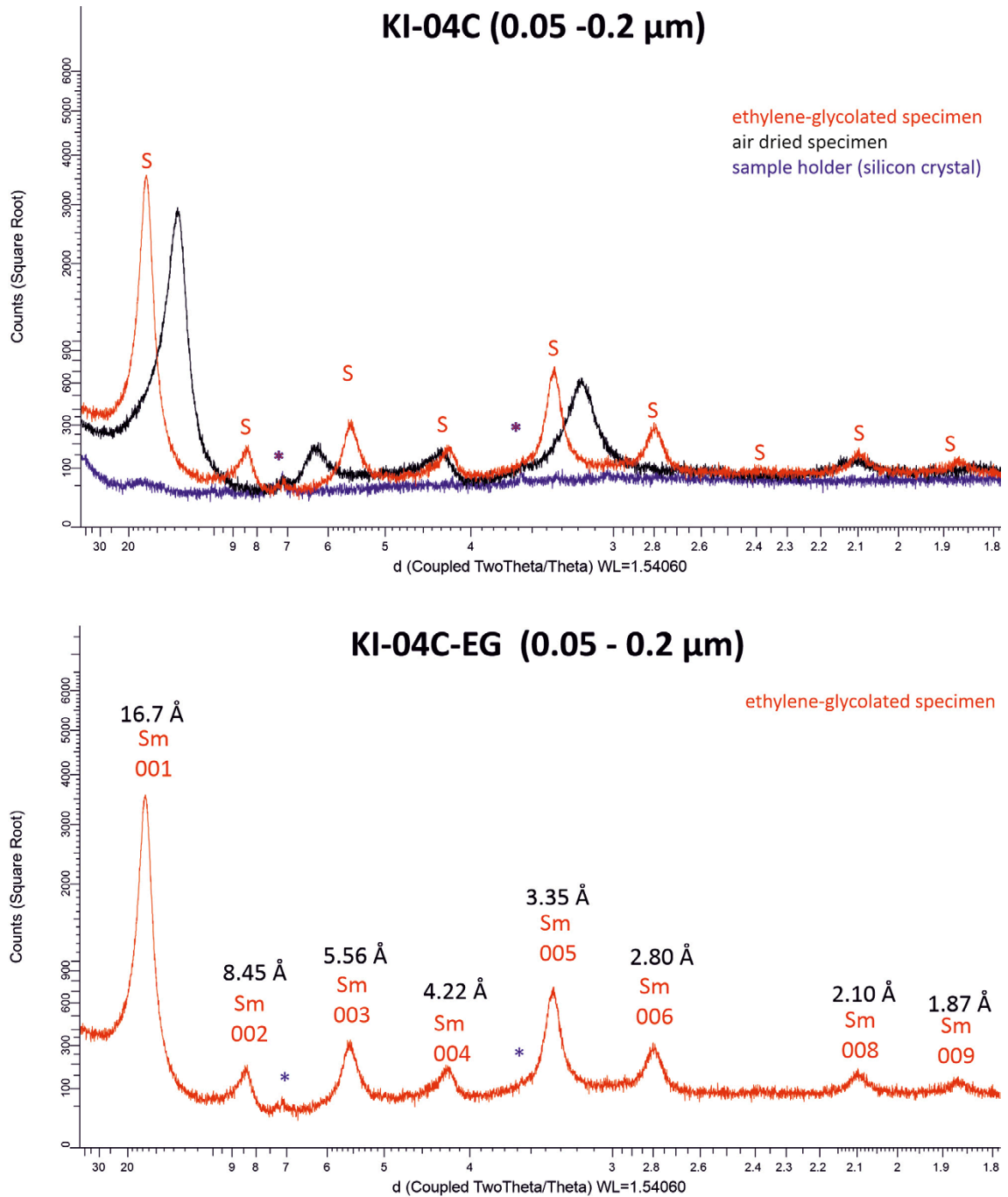


Figure E-13. X-ray diffractogram of air-dried and ethylene-glycolated oriented specimen of sample KI-04C and d-value of 00l peaks of montmorillonite (S, Sm). * = peaks from sample holder.

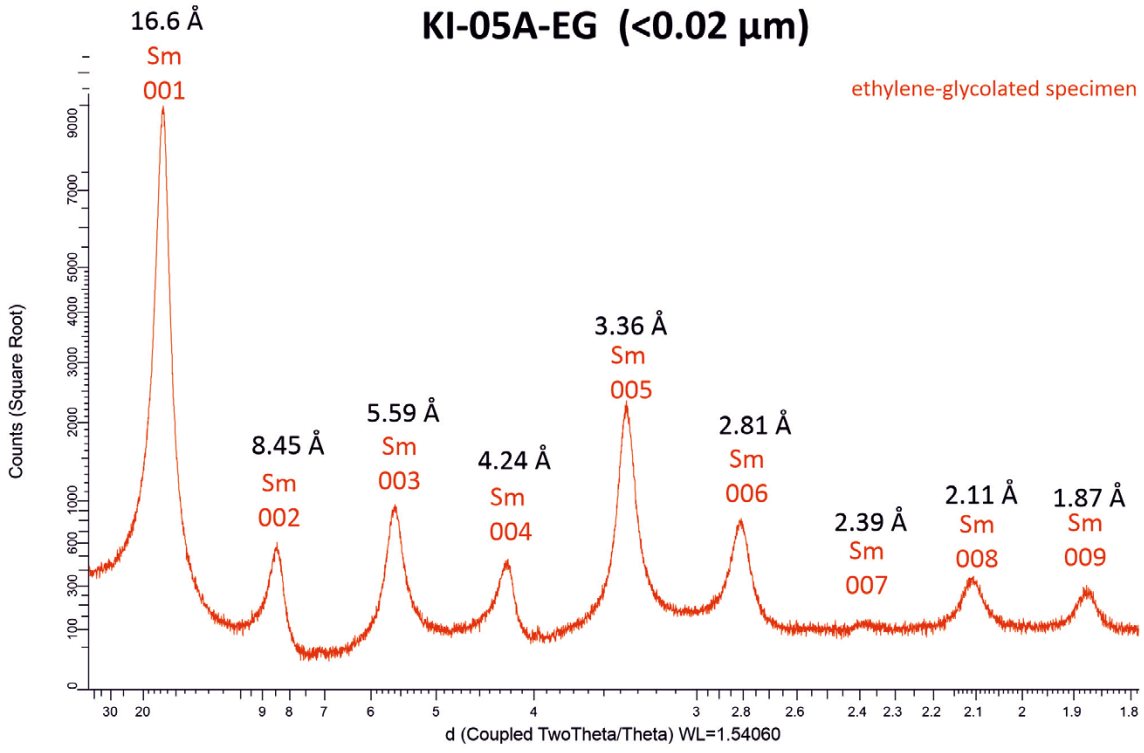
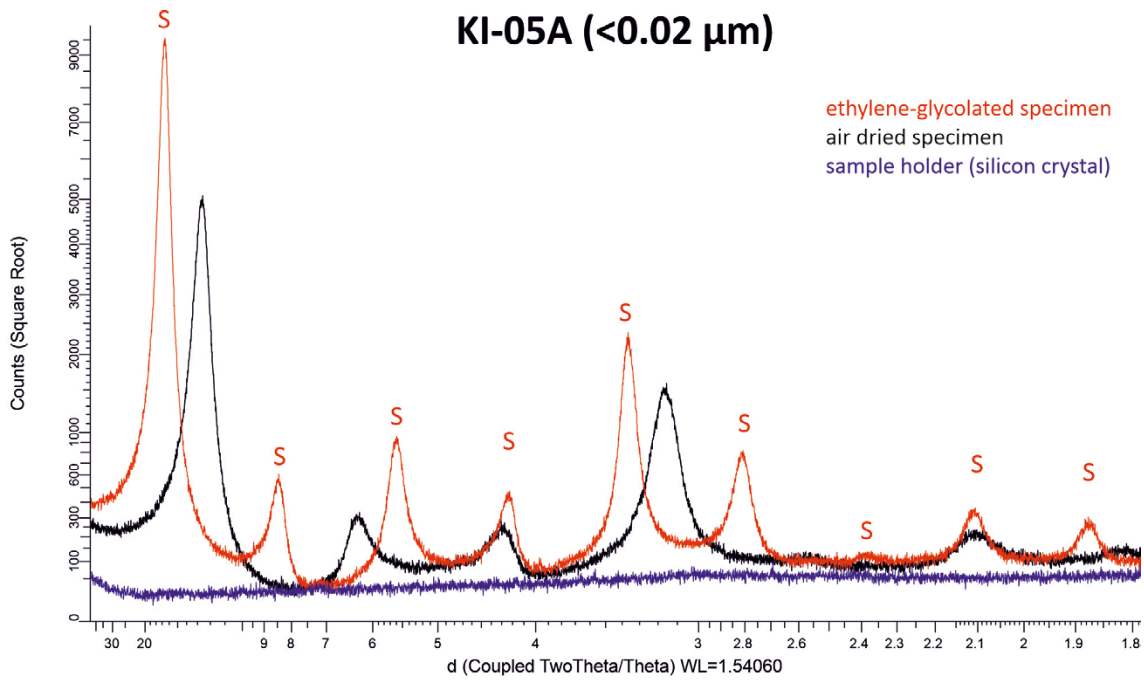


Figure E-14. X-ray diffractogram of air-dried and ethylene-glycolated oriented specimen of sample KI-05A and d-value of 00l peaks of montmorillonite (S, Sm).

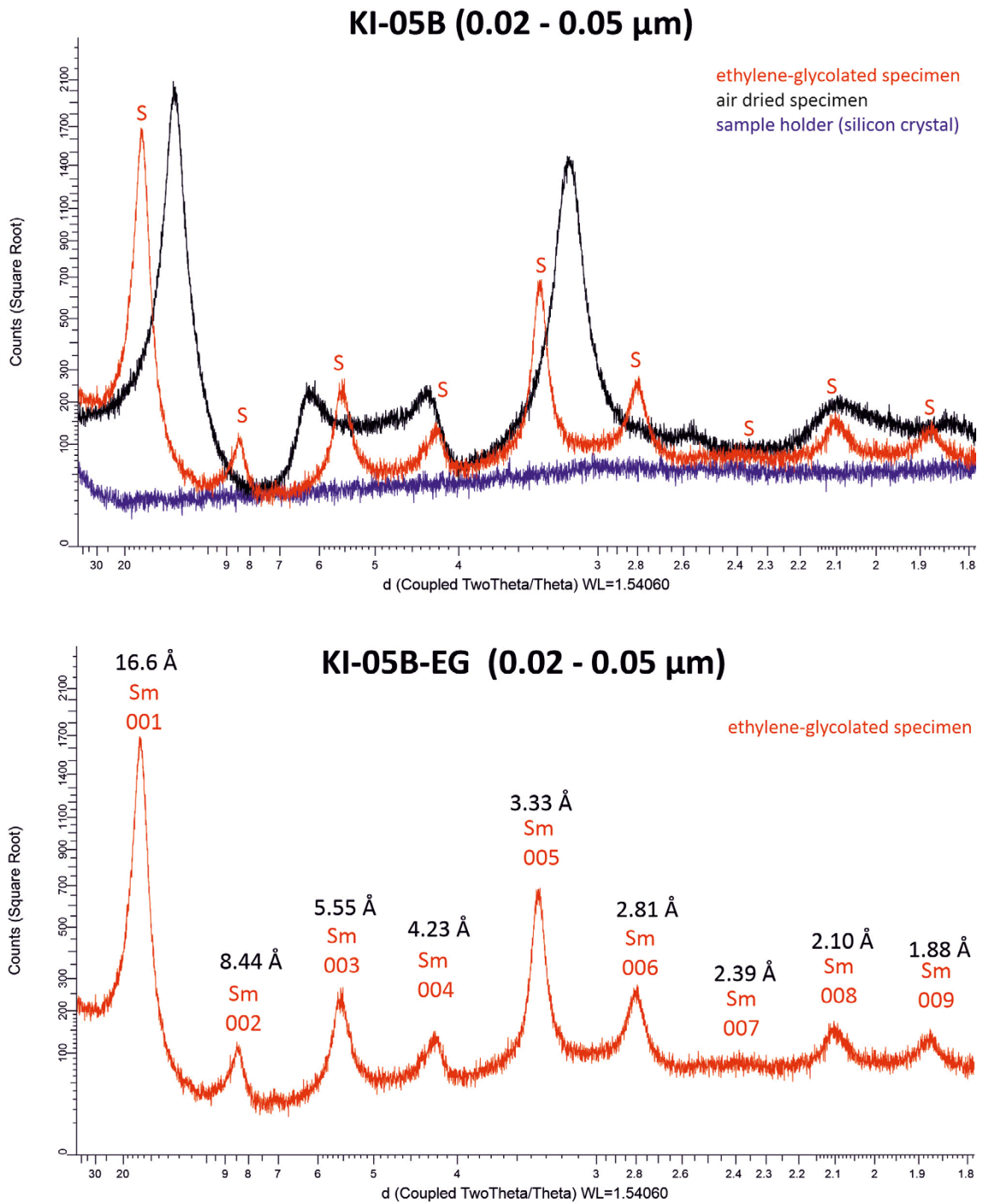


Figure E-15. X-ray diffractogram of air-dried and ethylene-glycolated oriented specimen of sample KI-05B and d-value of 00l peaks of montmorillonite (S, Sm).

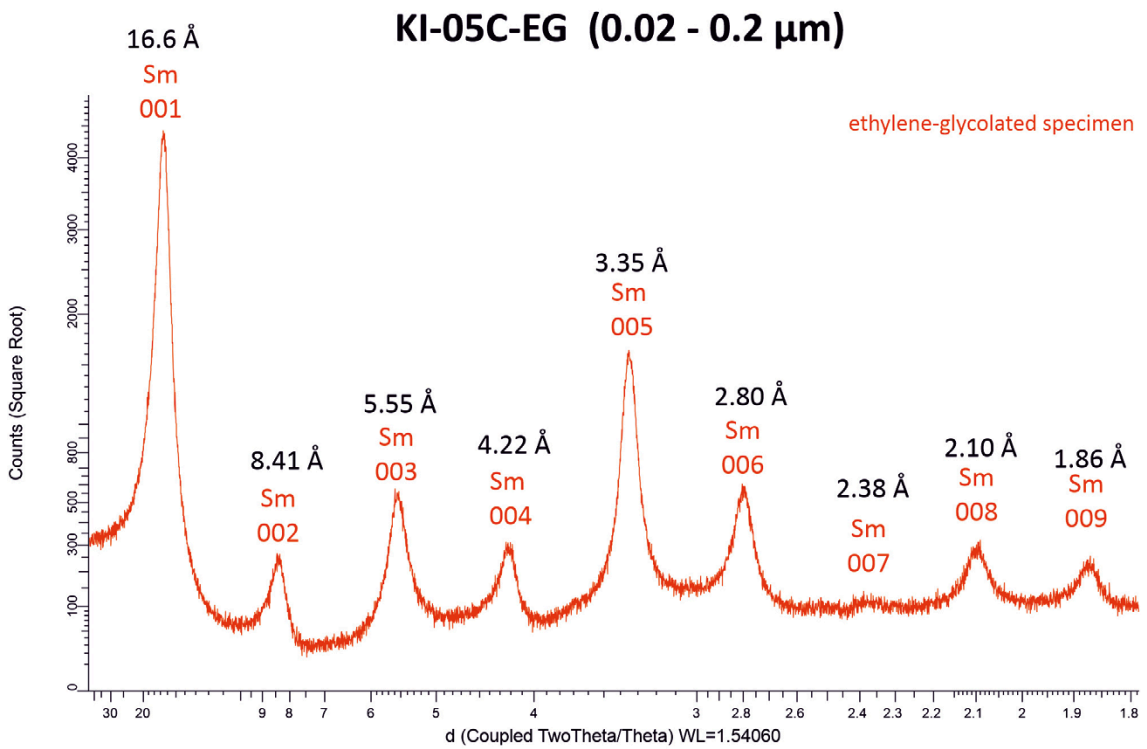
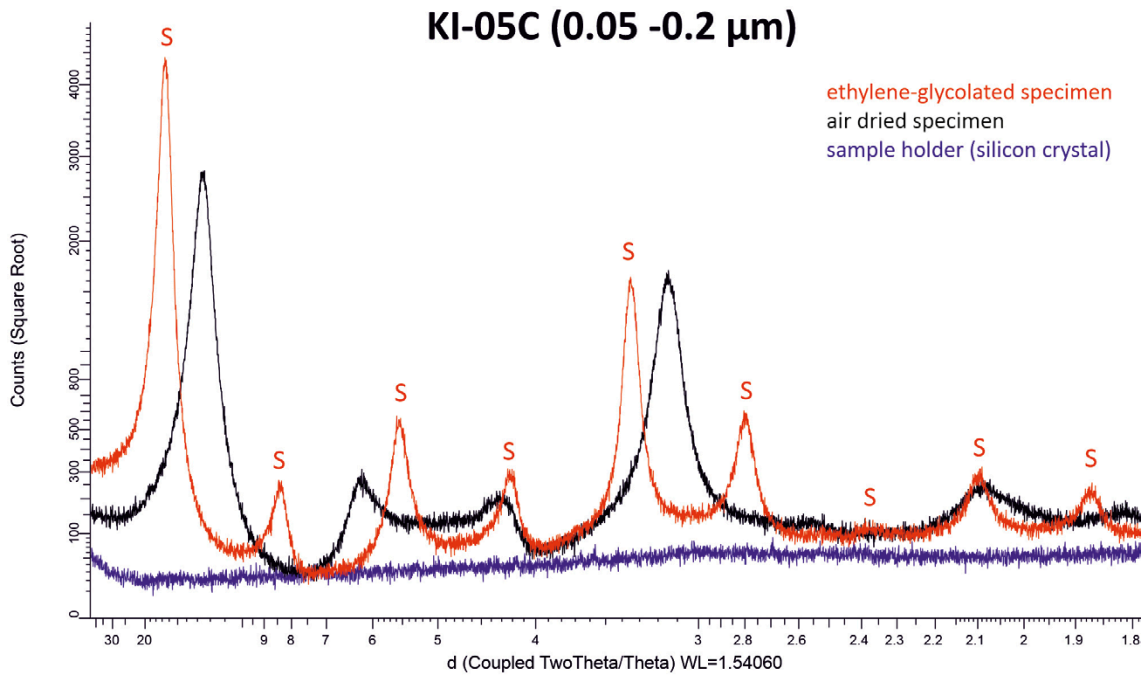
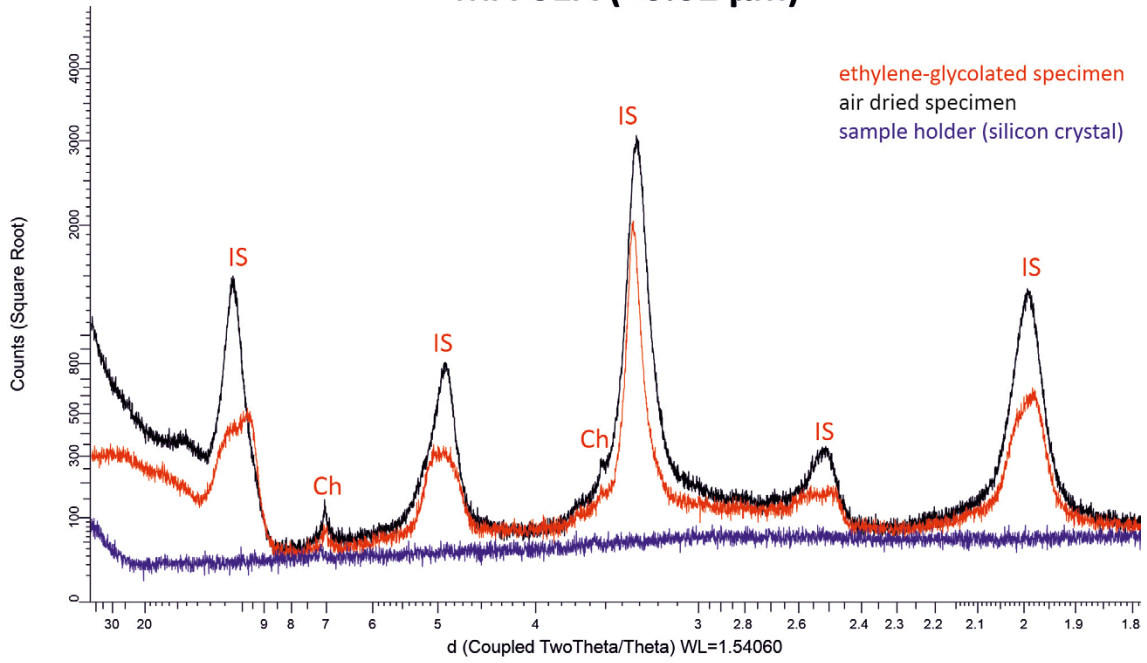


Figure E-16. X-ray diffractogram of air-dried and ethylene-glycolated oriented specimen of sample KI-05C and d-value of 00l peaks of montmorillonite (S, Sm).

MA-01A (<0.02 μm)



MA-01A-EG (<0.02 μm)

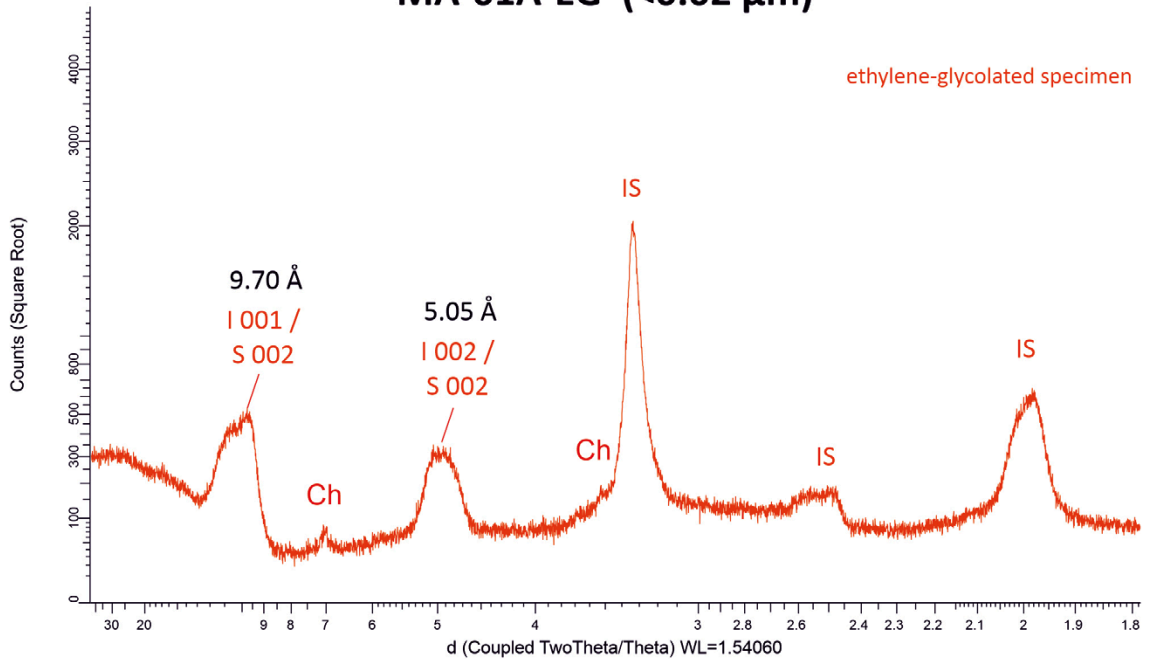
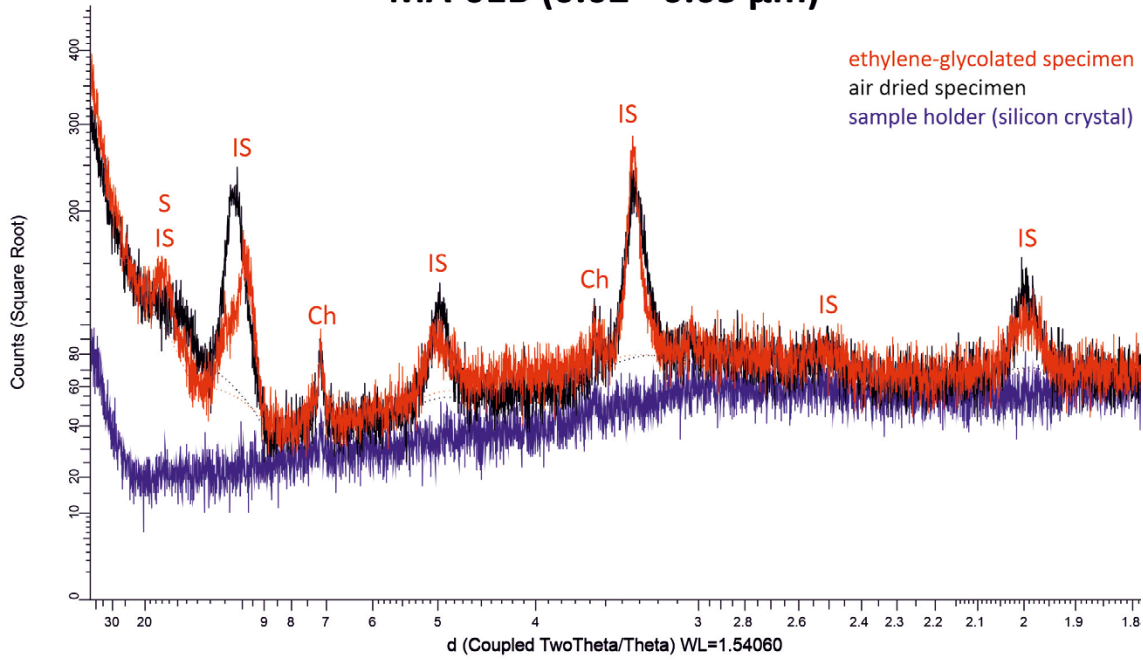


Figure E-17. X-ray diffractogram of air-dried and ethylene-glycolated oriented specimen of sample MA-01A and selected d-value of 00l peaks of R3 illite-smectite (IS). Ch = chlorite.

MA-01B (0.02 - 0.05 μm)



MA-01B-EG (0.02 - 0.05 μm)

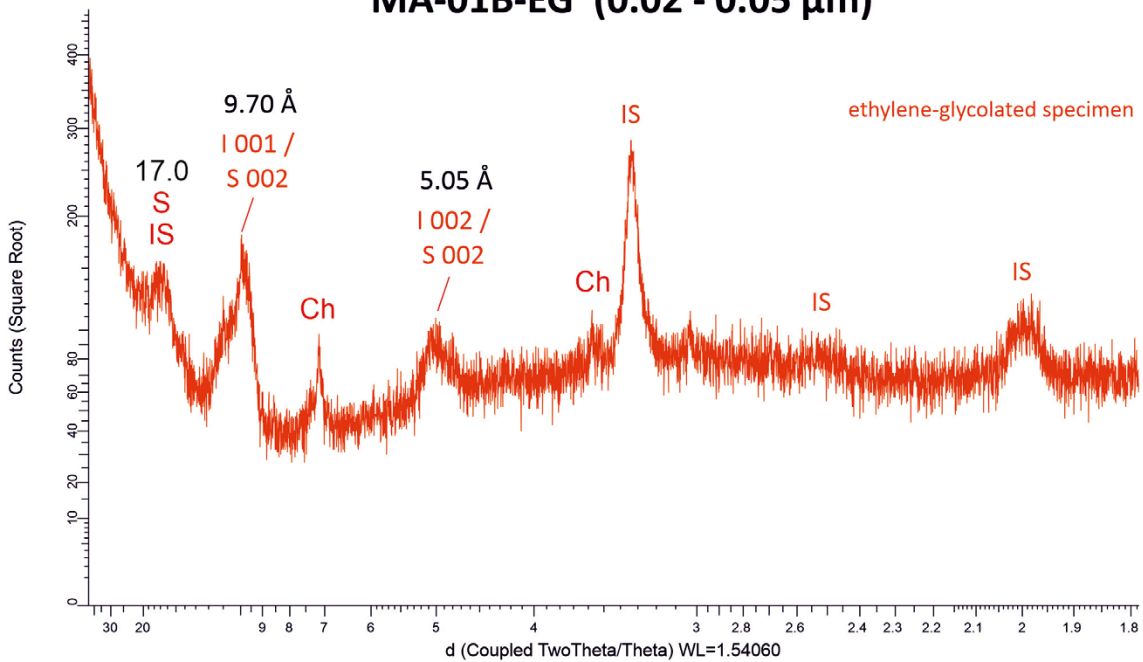


Figure E-18. X-ray diffractogram of air-dried and ethylene-glycolated oriented specimen of sample MA-01B and selected d -value of 001 peaks of R3 illite-smectite (IS). Ch = chlorite.

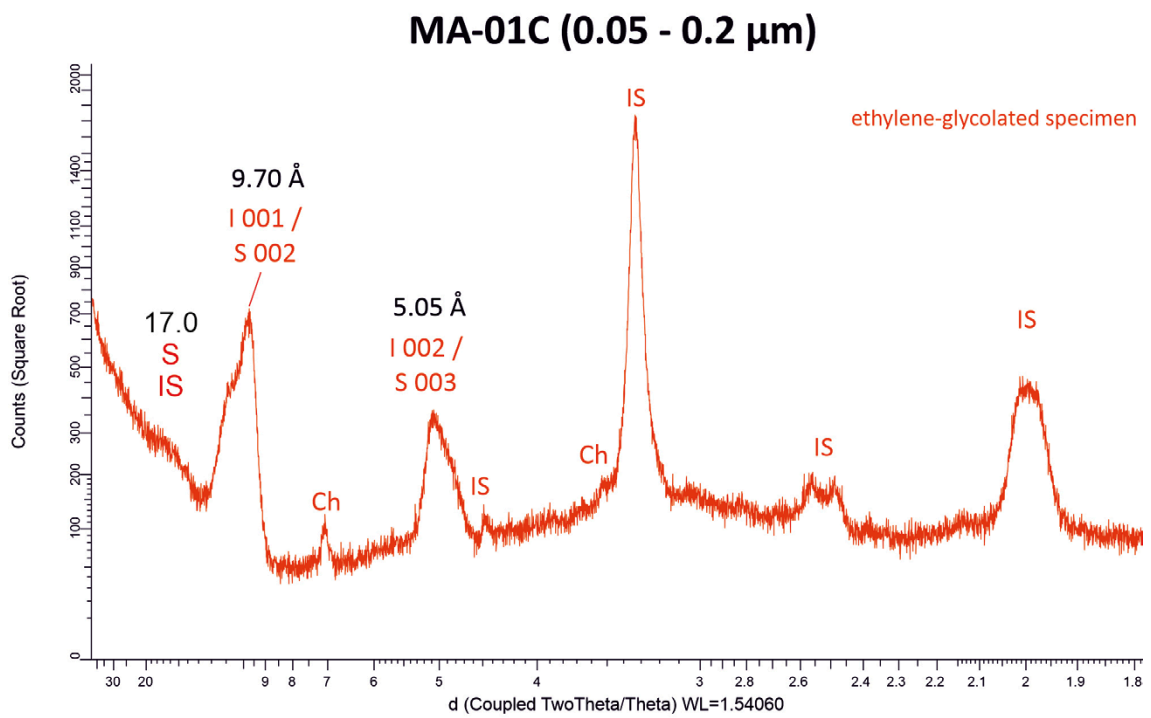
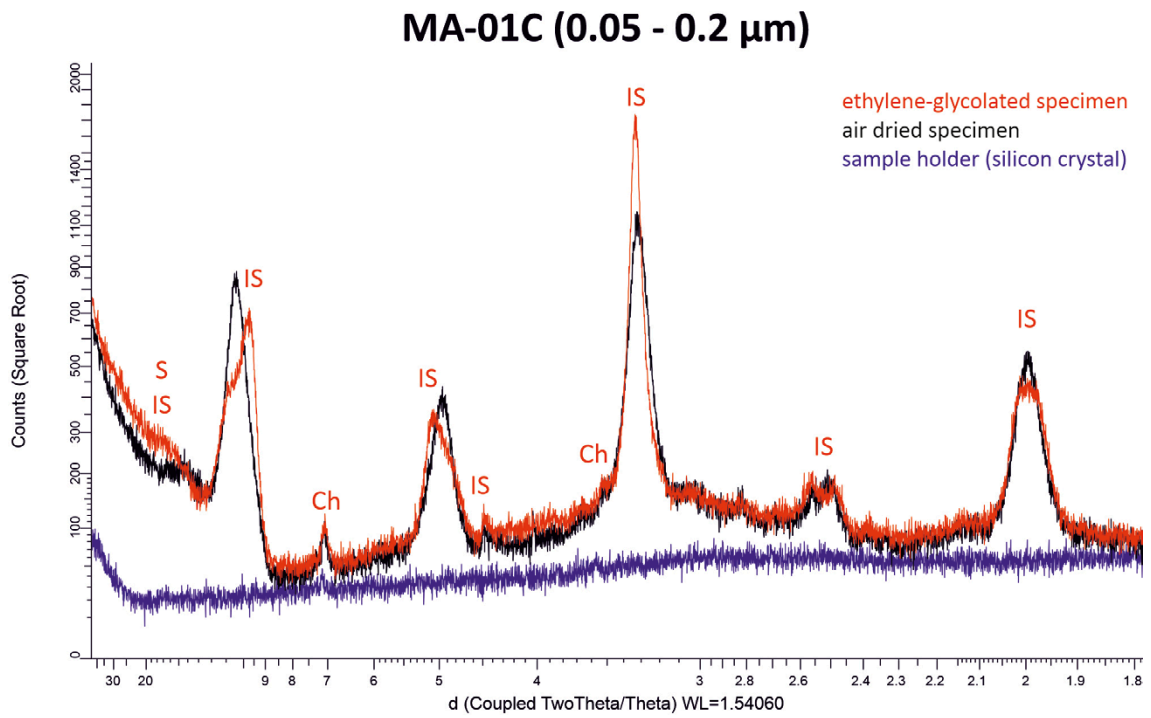


Figure E-19. X-ray diffractogram of air-dried and ethylene-glycolated oriented specimen of sample MA-01C and selected d -value of 00l peaks of R3 illite-smectite (IS). Ch = chlorite.

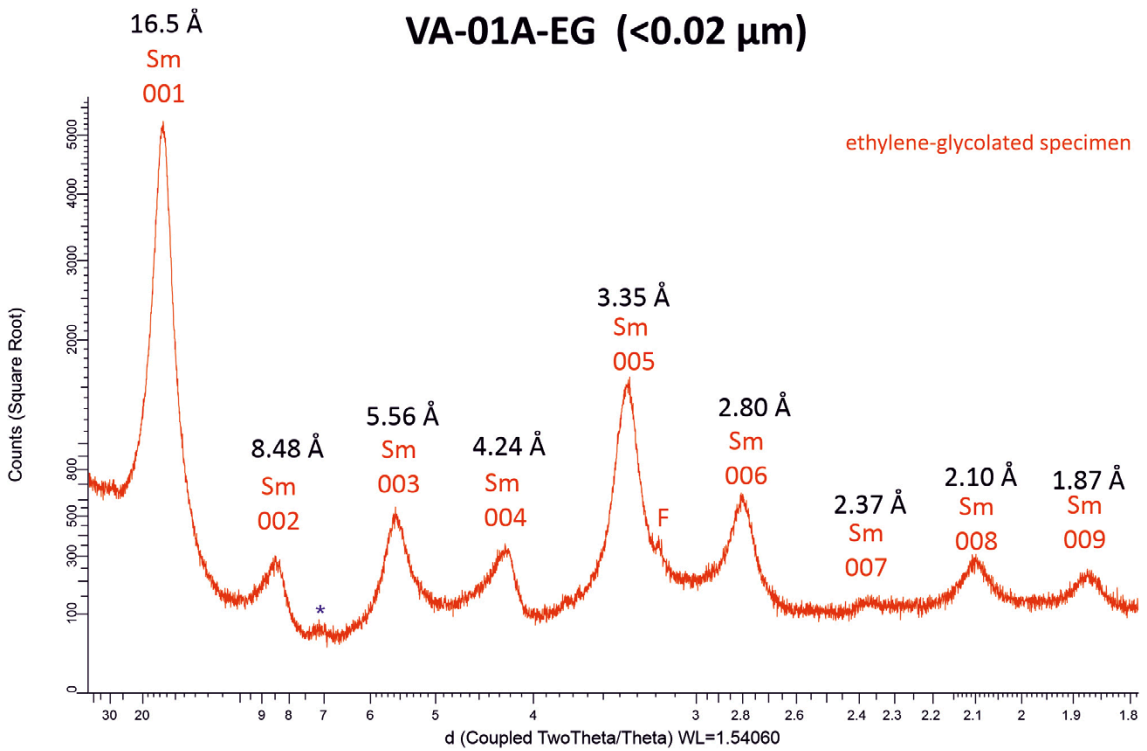
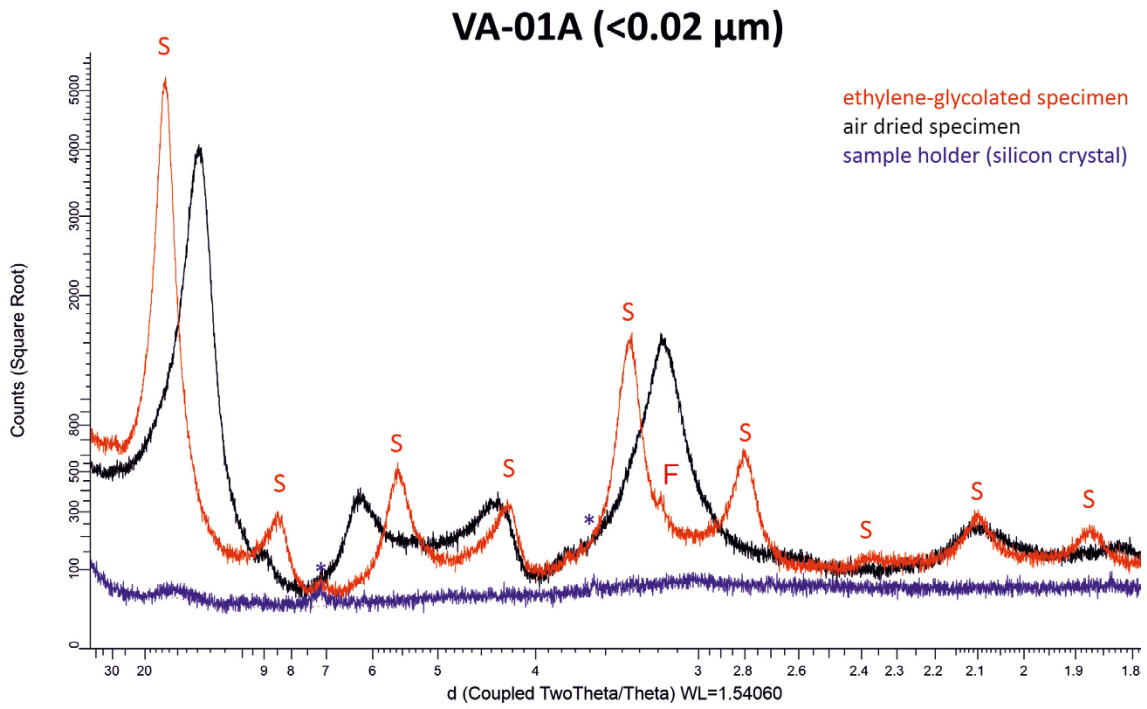
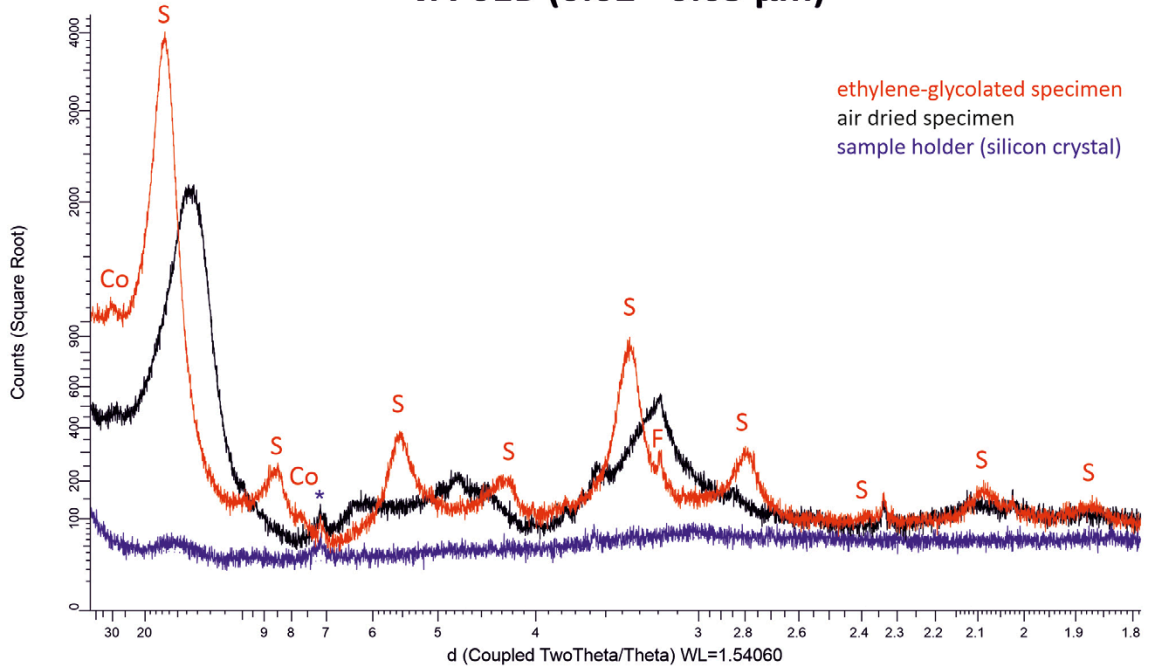


Figure E-20. X-ray diffractogram of air-dried and ethylene-glycolated oriented specimen of sample VA-01A and d-value of 00l peaks of montmorillonite (S, Sm). F = feldspar; * = peak from sample holder.

VA-01B (0.02 - 0.05 μm)



VA-01B (0.02 - 0.05 μm)

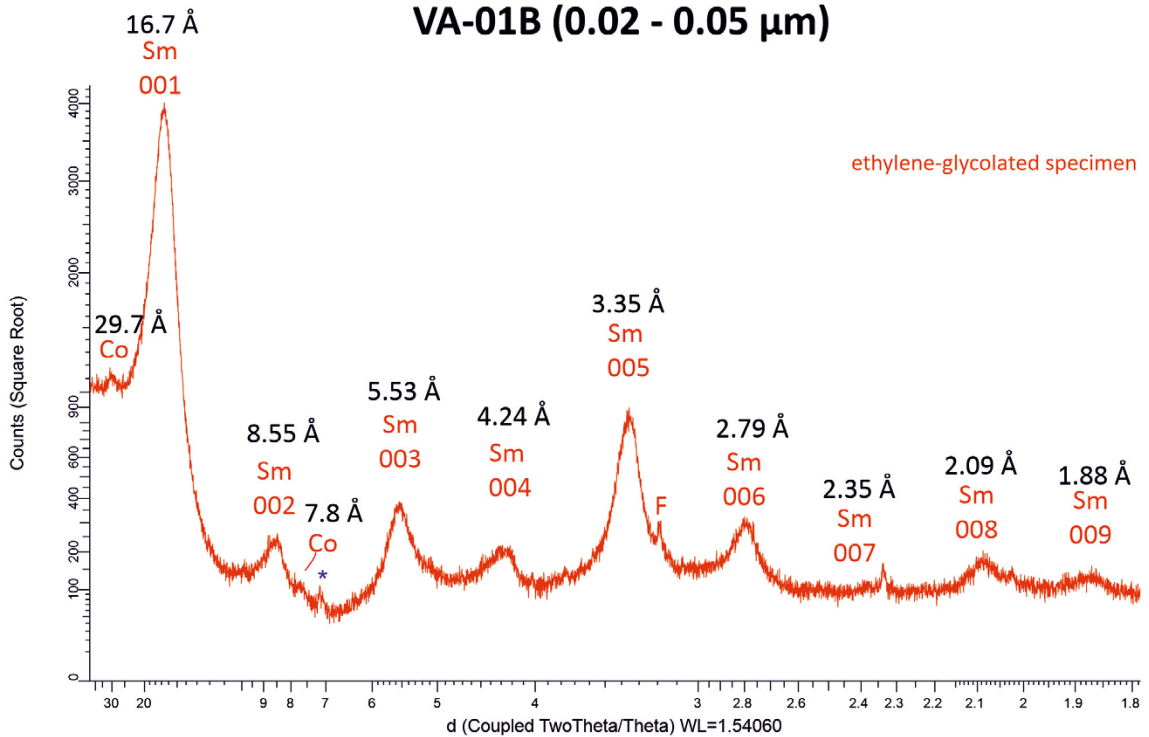
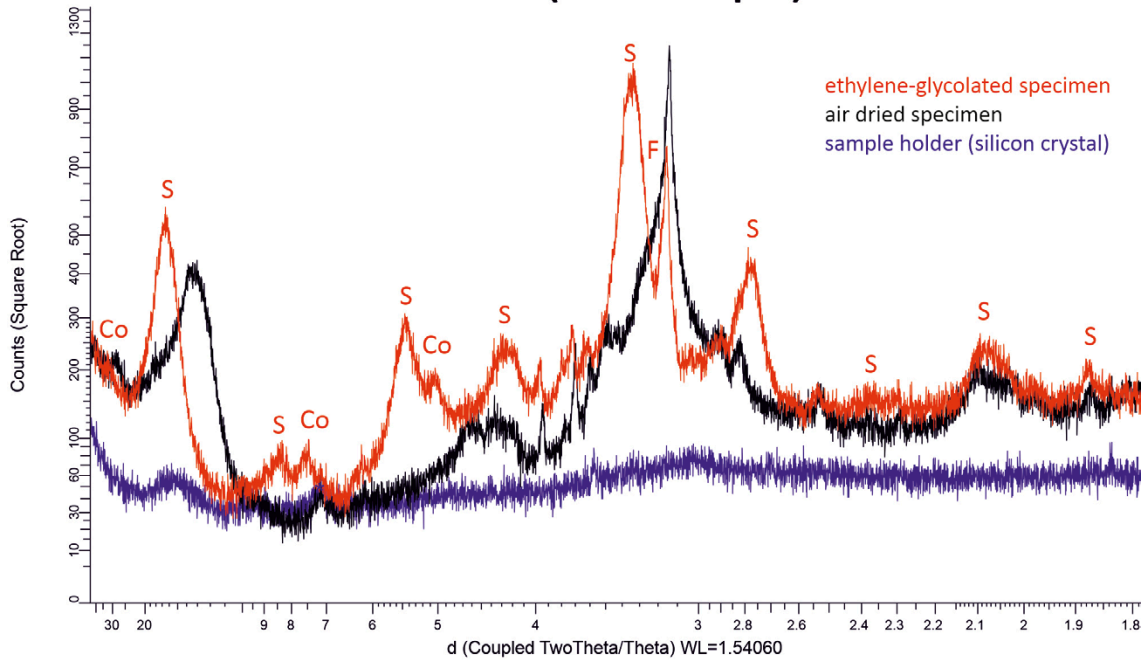


Figure E-21. X-ray diffractogram of air-dried and ethylene-glycolated oriented specimen of sample VA-01B and d-value of 00l peaks of montmorillonite (S, Sm). Co = corrensite, F = feldspar; * = peak from sample holder.

VA-01C (0.05 - 0.2 μm)



VA-01C (0.05 - 0.2 μm)

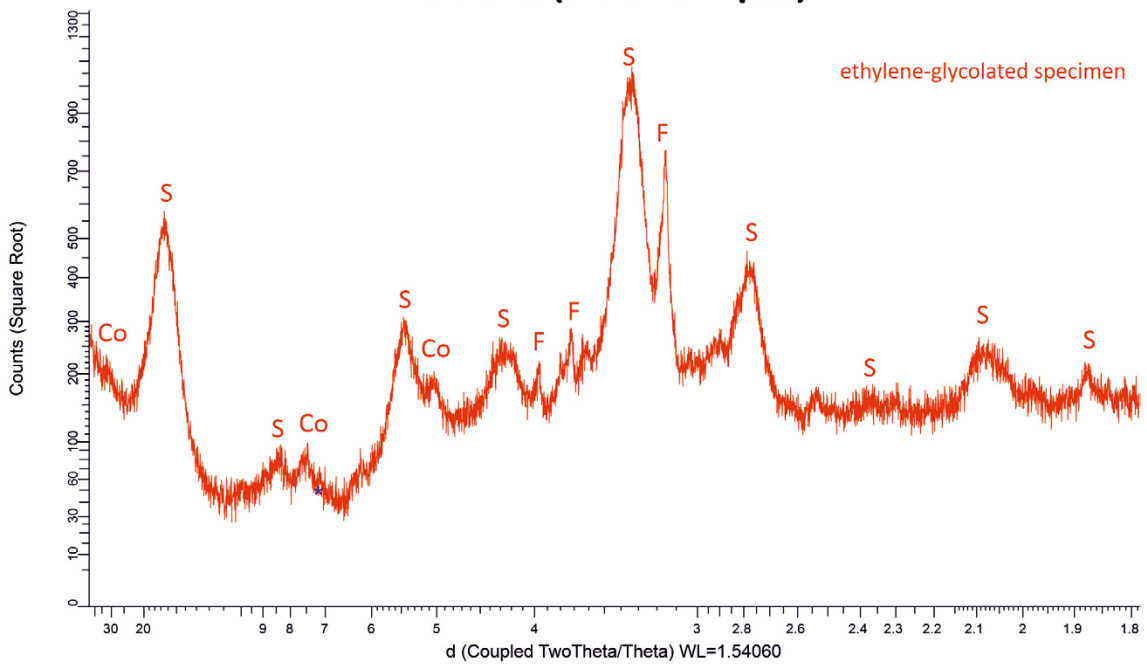


Figure E-22. X-ray diffractogram of air-dried and ethylene-glycolated oriented specimen of sample VA-01C. Co= corrensite, F = feldspar, S = montmorillonite, * = peak from sample holder.

James Hutton XRPD scan plots

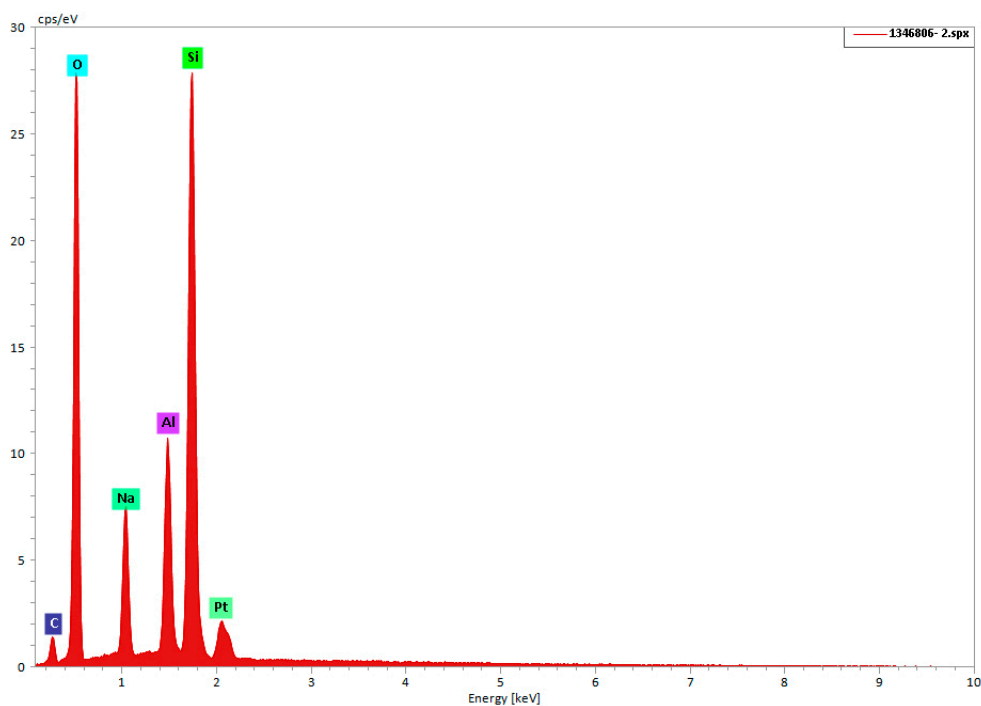


Figure F-1. XRPD pattern for sample 1346806-2 (KINA sample ID 2019 solid c65ff9; see Table 3-14 for details)

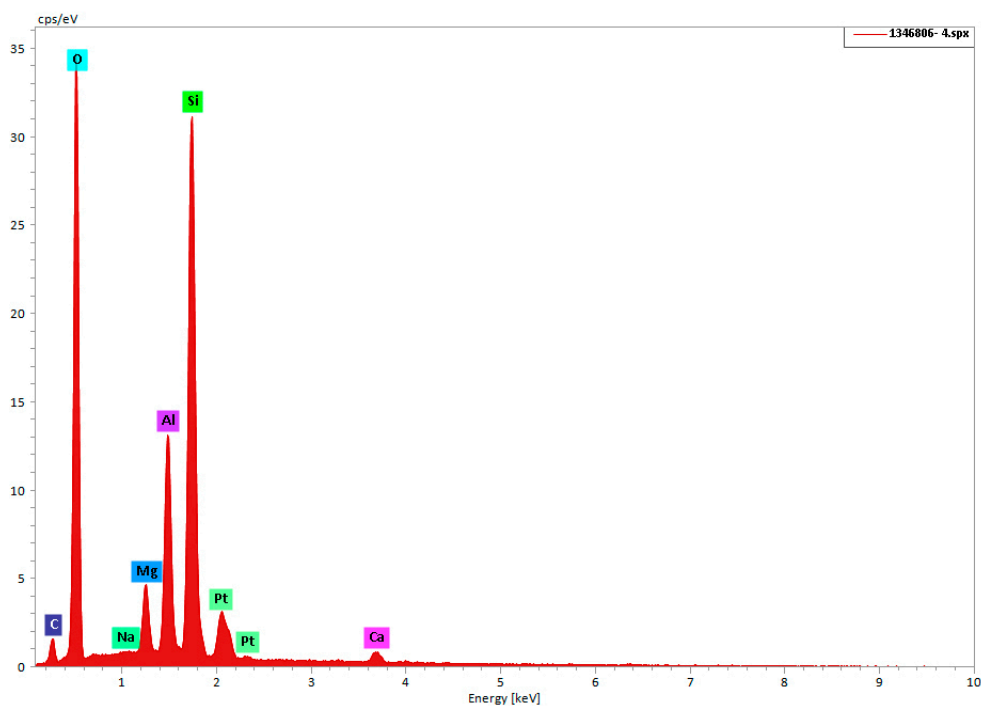
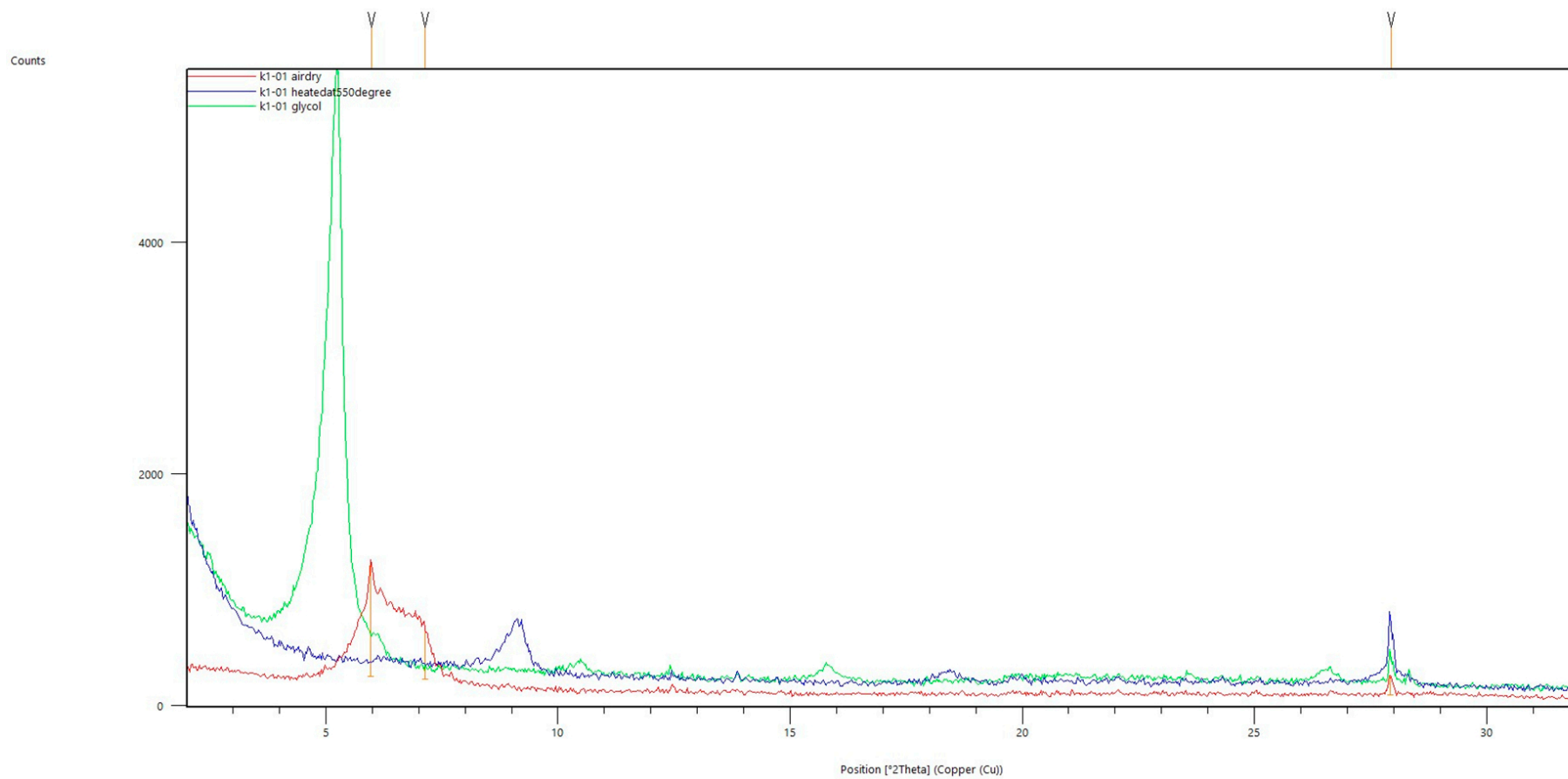
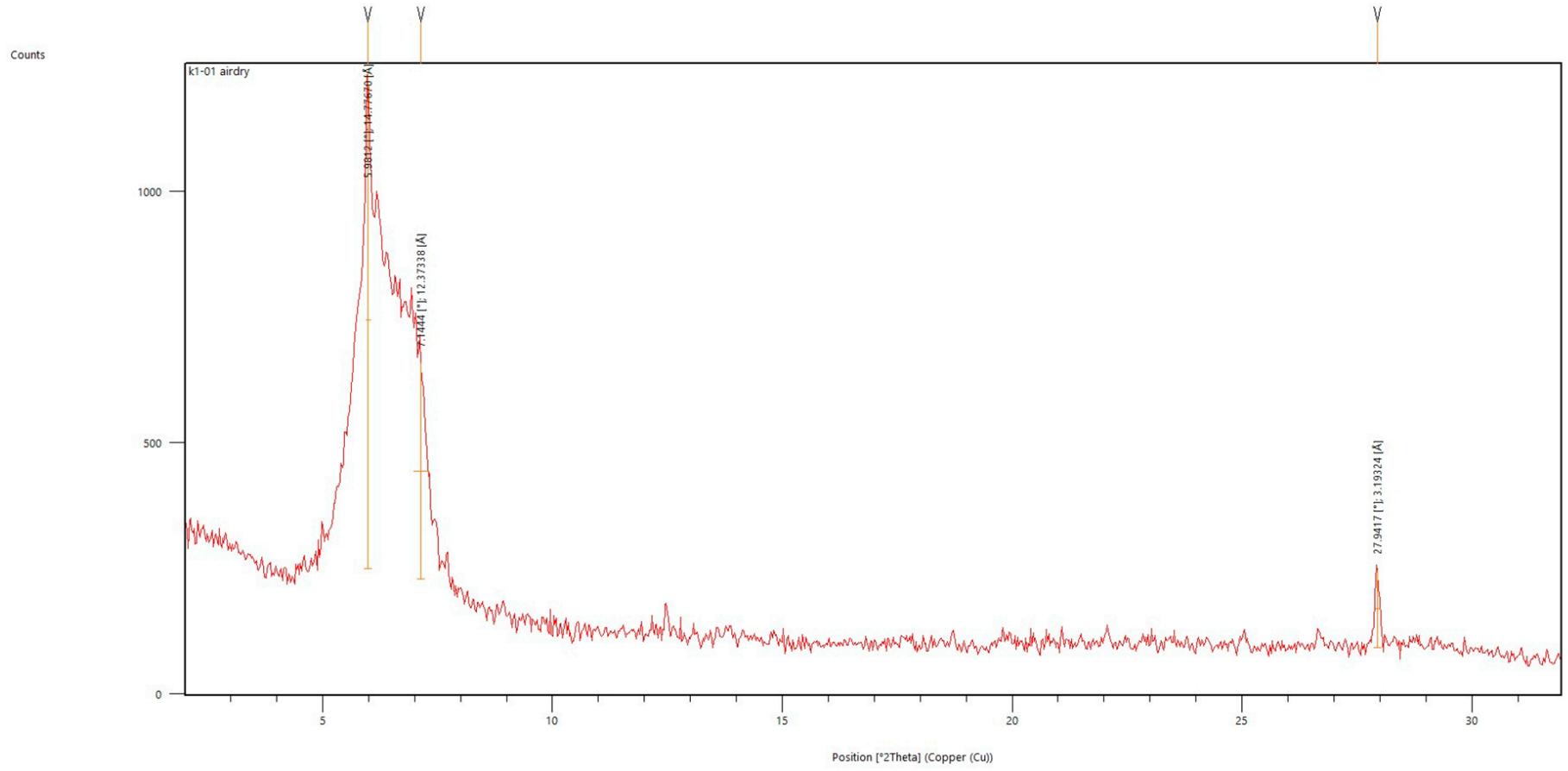
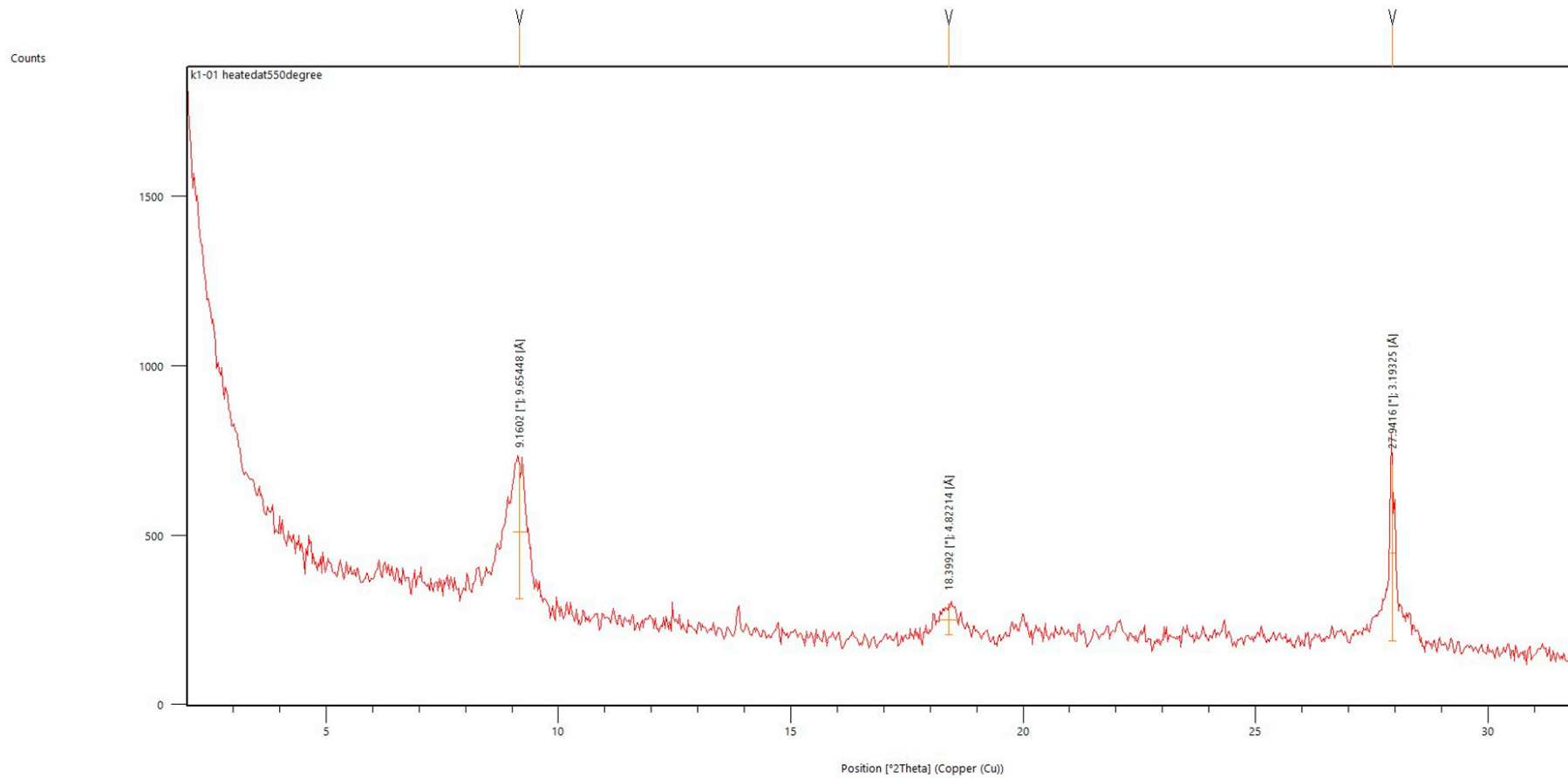


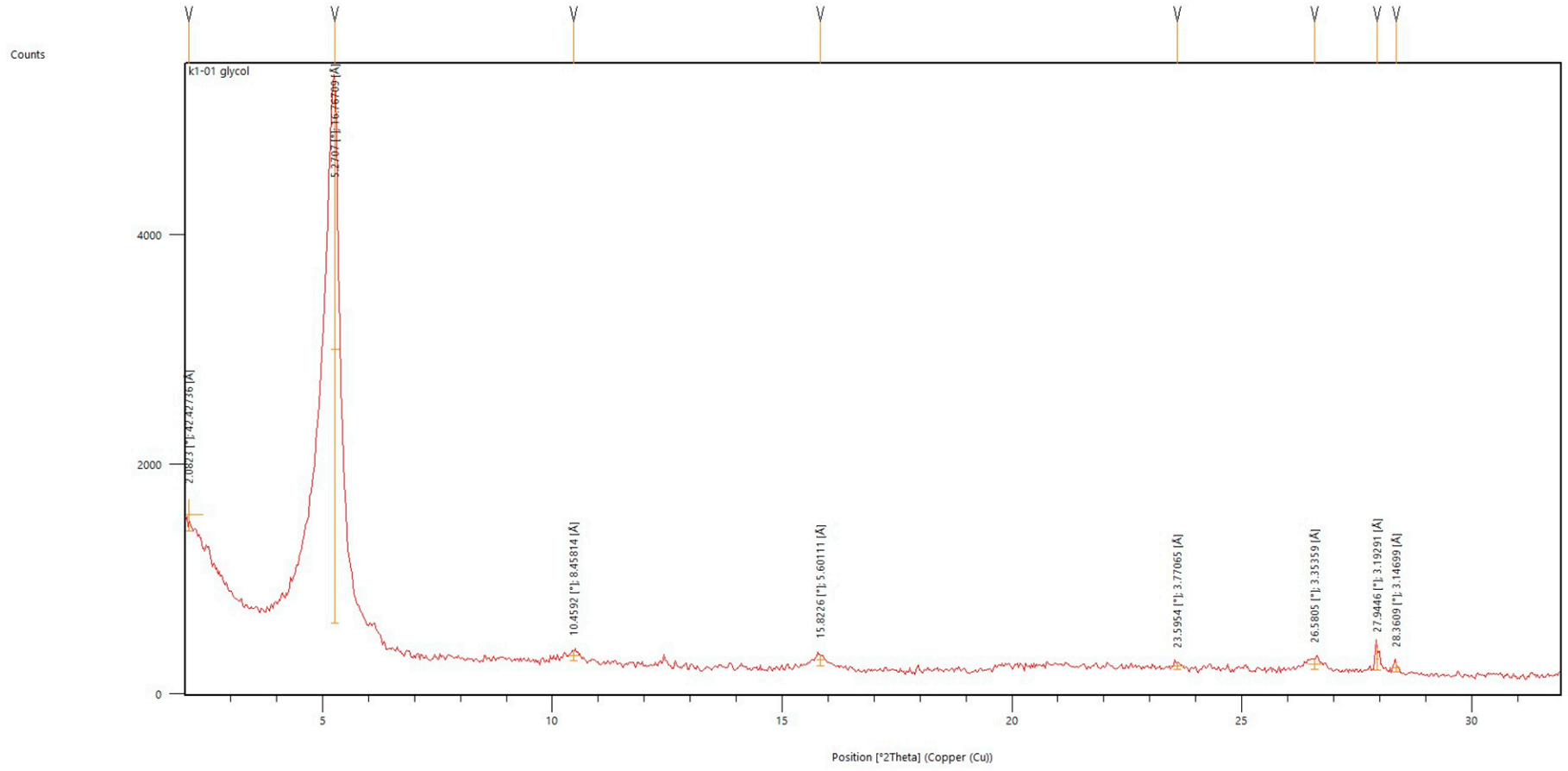
Figure F-2. XRPD pattern for sample 1346806-4 (KINA sample ID 2019 solid c65ff9; see Table 3-14 for details)

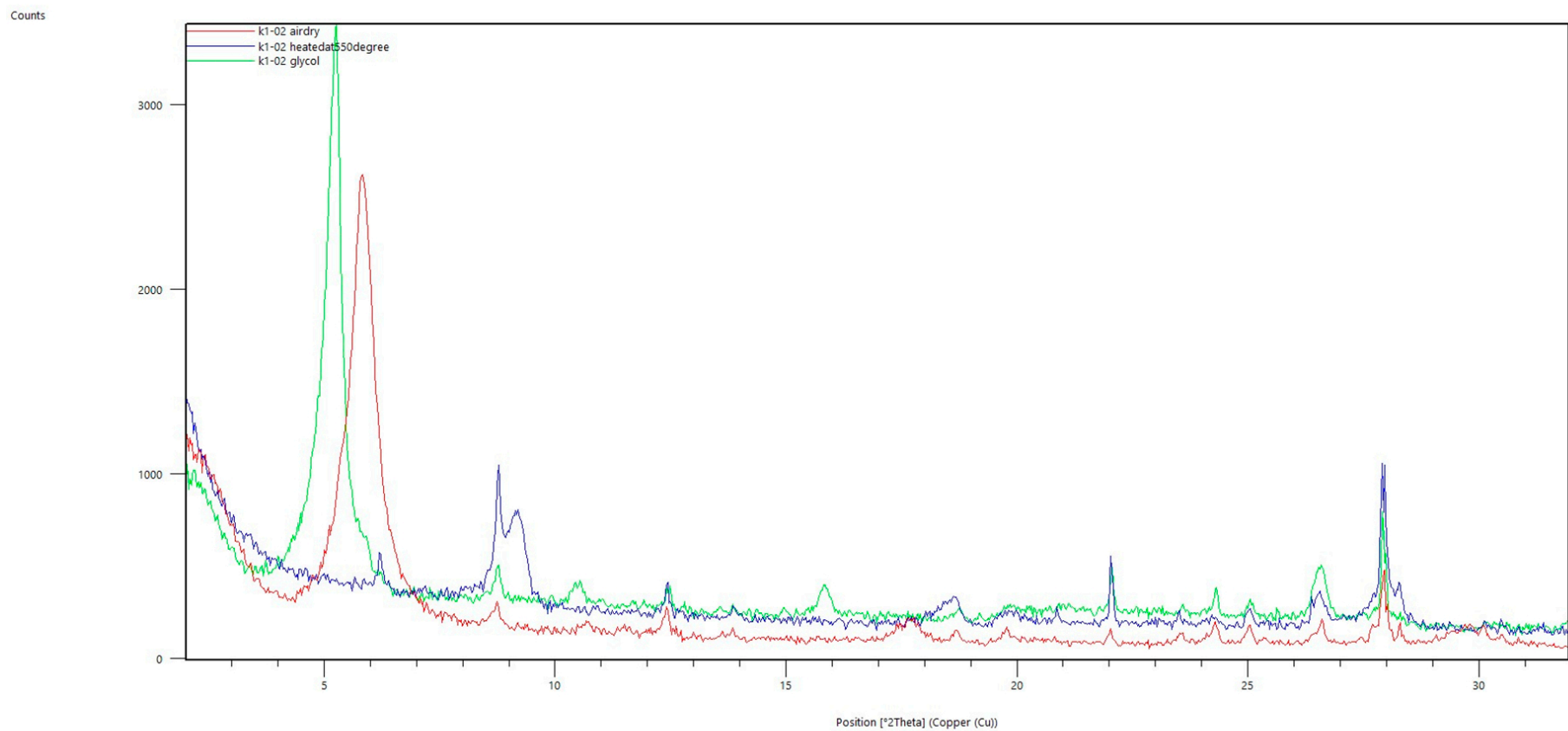
GSU XRD plots for samples K1-01 to -05 and MA-01

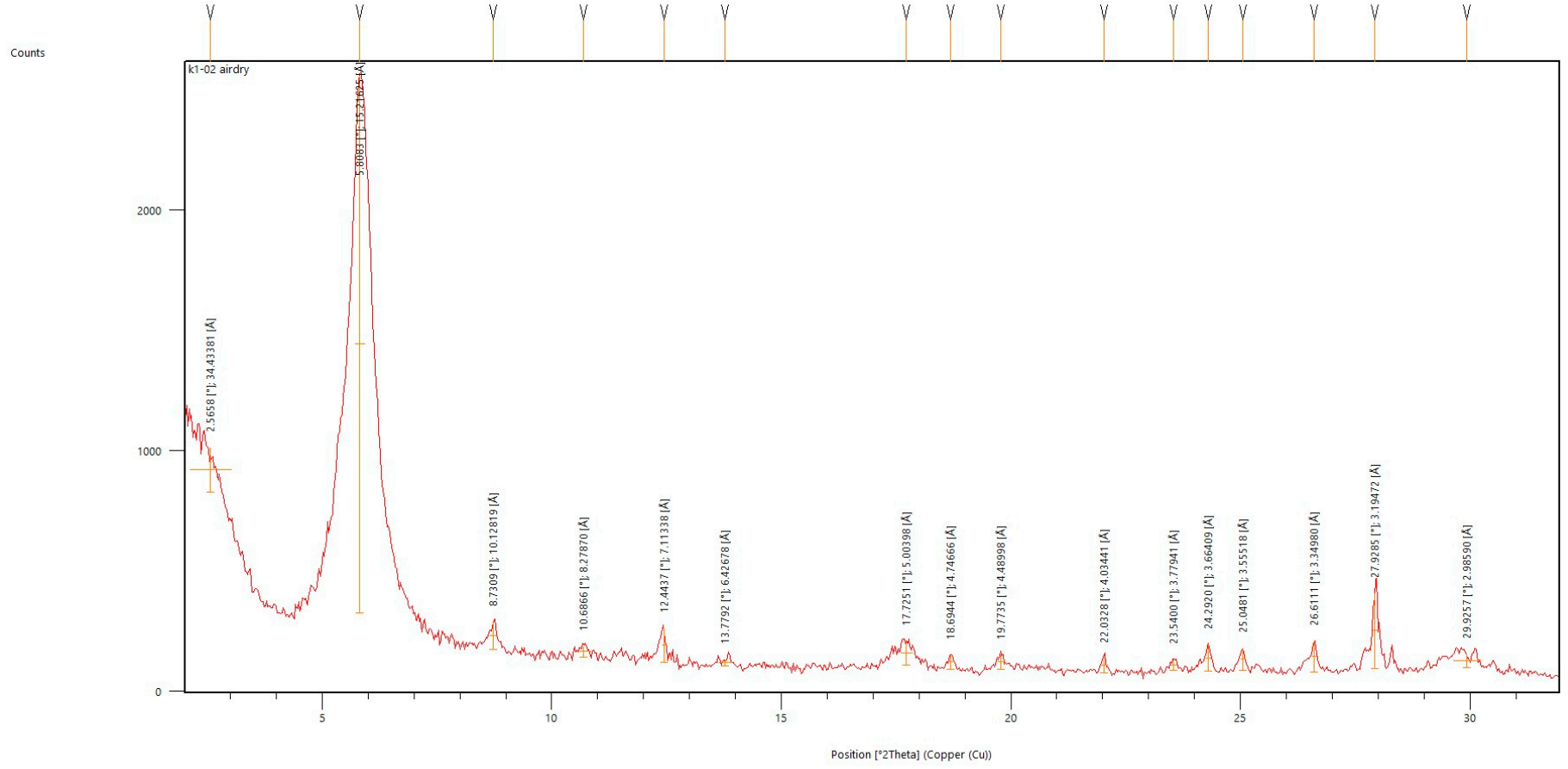


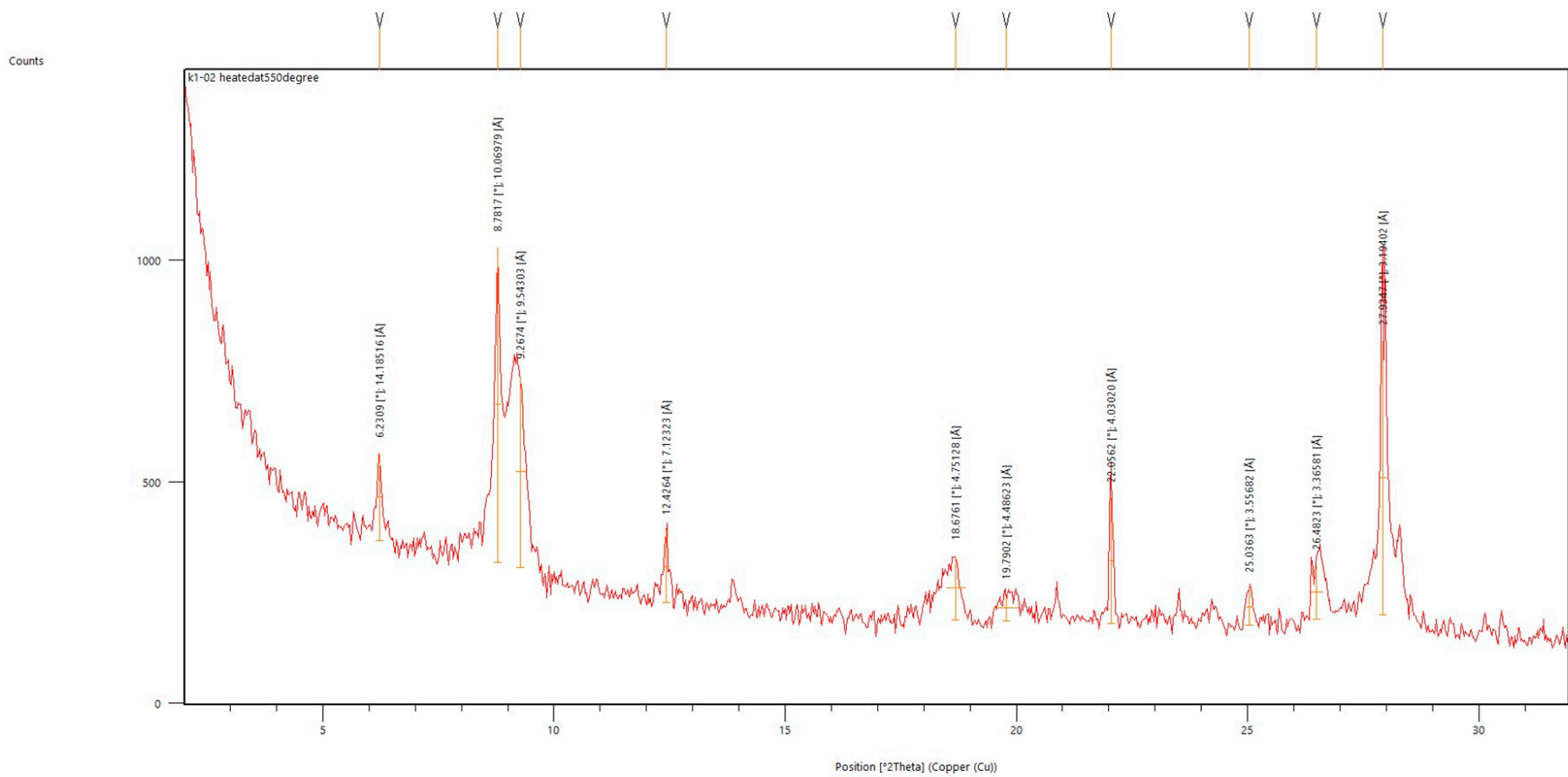


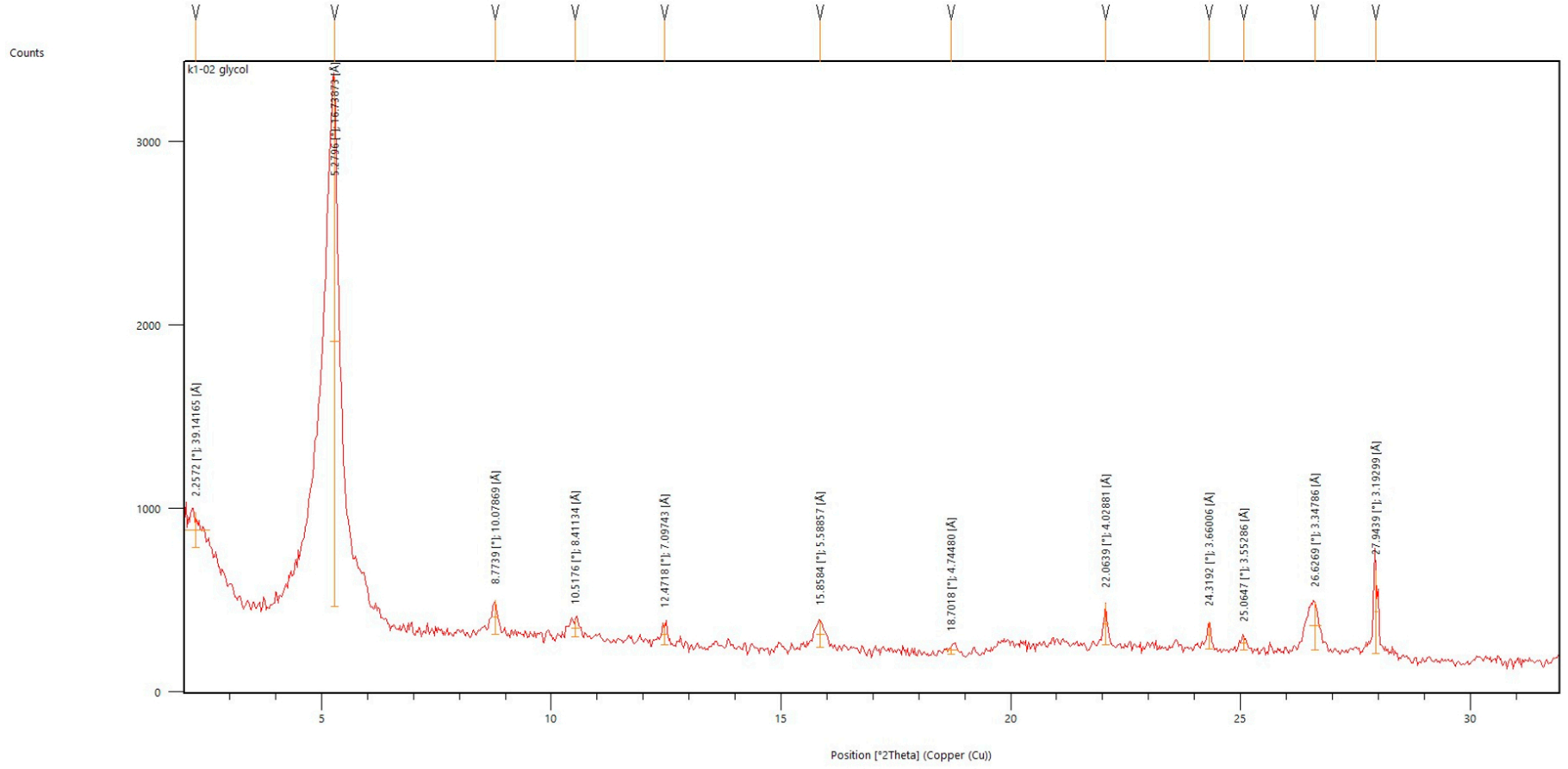


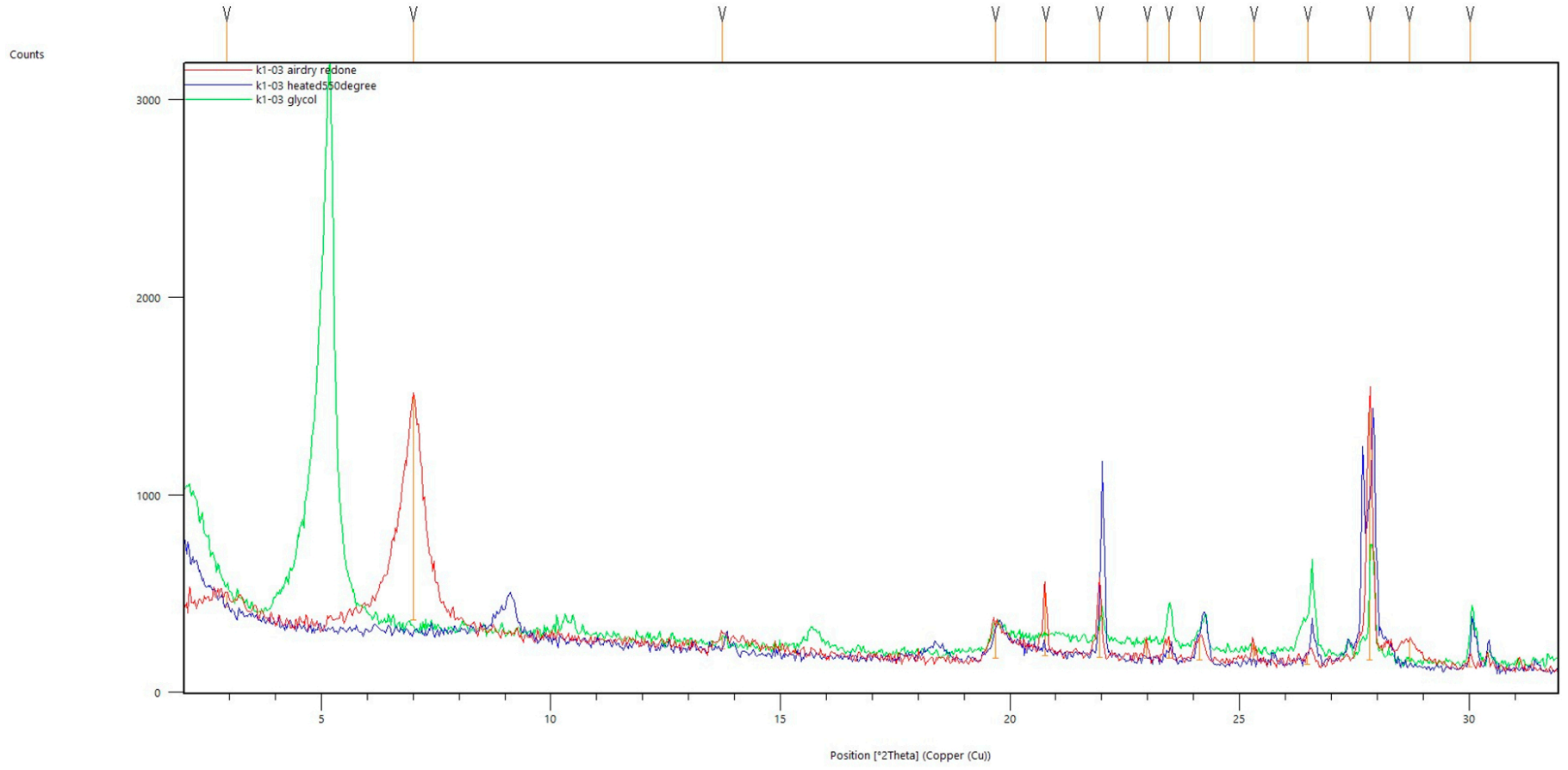


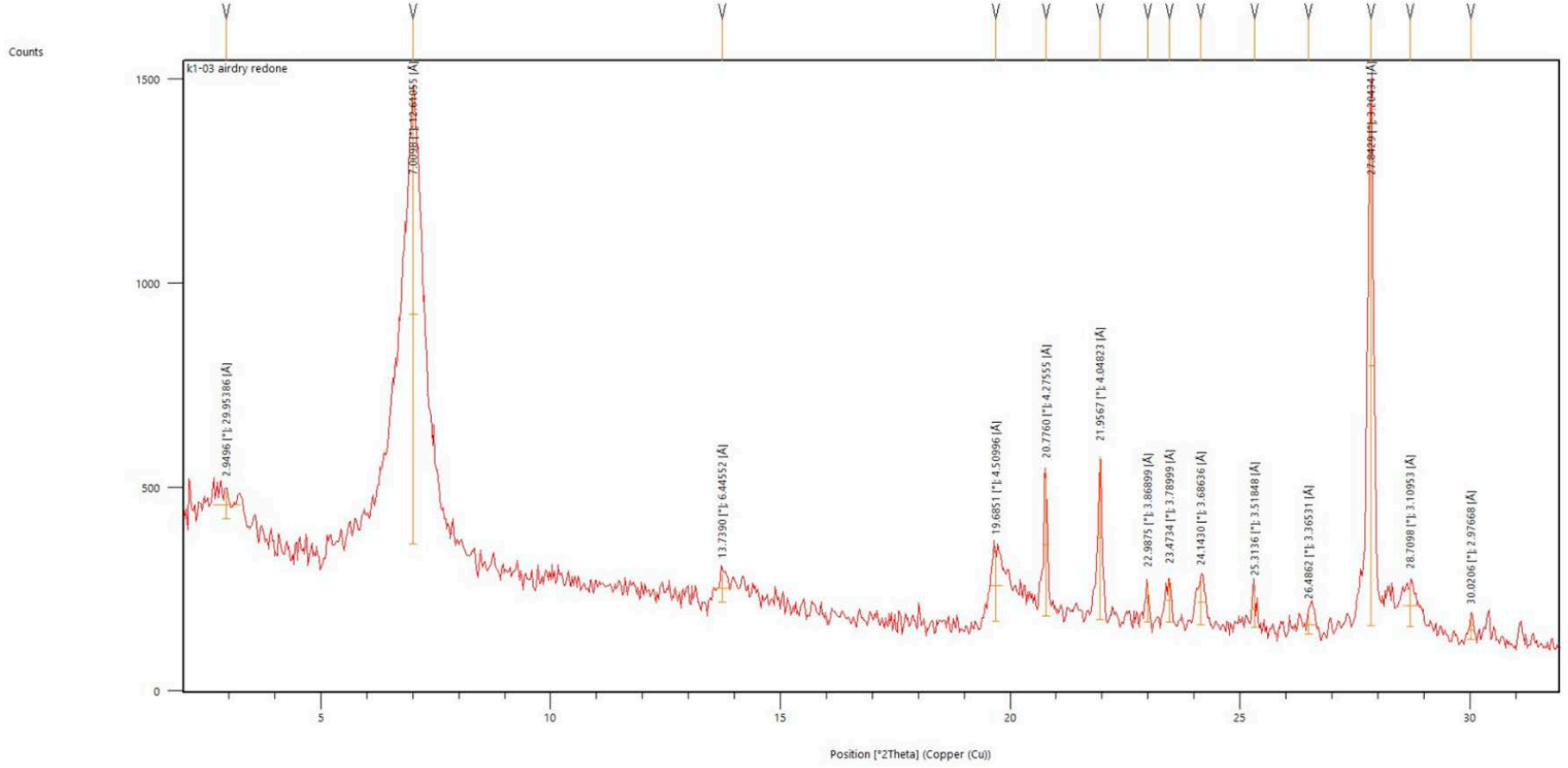


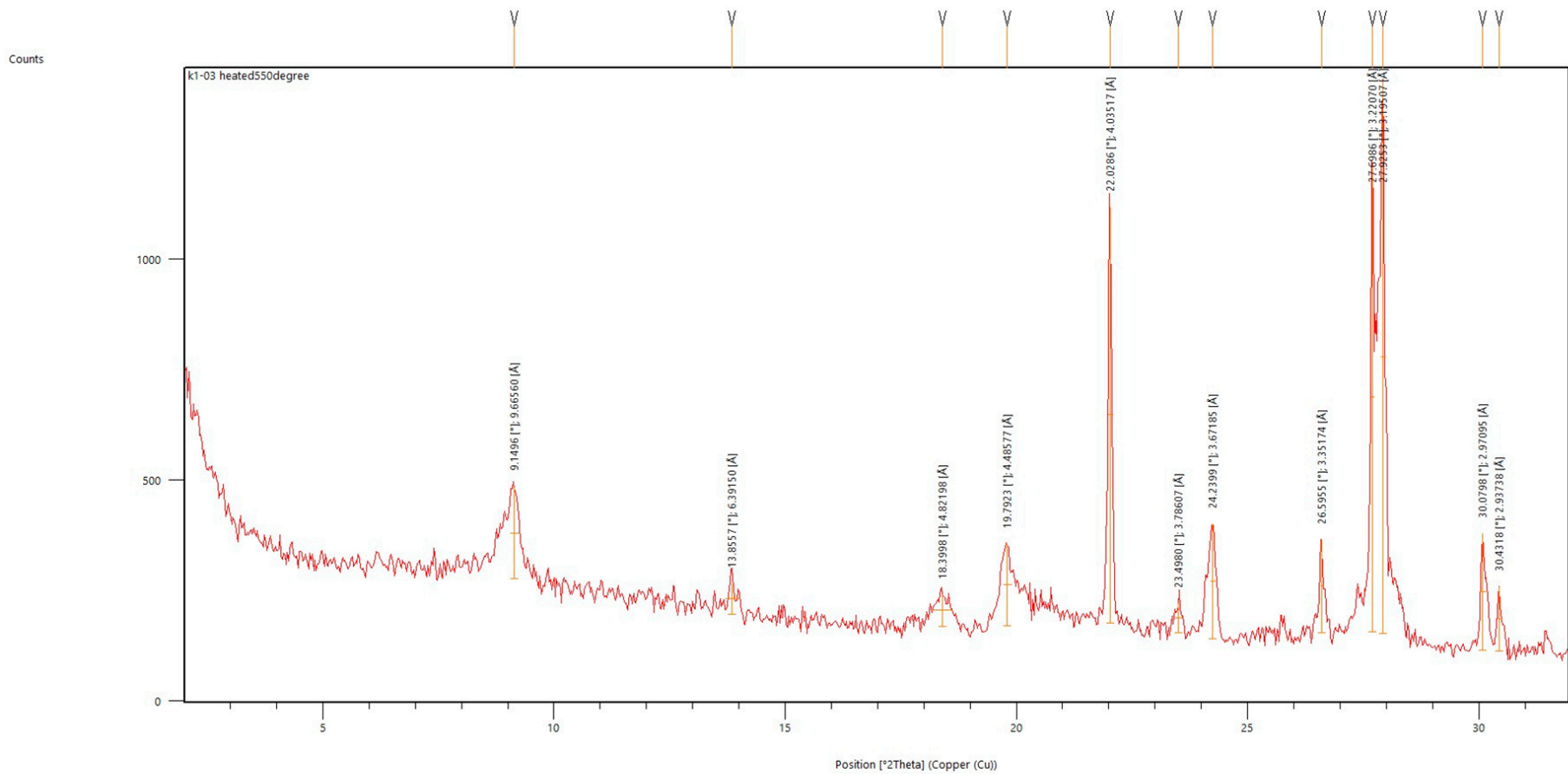


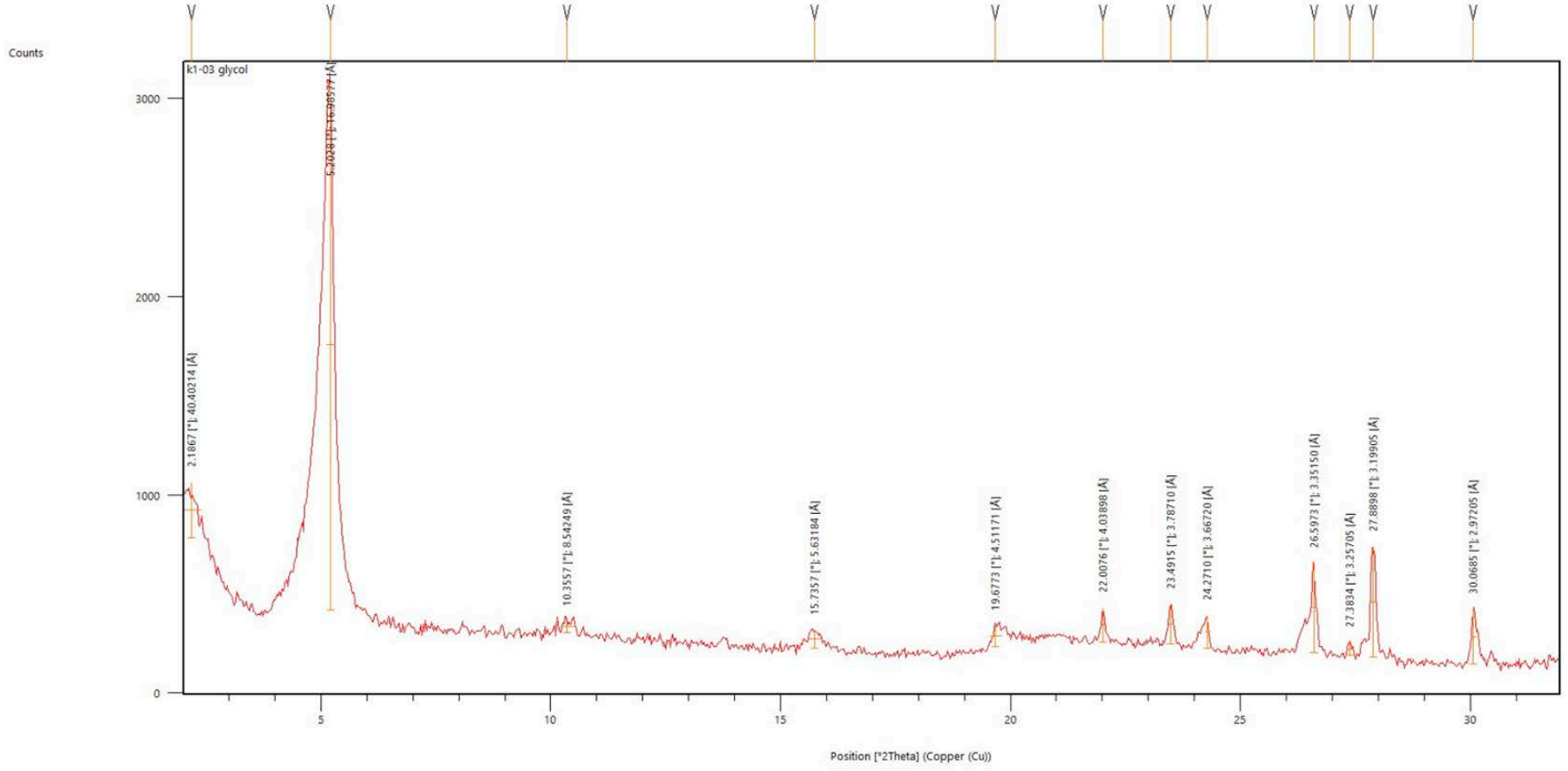


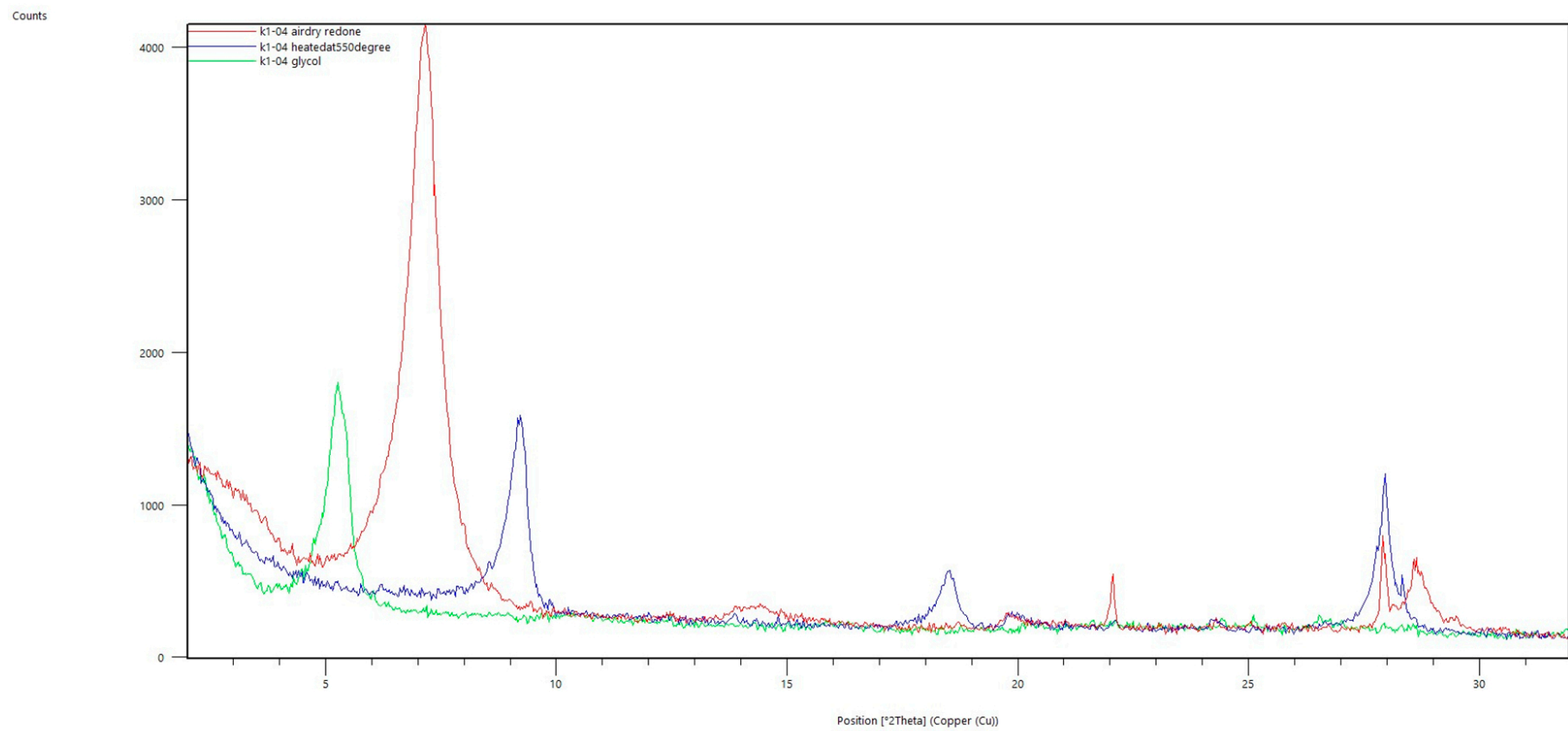


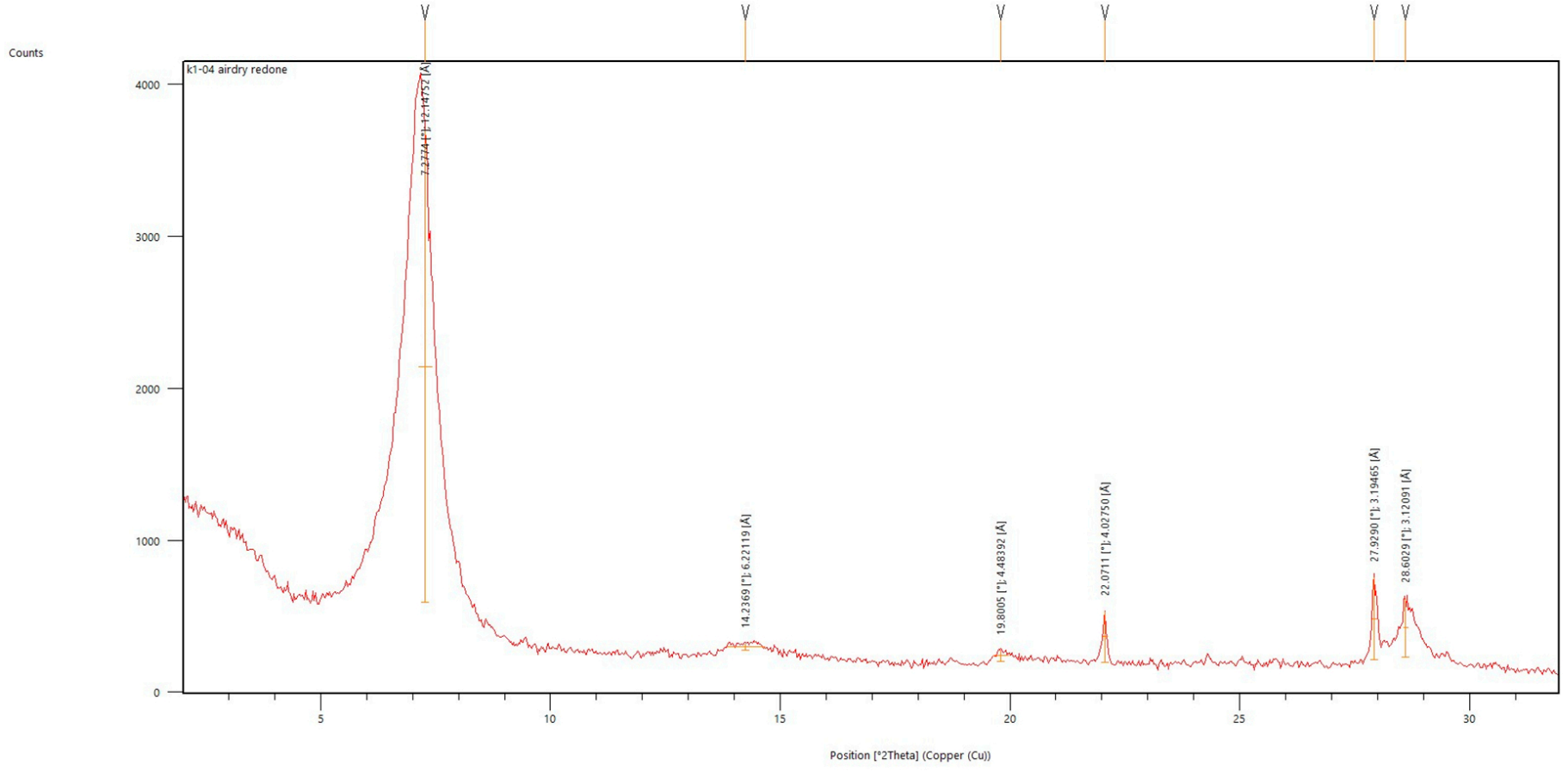


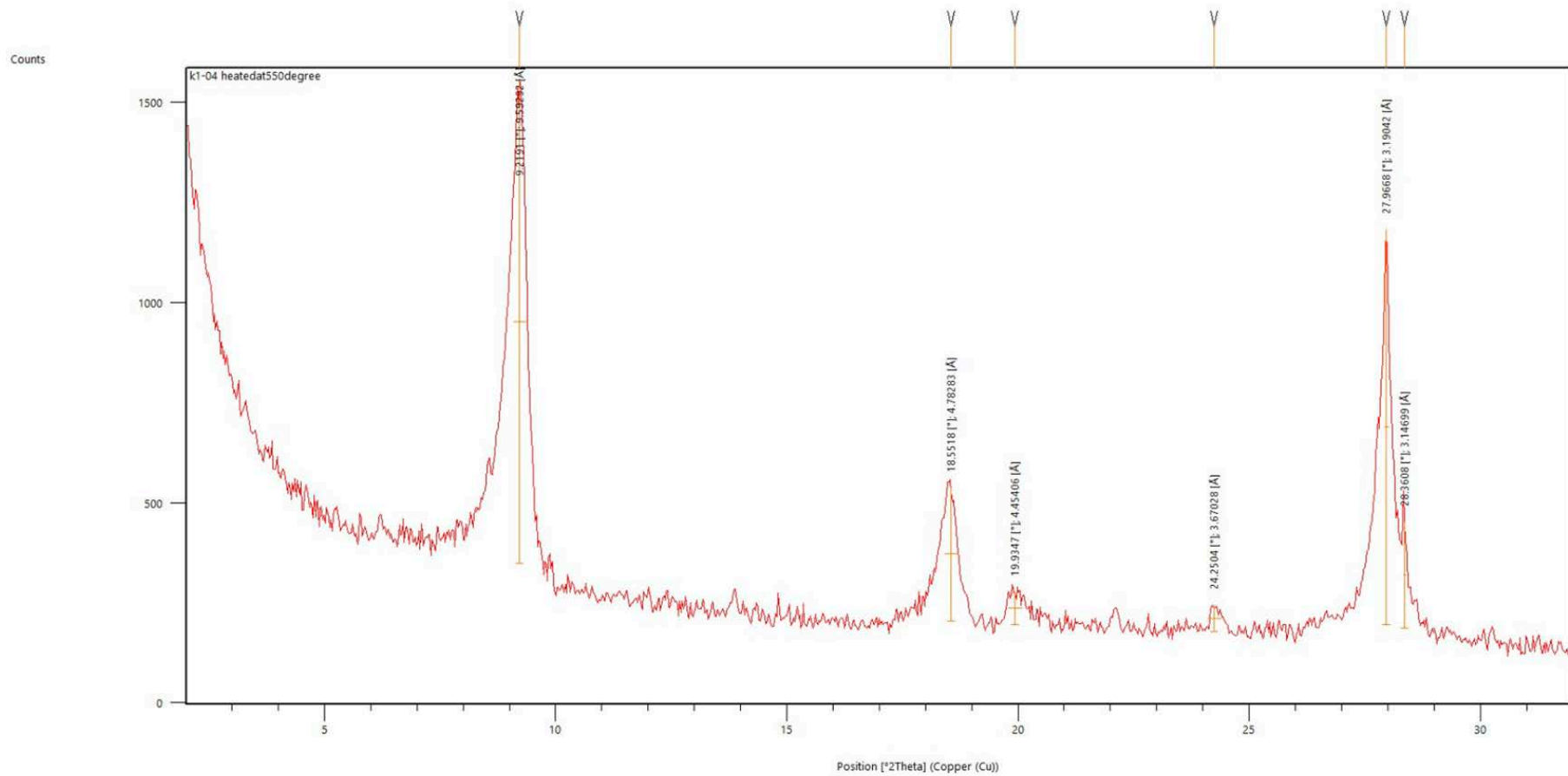


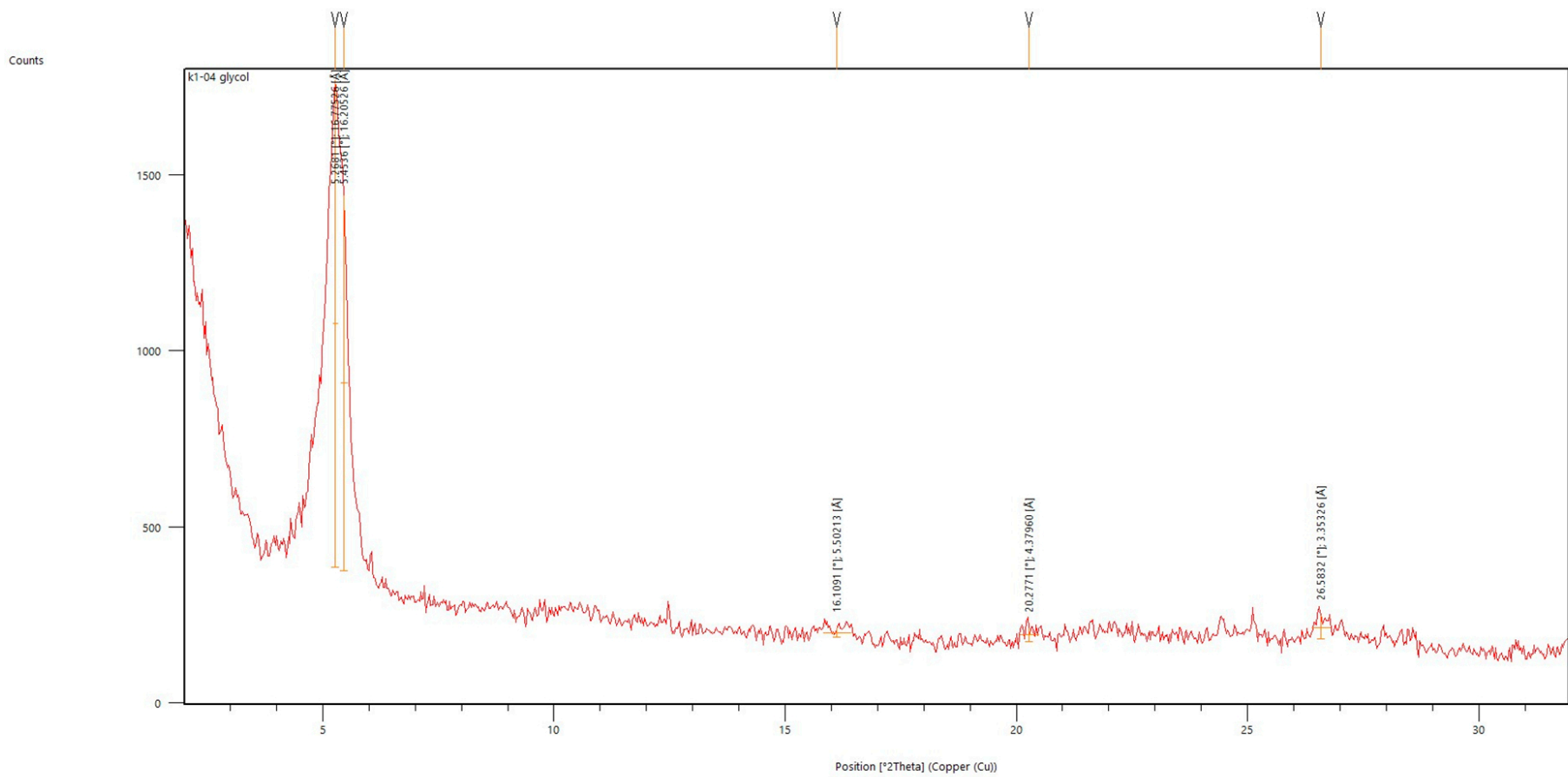


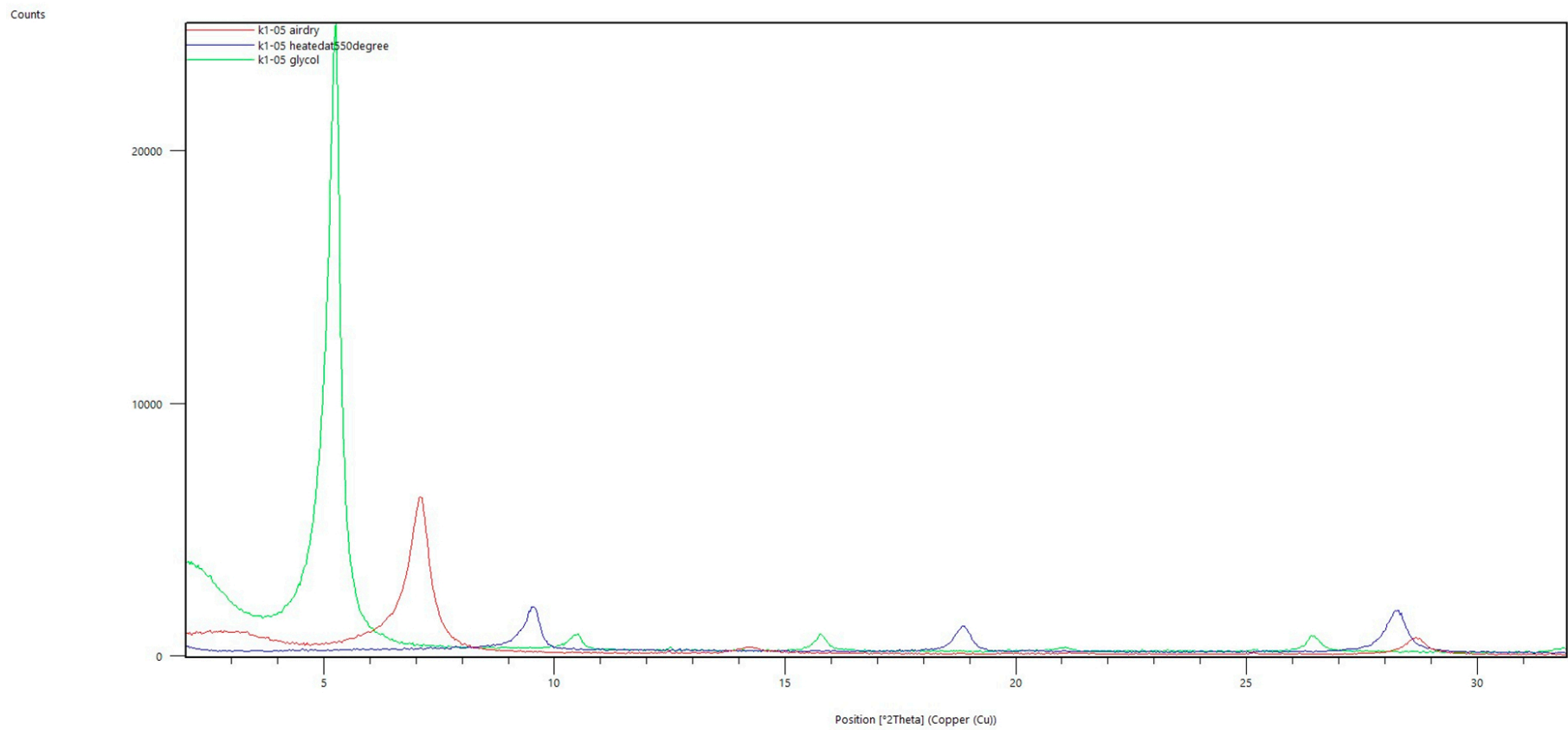


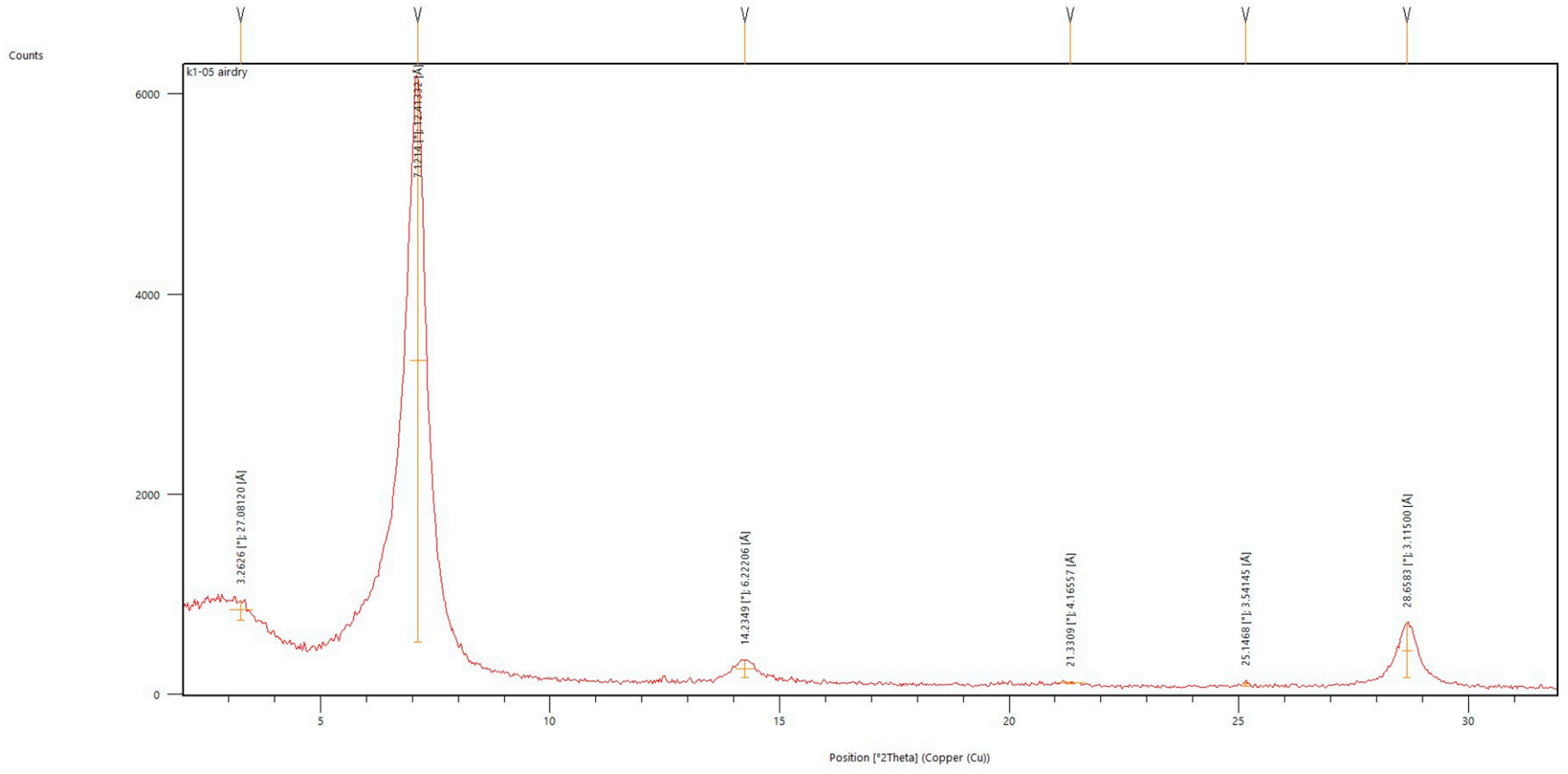


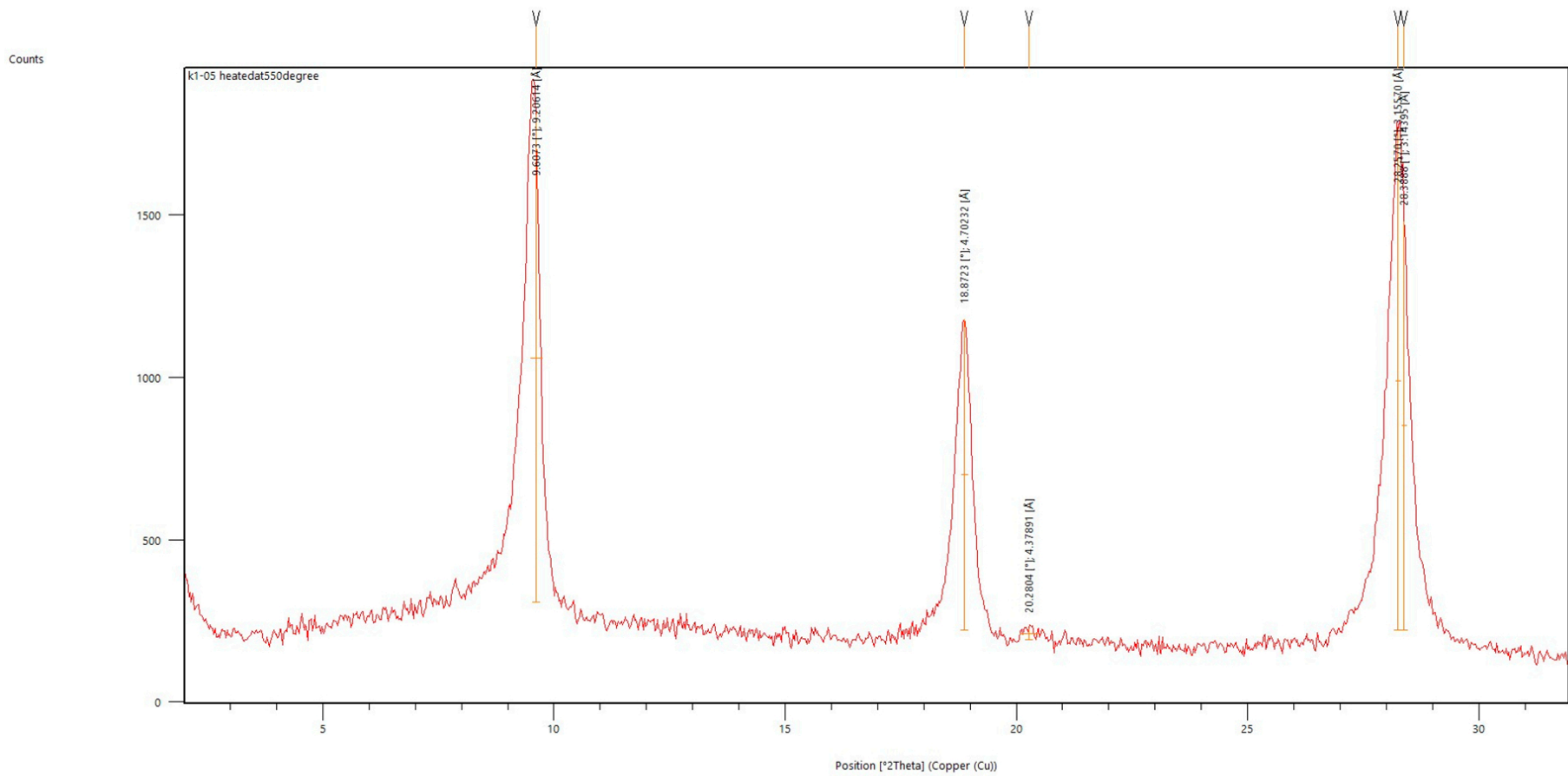


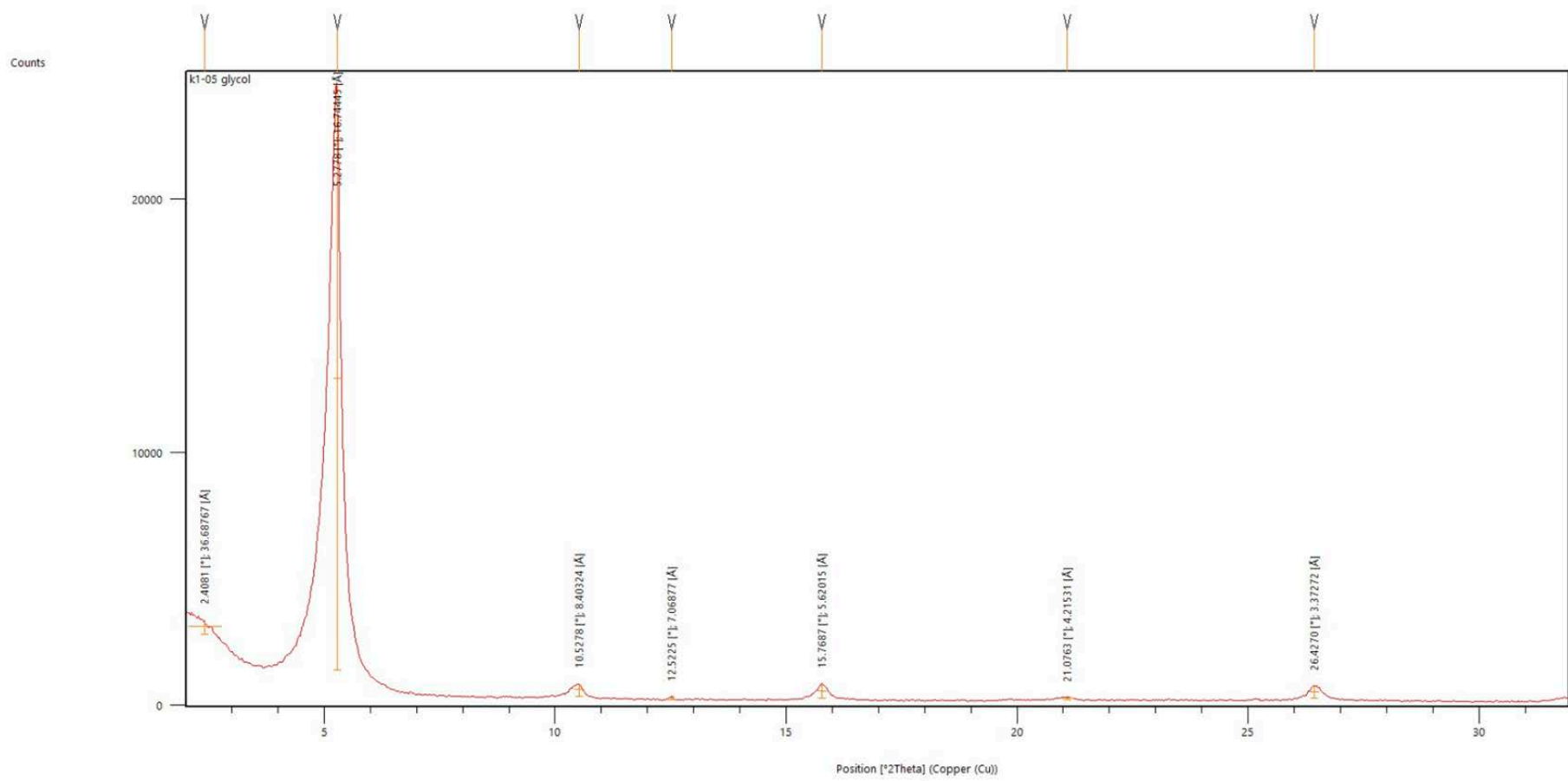


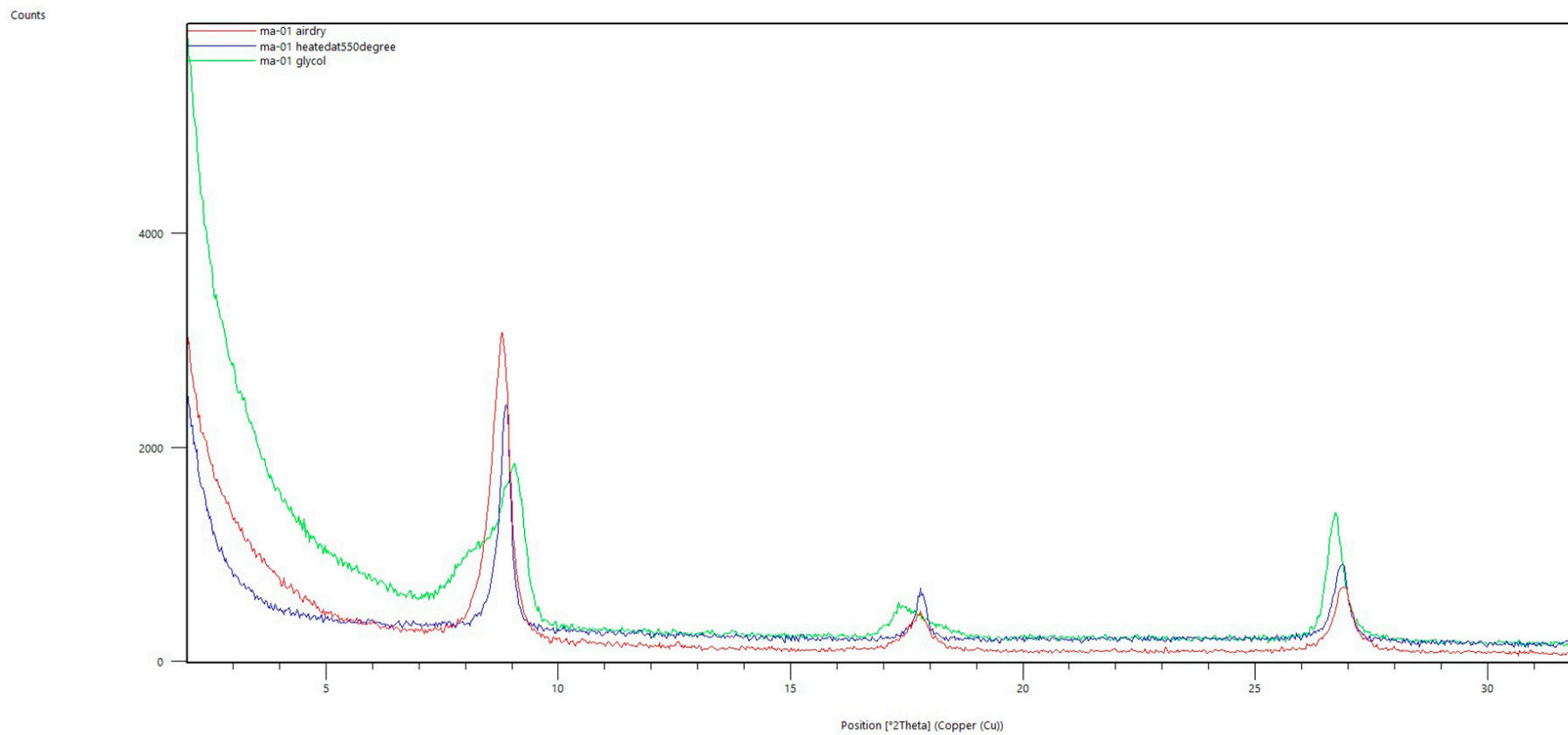


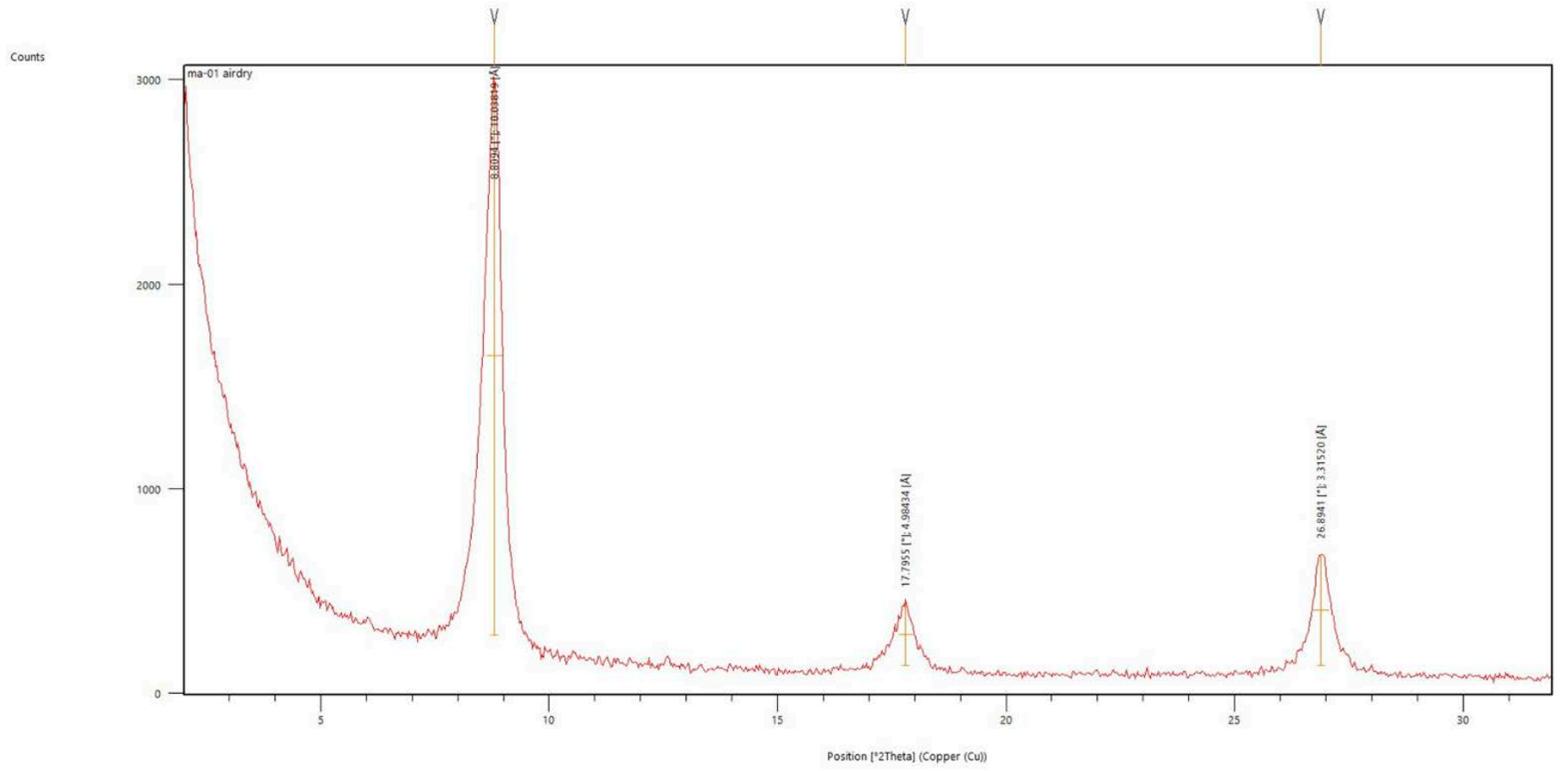


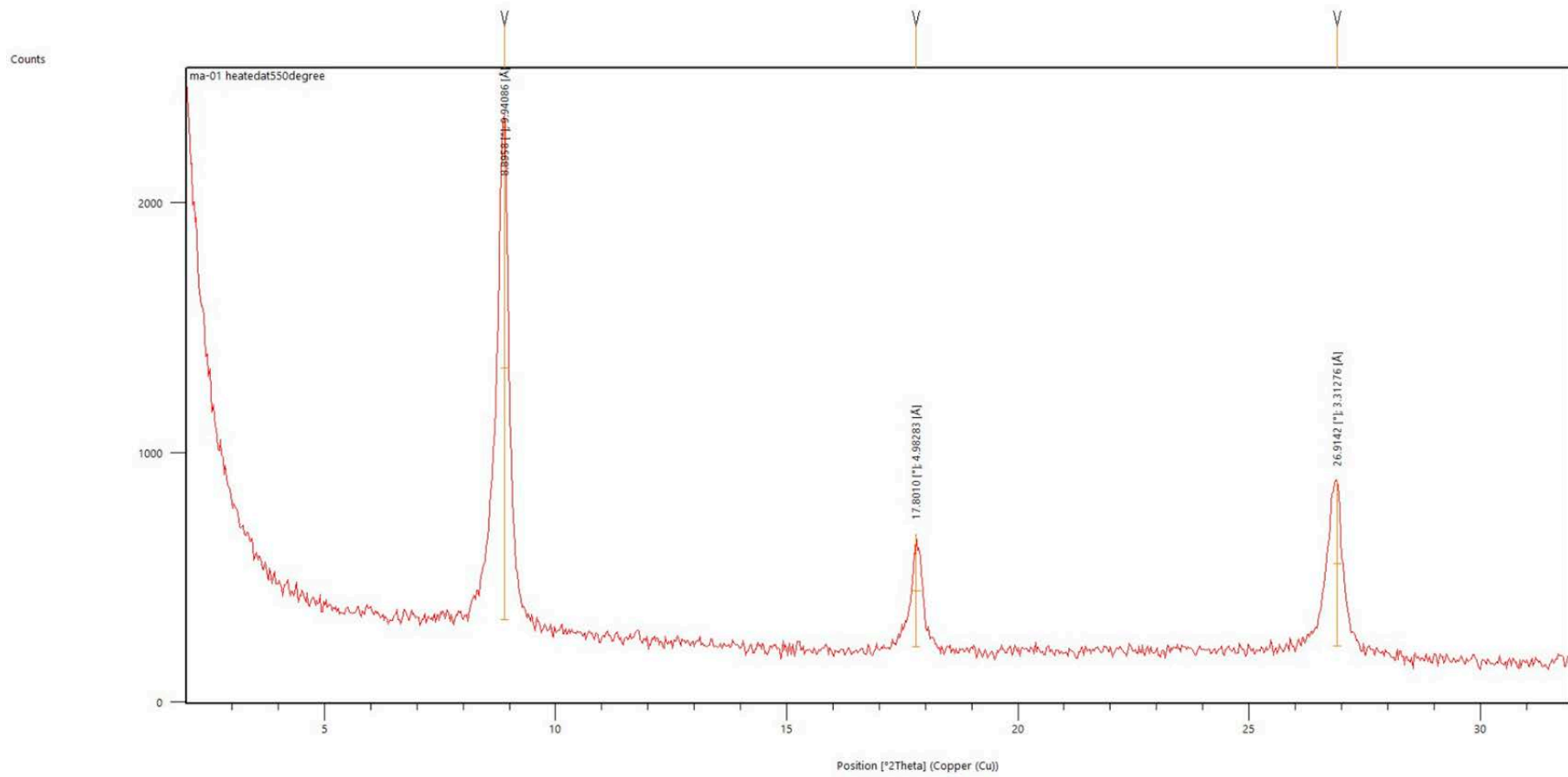


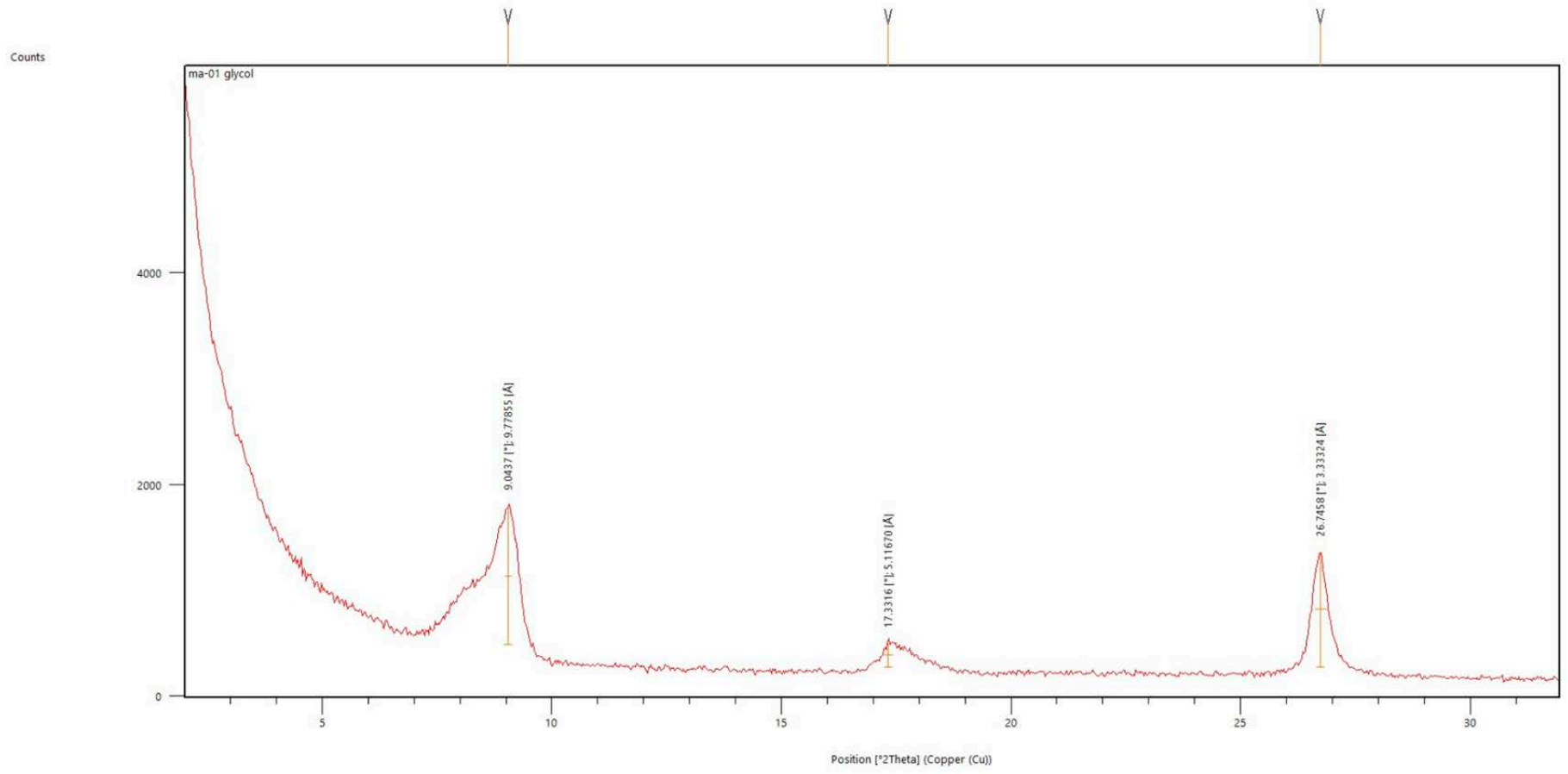


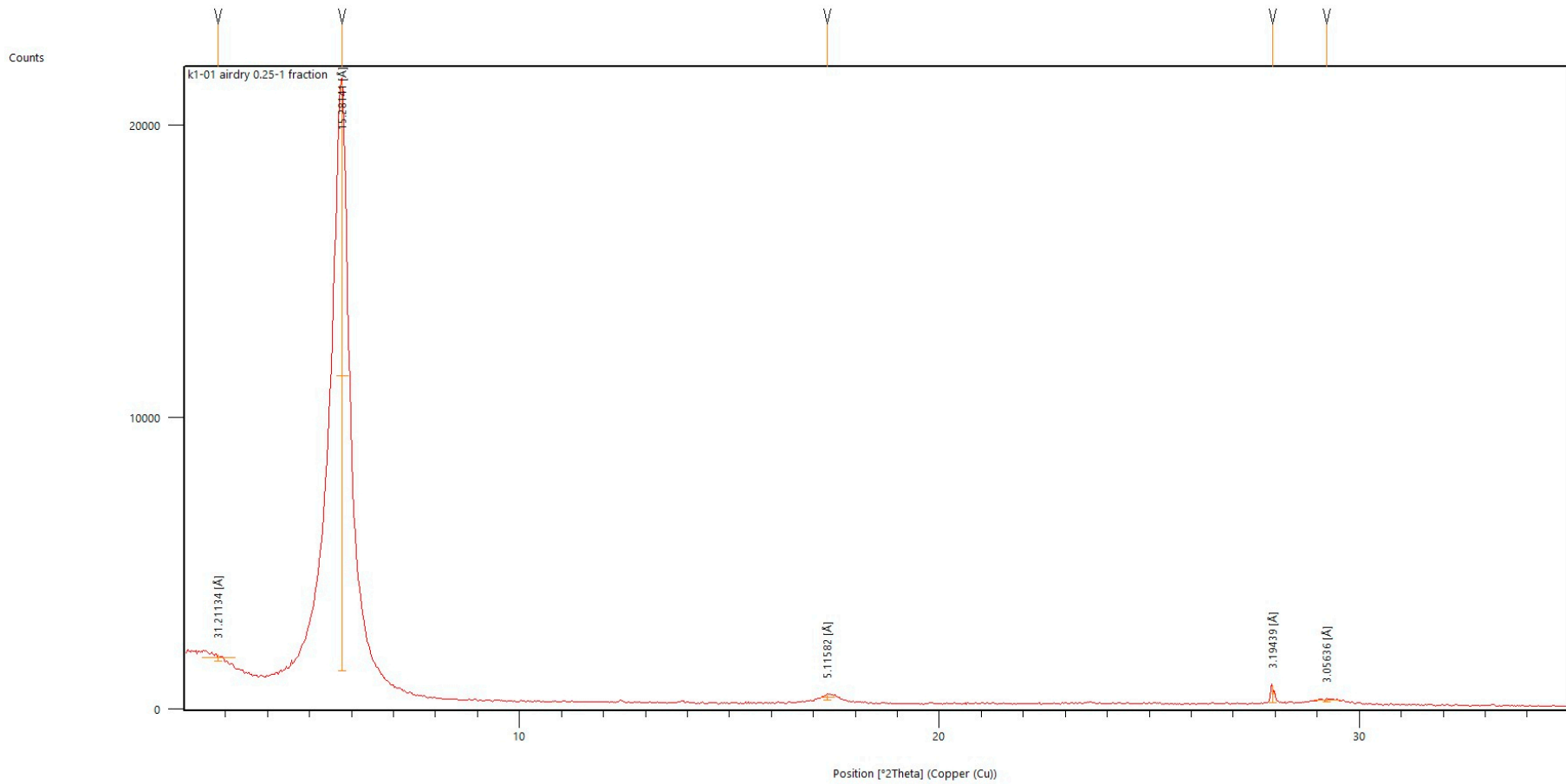


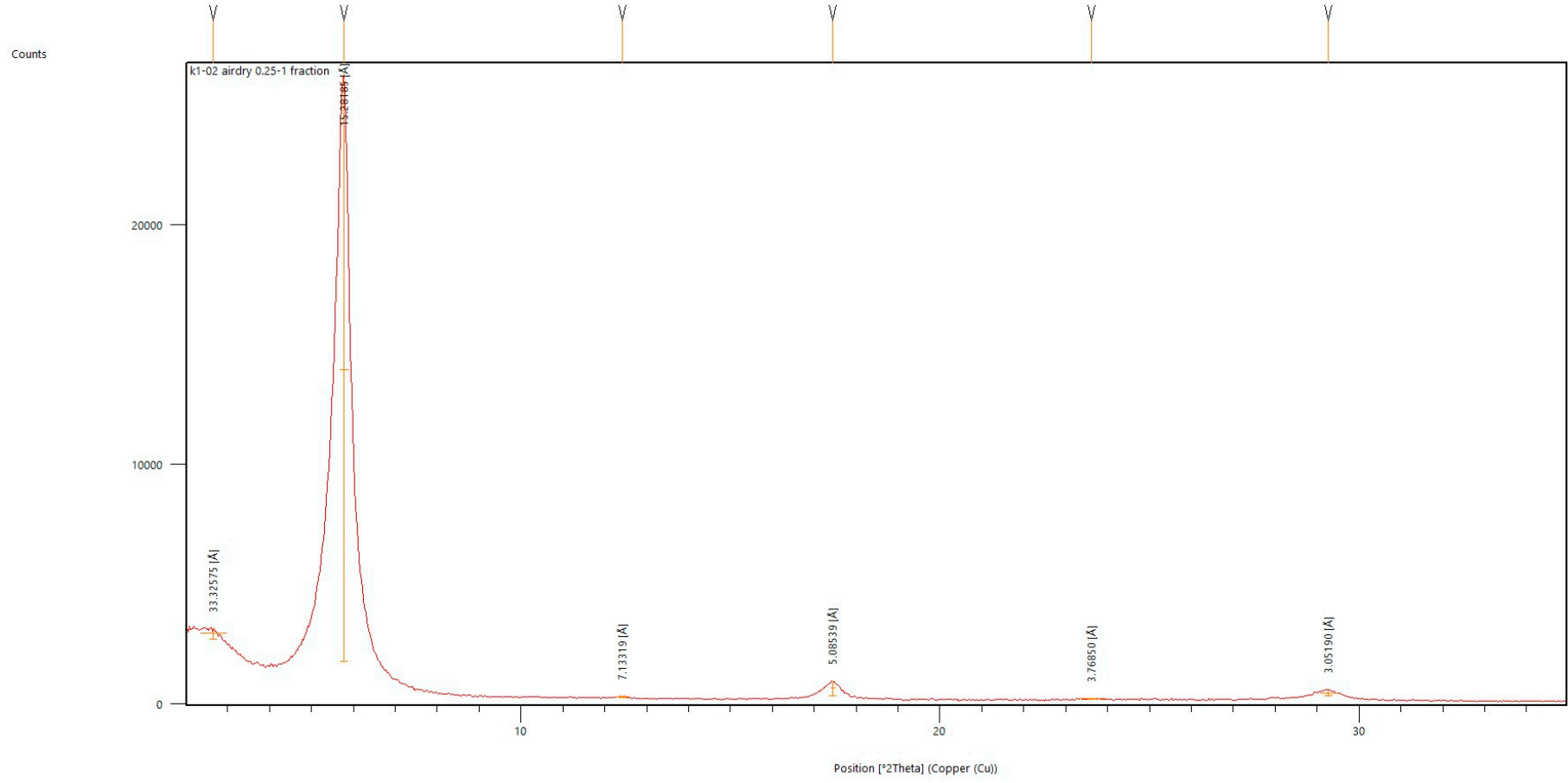


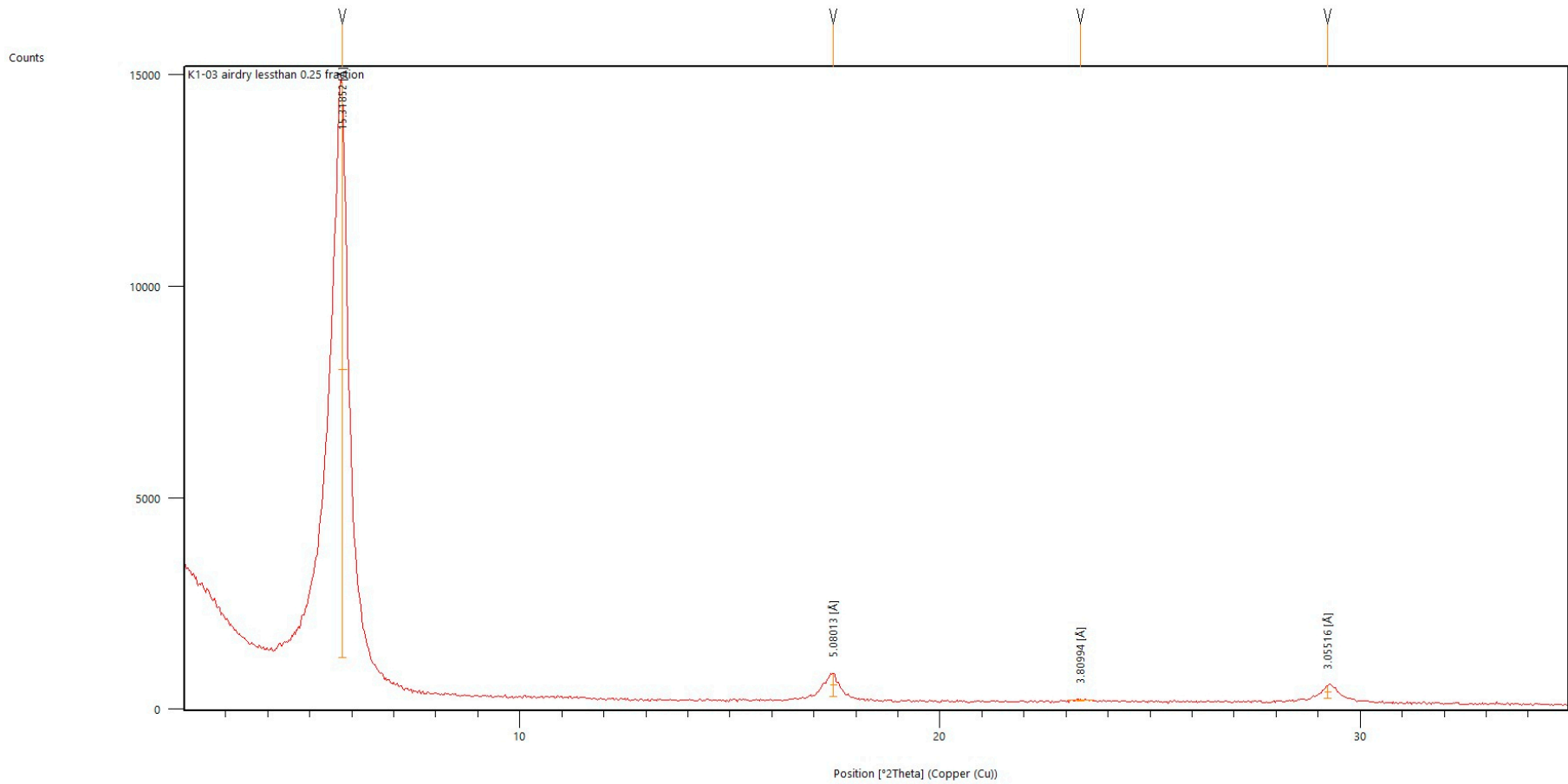


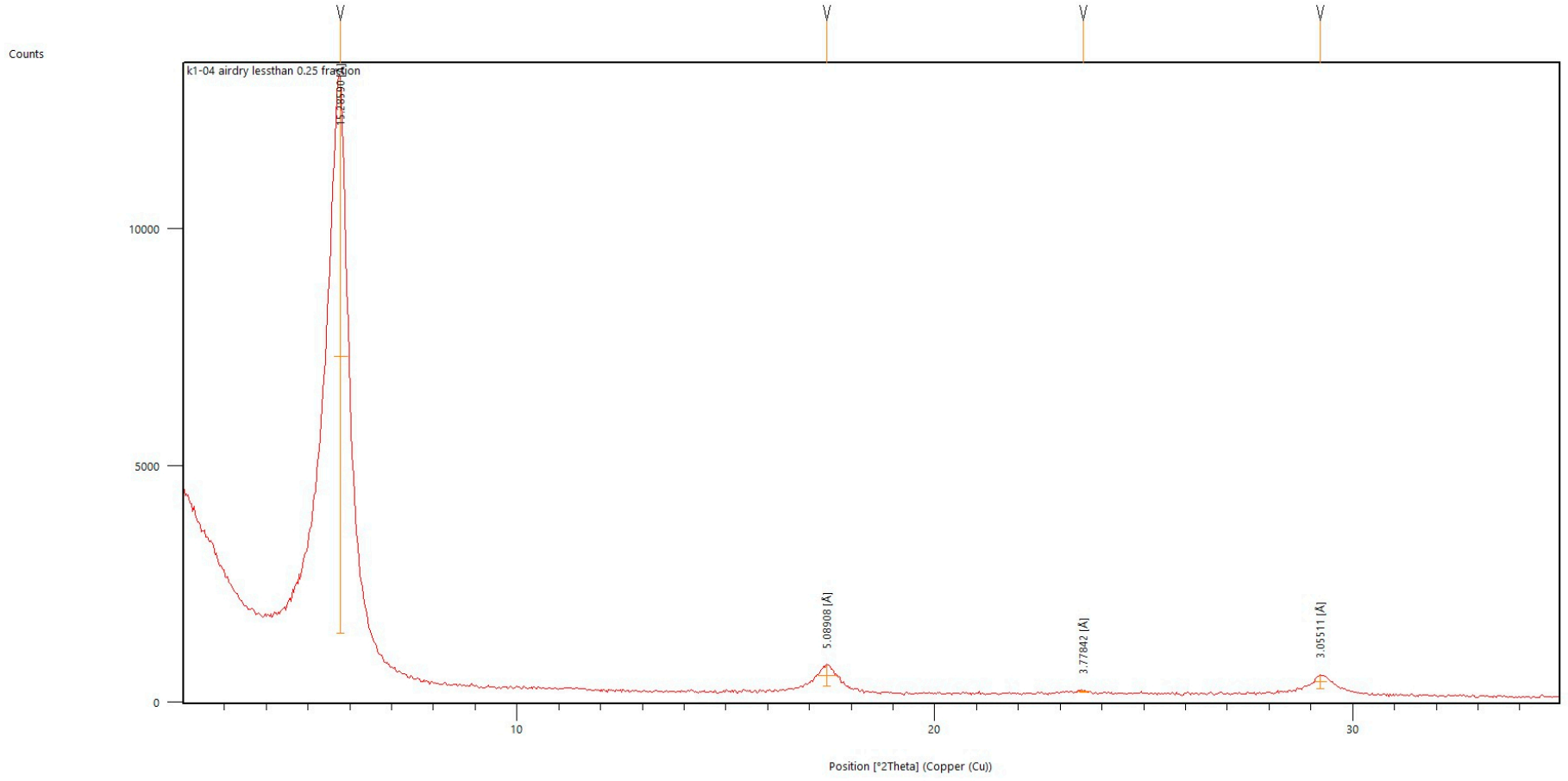


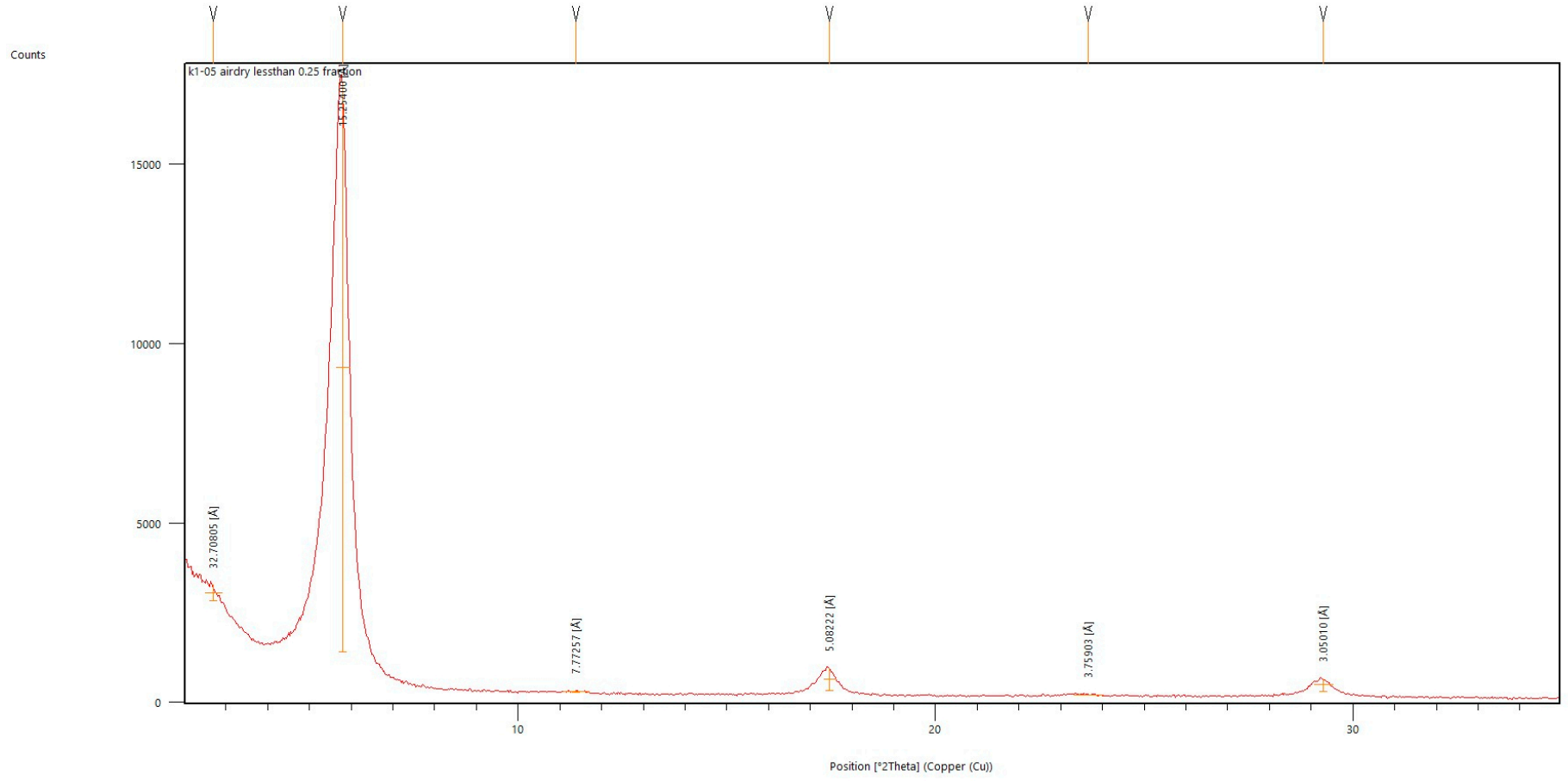


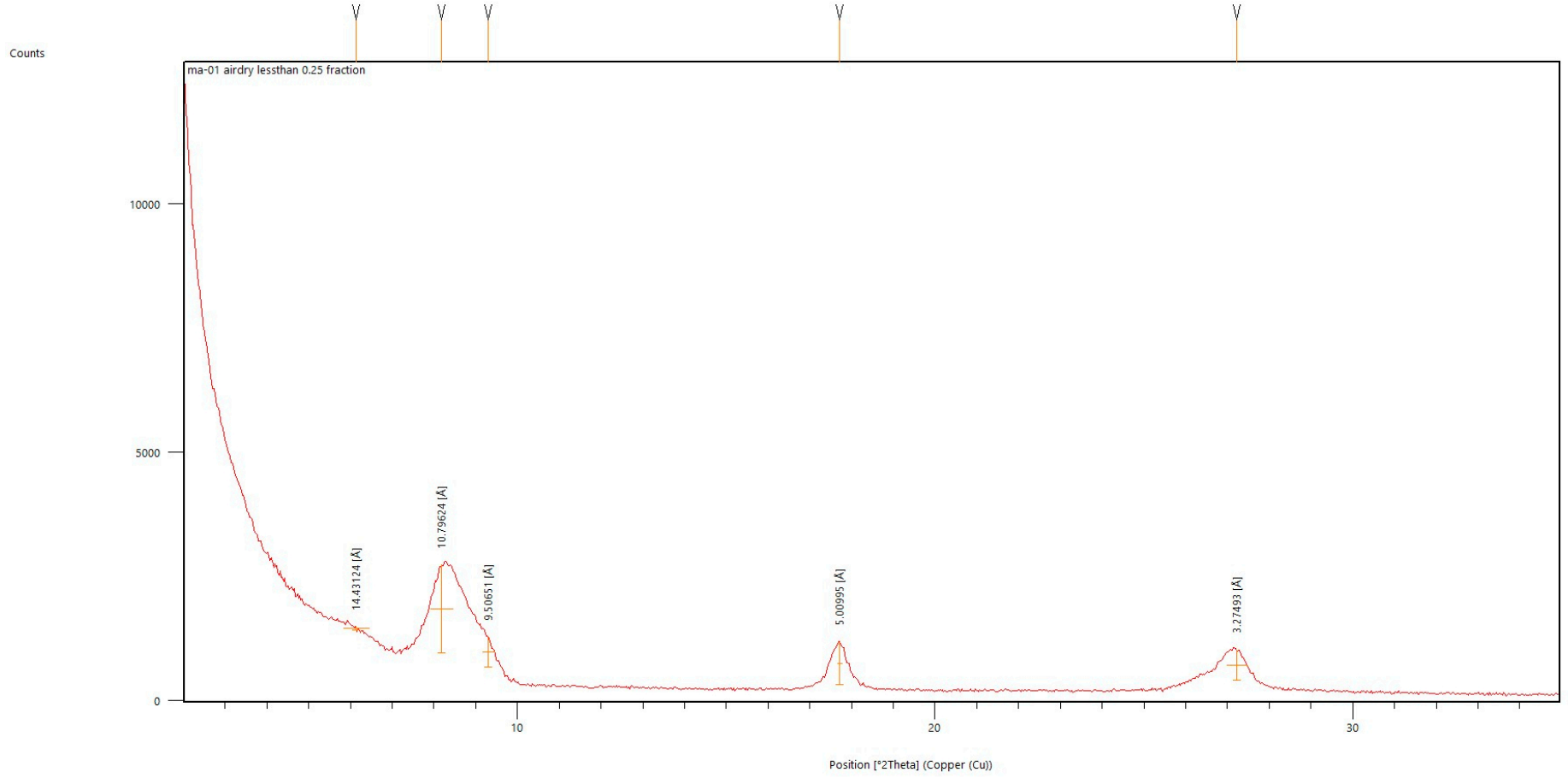


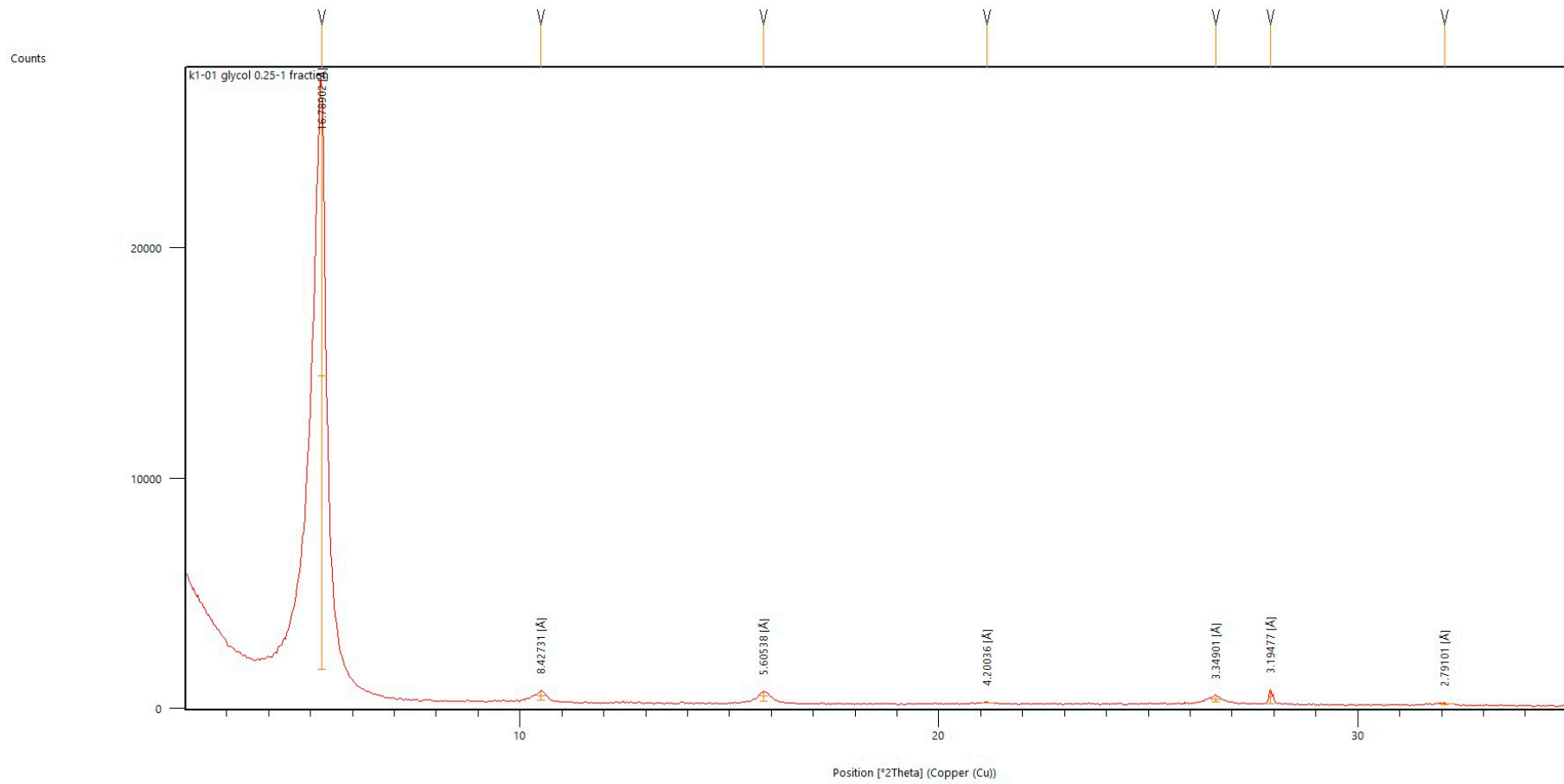


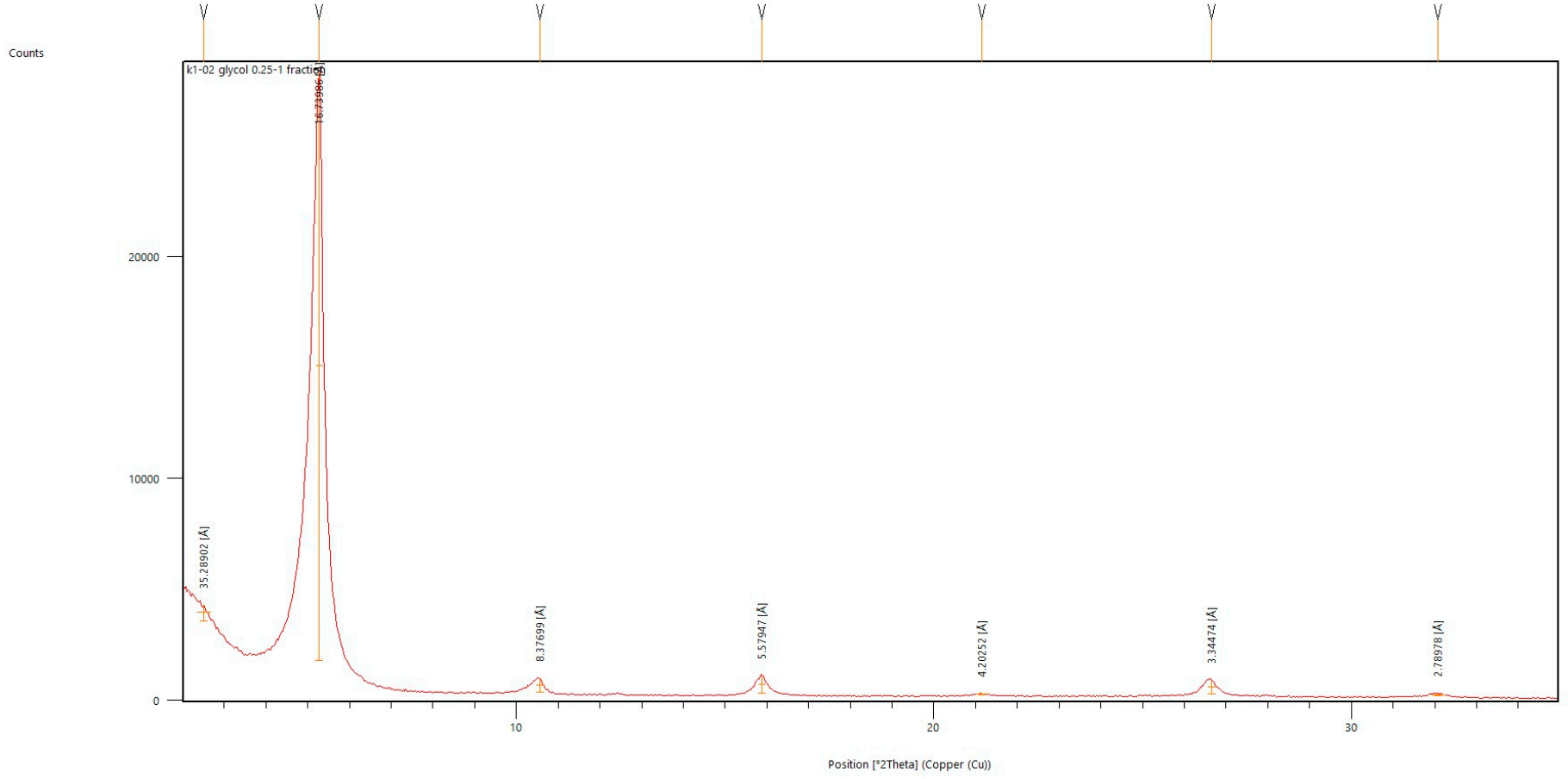


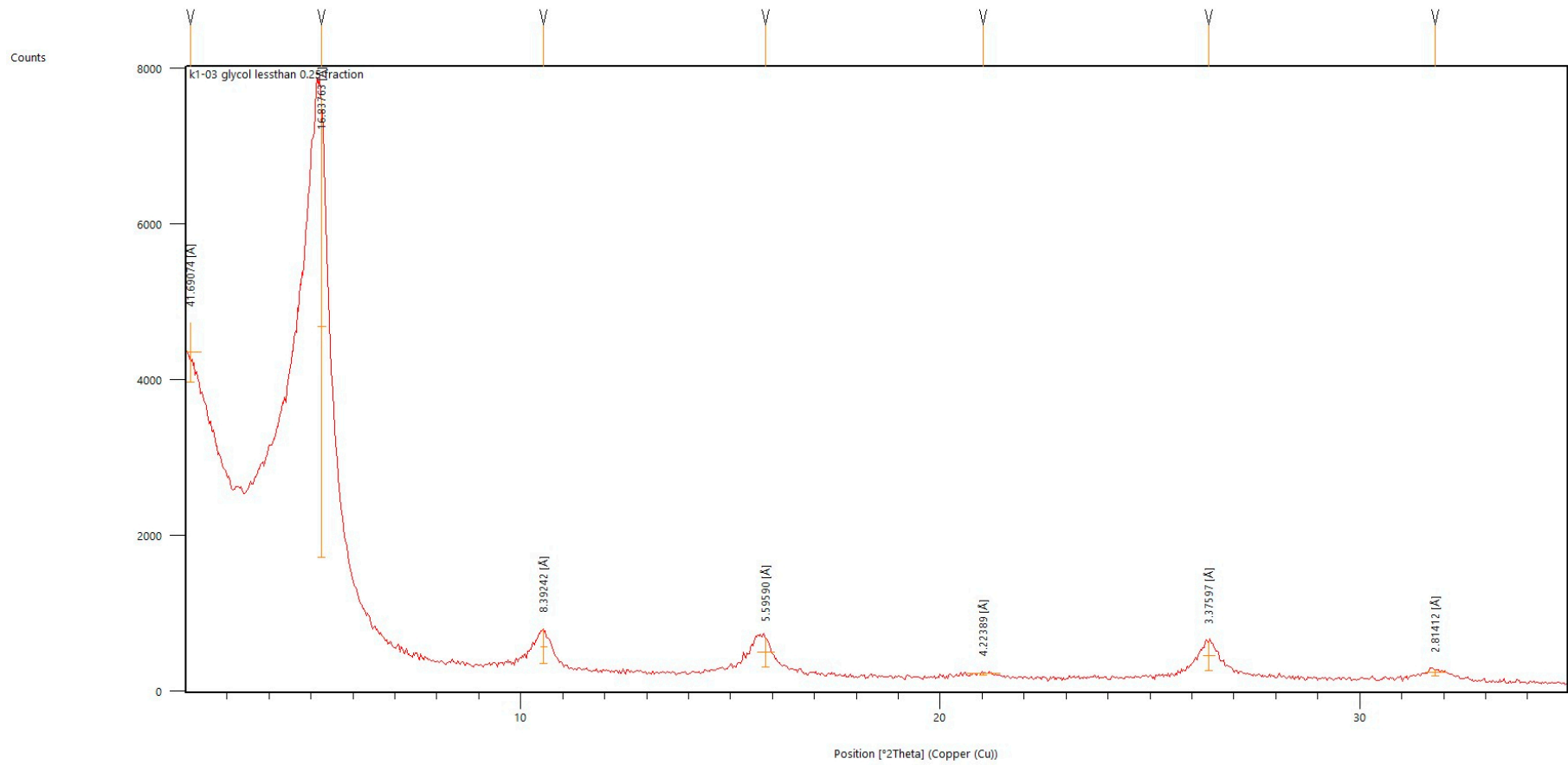


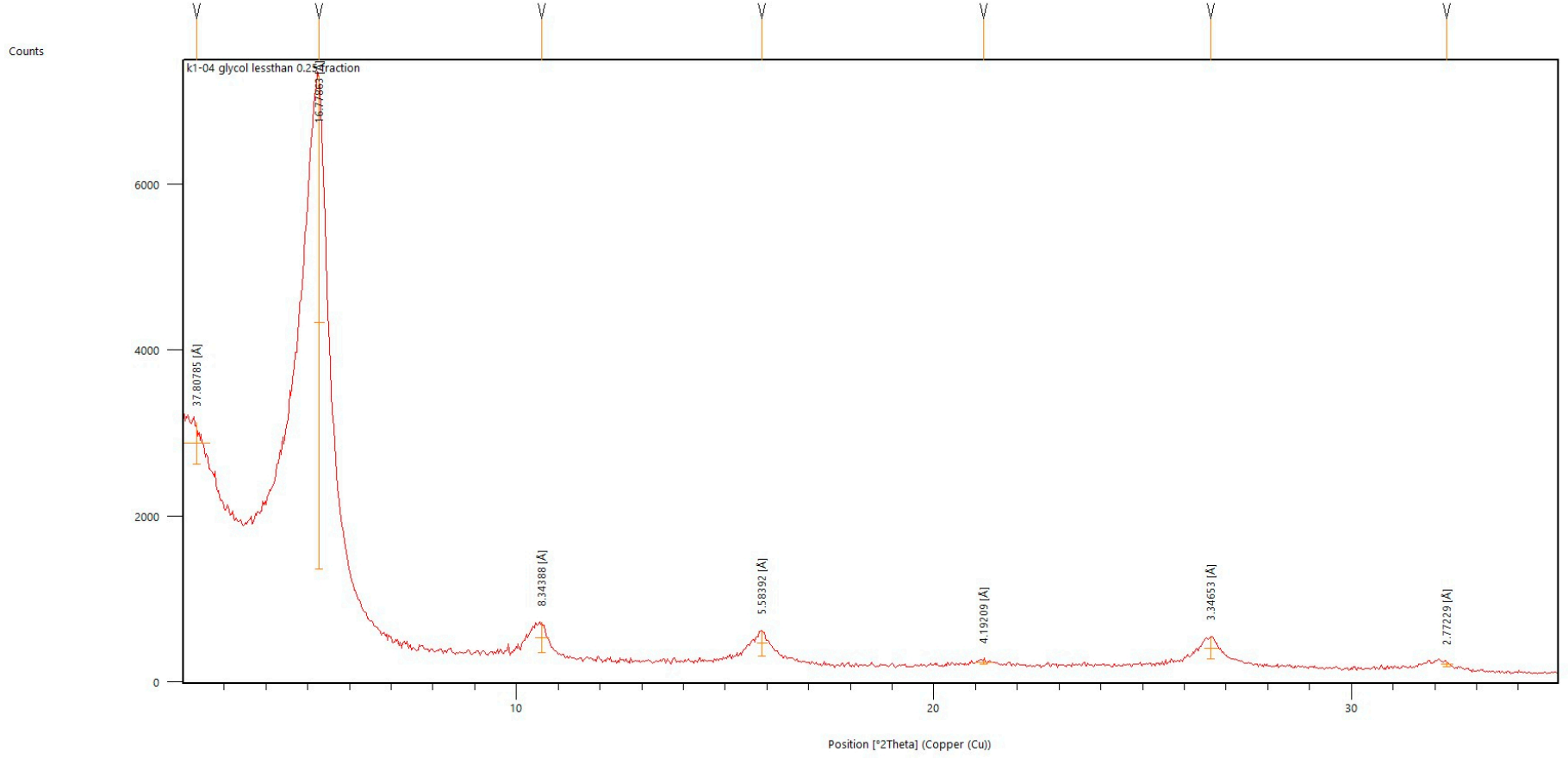


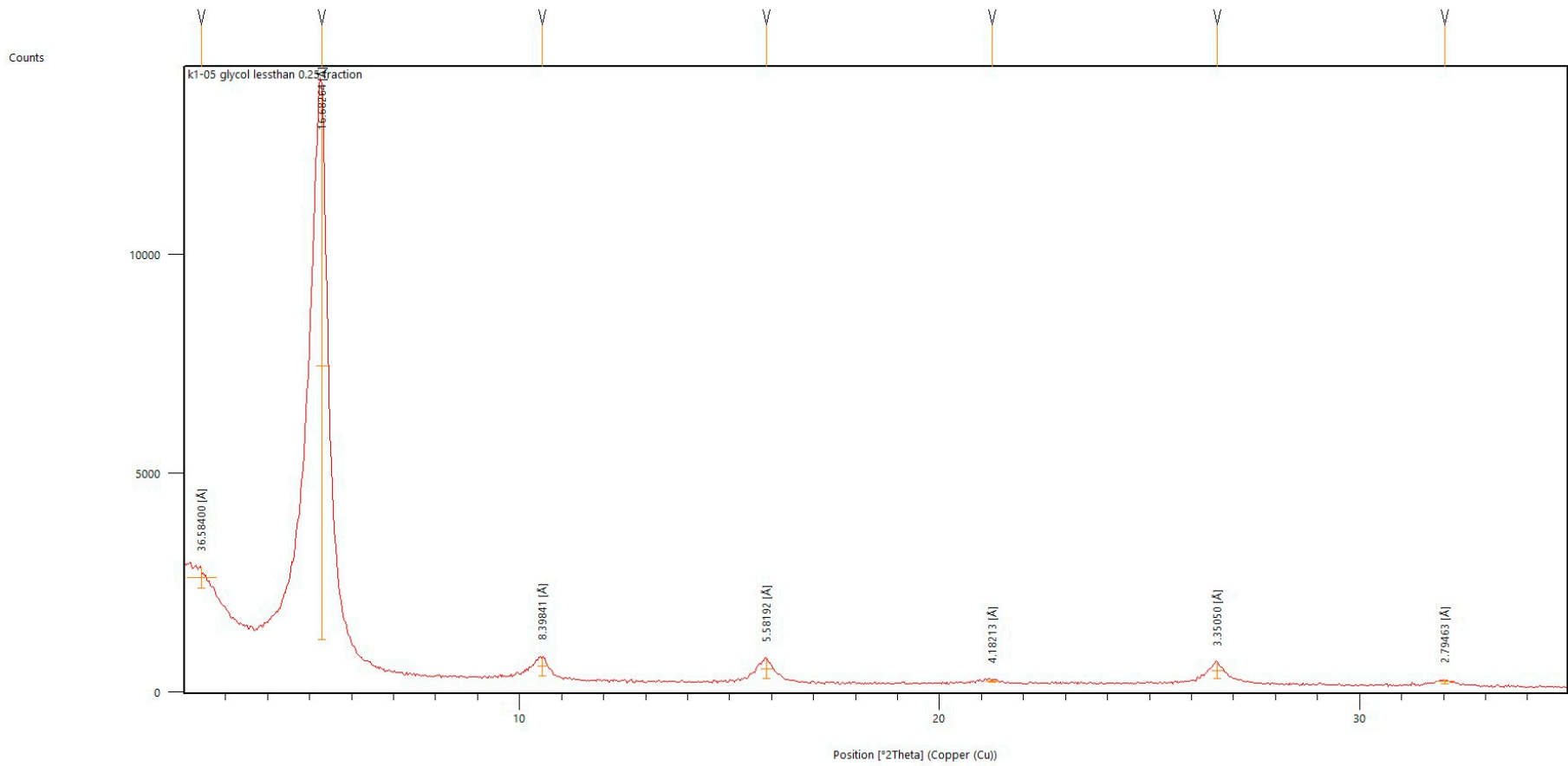


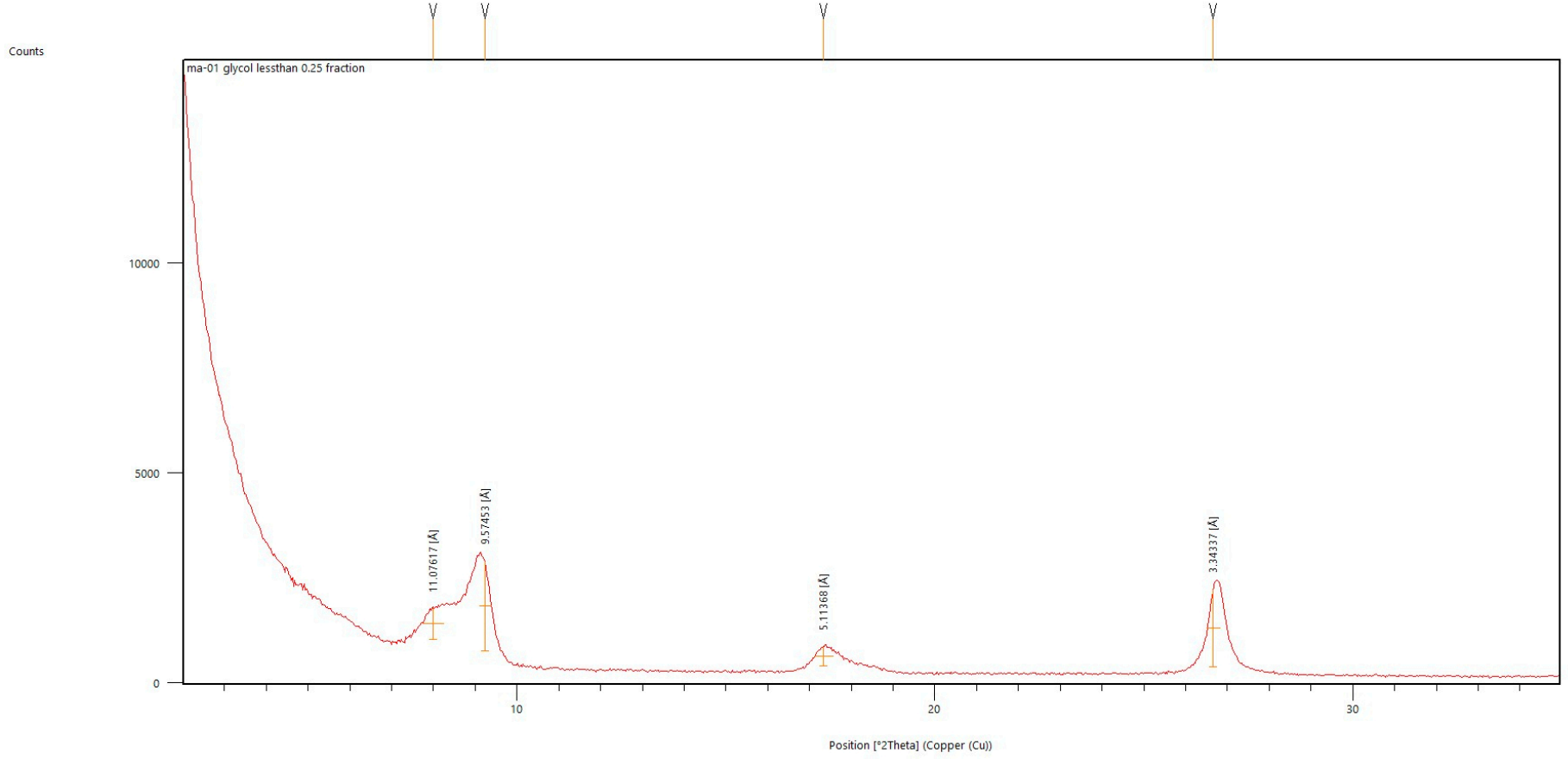


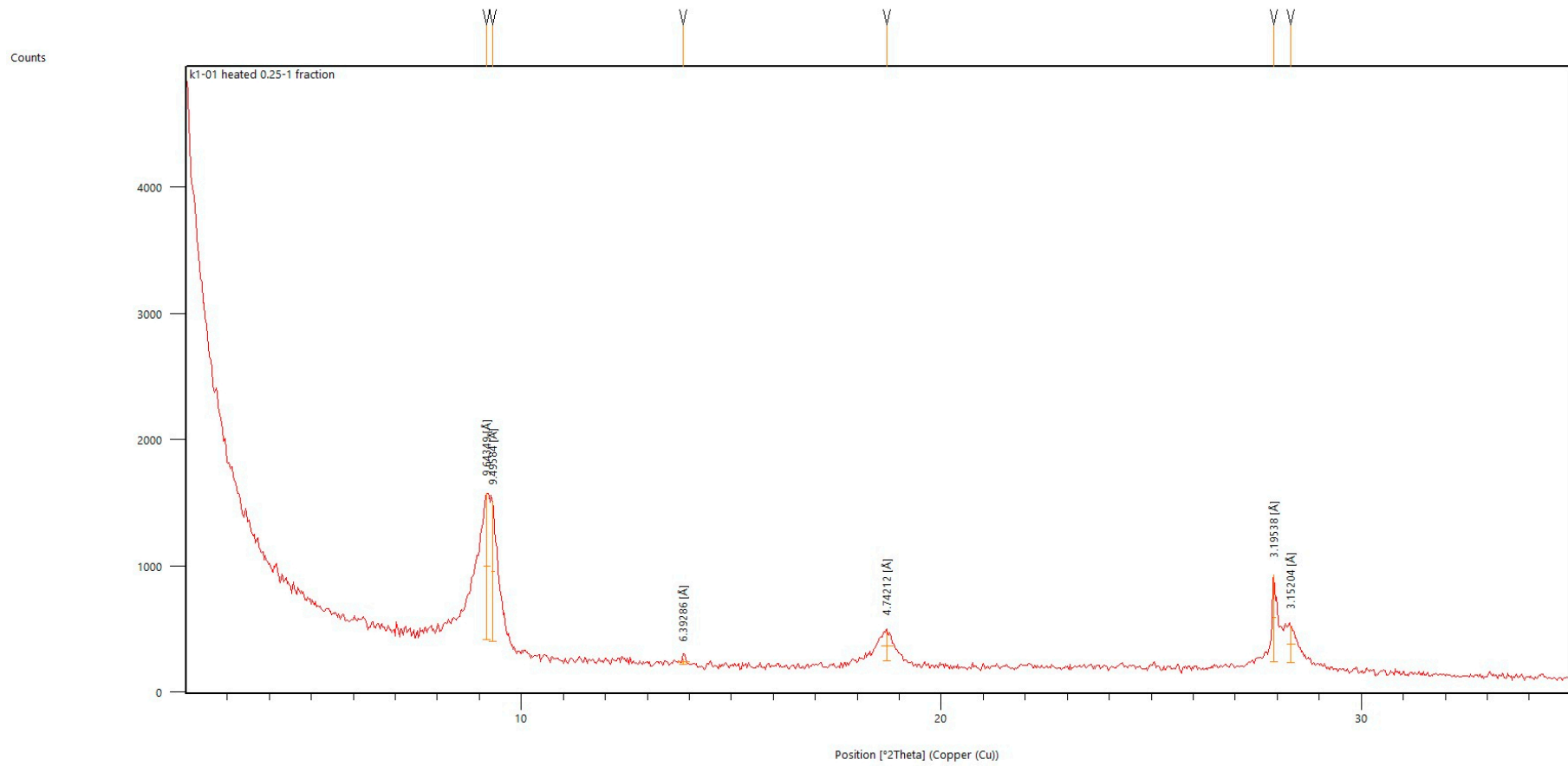


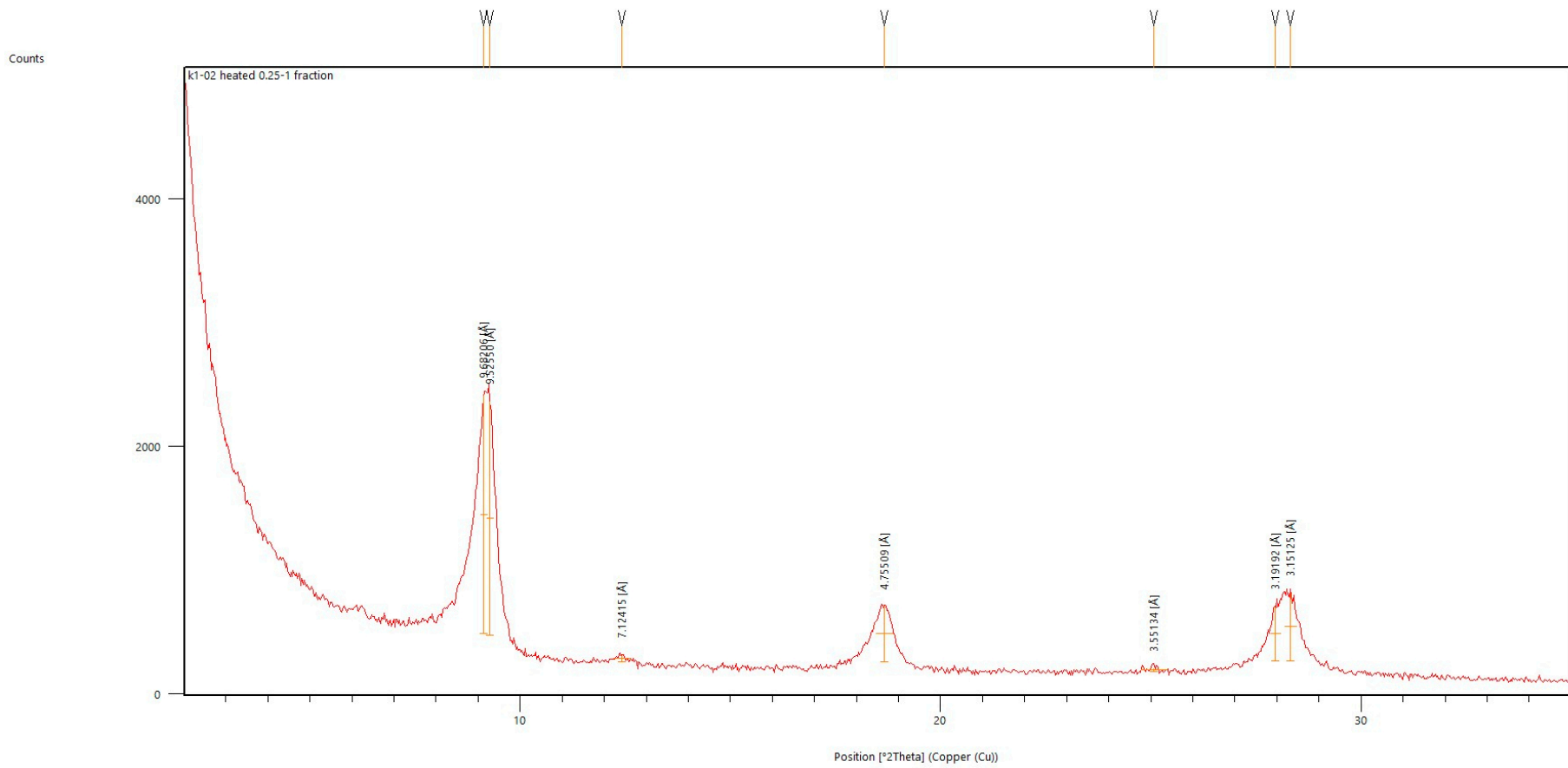


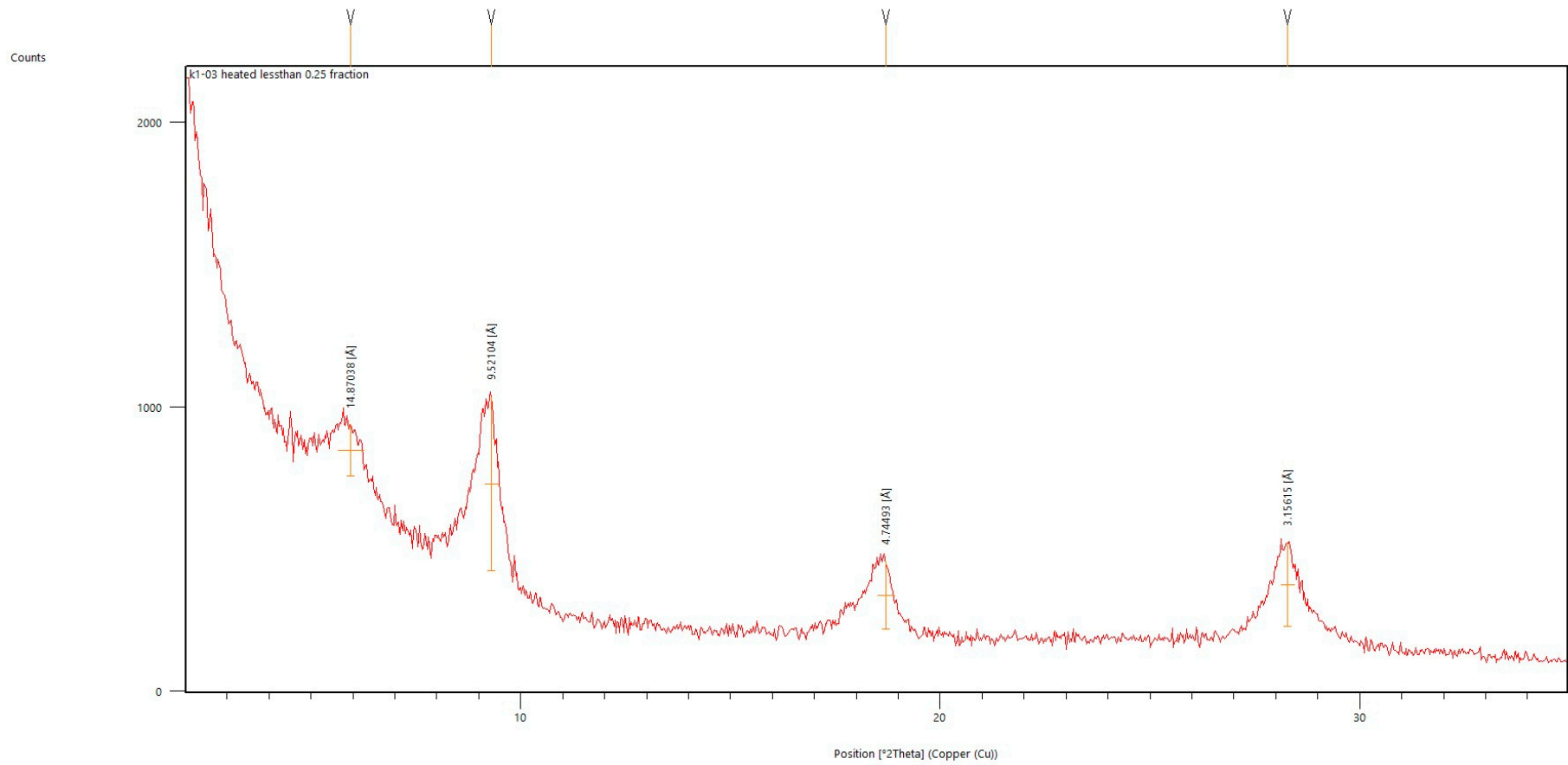


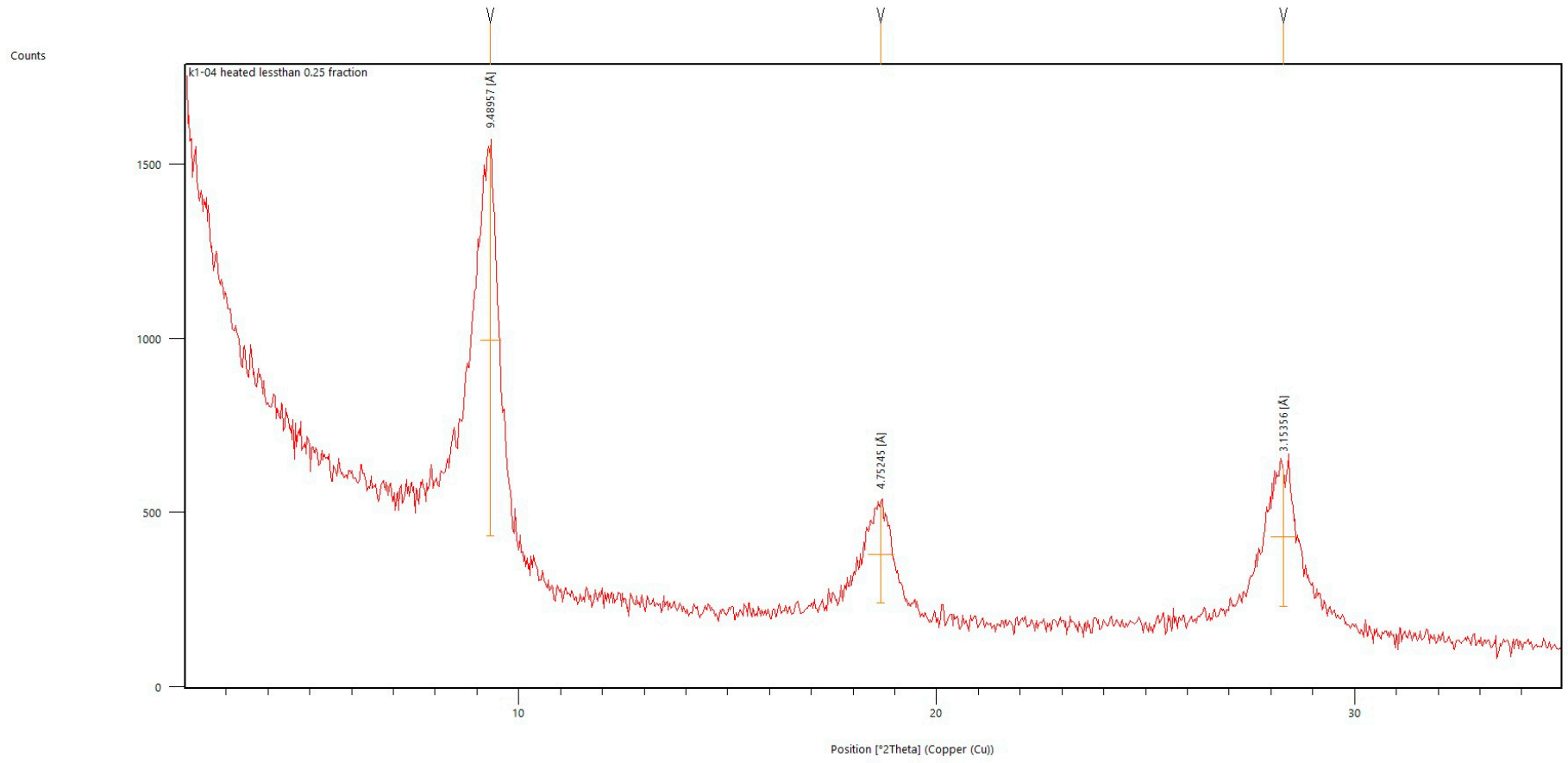


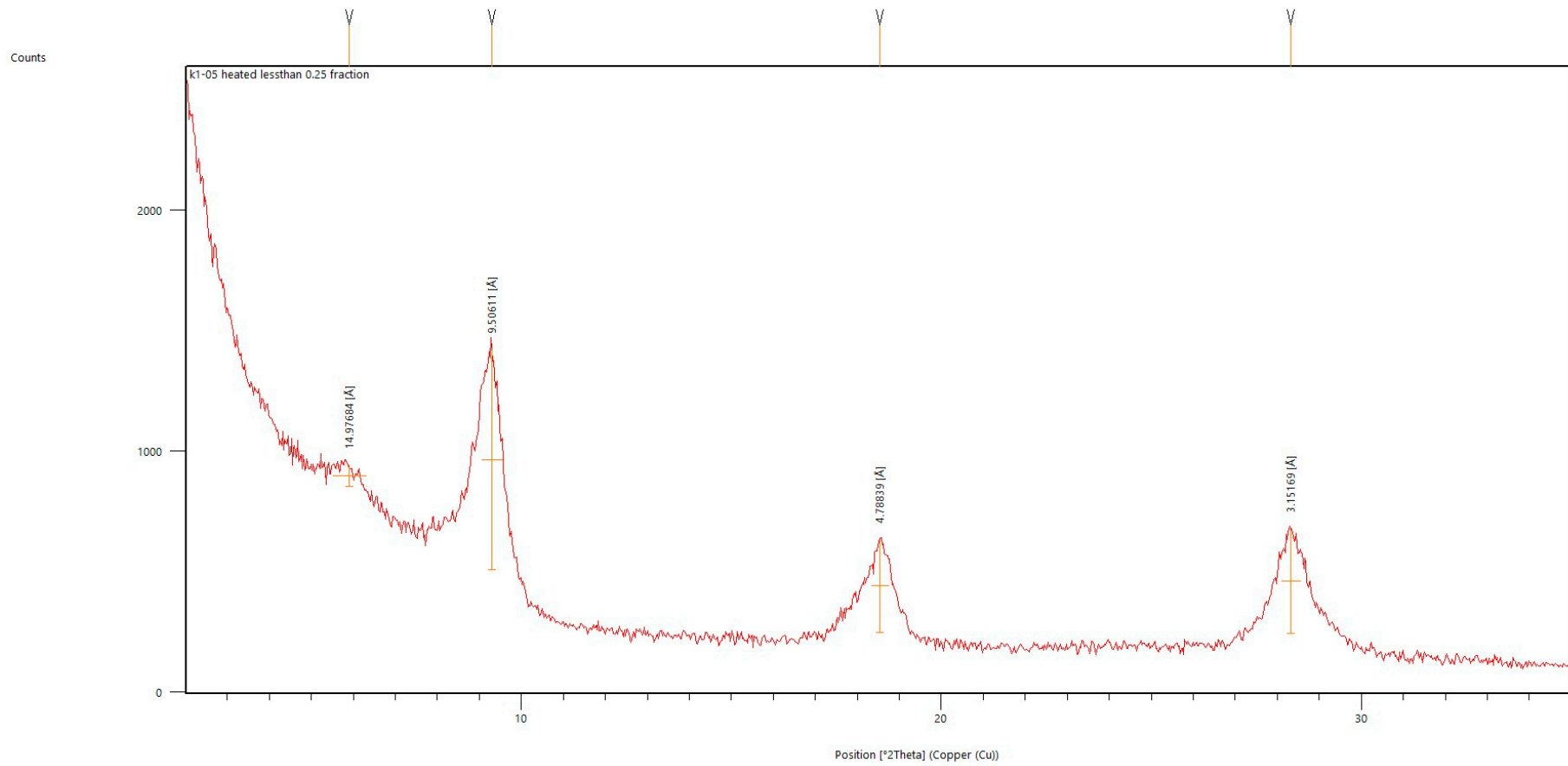


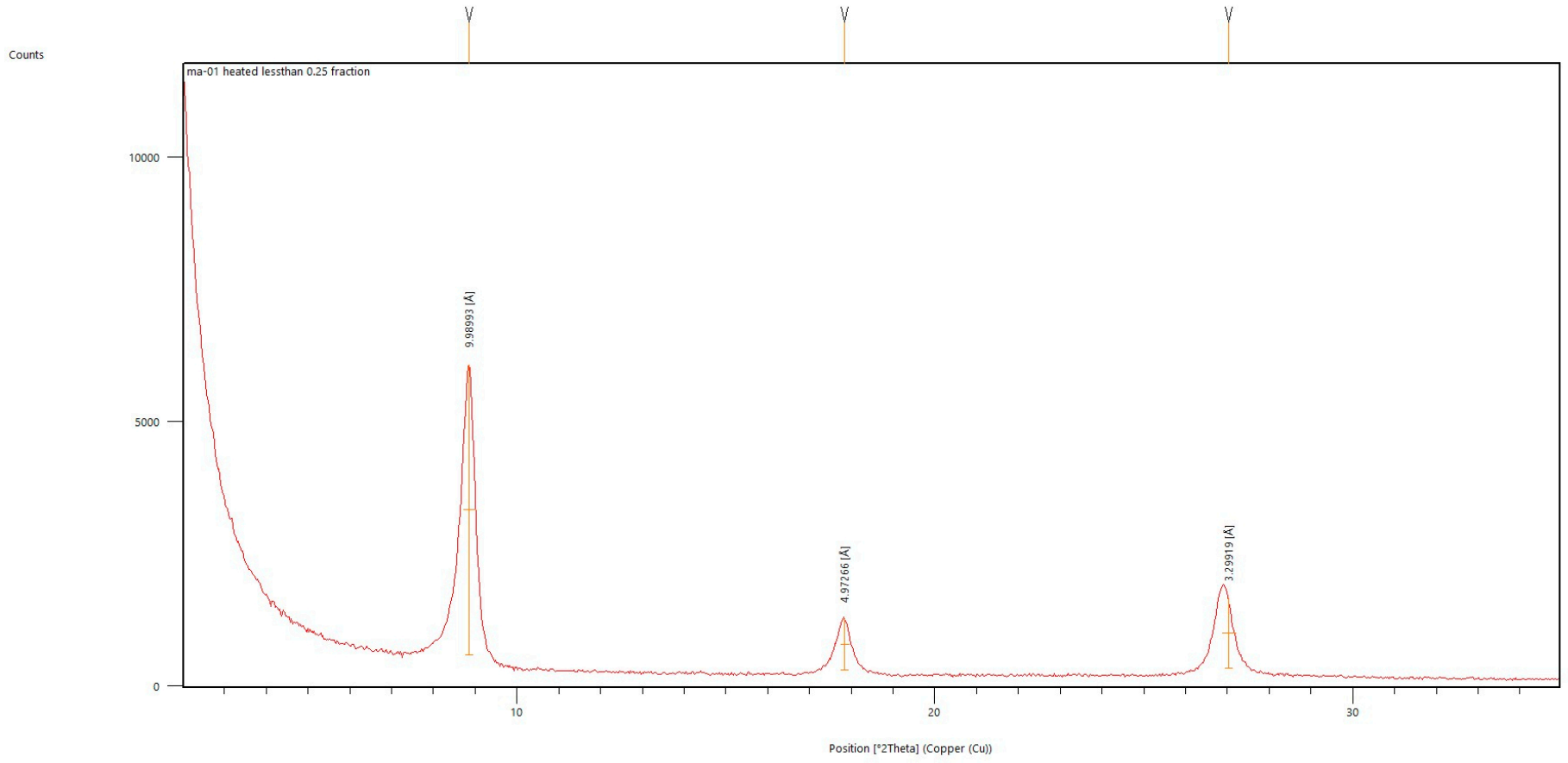












Re-Os dating of clay-associated pyrite

Holly J. Stein and Aaron Zimmerman

H1.1 Introduction

Four samples were provided, and a first analysis of these samples brought no immediately useful results: from the first four analyses, with surprise we learned that some of the pyrites were LLHR (Low-Level, Highly-Radiogenic; Stein et al. 2000). A LLHR sample has the possibility to yield single robust model ages with one analysis using a double Os spike. For LLHR samples, there is insignificant common (i.e. initial) Os. Other Kiirunavaara pyrite samples have significant common Os, which requires the isochron approach and use of a single Os spike. This was challenging as we vacillated between using the double Os spike and the single Os spike, not knowing which pyrite samples would have LLHR compositions and which would not. The challenge of unpredictable Os isotopic compositions among the four samples, is in fact a significant finding. While the four samples may have shared an initial depositional history, some of them (LLHR samples) seem to record a younger overprint. In appendix H2, tabs are labelled either “Trad Iso” or “187Iso”, respectively corresponding to plots that accommodate common Os in samples versus plots for samples with little to no common Os. Even as many plots are 2-point regressions, every conceivable plot was made as a matter of thorough treatment of these limited data. In sum, many of the 2-point plots are not useful. All plots are annotated. Nevertheless, with the eight analyses we have tantalizing results, keeping in mind that 2-point and 3-point isochrons (regressions) are not publishable. In sum, it was not possible to adequately explore four pyrite samples, apparently with different geologic histories and/or overprints, with funding for only four Re-Os analyses.

H1.2 Samples

Four different pyrite(-chalcopyrite)-bearing samples from the Kiirunavaara mine, with the LKAB site codes 405-1194, 386-1194, 307-1165 and 384-1137, were supplied to AIRIE by Ulf B. Andersson (LKAB). All samples contain gangue carbonate and clay, plus anhydrite and magnetite. AIRIE Run numbers on following slides and in data table denote use of single ^{185}Re and ^{190}Os spike solutions (LL-XXXX) or a mixed ^{185}Re -double ^{188}Os - ^{190}Os spike (MD-XXXX). 3D photos acquired by AIRIE used a Keyence digital microscope. The photos clearly illustrate differences in the pyrite morphology and grain-size and the presence of intergrown pyrite-chalcopyrite in one sample. Sample sites are marked in Appendix B.

AIRIE sample MD-2256 (LKAB 405-1194) Kiirunavaara mine pyrite, unconsolidated

Loose, unconsolidated material was supplied in a bag (Figure H-1) with a few larger competent pieces (although there was no obviously visible sulphide in hand specimens). Material was packaged wet, with visible condensation inside the bag, so dried at 100 °C for 2 hours (Figure H-2). Figure H-3 shows a magnified image of sample MD-2256. Using a digital Keyence scope, identified sulphide but at a sufficiently low abundance that hand-picking is not viable. Therefore, just added ~200 mg of the bulk material to the Carius tube for Re-Os analysis. Estimate 1–2 % sulphide in the bulk material. Mineralogy dominantly quartz, calcite, biotite, and magnetite.

AIRIE samples LL-1380 and LL-1388 (LKAB405-1194) Kiirunavaara pyrite, unconsolidated, (c, same mineral separate as b)

Took additional fine-grained powder from the unconsolidated sediment sample and analysed as a whole rock, trying to concentrate the pyrite, which was somewhat successful. Too fine-grained to hand-pick. Separates (b) and (c) had perhaps 3–5 % pyrite¹⁶.

¹⁶ NB no images supplied by AIRIE.



Figure H-1. Sample MD-2256 (LKAB 405-1194) as supplied by Nagra.



Figure H-2. Sample MD-2256 (LKAB 405-1194), left before drying, right after drying.



Figure H-3. Sample MD-2256 (LKAB 405-1194), magnified image Scale bar bottom right.

AIRIE sample LL-1382 (LKAB 386-1194 Kiirunavaara pyrite, hand-picked pyrite fraction)

Unconsolidated material with pyrite at a size for hand-picking (Figure H-4). Pyrite occurs as isolated euhedral crystals. Hand-picked purest pyrite crystals. Selected smaller crystals leaving larger pieces, including the large crystal (Figure H-4) for later analyses if needed. Magnetite present. Sample was more orange than the others, assumed the orange mineral is a friable carbonate.



Figure H-4. Sample LL-1382 (LKAB 386-1194) showing large single pyrite (scale bar on bottom right).



Figure H-5. Sample LL-1382 (LKAB 386-1194), left showing large single pyrite crystals (magnification note at top left), right wider view (NB no scale provided).

AIRIE sample MD-2278 (LKAB 386-1194, Kiirunavaara pyrite, hand-picked pyrite fraction

Separate (Figure H-6) acquired from same vial of hand-picked pyrite crystals (contrasting with sample 307-1165, Figure H-7) which is dominated by pyrite aggregates). As seen in digital microscope photos below, individual pyrite crystals range from euhedral to anhedral with various sizes. Only 5 of the smallest crystals were used for analysis as this separate has the highest Re concentrations of the suite; however, Re concentrations are highly variable, making spiking challenging.



Figure H-6. Pyrite separates from sample MD-2278 (LKAB 386-1194). Scale bar bottom right.



Figure H-7. Sample LL-1383 (LKAB 307-1165) showing variable pyrite habit. Scale bars bottom right.

AIRIE sample LL-1383 (LKAB 307-1165), Kiirunavaara pyrite, hand-picked pyrite fraction

Different pyrite habit compared to other samples in this suite. Chalcopyrite is present, as is magnetite. Large aggregates of sulphide of a size where hand-picking was possible. Selected the smaller, mono-sulphide pieces though chalcopyrite was present with most of the pyrite throughout. Plenty of sample remaining for additional analyses, as required.

AIRIE sample MD-2277 (LKAB 307-1165), Kiirunavaara pyrite, hand-picked larger pyrite fraction

Working from the same vial of hand-picked chalcopyrite-pyrite clusters as used in LL-1383 analysis, used all but the largest piece (circled red in Figure H-8) in this analysis. Digital photos (Figure H-9) taken with the Keyence scope feature the clustered, aggregated nature of the sulphide pieces.



Figure H-8. Sample MD-2277 (LKAB 307-1165) indicating material used in the analysis (all but that piece circled in red). No scale bar, see picker tool on right.



Figure H-9. Sample MD-2277 (LKAB 307-1165), note the clustered, aggregated nature of the sulphide (scale bar on bottom right).

AIRIE sample LL-1381 (LKAB 384-1137), Kiirunavaara pyrite, unconsolidated

Not much to photograph for this sample. No pickable sulphide in this sample but plenty of extremely fine-grained pyrite crystals (Figure H-10, pyrite grain centred in red circle, noted by small white arrow). Removed the larger pieces of material and attempted to get the finest fraction for analysis. May have been some oxidised pyrite observed under the binocular scope (Figure H-11). Abundant slate-gray mineral is magnetite (Figure H-12). Used the whole rock approach on the fine-grained fraction in which pyrite was concentrated.



Figure H-10. Sample LL-1381 (LKAB 384-1137), only the finest fraction sampled (e.g. as highlighted in the red circle). Scale bar bottom right.



Figure H-11. Sample LL-1381 (LKAB 384-1137), potentially oxidised pyrite as indicated by the rust brown colouring of the sample. Scale bar bottom right.



Figure H-12. Sample LL-1381 (LKAB 384-1137), magnetite in the bulk sample.

AIRIE sample LL-1389 (LKAB 384-1137 Kiirunavaara pyrite, unconsolidated, (b, same mineral separate)

Took additional fine-grained powder from the unconsolidated sediment sample and analysed as a whole rock; tried to concentrate the pyrite with an estimated 1–2 % pyrite in analysed whole rock. No image was provided by AIRIE.

H1.3 Methods

This report is accompanied by a detailed Re-Os data set (Appendix H2) whose results are annotated with plots and discussed in this report. A second tab within Appendix H2, “Input Data for Plots”, isolates the specific Re-Os data that were used to construct each plot. Please do not remove the AIRIE Run Number column from the data table as this is our only means to trace all details for a particular analysis. Throughout this report, the MD notation refers to the mixed Re-double Os spike whereas the LL notation refers to analyses made using separate single ^{185}Re and ^{190}Os spike solutions. The Re-Os analyses were acquired using a Carius tube for sample dissolution and spike equilibration in 12mL 6N HNO_3 . The sealed Carius tube is heated overnight at 230°C. Following chemical separation of Re from Os, isotopic ratios are measured by NTIMS (Negative Thermal Ionization Mass Spectrometry) on

a Triton machine held by the AIRIE Program. All data are blank-corrected and reported at 2-sigma uncertainty. Re and Os blanks are insignificant relative to the Re and Os concentrations in the samples. Blanks are reported in the Re-Os data table footnotes.

H1.4 Results

While viewing Appendix H2 and moving tab-to-tab, please note the explanatory and interpretive text below. Using the notes placed directly on the plots and my assessment of the Re-Os data presented in the data table (plus my experience with limited and complex Re-Os data sets), the following summary can be made for each of the four analysed samples (sample sites are shown in Appendix B):

LKAB405-1194 – The traditional $^{187}\text{Re}/^{188}\text{Os}$ versus $^{187}\text{Os}/^{188}\text{Os}$ plot must be used as all three aliquots analysed have significant common Os, one with a radiogenic ^{187}Os to common Os ratio of unity (orange-filled boxes in data tables in Appendix H2). Re concentrations are low ppb level but easily and precisely measured. Blank contribution is negligible. This would be a good sample for further work, resulting in a better constrained isochron. I'm confident, based on these three data points, that there is a younger event ~ 1615 Ma. The MSWD is moderately supportive, as also is the Os initial ratio, even with its large uncertainty.

LKAB386-1194 – These two analyses have molybdenite-like Os isotopic compositions – extremely high $^{187}\text{Re}/^{188}\text{Os}$ ratios (250 000) coupled with Os that is almost entirely radiogenic ^{187}Os daughter. There is essentially no common Os in the analysed pyrite aliquots. Such samples are classified as LLHR (Stein et al. 2000). Therefore, the only regression to represent these data is a ^{187}Re versus ^{187}Os plot, keeping in mind that two-point regressions are not publishable. Analysis LL-1382 is severely underspiked (large error ellipse). Thus, as illustrated in the plots, 2-point regressions are nonsensical. However, with confidence we can fall back on the Re-Os model age of 1921 ± 8 Ma acquired with the double Os spike for the second analysis (MD-2278). The single spike was a logical approach for the first analysis, as we expected some common Os, as was the case for 405 from the FIRST batch (MD-2256). However, the first analysis of 386 (MD-1382) told us that we needed to use the double Os spike. This was wholly unexpected. We ran the sample again using the double Os spike (MD-2278). This is a solid result yielding a LLHR age of 1921 ± 8 Ma. It is particularly solid as the Re concentration is generous (42 ppb). What is particularly intriguing is that although with a very large uncertainty, separating small euhedral pyrite crystals for analysis in LL-1382 yields a 1630 Ma result. Most pyrite occurs as ill-defined aggregates, but in this case small euhedral pyrite crystals were isolated. The Re concentration is notably higher than for aggregate pyrites (133 ppb). This suggests that small euhedral pyrite grain with notably higher Re concentrations may have formed during a younger 1630 Ma event. This can be tested and confirmed with more analyses.

LKAB307-1165 – Similar to the above described 386/1194 data, the two analyses from 307/1165 have high $^{187}\text{Re}/^{188}\text{Os}$ ratios and low common Os, although LL-1383 has some (still insignificant) common Os. The LL-1383 analysis is also significantly underspiked (large error ellipse). With only two data points, regressions are again tenuous, and the best course of action is to use the well-determined Re-Os model age for MD-2277, as this sample is essentially without common Os and optimally spiked. The take-home message from this sample is a Re-Os model age of 1962 ± 7 Ma. However, I interpret this older model age as compromised. It is more likely that the primary age is closer to 1920 Ma. This interpretation is further discussed under the tab labelled “Two MD Samples” in Appendix H2.1 where a plot of the two perfectly spiked LLHR samples (MD-2277 and MD-2278), both with abundant Re, yield a 2-point regression at 1871 Ma. With a few additional analyses, a reorganization of the Re-Os systematics in these samples at ~ 1870 Ma can be established (or not).

LKAB384-1137 – With only two data points, both showing poor spiking, and with both analyses markedly dominated by common Os, this is not a promising sample for continued work. Further, this sample displayed clear evidence of oxidation, which compromises isotopic integrity. The sandy material in the bag was also discoloured relative to the other three samples. Lastly, the Re and Os concentrations are low, which is also unfavourable for further work. The plotting of all combinations of samples is not intended to be alarming but is for illustration purposes to show the challenges faced with these samples, both geologically and in predicting spiking.

Using groupings of LL-XXXX analyses versus MD-XXXX analyses, the Re-Os data are further explored in the sequence of four gray and three blue-gray tabs in Appendix H2.1, beginning with the first tab labelled “ALL 6 LL Runs”. The samples are labelled on the plots, with successive removal of a particular datum point on tabs moving from left to right. Ultimately, this is not an ideal mechanism to explore the Re-Os data but, unless we have additional data points to fill out these results, I’m taking this approach to create a first-response interpretation.

H1.5 Discussion

Collectively analysing the data, albeit with a limited pilot data set of eight analyses spread over four samples with apparently different overprints, the following observations are possible:

- 1) A traditional Re-Os isochron plot using data from two samples (Excel, blue tab labelled 3-405 and 1-386LL 4pts) suggests that the 1 615 Ma pyrites from 405-1194 may share a younger history with LKAB386-1194 providing an isochron regression of $1\ 615 \pm 120$ Ma, noting the severe underspiking for LL-1382. However, LKAB386-1194 does give a model age of 1 631, albeit with a very large uncertainty. This plot essentially functions as a two-point regression, but the Os initial ratio for this plot and the LKAB405-1194 three-point regression are elevated (2.7). The MSWD is acceptable (7.0) even as uncertainties are large. Additional data should secure (or refute) this interpretation. It is hard to function and interpret with so few data points, but experience has shown that often a few data set the stage for a result that becomes clearer with additional analyses.
- 2) The ages and uncertainties discussed in this report should not be taken *sensu stricto* as more data are needed to truly confirm the results. However, for a pilot study such as this one I can confidently say that there appear to be at least two events bound up in the four samples we analysed, and perhaps three events. The Re-Os systematics are complex, but not insurmountable with additional dedicated analytical work. The Re and Os concentrations are workable, with two of the four samples (LKAB386-1194 and LKAB307-1165) carrying significant Re and Os. I’m guessing there must be a shared geological history between samples LKAB386-1194 and LKAB307-1165. Are they in close proximity, as a first query? Do they represent the same unit or vein material, or is it possible to determine this? Interestingly there is little or no direct evidence for pyrite formation associated with peak Svecofennian metamorphism, unless my hypothesis under the tab “Two MD Samples” is correct. This hypothesis is easily testable.
- 3) The proposed ~1 920 Ma age as a primary depositional age is further supported by the two plots labelled “All 3 MD Trad Iso”, and “All 3 MD 187Iso”. Additional data points will likely secure this primary age. A 3-point isochron will not pass journal review, if that is a possibility going forward. I’m confident that we can come up with a well constrained isochron result establishing the ~1 920 Ma age. As an aside, about 20 years ago when we were building the AIRIE Program we obtained a piece of Kiirunavaara drill core that was essentially massive magnetite and we had a similar age result for this core sample, as I recall. We had no funding for that work, so couldn’t take it further. However, it (again) showed that we could work with magnetite for Re-Os dating.

H1.6 Conclusions

This pilot study suggests a pyrite-(mineralisation) history with ages of ~1 920 Ma, with a likely reworking of the Re-Os systematics in at least one of the pyrite samples at ~1 615 Ma. There is little direct suggestion of pyrite deposition associated with the main stage Svecofennian orogeny, although one 2-point slope through two different LLHR samples with pyrite model ages at ~1 920 and ~1 960 yields an age of 1 870 Ma. This may be significant, and I’m confident this can be easily explored. We should seek to understand why pyrites from two of the four samples have LLHR compositions, and the other two do not. This is an important point and suggests that not all four pyrites share the same post-depositional overprinting, and/or there is a younger pyrite event at ~1 615 Ma. This is resolvable. With additional analyses, tentative indications can be securely nailed down. I am confident in suggesting this preliminary temporal history for the pyrites as described in the above paragraph. At the end of this report, I provide some suggestions for how we can quickly and efficiently fill out this Kiirunavaara pyrite data set.

Depending on geologic relationships, the pyrite ages we obtained are likely associated with development of the smectite. Might the smectite be associated with development of carbonate and anhydrite with the younger ~1 615 Ma event? How far apart are the pyrite samples? Are they from the same “unit” or can that be determined? Were the pyrites collected underground, or are they rubble acquired from drill core? I understand they are from “deep in the Kiruna system”. On reviewing the photos sent, the samples appear to be from underground. Ulf, you also mention the possibility that nearby chalcopyrite may or may not represent the same event as the pyrites. It is possible that the pyrite samples may all share a ~1 920 Ma, but experienced different overprints. For example, it is intriguing that Re concentrations in the pyrites are wildly different sample to sample, and that common Os is missing in some of the pyrites.

This begs for explanation and is without doubt significant to the story. It is possible that the two pyrites with > 1 900 Ma model ages became LLHR in composition at ~1 870 Ma. These sample-to-sample differences made the project particularly challenging, forcing additional analyses to even begin to elucidate the geologic history for these pyrite samples. The reported uncertainties should not be scrutinized for precision at this stage, but rather for a broad message that may be refined on further analytical work.

Recommendations for further work

Below are two recommendations for further work to transform this pilot pyrite data set into publishable isochrons, with further supporting single aliquot model ages from the two LLHR pyrites. I’m confident that we will obtain a solidified story if we take the following steps:

Recommendation 1 – Confirm the ~1 615 Ma Event

Sample LKAB405-1194 has common Os in all three aliquots. About 4–5 additional analyses should pin down the ~1 615 Ma age on a traditional $^{187}\text{Re}/^{188}\text{Os}$ versus $^{187}\text{Os}/^{188}\text{Os}$ plot with a respectable precision ($\pm 10\text{--}30$ m.y.), while also constraining the Os initial ratio. With a well-constrained $^{187}\text{Os}/^{188}\text{Os}$ initial ratio, we will be able to reach back in time to determine if the ~1 615 Ma pyrite is a completely new generation of pyrite, or if it is a re-equilibration (resetting) of older pyrite during a ~1 615 Ma event. This will secure information that will be useful for both this project and the Kiiirunavaara ore history.

Recommendation 2 – Secure the ~1 920 Ma pyrite age and confirm any Svecofennian (1 870 Ma) overprint

Samples LKAB386-1194 and LKAB307-1165 both provide ^{187}Re - ^{187}Os model ages, as these pyrites have essentially no common Os and extremely high $^{187}\text{Re}/^{188}\text{Os}$ ratios (accompanied by very high measured $^{187}\text{Os}/^{188}\text{Os}$ ratios). The two ^{187}Re - ^{187}Os model ages appear to be slightly different, even as we have only one age from 305 and one from 307 to compare. Both samples are well spiked, with MD-2278 very slightly overspiked. It should be straightforward to explore this data set and determine if these two pyrites had a ~1 920 Ma origin. About 3–4 additional analyses for each of these samples (LKAB305 and LKAB307) should seal the story.

Re-Os data tables and plots

H2.1 Re-Os Data Table, Kiirunavaara Pyrites, Northern Sweden

Holly J Stein

Organized by AIRIE Run Number, two data sets, one using the double Os spike (MD-XXXX) and one using single spikes (LL-XXXX).

FIRST, SECOND, THIRD denotes three sequential batches where information from prior batch guided spiking for subsequent analyses of samples.

Re-Os Data Table, Kiirunavaara Pyrites, Northern Sweden

Holly Stein (holly@airieprogram.org), May 28, 2023

Organized by AIRIE Run Number, two data sets, one using the double Os spike (MD-XXXX) and one using single spikes (LL-XXXX)

FIRST, SECOND, THIRD denotes three sequential batches where information from prior batch guided spiking for subsequent analyses of samples

| AIRIE Run # | Sample Name | Re, ppb | Re err, abs (ppb) | Re err, percent | ¹⁸⁷ Os, ppb | ¹⁸⁷ Os err, abs (ppb) | ¹⁸⁷ Os err, percent | OsC, ppb | OsC err, abs (ppb) | OsC err, percent | Model Age, Ma | Age analytical err, abs (Ma) | Age analytical err, percent | abs err, w/λ | % err w/λ | Sample Weight (g) | Re Blank Contribution | Radiogenic ¹⁸⁷ Os Blank Contribution | Common Os Blank Contribution |
|-------------|---|---------|-------------------|-----------------|------------------------|----------------------------------|--------------------------------|----------|--------------------|------------------|---------------|------------------------------|-----------------------------|--------------|-----------|-------------------|-----------------------|---|------------------------------|
| MD-2256 | FIRST 405/1194 unconsolidated whole rock (<1% pyrite) | 0.6778 | 0.0012 | 0.17 | 0.01591 | 0.00024 | 1.5 | 0.01542 | 0.00086 | 5.6 | 2200 | 33 | 1.5 | 33 | 1.5 | 0.2998 | 0.0024% | 0.0072% | 0.0074% |
| MD-2277 | THIRD 307/1165, hand-picked larger pyrite grains (~100% pyrite) | 23.215 | 0.012 | 0.052 | 0.48471 | 0.00074 | 0.15 | 0.00565 | 0.00067 | 12 | 1961.5 | 3.1 | 0.16 | 7.0 | 0.36 | 0.3699 | 0.0017% | 0.0186% | 1.5975% |
| MD-2278 | THIRD 386/1194 hand-picked larger aggregate sulfide (95% pyrite, 5% chalcopyrite) | 42.499 | 0.071 | 0.17 | 0.8685 | 0.0014 | 0.16 | 0.0009 | 0.0027 | 300 | 1920.6 | 4.4 | 0.23 | 7.6 | 0.39 | 0.1178 | 0.0029% | 0.0326% | 32.0479% |

For MD-2256, Re blank = 0.4943 ± 0.0064 pg, Os blank = 0.034 ± 0.011 pg with ¹⁸⁷Os/¹⁸⁸Os = 0.325 ± 0.96

For MD-2277 and 2278, Re blank = 0.143 ± 0.039 pg, Os blank = 0.033 ± 0.019 pg with ¹⁸⁷Os/¹⁸⁸Os = 0.54 ± 0.22

OsC is measured common (or initial) Os; note significant common Os relative to radiogenic ¹⁸⁷Os for MD-2256 (light orange box).

Assumed Os initial ratio for age calculation is 0.2; value assumed for the Os initial ratio has nearly no effect on the age calculation.

Lambda (λ) is the decay constant for ¹⁸⁷Re; w/λ is the age uncertainty inclusive of the uncertainty in the ¹⁸⁷Re decay constant.

All data reported are at 2-sigma uncertainty.

| AIRIE Run # | Sample Name | Re (ppb) | Re Abs Err (2σ) | Re % Error | Total Os (ppb) | Os Abs Err (2σ) | Os % Error | OsC (ppb) | ¹⁸⁷ Re/ ¹⁸⁸ Os | Err (2σ) | ¹⁸⁷ Os/ ¹⁸⁸ Os | Err (2σ) | rho | Model Age (Ma) | Err (w/λ) | Err (no λ) | Sample Weight (g) | Re Blank Contribution | Os Blank Contribution |
|-------------|--|----------|-----------------|------------|----------------|-----------------|------------|-----------|--------------------------------------|----------|--------------------------------------|----------|--------|----------------|-----------|------------|-------------------|-----------------------|-----------------------|
| LL-1380 | SECOND 405/1194 unconsolidated whole rock (b, updated separate, 3-5% pyrite) | 5.631 | 0.014 | 0.26 | 0.1187 | 0.0033 | 2.8 | 0.0170 | 1612 | 30 | 46.5 | 1.2 | 0.6919 | 1699 | 42 | 38 | 0.4133 | 0.100% | 0.086% |
| LL-1381 | SECOND 384/1137 unconsolidated whole rock (<1% pyrite) | 0.7598 | 0.0096 | 1.3 | 0.1044 | 0.0035 | 3.3 | 0.0957 | 38.6 | 2.6 | 0.900 | 0.083 | 0.6801 | | | | 0.5581 | 0.547% | 0.073% |
| LL-1382 | SECOND 386/1194 hand-picked small euhedral pyrite crystals (100% pyrite) | 132.9 | 3.6 | 2.7 | 2.30 | 0.90 | 39 | 0.0019 | 338554 | 83616 | 9327 | 3032 | 0.7428 | 1631 | 476 | 476 | 0.1835 | 0.010% | 0.010% |
| LL-1383 | SECOND 307/1165, hand-picked smaller aggregate sulfide (95% pyrite, 5% chalcopyrite) | 24.493 | 0.051 | 0.21 | 0.566 | 0.045 | 7.9 | 0.0117 | 10174 | 466 | 367 | 24 | 0.6985 | 2123 | 119 | 117 | 0.1932 | 0.049% | 0.038% |
| LL-1388 | THIRD 405/1194 unconsolidated whole rock, (c, same separate as b, 3-5% pyrite) | 1.5765 | 0.0030 | 0.19 | 0.0522 | 0.0013 | 2.5 | 0.0182 | 420.8 | 9.0 | 14.61 | 0.44 | 0.6979 | 2021 | 56 | 52 | 0.3671 | 0.050% | 0.344% |
| LL-1389 | THIRD 384/1137 unconsolidated whole rock (b, same separate, 1-2% pyrite) | 3.837 | 0.021 | 0.55 | 0.10895 | 0.00086 | 0.79 | 0.1000 | 186.7 | 3.2 | 0.894 | 0.020 | 0.6194 | | | | 0.6613 | 0.011% | 0.092% |

For LL-1380, LL-1381, LL-1382, LL-1383, Re blank = 2.3329 ± 0.0063 pg, Os blank = 0.043 ± 0.023 pg with ¹⁸⁷Os/¹⁸⁸Os = 0.54 ± 0.25

For LL-1388, LL-1389, Re blank = 0.287 ± 0.078 pg, Os blank = 0.068 ± 0.037 pg with ¹⁸⁷Os/¹⁸⁸Os = 0.54 ± 0.22

OsC is measured common (or initial) Os; note significant common (initial) Os relative to total Os for LL-1381, LL-1388, and LL-1389 (light orange boxes).

Assumed Os initial ratio for age calculation is 0.2; calculation of model ages is only possible when ¹⁸⁷Re/¹⁸⁸Os (and ¹⁸⁷Os/¹⁸⁸Os) are very high; LL-1381 and LL-1389 are not candidates for model age calculations.

Lambda (λ) is the decay constant for ¹⁸⁷Re; w/λ is the age uncertainty inclusive of the uncertainty in the ¹⁸⁷Re decay constant.

All data reported are at 2-sigma uncertainty.

H2.2 Kiirunavaara Pyrites, Re-Os data sets used to construct isochrons (Holly Stein, holly@airieprogram.org), March 8, 2023

| ¹⁸⁷ Re/ ¹⁸⁸ Os versus ¹⁸⁷ Os/ ¹⁸⁸ Os (Traditional Isochron Plot) | | | | | LL analyses report Total Os (ppb); MD analyses report ¹⁸⁷ Os (ppb) | denotes significant common Os relative to radiogenic ¹⁸⁷ Os | MD = Mixed Re-Double Os Spike LL = Single ¹⁸⁵ Re and ¹⁹⁰ Os Spikes | | | | |
|--|--------------------------------------|------------|--------------------------------------|-------------|--|---|---|----------------|-----------------------|-----------------------|------------|
| 405/1194 | ¹⁸⁷ Re/ ¹⁸⁸ Os | 2σ abs err | ¹⁸⁷ Os/ ¹⁸⁸ Os | 2σ abs err | rho | Re, ppb | ¹⁸⁷ Os, ppb | OsC, ppb | Re Blank contribution | Os Blank contribution | %OsC Blank |
| MD-2256 | 213.5 | 1.6 | 8.17 | 0.25 | 0.1959 | 0.6778 | 0.01591 | 0.01542 | 0.002% | 0.0072% | 0.0074% |
| LL-1380 | 1612 | 30 | 46.5 | 1.2 | 0.6919 | 5.631 | 0.1187 | 0.01683 | 0.100% | 0.086% | |
| LL-1388 | 420.8 | 9.0 | 14.61 | 0.44 | 0.6979 | 1.5765 | 0.0522 | 0.01805 | 0.050% | 0.344% | |
| | | | | | | | Total Os, ppb | | | | |

| ¹⁸⁷ Re versus ¹⁸⁷ Os (¹⁸⁷ Re Parent- ¹⁸⁷ Os Daughter Isochron) | | | | |
|---|------------------------|------------|------------------------|------------|
| 405/1194 | ¹⁸⁷ Re, ppb | 2σ abs err | ¹⁸⁷ Os, ppb | 2σ abs err |
| MD-2256 | 0.4260 | 0.0007 | 0.0159 | 0.0002 |
| LL-1380 | 3.5395 | 0.0121 | 0.1021 | 0.0019 |
| LL-1388 | 0.9909 | 0.0025 | 0.0344 | 0.0007 |

| ¹⁸⁷ Re/ ¹⁸⁸ Os versus ¹⁸⁷ Os/ ¹⁸⁸ Os (Traditional Isochron Plot) | | | | | LL analyses report Total Os (ppb); MD analyses report ¹⁸⁷ Os (ppb) | denotes significant common Os relative to radiogenic ¹⁸⁷ Os | MD = Mixed Re-Double Os Spike LL = Single ¹⁸⁵ Re and ¹⁹⁰ Os Spikes | | | | |
|--|--------------------------------------|--------------|--------------------------------------|-------------|--|---|---|---------------|-----------------------|-----------------------|------------|
| 386/1194 | ¹⁸⁷ Re/ ¹⁸⁸ Os | 2σ abs err | ¹⁸⁷ Os/ ¹⁸⁸ Os | 2σ abs err | rho | Re, ppb | ¹⁸⁷ Os, ppb | OsC, ppb | Re Blank contribution | Os Blank contribution | %OsC Blank |
| MD-2278 | 233543 | 113384 | 7594 | 3687 | 1.0000 | 42.50 | 0.8685 | 0.0009 | 0.003% | 0.033% | 32.05% |
| LL-1382 | 338554 | 83616 | 9327 | 3032 | 0.7428 | 132.9 | 2.30 | 0.0019 | 0.010% | 0.010% | |
| | | | | | | | Total Os, ppb | | | | |

| ¹⁸⁷ Re versus ¹⁸⁷ Os (¹⁸⁷ Re Parent- ¹⁸⁷ Os Daughter Isochron) | | | | |
|---|------------------------|------------|------------------------|------------|
| 386/1194 | ¹⁸⁷ Re, ppb | 2σ abs err | ¹⁸⁷ Os, ppb | 2σ abs err |
| MD-2278 | 26.712 | 0.044 | 0.8685 | 0.0014 |
| LL-1382 | 83.5 | 3.1 | 2.30 | 0.49 |

¹⁸⁷Re/¹⁸⁸Os versus ¹⁸⁷Os/¹⁸⁸Os (Traditional Isochron Plot)

| 307/1165 | ¹⁸⁷ Re/ ¹⁸⁸ Os | 2σ abs err | ¹⁸⁷ Os/ ¹⁸⁸ Os | 2σ abs err | rho | Re, ppb | ¹⁸⁷ Os, ppb | OsC, ppb | Re Blank contribution | Os Blank contribution | %OsC Blank |
|-----------------|--------------------------------------|------------|--------------------------------------|------------|--------|---------|------------------------|----------|-----------------------|-----------------------|------------|
| MD-2277 | 19976 | 484 | 664 | 16 | 0.9912 | 23.21 | 0.4847 | 0.0056 | 0.0017% | 0.0186% | 1.5975% |
| LL-1383 | 10174 | 466 | 367 | 24 | 0.6985 | 24.49 | 0.566 | 0.0116 | 0.049% | 0.038% | |
| | | | | | | | Total Os, ppb | | | | |

¹⁸⁷Re versus ¹⁸⁷Os (¹⁸⁷Re Parent-¹⁸⁷Os Daughter Isochron)

| 307/1165 | ¹⁸⁷ Re, ppb | 2σ abs err | ¹⁸⁷ Os, ppb | 2σ abs err |
|-----------------|------------------------|------------|------------------------|------------|
| MD-2277 | 14.5912 | 0.0076 | 0.48471 | 0.00074 |
| LL-1383 | 15.395 | 0.043 | 0.555 | 0.026 |

¹⁸⁷Re/¹⁸⁸Os versus ¹⁸⁷Os/¹⁸⁸Os (Traditional Isochron Plot)

| 384/1137 | ¹⁸⁷ Re/ ¹⁸⁸ Os | 2σ abs err | ¹⁸⁷ Os/ ¹⁸⁸ Os | 2σ abs err | rho | Re, ppb | Total Os, ppb | OsC, ppb | Re Blank contribution | Os Blank contribution | %OsC Blank |
|-----------------|--------------------------------------|------------|--------------------------------------|------------|--------|---------|----------------------|----------|-----------------------|-----------------------|------------|
| LL-1381 | 38.6 | 2.6 | 0.900 | 0.083 | 0.6801 | 0.760 | 0.104 | 0.0948 | 0.547% | 0.073% | |
| LL-1389 | 186.7 | 3.2 | 0.894 | 0.020 | 0.6194 | 3.837 | 0.109 | 0.0990 | 0.011% | 0.092% | |
| | | | | | | | Total Os, ppb | | | | |

¹⁸⁷Re versus ¹⁸⁷Os (¹⁸⁷Re Parent-¹⁸⁷Os Daughter Isochron)

| 384/1137 | ¹⁸⁷ Re, ppb | 2σ abs err | ¹⁸⁷ Os, ppb | 2σ abs err |
|-----------------|------------------------|------------|------------------------|------------|
| LL-1381 | 0.4775 | 0.0083 | 0.0111 | 0.0007 |
| LL-1389 | 2.412 | 0.018 | 0.0116 | 0.0002 |

¹⁸⁷Re/¹⁸⁸Os versus ¹⁸⁷Os/¹⁸⁸Os (Traditional Isochron Plot)

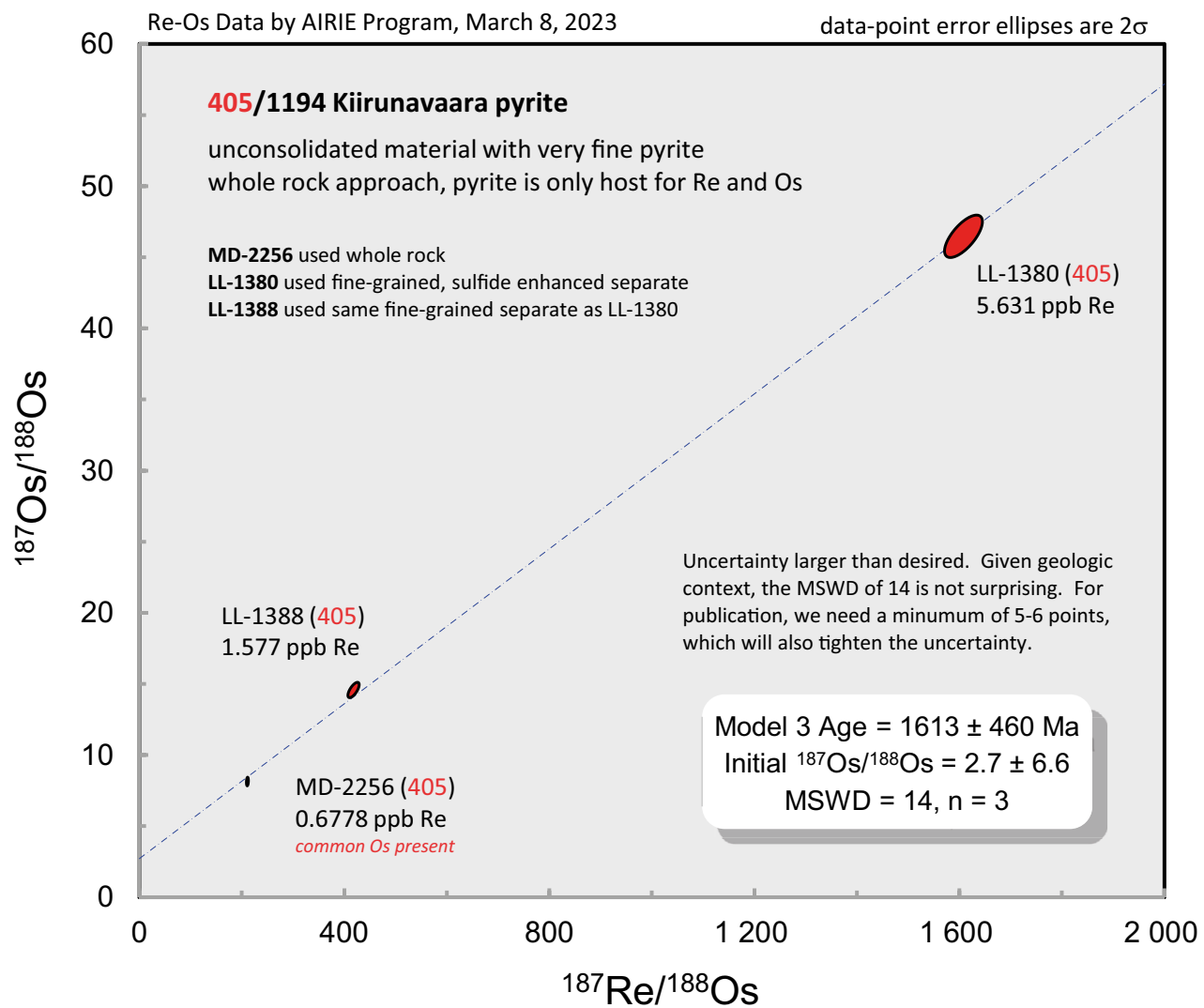
| All MD Runs | ¹⁸⁷ Re/ ¹⁸⁸ Os | 2σ abs err | ¹⁸⁷ Os/ ¹⁸⁸ Os | 2σ abs err | rho | Re, ppb | ¹⁸⁷ Os, ppb | OsC, ppb | Re Blank contribution | Os Blank contribution | %OsC Blank | 249/251 |
|-------------|--------------------------------------|------------|--------------------------------------|------------|--------|---------|------------------------|----------|-----------------------|-----------------------|------------|---------|
| MD-2256 | 213.5 | 1.6 | 8.17 | 0.25 | 0.1959 | 0.6778 | 0.0159 | 0.0154 | 0.002% | 0.0072% | 0.0074% | 18.08 |
| MD-2277 | 19976 | 484 | 664 | 16 | 0.9912 | 23.21 | 0.4847 | 0.0056 | 0.0017% | 0.0186% | 1.5975% | 4.78 |
| MD-2278 | 233543 | 113384 | 7594 | 3687 | 1.0000 | 42.50 | 0.8685 | 0.0009 | 0.0029% | 0.0326% | 32.0479% | 11.22 |

¹⁸⁷Re versus ¹⁸⁷Os (¹⁸⁷Re Parent-¹⁸⁷Os Daughter Isochron)

| All MD Runs | ¹⁸⁷ Re, ppb | 2σ abs err | ¹⁸⁷ Os, ppb | 2σ abs err |
|-------------|------------------------|------------|------------------------|------------|
| MD-2256 | 0.42602 | 0.00073 | 0.01591 | 0.00024 |
| MD-2277 | 14.5912 | 0.0076 | 0.48471 | 0.00074 |
| MD-2278 | 26.712 | 0.044 | 0.8685 | 0.0014 |

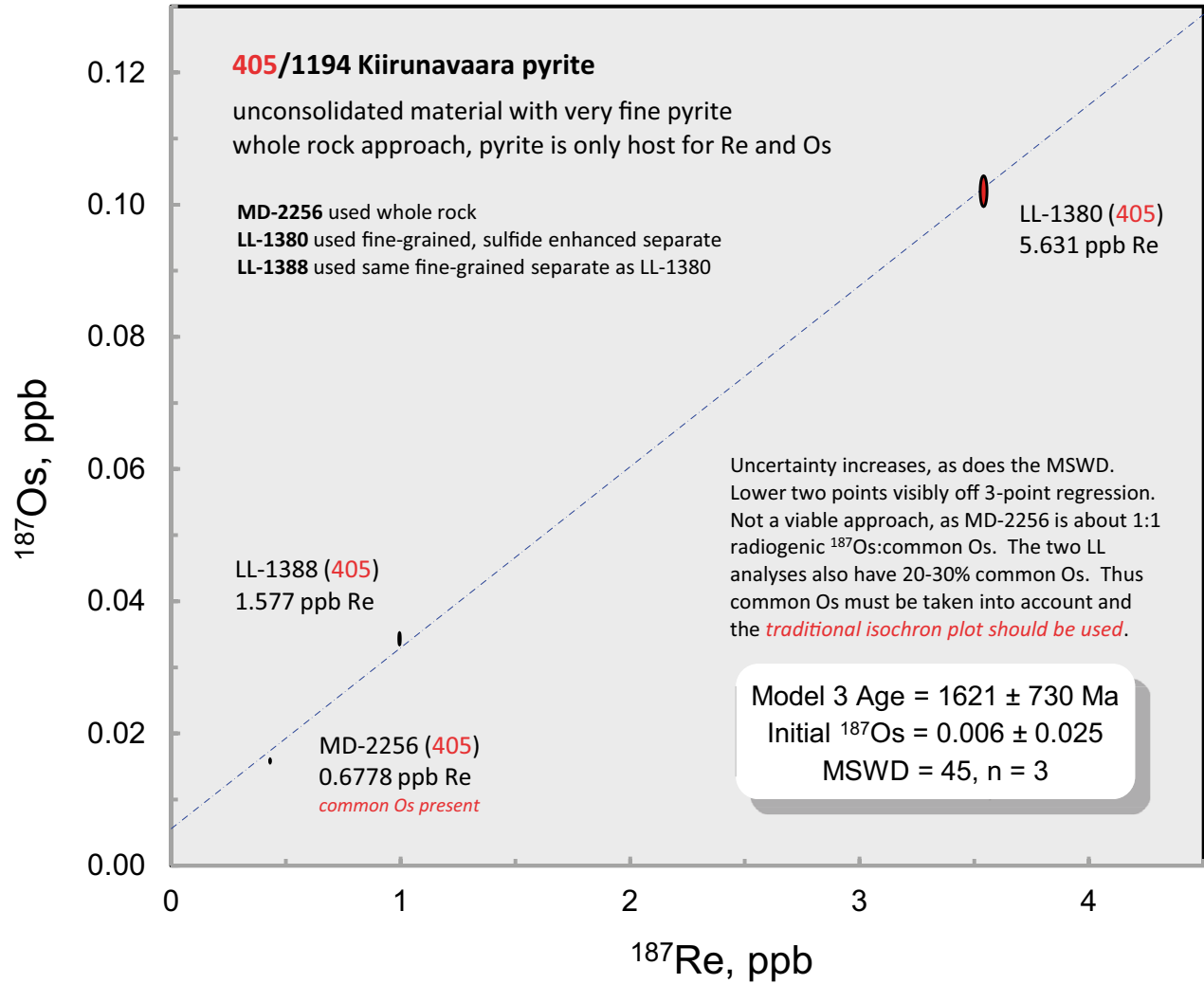
¹⁸⁷Re/¹⁸⁸Os versus ¹⁸⁷Os/¹⁸⁸Os (Traditional Isochron Plot)

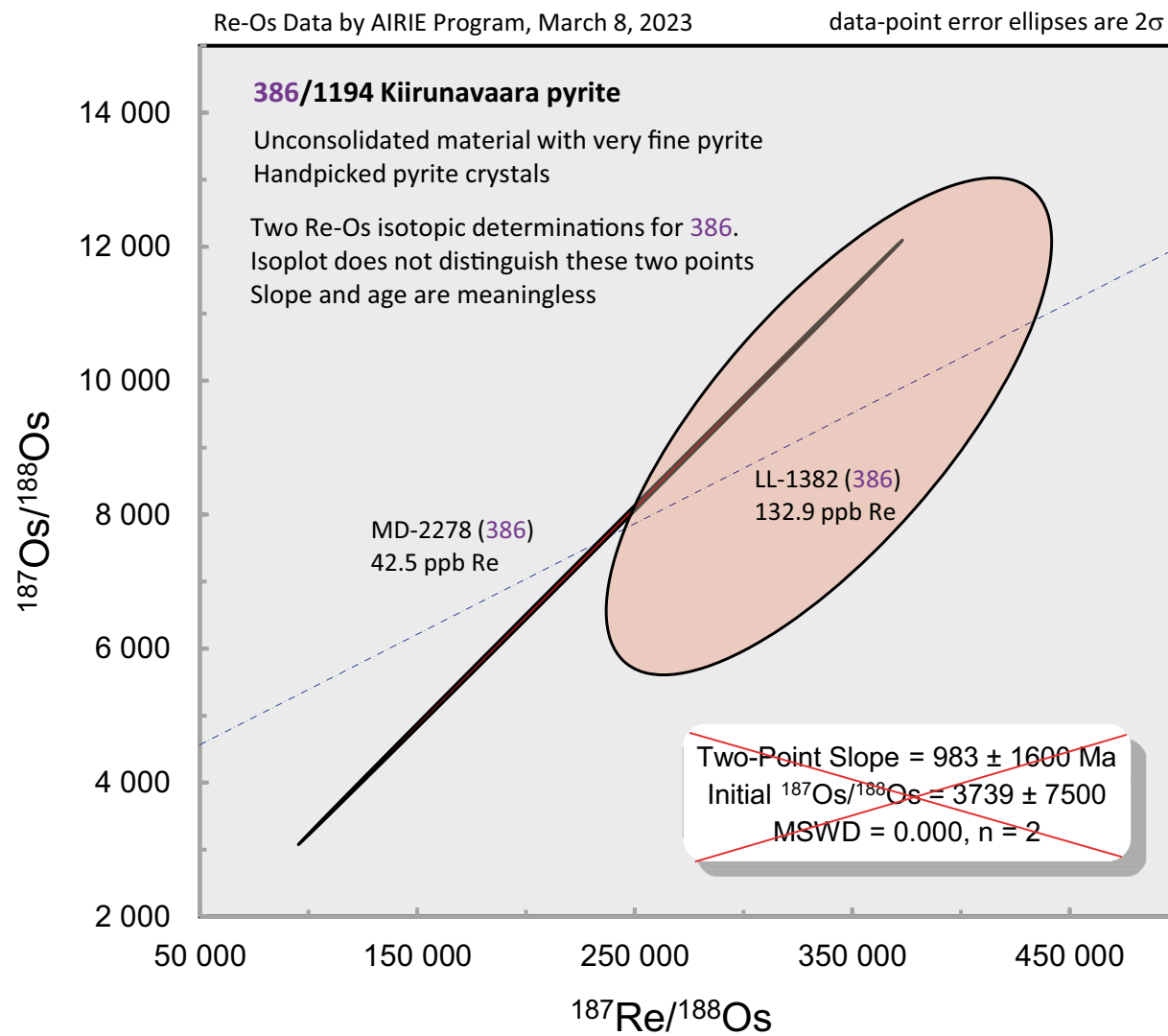
| All LL Runs | ¹⁸⁷ Re/ ¹⁸⁸ Os | 2σ abs err | ¹⁸⁷ Os/ ¹⁸⁸ Os | 2σ abs err | rho | Re, ppb | Total Os, ppb | OsC, ppb | Re Blank contribution | Os Blank contribution | %OsC Blank | 249/251 |
|-------------|--------------------------------------|------------|--------------------------------------|------------|--------|---------|---------------|----------|-----------------------|-----------------------|------------|---------|
| LL-1380 | 1612 | 30 | 46.5 | 1.2 | 0.6919 | 5.631 | 0.119 | 0.0168 | 0.100% | 0.086% | | 1.00 |
| LL-1381 | 38.6 | 2.6 | 0.900 | 0.083 | 0.6801 | 0.760 | 0.104 | 0.0948 | 0.547% | 0.073% | | 3.19 |
| LL-1382 | 338554 | 83616 | 9327 | 3032 | 0.7428 | 132.9 | 2.304 | 0.0019 | 0.010% | 0.010% | | 0.68 |
| LL-1383 | 10174 | 466 | 367 | 24 | 0.6985 | 24.493 | 0.566 | 0.0116 | 0.049% | 0.038% | | 1.04 |
| LL-1388 | 420.8 | 9.0 | 14.61 | 0.44 | 0.6979 | 1.576 | 0.052 | 0.0181 | 0.050% | 0.344% | | 7.50 |
| LL-1389 | 186.7 | 3.2 | 0.894 | 0.020 | 0.6194 | 3.837 | 0.109 | 0.0990 | 0.011% | 0.092% | | 0.97 |

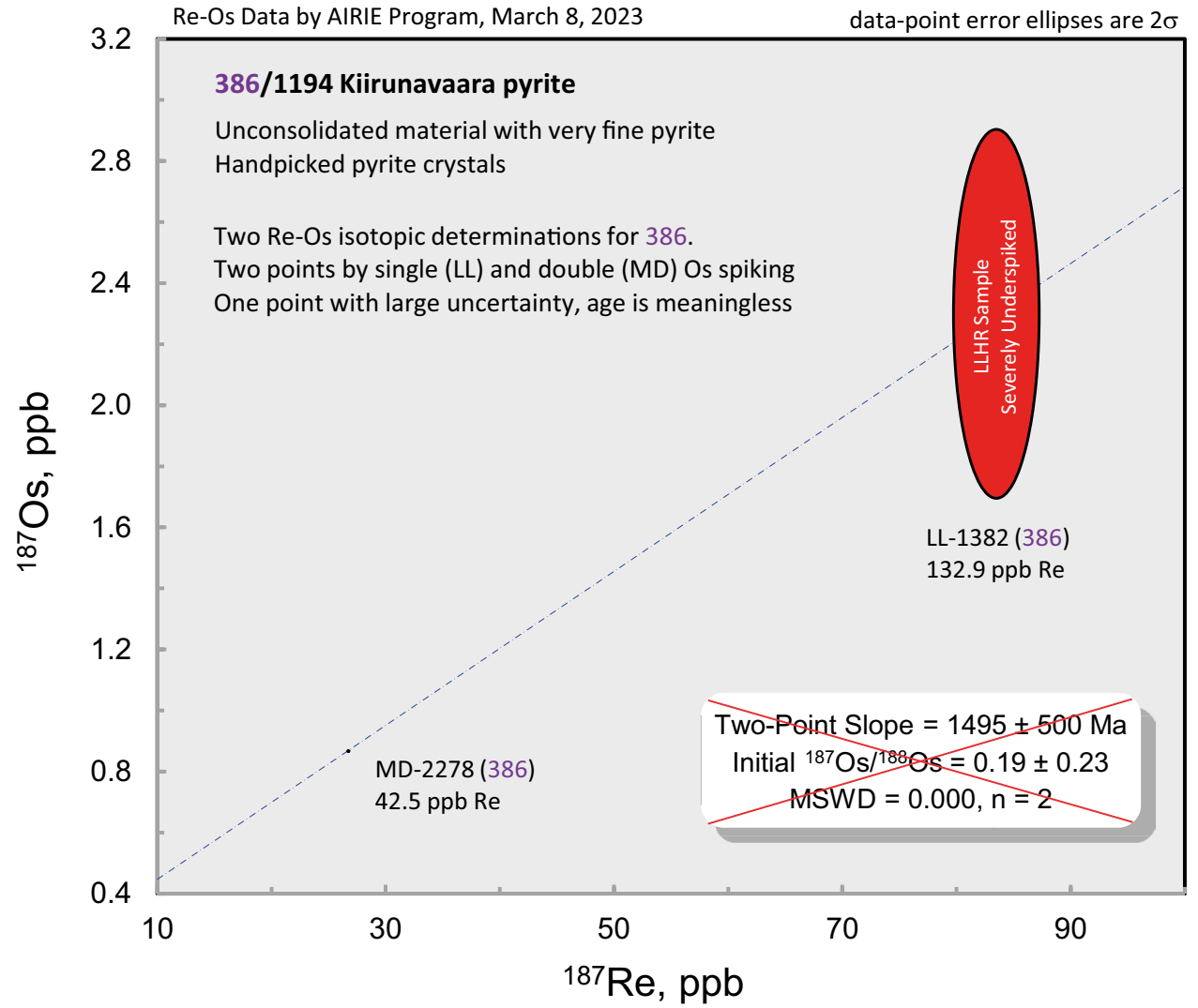


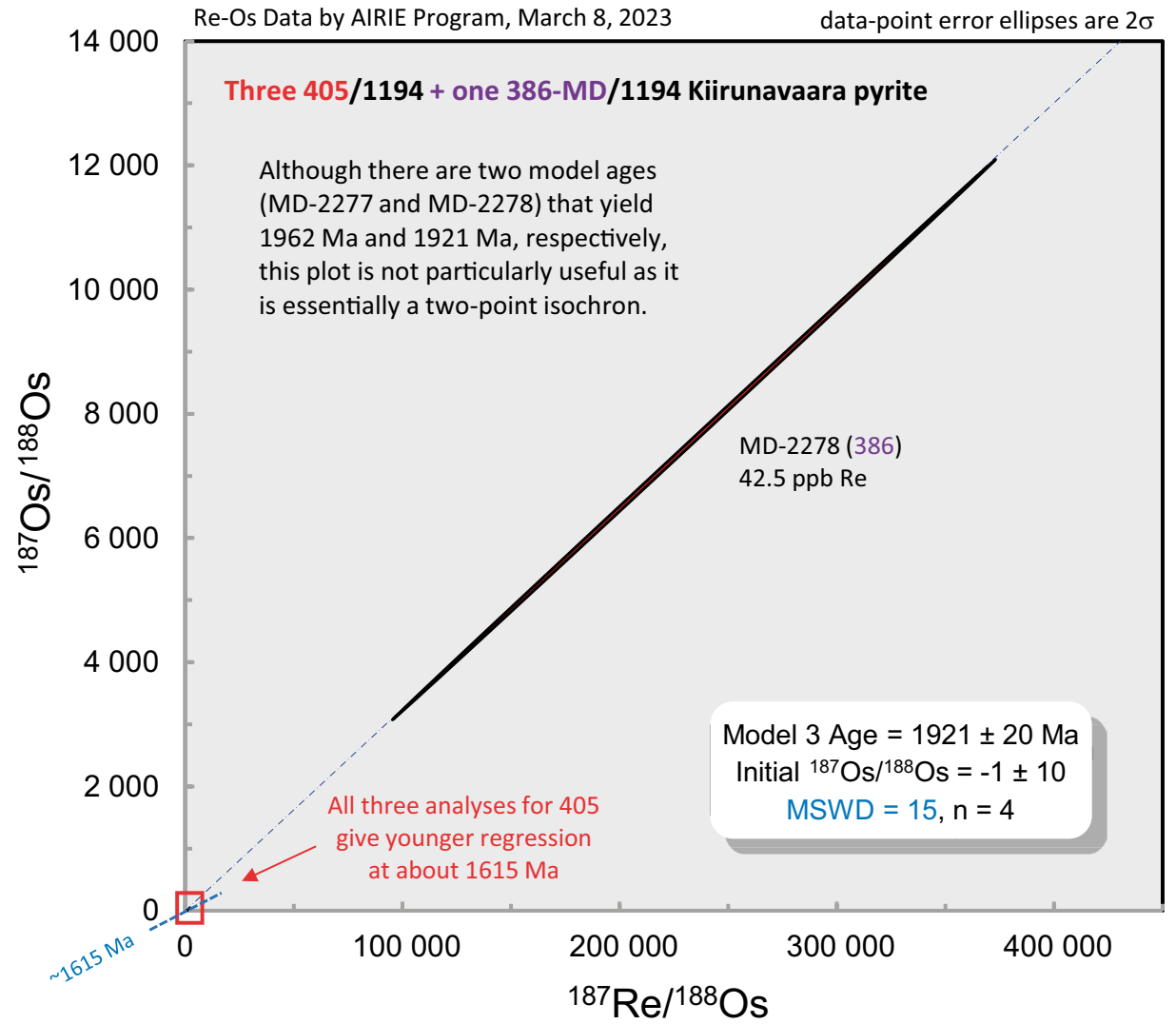
Re-Os Data by AIRIE Program, March 8, 2023

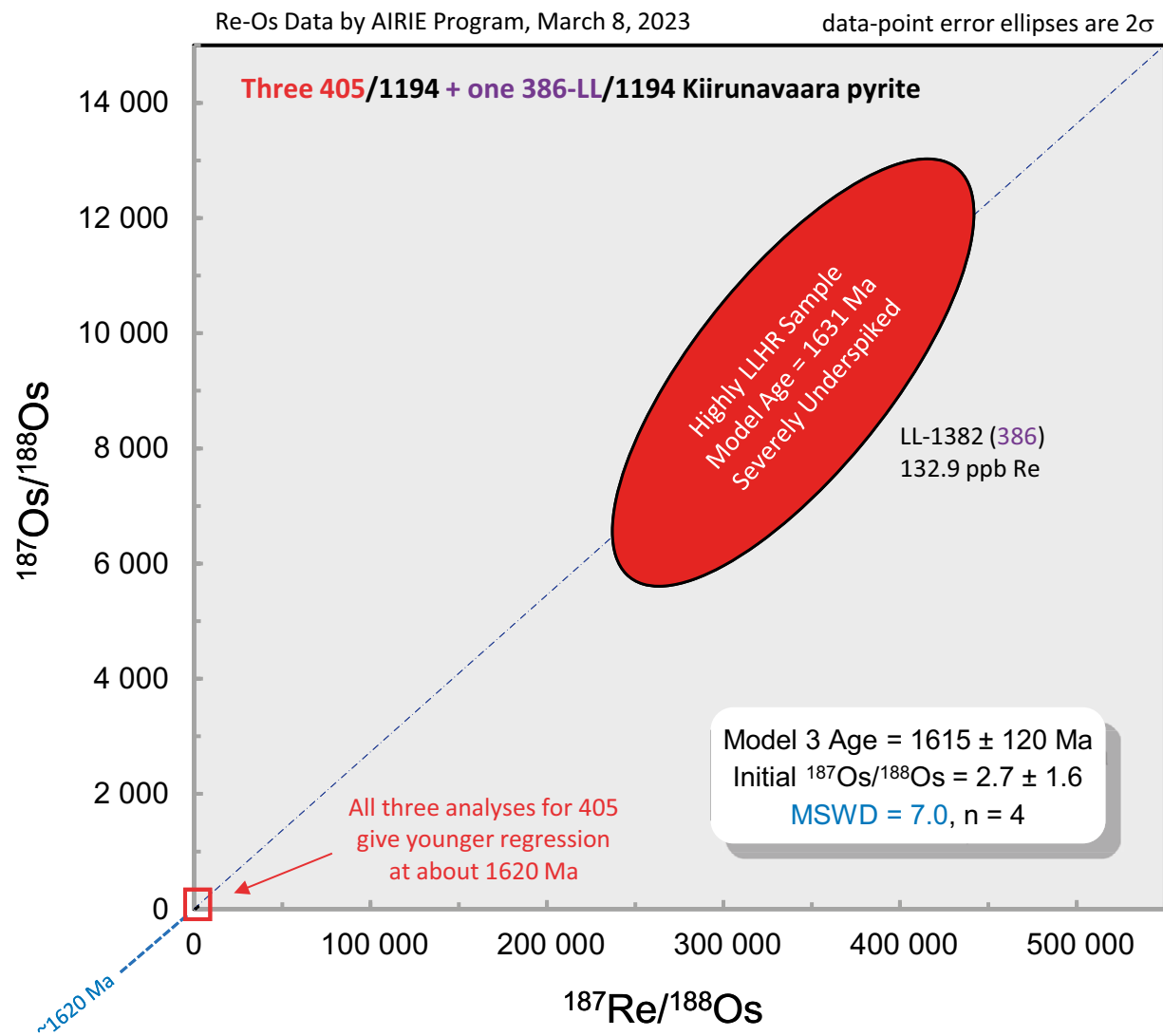
data-point error ellipses are 2σ

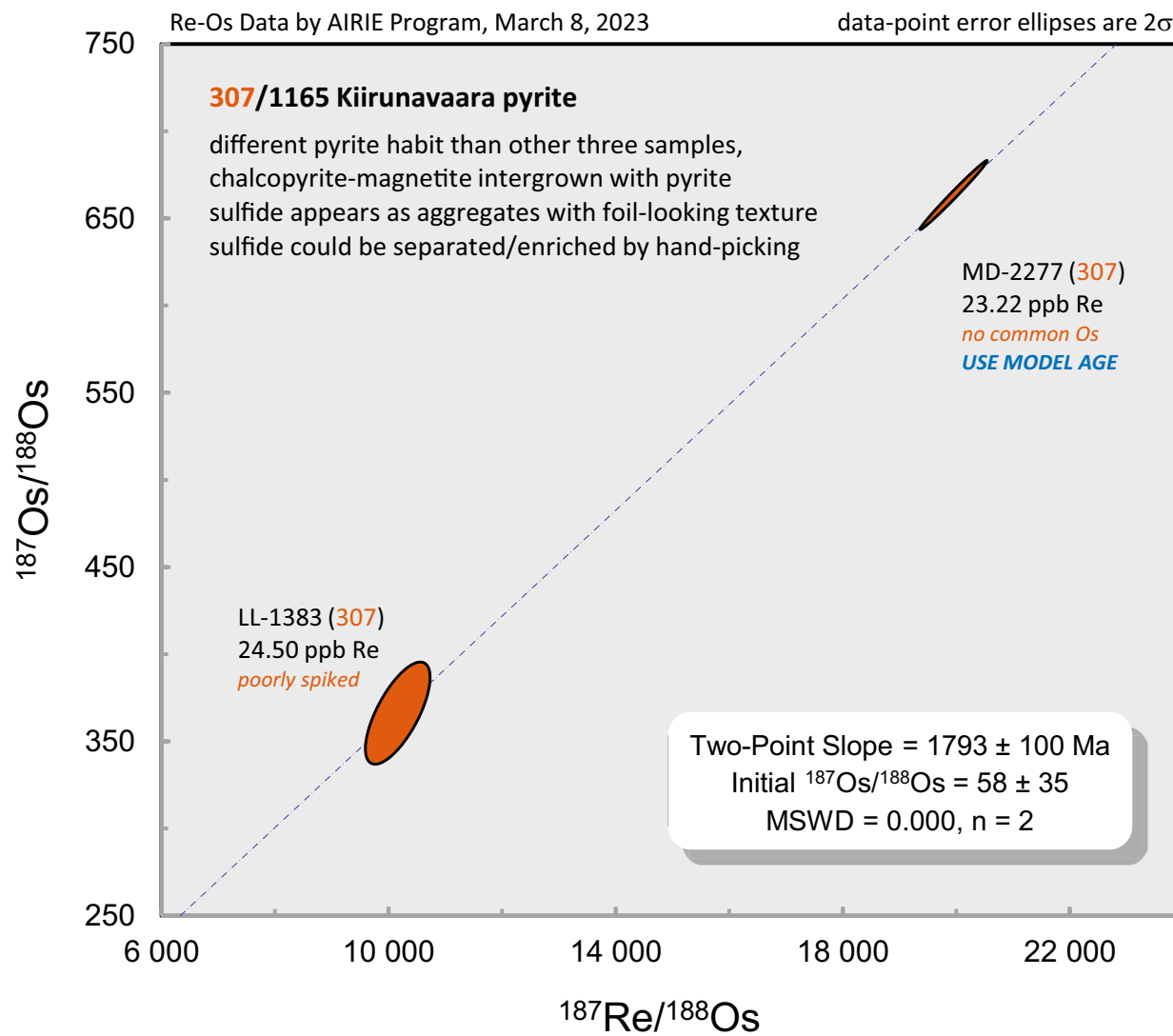


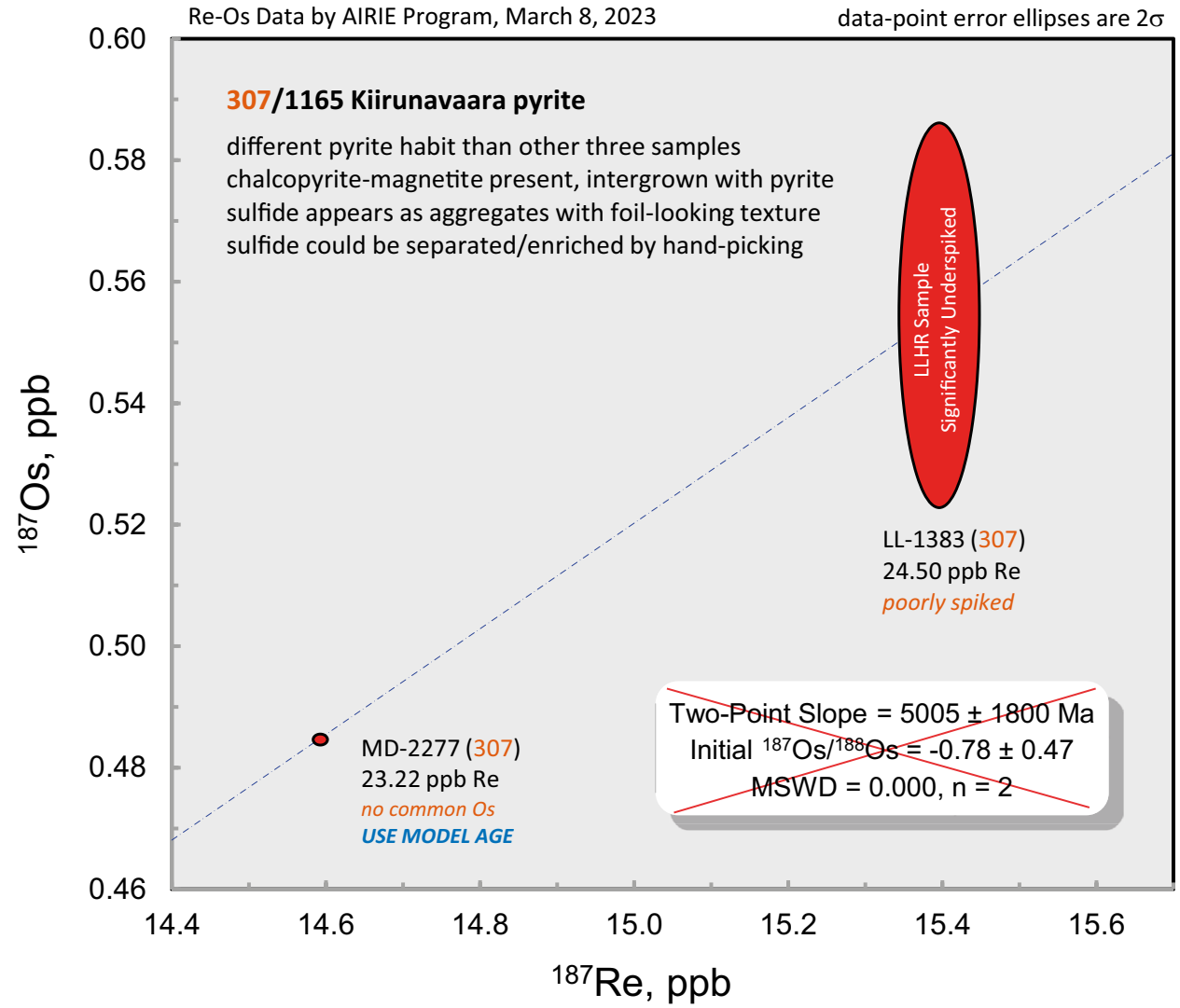


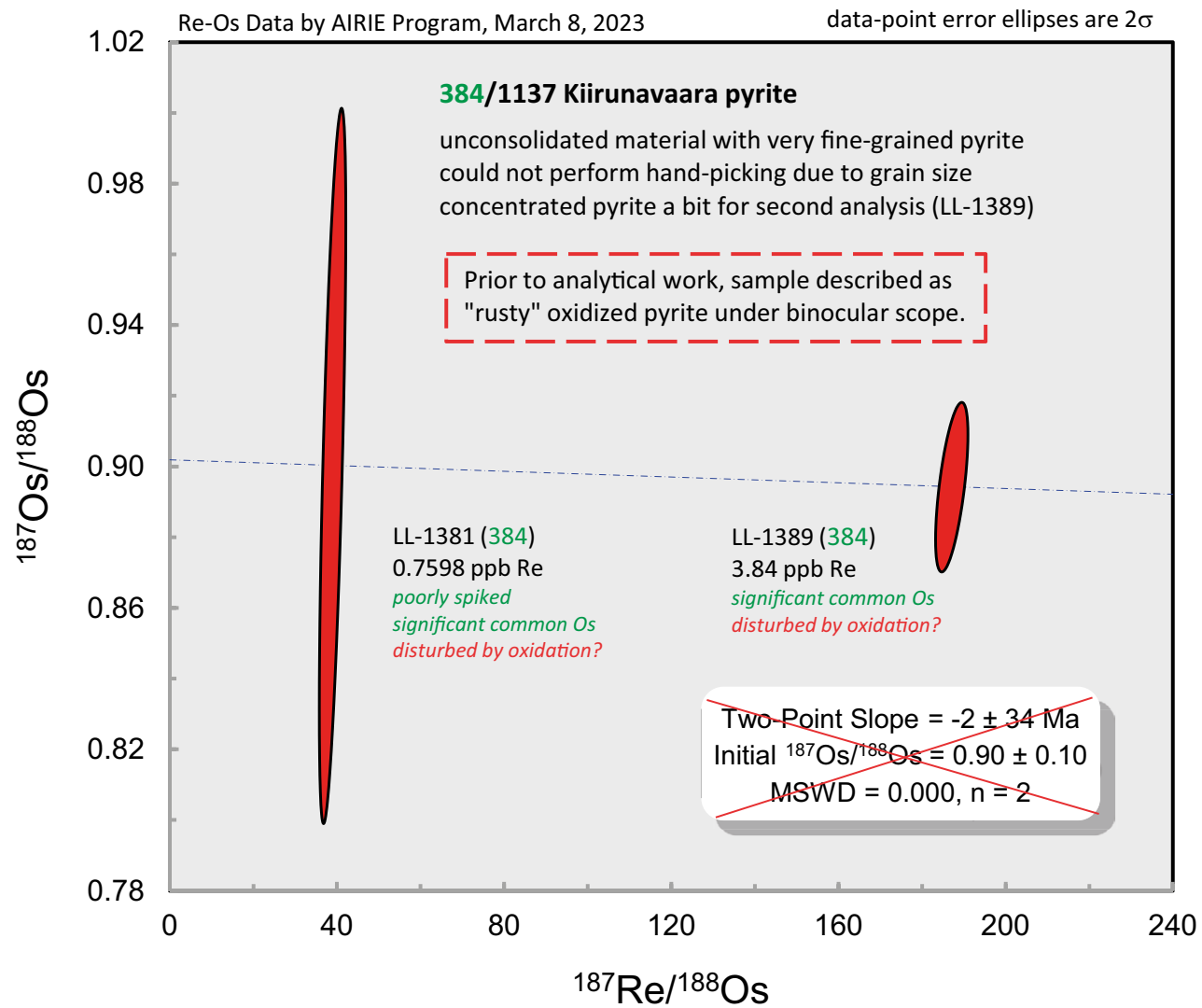


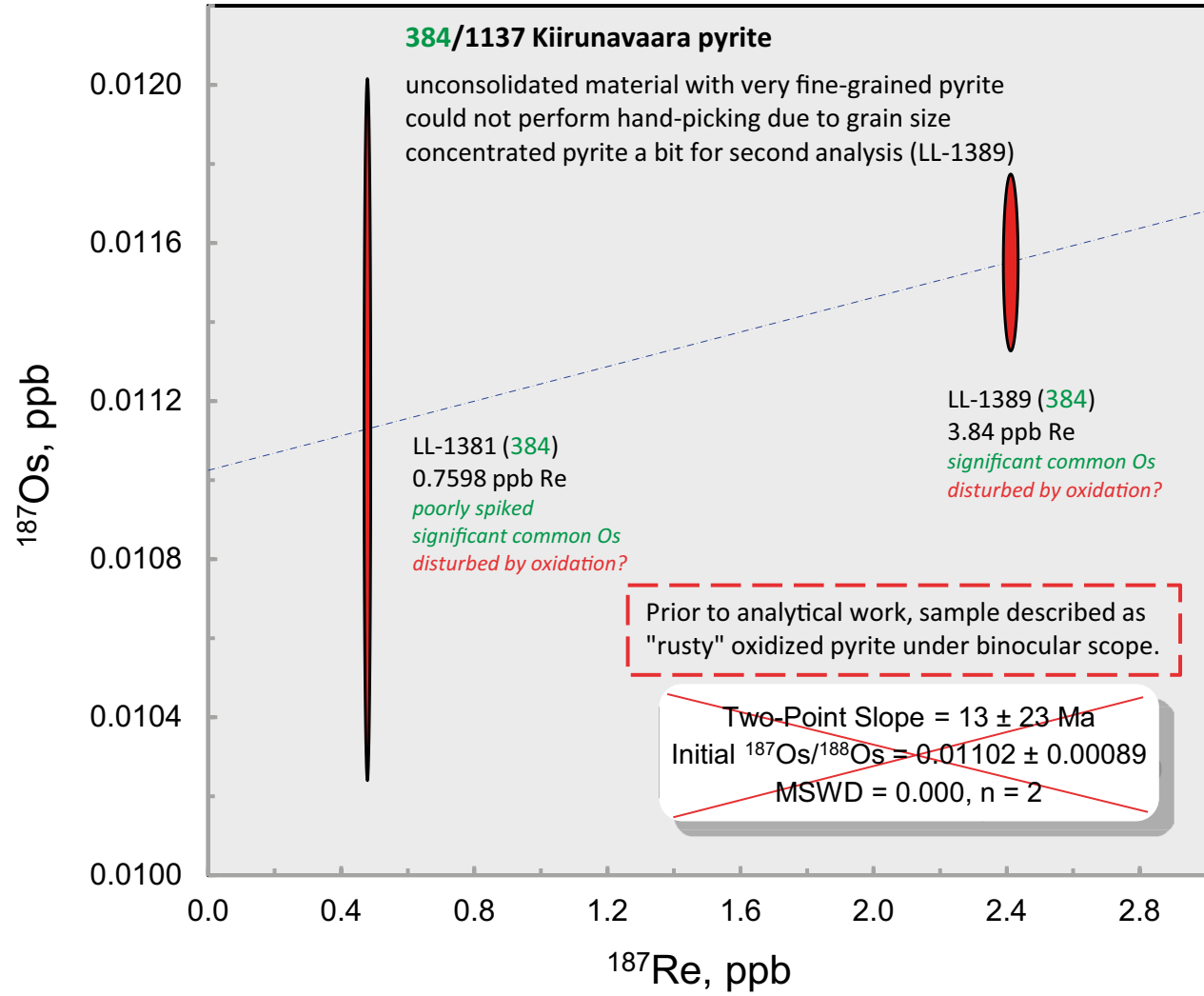


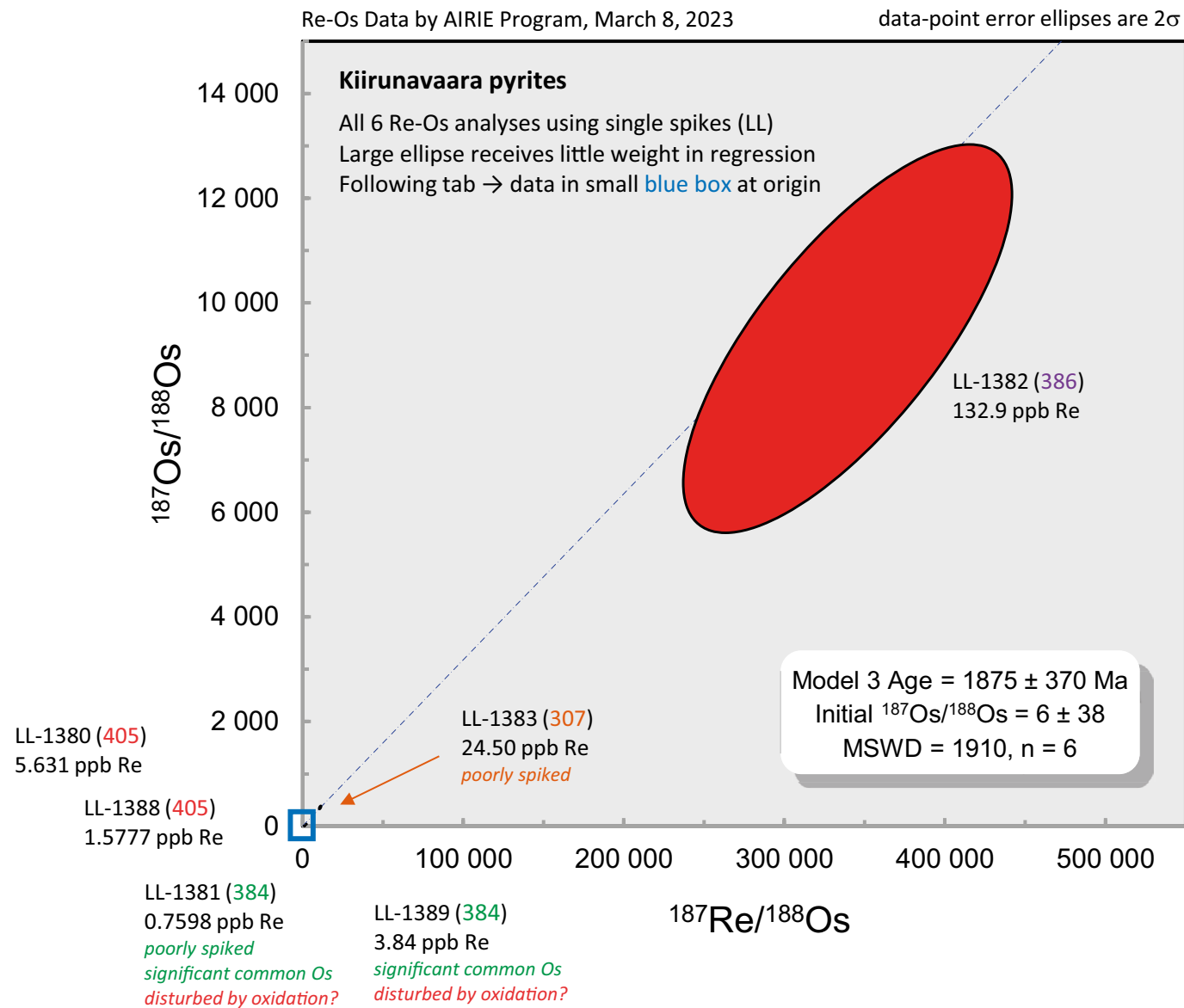


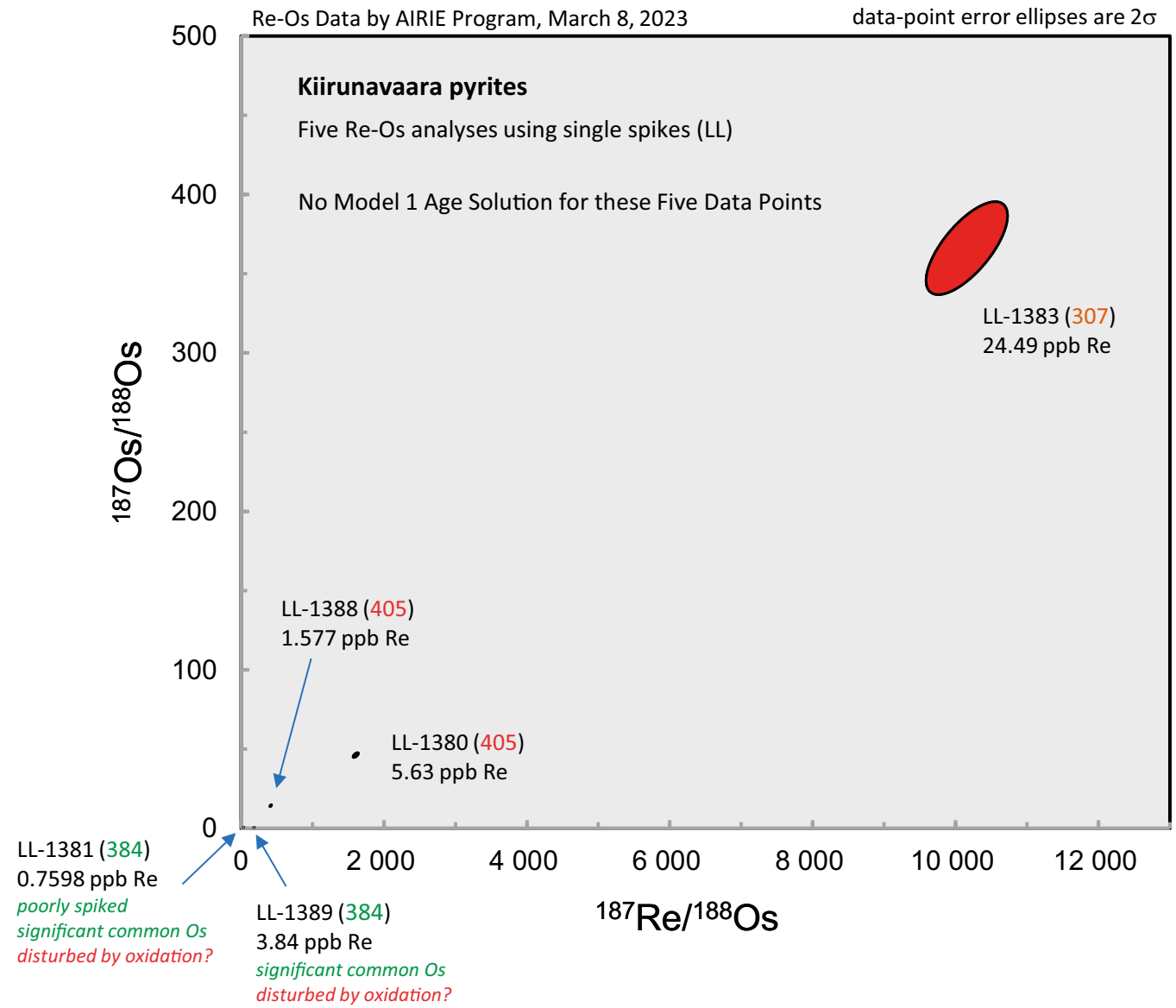


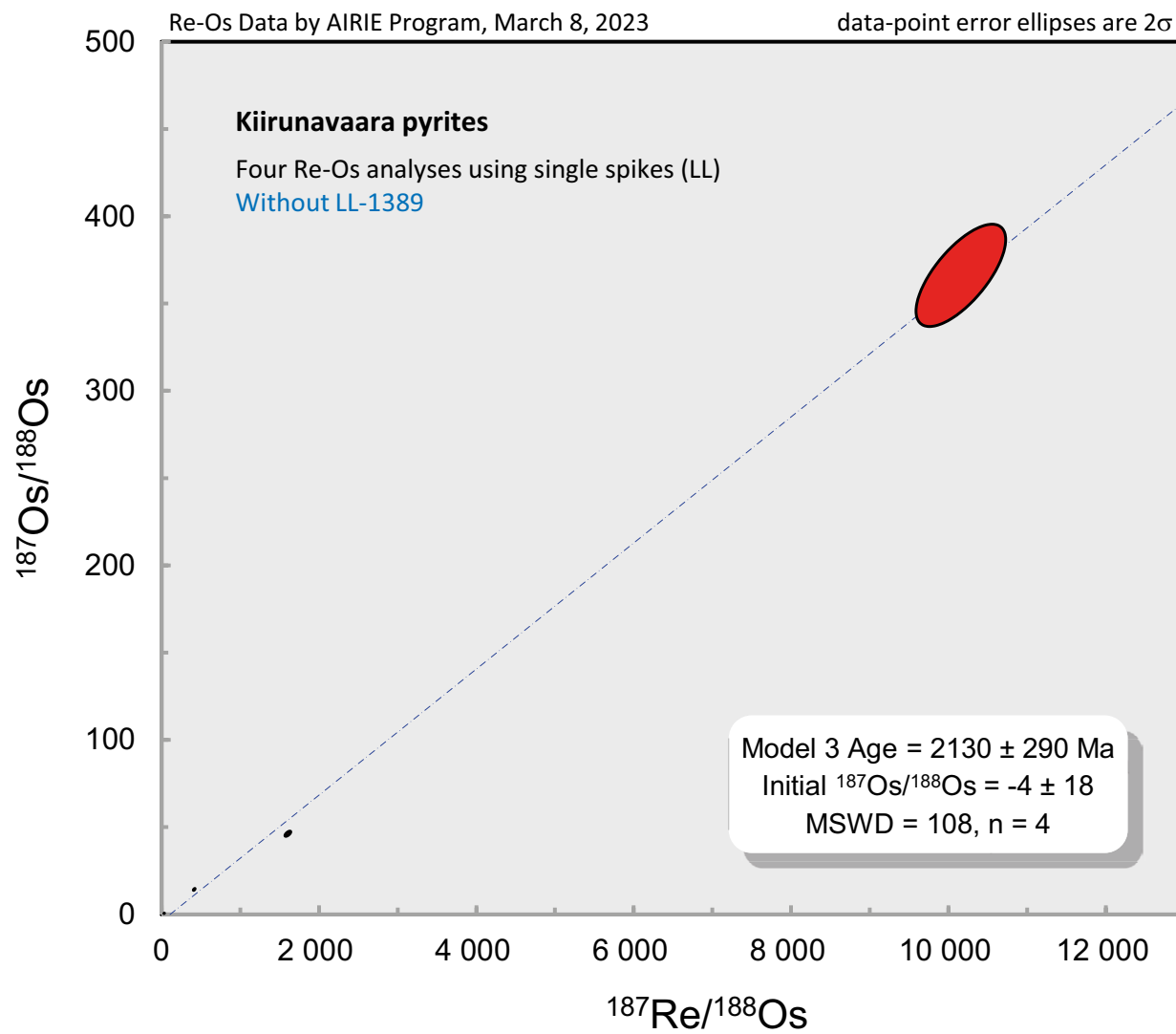


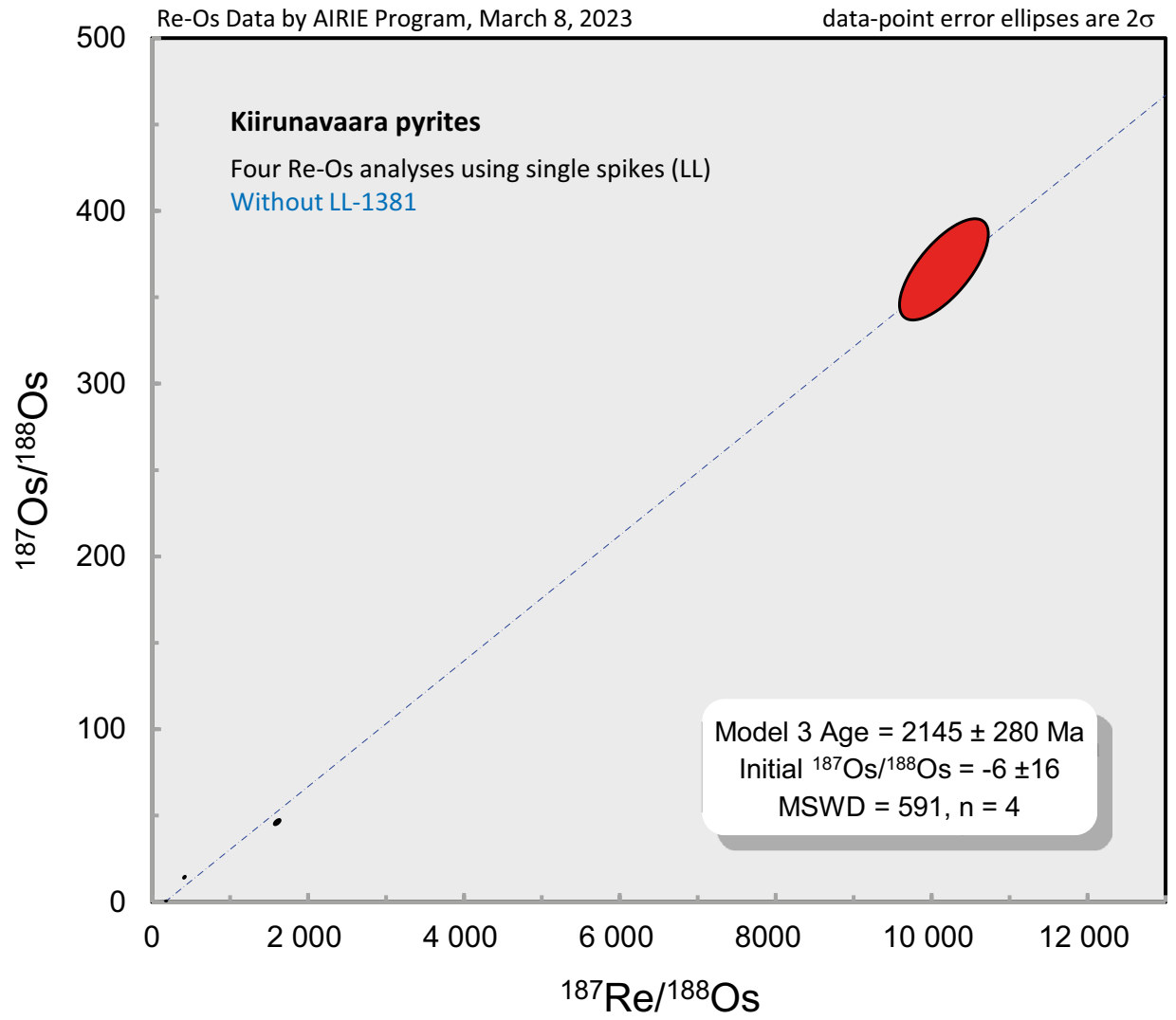


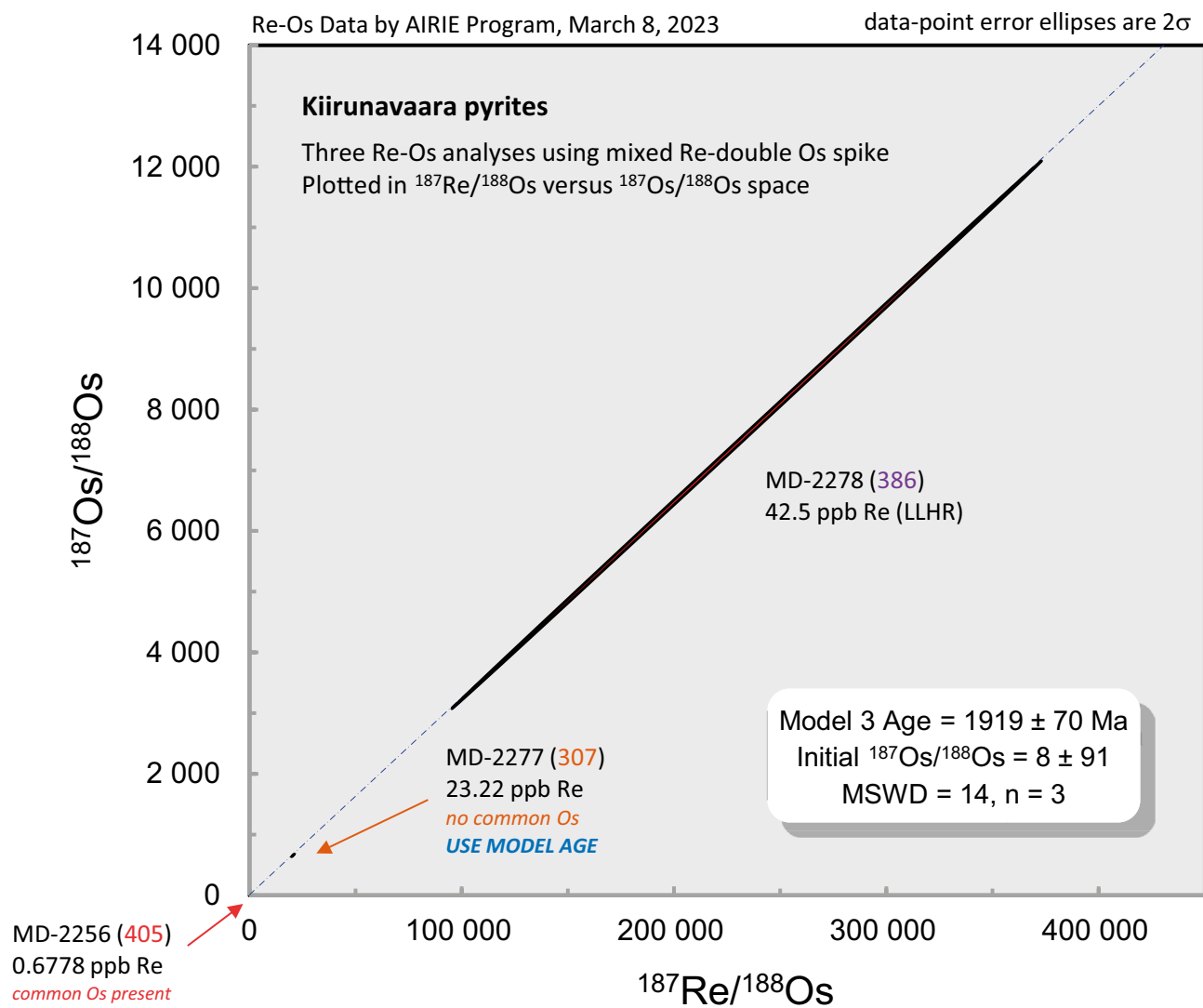


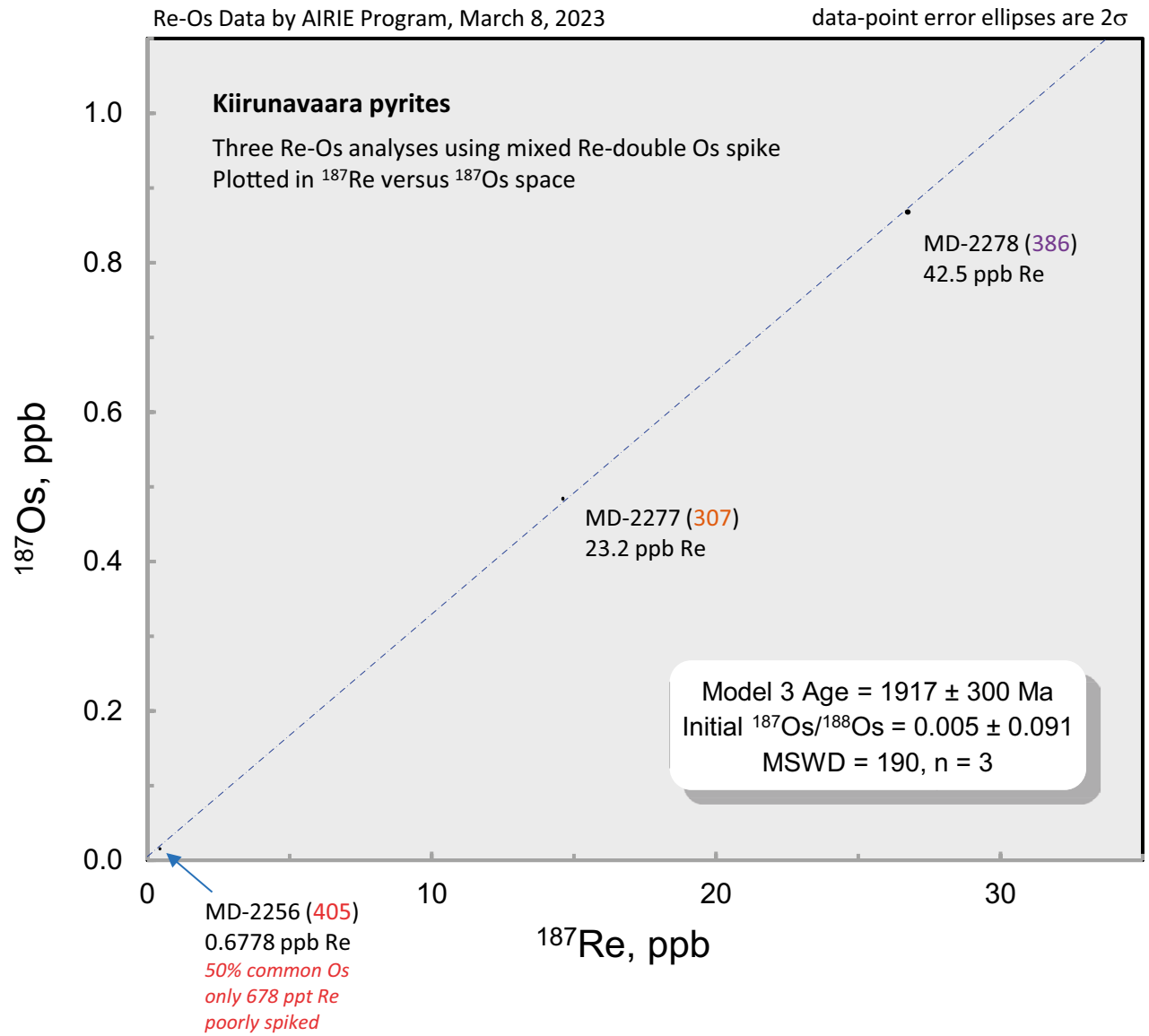




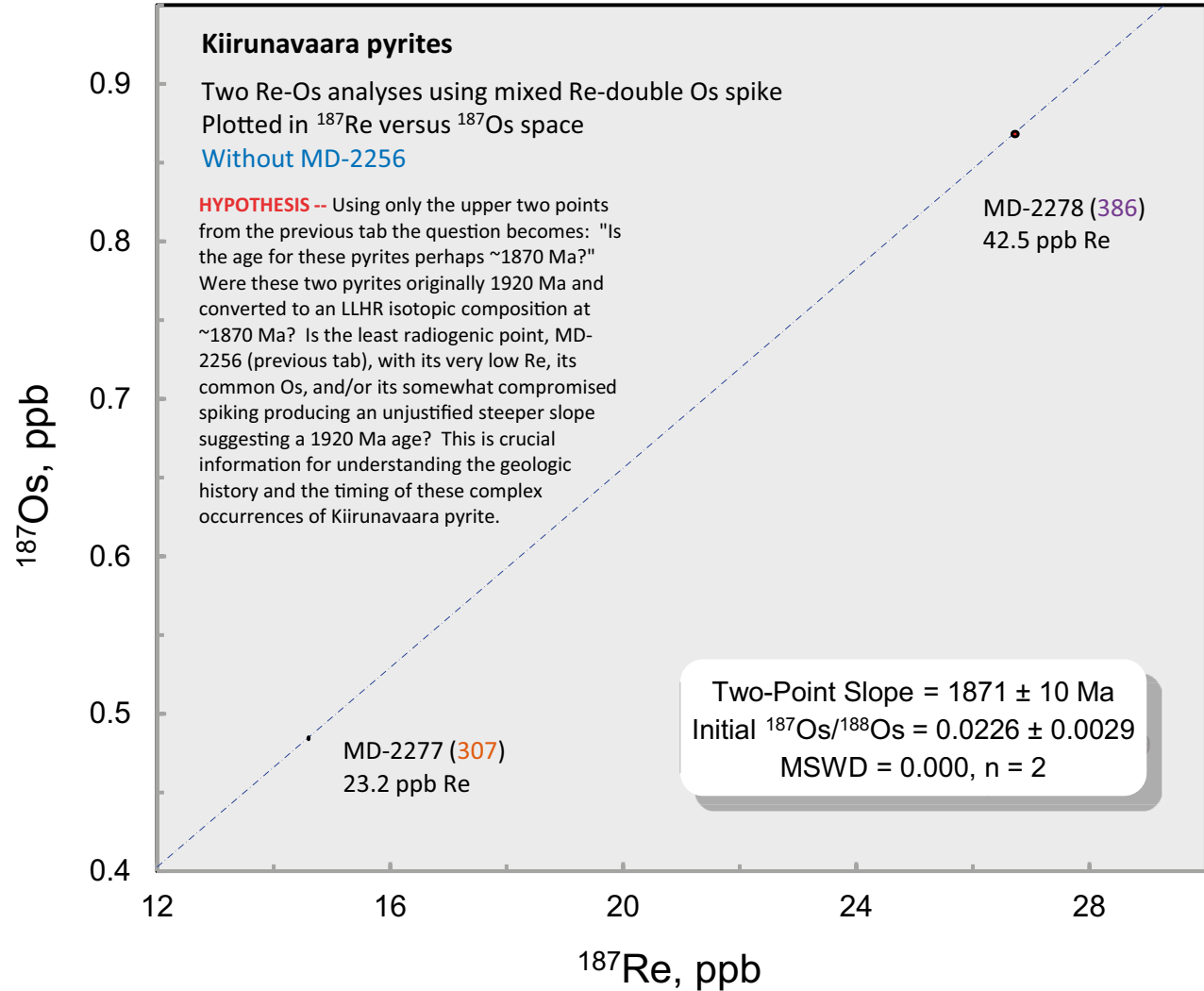








Re-Os Data by AIRIE Program, March 8, 2023

data-point error ellipses are 2σ 

Example of the ongoing work on the iron-clay interface (University of Hokkaido)

I.1 Results of SEM-EDS analysis for sample KINA2-2

Quartz, magnetite, biotite, glauconite, smectite, and calcite were found in a thin section of sample KINA 2-2. Most of the magnetite surface was covered with biotite aggregates (Figure I1-1) and the full magnetite-clay interface was rarely found (Figure I1-2). The chemical composition of clay in contact with magnetite was analysed along the line shown in Figure I1-3. The analytical results for the measured points are summarised in Table I1-1. Iron content as Fe_2O_3 was in the range from 0.67 to 0.88 and independent of distance from the magnetite-clay interface. In Figure I1-4, the magnetite-biotite interface with the clay is shown. In this case, while the iron content of the biotite was appreciable, the iron content of the smectite at the measured location was below the detection limit (as noted in Table I1-2). Although this has not been addressed here in detail, it is possible that magnetite has reacted with smectite to form a non-swelling phase (i.e. biotite) at relatively high temperature so preventing smectite incorporating iron (see also Section 7.2).

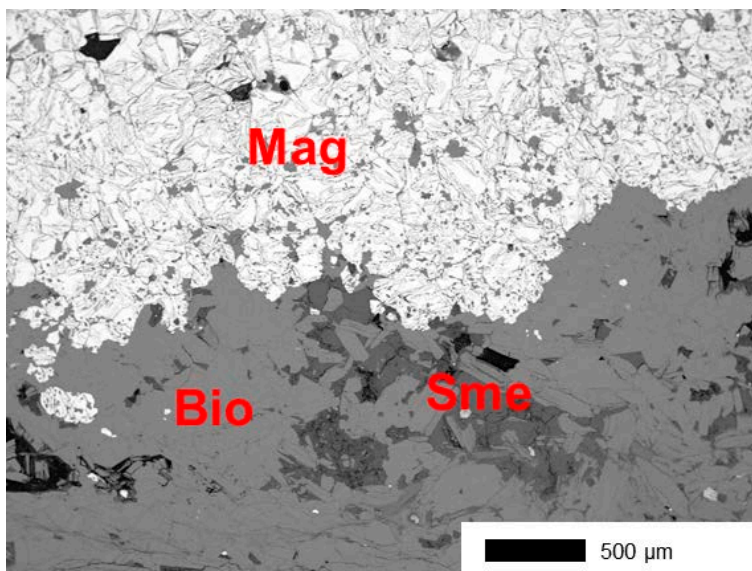


Figure I1-1. Magnetite-clay interface in sample KINA 2-2.
Mag: Magnetite Bio: Biotite Sme: Smectite.

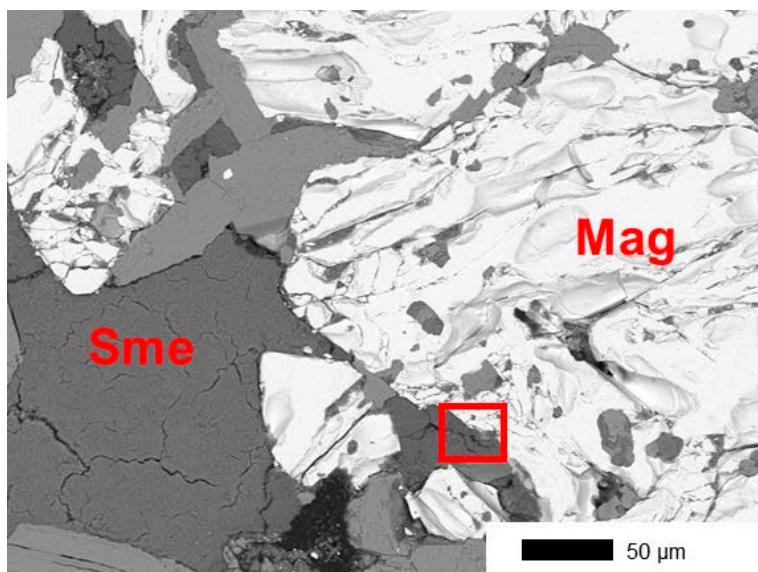


Figure II-2. Magnetite-smectite boundary in sample KINA 2-2.
Mag: Magnetite Sem: Smectite.

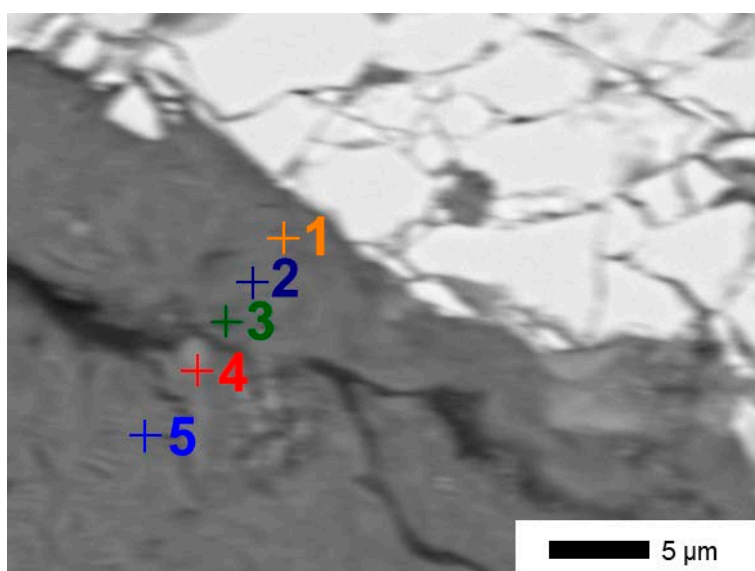


Figure II-3. Sample KINA 2-2. SEM-EDS point analysis for smectite at the magnetite-smectite interface (analysis position).

Table I1-1. Sample KINA 2-2. Results of SEM-EDS point analysis for smectite at the magnetite-smectite interface.

| Mol% | MgO | Al ₂ O ₃ | SiO ₂ | CaO | Fe ₂ O ₃ | Total |
|------|------|--------------------------------|------------------|------|--------------------------------|-------|
| 1 | 7.26 | 15.60 | 72.44 | 3.82 | 0.88 | 100 |
| 2 | 7.85 | 14.94 | 72.71 | 3.47 | 0.84 | 100 |
| 3 | 7.63 | 15.11 | 72.47 | 4.06 | 0.72 | 100 |
| 4 | 6.85 | 15.71 | 73.02 | 3.59 | 0.82 | 100 |
| 5 | 7.70 | 15.65 | 72.31 | 3.66 | 0.67 | 100 |

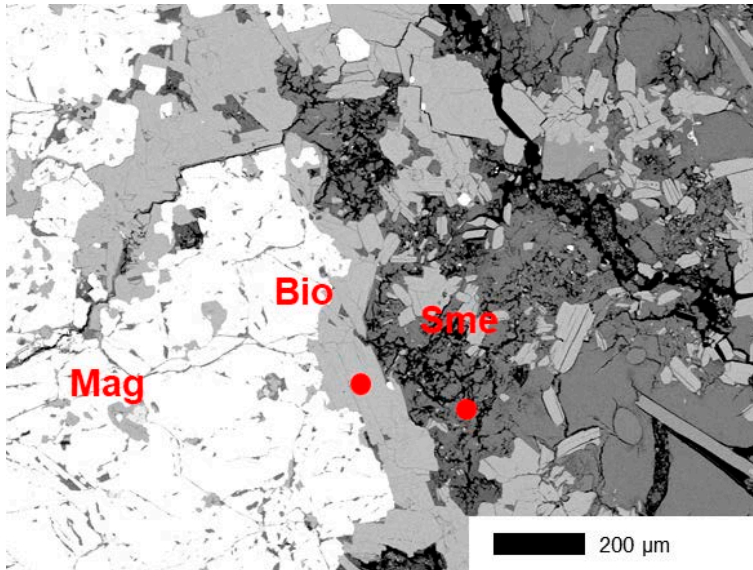


Figure II-4. Sample KINA 2-2. SEM-EDS point analysis of biotite and smectite at the magnetite-biotite boundary at the magnetite-biotite boundary (red dots indicate positions of analyses).
 Bio: Biotite Mag: Magnetite Sem: Smectite.

Table I1-2. Sample KINA 2-2. SEM-EDS point analysis results for biotite and smectite at the magnetite-biotite boundary (- indicates below detection limit).

| Mol% | MgO | Al ₂ O ₃ | SiO ₂ | CaO | K ₂ O | TiO ₂ | Fe ₂ O ₃ | Total |
|------|-------|--------------------------------|------------------|------|------------------|------------------|--------------------------------|-------|
| Sme | 8.17 | 15.55 | 72.16 | 4.11 | - | - | - | 100 |
| Bio | 28.86 | 10.23 | 46.08 | - | 7.29 | 1.57 | 5.98 | 100 |

SKB raw data for samples Kiruna 2018 and 2019

| | Density (kgm ⁻³) | Water content | Gradient (mm ⁻¹) | Hydraulic conductivity Kw (ms ⁻¹) | Swelling Pressure (kPa) | Swelling Pressure after hydraulic conductivity (kPa) | Gradient (mm ⁻¹) | Hydraulic conductivity Kw (ms ⁻¹) | Swelling pressure (kPa) | Swelling pressure after hydraulic conductivity (kPa) | Swelling Pressure (kPa) |
|-------------------------|---------------------------------|------------------|---------------------------------|---|-------------------------------|---|---------------------------------|---|-------------------------------|---|-------------------------------|
| Test No | | | deionised water | deionised water | deionised water | deionised water | 1 Mol CaCl2 | 1 Mol CaCl2 | 1 Mol CaCl2 | 1 Mol CaCl2 | deionised water after |
| Test Kiruna 2018 1 | 1876 | 0.379 | 5762 | 5.7E-13 | 1467 | 1532 | 4802 | 4.6E-13 | 887 | 891 | 1258 |
| Test Kiruna 2018 2 | 1915 | 0.333 | 5924 | 2.5E-13 | 2677 | 2723 | 4936 | 2.0E-13 | 1584 | 1606 | 2525 |
| Test Kiruna 2018 3 | 1932 | 0.310 | 5944 | 1.6E-13 | 3853 | 3894 | 10897 | 5.6E-14 | 2278 | 2474 | 3670 |
| Test Kiruna 2018 4 | 1933 | 0.309 | 11830 | 1.7E-13 | 3881 | 4086 | 8873 | 1.6E-13 | 2344 | 2387 | 3662 |
| Test Kiruna 2018 5 | 1970 | 0.276 | 11911 | 5.4E-14 | 6202 | 6417 | 8933 | 5.1E-14 | 3939 | 3981 | 5911 |
| Test Kiruna 2018 6 | 2034 | 0.294 | 11911 | 6.6E-14 | 7539 | 7730 | 8933 | 6.0E-14 | 5078 | 5141 | 7133 |
| Test Kiruna 2018 7 | 1944 | 0.301 | 14625 | 1.4E-13 | 4308 | 4493 | 11700 | 1.3E-13 | 2690 | 2683 | 4050 |
| Test Kiruna 2018 8 | 1980 | 0.259 | 14717 | 6.9E-14 | 7532 | 7722 | 11773 | 5.8E-14 | 5149 | 5219 | 7196 |
| Test Kiruna 2018 9 | 2038 | 0.238 | 14932 | 3.9E-14 | 11416 | 11562 | 11946 | 2.8E-14 | 8589 | 8677 | 11026 |
| Test Kiruna 2018 1 mQ | 1862 | 0.373 | | | 1527 | | | | | | |
| Test Kiruna 2018 1 mQ | 1910 | 0.340 | | | 2890 | | | | | | |
| Test Kiruna 2018 1 mQ | 1952 | 0.312 | | | 4362 | | | | | | |
| Test Kiruna 2018 1 mQ | 1949 | 0.306 | | | 4628 | | | | | | |
| Test Kiruna 2018 1 mQ | 1985 | 0.290 | | | 6422 | | | | | | |
| Test Kiruna 2018 1 mQ | 1995 | 0.298 | | | 6276 | | | | | | |
| Test Kiruna 2018 1 mQ | 1970 | 0.311 | | | 4821 | | | | | | |
| Test Kiruna 2018 1 mQ | 1993 | 0.276 | | | 7746 | | | | | | |
| Test Kiruna 2018 1 mQ | 2057 | 0.268 | | | 10658 | | | | | | |
| Test Kiruna 2019 mald 1 | 1948 | 0.316 | 5878 | 1.1E-12 | 2928 | 2870 | 2939 | 7.9E-13 | 1910 | | 2701 |
| Test Kiruna 2019 mald 2 | 1957 | 0.299 | 5724 | 6.4E-13 | 3967 | 3964 | 2862 | 4.9E-13 | 2721 | | 3725 |
| Test Kiruna 2019 mald 3 | 1959 | 0.297 | 5583 | 5.4E-13 | 3962 | 3968 | 2792 | 4.0E-13 | 2722 | | 3731 |
| Test Kiruna 2019 mald 4 | 1960 | 0.310 | 5751 | 1.9E-12 | 3627 | | 2876 | 1.5E-12 | 2445 | | 3300 |
| Test Kiruna 2019 mald 5 | 1948 | 0.279 | 5765 | 5.5E-13 | 4286 | | 2882 | 4.2E-13 | 2865 | | 4054 |
| Test Kiruna 2019 mald 6 | 1983 | 0.304 | 5586 | 6.0E-13 | 4570 | | 2793 | 4.7E-13 | 3185 | | 4353 |
| Test Kiruna 2019 mald 7 | 1967 | 0.264 | 5795 | 3.8E-13 | 5497 | 5493 | 4829 | 2.9E-13 | 3816 | 3747 | 5184 |
| Test Kiruna 2019 mald 8 | 1973 | 0.270 | 5485 | 3.7E-13 | 5559 | 5551 | 4571 | 3.0E-13 | 3851 | 3788 | 5264 |
| Test Kiruna 2019 mald 9 | 2015 | 0.261 | 5543 | 2.4E-13 | 8253 | 8222 | 4619 | 1.5E-13 | 6028 | 5952 | 7836 |